

**Combined Electromagnetic Heating and Solvent Injection  
for Heavy Oil Recovery**

by

Lanxiao Hu

A thesis submitted in partial fulfillment of the requirements for the degree of

Doctor of Philosophy

in

Petroleum Engineering

Department of Civil and Environmental Engineering  
University of Alberta

©Lanxiao Hu, 2018

## ABSTRACT

To meet the increasing energy demand, there is a growing interest in exploiting the unconventional hydrocarbon resources such as heavy oil, bitumen, and shale oil. Combined electromagnetic (EM) heating and solvent injection is recently proposed to enhance oil recovery. The EM heating, converting the electrical energy into heat, reduces carbon emission caused by steam generation, avoids excessive water usage, and holds great potential to recover heavy oil from reservoirs where steam-based methods are less effective. The solvent injection also plays an important role in this hybrid process, which further thins the heavy oil by dilution, reduces the residual oil saturation, forms a vapor chamber to facilitate the gravity drainage, and supplements the natural energy for oil production.

The combined EM heating and solvent injection is a multi-physics process involving the propagation and absorption of electromagnetic waves, the frictional heat generated by the interactions of the polarized reservoir materials and electromagnetic waves, and the heat/mass transfer in porous media. We are currently at the initial stage of the study of this hybrid process. It is of great importance to measure the fundamental data, conduct experimental investigations, and develop mathematical models, for achieving better understanding, design, and optimization of this hybrid technique.

In the dissertation, we first use an open-ended co-axial probe method to measure the permittivity of the constituents of oil sands, oil sands mixtures with different porosity and water saturation, *n*-hexane/bitumen mixtures, and *n*-hexane/oil sands mixtures; the permittivity data ranging from 200 MHz to 10 GHz are obtained. Based on the experimental results obtained, the commonly used mixing models are evaluated in terms of their accuracies in predicting the permittivity of *n*-hexane/oil sands mixtures.

Next, we build an experimental setup to investigate the essential recovery mechanisms and to evaluate the effects of major influential factors on the recovery performance of this hybrid process. A series of experiments including premixed experiments (the solvent is premixed with heavy oil in the sand pack) and dynamic flow experiments (the solvent is injected into the sand pack) are performed to examine the effects of EM heating power, solvent type, and water saturation on the recovery performance. We also explore different ways of combining the EM heating and solvent injection to achieve a better performance of this hybrid process. In addition, the compositions of the produced oil samples are characterized by saturates, aromatics, resins, and asphaltenes tests to examine the *in-situ* upgrading effect of EM heating.

Then, we investigate the effect of EM heating on changing the petrophysical properties of formation rocks. Different formation rocks, including continental shale, Berea-sandstone, tight sandstone, and Indiana-carbonate, are exposed to EM heating for three minutes. Subsequently, scanning electron microscopy (SEM), energy dispersive X-ray (EDX), N<sub>2</sub> adsorption/desorption, and core flooding experiments are used to characterize the petrophysical properties changes of rock samples caused by EM heating. Oven-heating experiments are also conducted to distinguish the effects of EM heating and conductive heating. Lab-scale finite element simulations are performed to verify the experimental results and to further analyze the temperature and stress distribution of rock samples under EM heating.

Lastly, we propose a semi-analytical model to simulate the oil recovery of the combined EM heating and solvent injection in SAGD-liked wells; the semi-analytical model is computationally efficient and preserves the essential mechanisms governing the hybrid process. The model consists of three major parts: estimation of the temperature distribution of EM heating, calculation of the solvent distribution, and evaluation of the oil flow rate based on the

temperature and solvent distributions. The proposed model is validated against the experimental results. Finally, we use the proposed semi-analytical model to explore the dependence of recovery performance on the major process parameters, as well as determine the optimal process parameters that can yield the maximum economic benefits.

## PREFACE

This research is conducted under the supervision of Dr. Huazhou Andy Li (supervisor) and Dr. Tayfun Babadagli (co-supervisor) at the University of Alberta. The introduction in chapter 1 and contributions and recommendations in chapter 6 are my original work.

Chapter 2 of this thesis was published as Hu, L., Li, H., and Ahmadloo, M. 2018. Determination of the permittivity of *n*-hexane/oil sands mixtures over the frequency range of 200 MHz to 10 GHz. *Can. J. Chem. Eng.*, Preprint. I was responsible for conducting the experiments, analyzing the data, and drafting the manuscript. Dr. Majid Ahmadloo provided expertise in the electromagnetics, helped analyze data, and revised the manuscript. Dr. Huazhou Andy Li was the supervisory author and was involved with concept formation and manuscript composition.

Chapter 3 of this thesis was published as Hu, L., Li, H., Babadagli, T., and Ahmadloo, M. 2017. Experimental investigation of combined electromagnetic heating and solvent assisted gravity drainage for heavy oil recovery. *J. Petr. Sci. Eng.* **154**: 589–601. I was responsible for conducting the experiments, analyzing the data, and drafting the manuscript. Dr. Tayfun Babadagli helped design the experiments and revised the manuscript. Dr. Majid Ahmadloo helped resolve the technical difficulties encountered when operating the electromagnetic heating device. Dr. Huazhou Andy Li was the supervisory author and was involved with concept formation and manuscript composition.

Chapter 4 of this thesis was presented at the SPE Trinidad and Tobago Section Energy Resources Conference held on 25–26 June 2018, in Port of Spain, Trinidad and Tobago. I was responsible for conducting the experiments, analyzing the data, performing the simulations, and drafting the manuscript. Dr. Tayfun Babadagli helped initiated the idea of this study, helped design the

experiments, and revised the manuscript. Dr. Huazhou Andy Li was the supervisory author and was involved with concept formation and manuscript composition.

Chapter 5 of this thesis was published as Hu, L., Li, H., Babadagli, T. and Ahmadloo, M. 2018. A semi-analytical model for simulating the combined electromagnetic heating and solvent-assisted gravity drainage. *SPE J.* **23** (4): 1248-1270. I was responsible for developing the analytical model, analyzing the data, performing the simulations, and drafting the manuscript. Dr. Majid Ahmadloo provided expertise in the electromagnetics. Dr. Tayfun Babadagli provided great suggestions for modifying the manuscript and helped revise it. Dr. Huazhou Andy Li was the supervisory author and was involved with concept formation and manuscript composition.

## **DEDICATION**

This dissertation is dedicated to my dearest parents,

Mrs. Junlian Wang and Mr. Songchun Hu.

## ACKNOWLEDGEMENTS

I would like to express my sincere gratitude to my supervisor, Dr. Huazhou Andy Li, for providing the precious opportunity to study in his research group and his continuous guidance, advice, and support throughout my Ph.D. studies. I would also like to thank my co-supervisor, Dr. Tayfun Babadagli, for sharing his knowledge and providing many valuable suggestions. It is an honor to be supervised by two great supervisors; I have learned much from their creative, meticulous, industrious, and productive research style.

I would like to thank my committee members, Dr. Shengnan Chen, Dr. Ergun Kuru, Dr. Tayfan Babadagli, Dr. Nobou Maeda, Dr. Hongbo Zeng, and Dr. Huazhou Andy Li, for taking precious time to review my dissertation and providing valuable comments and suggestions on my research.

This research was financially supported by Dr. Huazhou Andy Li's NSERC Discovery Grant (NSERC RGPIN 05394) and Dr. Tayfun Babadagli's NSERC Industrial Research Chair in Unconventional Oil Recovery (industrial partners are Petroleum Development Oman, Total E&P Recherche Development, SiGNa Oilfield Canada, Husky Energy, Saudi Aramco, Devon, APEX Eng. and BASF).

I appreciate the support and help from the past and present group members of Dr. Huazhou Andy Li's research group and Dr. Tayfun Babadagli's EOGRRRC research group at the University of Alberta. I would also like to extend my appreciation to lab technicians, Mr. Lixing Lin, Mr. Todd Kinnee, Ms. Mihaela Istratescu, for their assistance in conducting the lab experiments, and research coordinator Ms. Pam Keegan for her assistance in manuscript preparations.

Last but not least, I am grateful to my parents for their unconditional support and love.

# TABLE OF CONTENTS

ABSTRACT .....	ii
PREFACE .....	v
DEDICATION .....	vii
ACKNOWLEDGEMENTS .....	viii
TABLE OF CONTENTS .....	ix
LIST OF TABLES .....	xiii
LIST OF FIGURES.....	xiv
CHAPTER 1 INTRODUCTION .....	1
1.1 Background .....	1
1.2 Literature Review .....	3
1.2.1 Maxwell’s Equations .....	3
1.2.2 Low-Frequency Heating.....	4
1.2.3 Inductive Heating .....	5
1.2.4 High-Frequency Heating .....	6
1.3 Problem Statement and Objectives .....	8
1.4 Solution Methodology.....	10
1.5 Thesis Structure.....	14
1.6 References .....	15
CHAPTER 2 DETERMINATION OF THE PERMITTIVITY OF.....	18
<i>N</i> -HEXANE/OIL SANDS MIXTURES OVER THE FREQUENCY .....	18
RANGE OF 200MHZ TO 10GHZ.....	18
Summary .....	19
2.1 Introduction .....	19
2.2 Theory .....	22
2.3 Experimental Section .....	24
2.3.1 Materials .....	24
2.3.2 Experimental Setup and Procedures .....	26
2.4 Results and Discussion.....	27
2.4.1 Permittivity of Constituents of Oil Sands.....	27
2.4.2 Effect of Water Content on Permittivity of Oil Sands.....	29
2.4.3 Effect of <i>n</i> -Hexane Addition .....	32
2.5 Evaluation of Mixing Models Used for the Permittivity Prediction of Oil Sands .....	37
2.5.1 Commonly-Used Mixing Models .....	37
2.5.2 Evaluation of Prediction Accuracy of Various Mixing Models.....	38
2.6 Conclusions .....	43

2.7 References .....	46
CHAPTER 3 EXPERIMENTAL INVESTIGATION OF COMBINED ELECTROMAGNETIC HEATING AND SOLVENT ASSISTED GRAVITY DRAINAGE FOR HEAVY OIL RECOVERY .....	49
Summary .....	50
3.1 Introduction .....	51
3.2 Statement of Problem .....	55
3.3 Experimental .....	56
3.3.1 Materials .....	56
3.3.2 Experimental Setup and Procedures .....	59
3.4 Results and Discussion.....	61
3.4.1 Microwave’s Selective Heating.....	61
3.4.2 Effects of Influencing Factors on the Performance of This Hybrid Process .....	63
3.4.2.1 EM Heating Power.....	63
3.4.2.2 Initial Water Saturation.....	65
3.4.2.3 Solvent Types and EM Heating Power .....	68
3.4.2.4 Combining Strategies of EM Heating and Solvent Injection.....	71
3.4.3 Further Analyses of the Experimental Results .....	75
3.4.3.1 Solvent Concentration in Heavy Oil .....	75
3.4.3.2 Asphaltene Precipitation and Breakage .....	77
3.4.3.3 Residual Oil Saturation .....	78
3.4.3.4 Analysis on the Energy Utilization .....	81
3.5 Conclusions .....	82
3.6 References .....	85
CHAPTER 4 EFFECT OF ELECTROMAGNETIC HEATING ON THE CHANGES IN PETROPHYSICAL PROPERTY OF FORMATION ROCKS .....	89
Summary .....	90
4.1 Introduction .....	91
4.2 Theory .....	94
4.3 Experimental .....	95
4.3.1 Materials .....	95
4.3.2 Characterization of Core Samples .....	96
4.3.3 Experimental Setup and Procedures .....	97
4.4 Experimental Results.....	98
4.4.1 Temperature Responses of Different Types of Formation Rocks .....	98

4.4.2 Effect of EM Heating on Shale Samples .....	98
4.4.2.1 Pyrite Content .....	99
4.4.2.2 Clay Content .....	99
4.4.2.3 SEM/EDX Characterization.....	102
4.4.2.4 N <sub>2</sub> Adsorption and Desorption Characterization .....	105
4.4.3 Comparison with Oven Heating Experiments .....	109
4.5 Numerical Analyses .....	111
4.5.1 Model Description .....	112
4.5.2 Assumptions .....	113
4.5.3 Governing Equations .....	114
4.5.4 Boundary Conditions and Mesh .....	115
4.5.5 Simulation Results .....	118
4.6 Conclusions and Further Remarks .....	124
4.7 References .....	126
CHAPTER 5 A SEMI-ANALYTICAL MODEL FOR SIMULATING THE COMBINED ELECTROMAGNETIC HEATING AND SOLVENT-ASSISTED GRAVITY DRAINAGE .	131
Summary .....	132
5.1 Introduction .....	133
5.2 Theory .....	137
5.3 Semi-Analytical Model .....	140
5.3.1 Model Description .....	140
5.3.2 Temperature Distribution by EM Heating.....	141
5.3.3 Solvent Concentration Distribution Ahead of the Chamber Edge .....	146
5.3.4 Calculation Procedure.....	150
5.4 Model Validation.....	153
5.5 Results and Discussion.....	157
5.5.1 Residual Oil Saturations .....	157
5.5.2 Effect of EM Heating Power .....	159
5.5.3 Effect of Solvent Type and Solvent Injection Pressure .....	162
5.5.4 Effect of Initial Reservoir Temperature.....	164
5.5.5 Chamber Edge Location and Average Oil Flow Rate .....	165
5.6 Economic Analysis.....	168
5.7 Conclusions .....	171
5.8 References .....	176

5.9 Appendix ..... 181  
CHAPTER 6 CONTRIBUTIONS AND RECOMMENDATIONS ..... 188  
6.1 Scientific and Practical Contributions to the Literature and Industry ..... 189  
6.2 Recommendations for Future Work ..... 190  
BIBLIOGRAPHY ..... 192

## LIST OF TABLES

<b>Table 2-1</b> Summary of previous measurements on dielectric properties of oil sands in the literature .....	21
<b>Table 2-2</b> GC and SARA analysis results of the bitumen sample.....	25
<b>Table 2-3</b> Viscosity-temperature data for bitumen and n-hexane/bitumen mixtures .....	25
<b>Table 2-4</b> Detailed experimental schemes used in this study.....	26
<b>Table 2-5</b> Comparison of the measured permittivity in this study and permittivity data from literature .....	29
<b>Table 2-6</b> Summary of AARDs for predicting the permittivity of ( <i>n</i> -hexane/) oil sands mixtures given by different mixing models .....	40
<b>Table 2-7</b> Coefficient values for calculating the loss factor of the ( <i>n</i> -hexane/) oil sands mixtures .....	41
<b>Table 3-1</b> Coefficients values in Equations (3-3) and (3-4).....	59
<b>Table 3-2</b> Experimental schemes employed in this study .....	61
<b>Table 3-3</b> Critical properties of n-hexane, n-octane and heavy oil and their binary interaction parameters used in the PR EOS model.....	76
<b>Table 3-4</b> Flash calculation results for premixed solvent/heavy oil mixtures under elevated temperatures and atmospheric pressure.....	76
<b>Table 3-5</b> Results on saturates, aromatics, resins and asphaltenes (SARA) tests for the original heavy oil and recovered oils that eliminate the influence of solvent presence .....	77
<b>Table 4-1</b> Dielectric properties of common materials in the formation rocks.....	95
<b>Table 4-2</b> Mineral compositions and TOCs of the core samples used in this study.....	96
<b>Table 4-3</b> Images of shale samples with different pyrite contents taken before and after EM heating experiments.....	100
<b>Table 4-4</b> Images of shale samples with different clay contents taken before and after EM heating experiments. ....	101
<b>Table 4-5</b> Porosity and permeability of Berea sandstone, tight sandstone, and Indiana carbonate measured before and after EM heating. ....	110
<b>Table 4-6</b> Material properties used in the numerical simulations .....	114
<b>Table 5-1</b> Reservoir and fluid properties used in the semi-analytical model. ....	144
<b>Table 5-2</b> Reservoir electrical properties at 13.56 MHz and room temperature. ....	144
<b>Table 5-3</b> Summary of the correlations used in the calculations and the corresponding parameters appearing in the correlations. ....	147
<b>Table 5-4</b> Detailed properties of the sandpack used in the experimental tests (Hu et al. 2016a). .....	155
<b>Table 5-5</b> Calculated residual oil saturations for different production scenarios. Eq. 5-22 is used to perform these calculations.....	159
<b>Table 5-6</b> Parameters used in the economic analysis. ....	169
<b>Table 5-7</b> Solvent-oil ratios calculated for the different test cases.....	170
<b>Table 5-8</b> Energy oil ratios calculated for different test cases. ....	171

## LIST OF FIGURES

<b>Figure 1-1</b> Schematic of the low-frequency heating for heavy oil recovery (Adapted from Bera and Babadagli 2015). The blue arrows indicate the electrical current flow.....	5
<b>Figure 1-2</b> Schematic of the inductive heating applied in a SAGD well pair (Adapted from Koolman et al. 2008).....	6
<b>Figure 1-3</b> Schematic of the combined EM heating and solvent injection for heavy oil recovery (Hu et al. 2018a).....	8
<b>Figure 1-4</b> Overview of the methodology used in this study .....	13
<b>Figure 2-1</b> Schematic of the experimental setup for conducting the permittivity measurements.	27
<b>Figure 2-2</b> Permittivity of the constituents of oil sands: a) dielectric constant, and b) loss factor. The solid lines represent the average values of the measured permittivity, while the corresponding belts are error bars of the measurements (standard deviation).....	28
<b>Figure 2-3</b> Permittivity of oil sands with different porosity: a) dielectric constant, and b) loss factor. The solid lines represent the average values of the measured permittivity, while the corresponding belts are error bars of the measurements (standard deviation).....	30
<b>Figure 2-4</b> Permittivity of oil sands with different water saturation: a) dielectric constant, and b) loss factor. The solid lines represent the average values of the measured permittivity, while the corresponding belts are error bars of the measurements (standard deviation).....	31
<b>Figure 2-5</b> Permittivity of <i>n</i> -hexane/bitumen mixtures: a) dielectric constant, and b) loss factor. The solid lines represent the average values of the measured permittivity, while the corresponding belts are error bars of the measurements (standard deviation).....	33
<b>Figure 2-6</b> Permittivity of <i>n</i> -hexane/oil sands mixtures: a) dielectric constant, and b) loss factor. The solid lines represent the average values of the measured permittivity, while the corresponding belts are error bars of the measurements (standard deviation).....	34
<b>Figure 2-7</b> Conceptual pictures of water distribution in oil sands: a) before <i>n</i> -hexane addition, and b) after <i>n</i> -hexane dilution. ....	36
<b>Figure 2-8</b> Comparison of the measured permittivity and calculated ones by different mixing models: a) dielectric constant of oil sands (the case with a porosity of 31 %), b) loss factor of oil sands (the case with a porosity of 31 %), c) dielectric constant of <i>n</i> -hexane/oil sands mixture (the case M1), and d) loss factor of <i>n</i> -hexane/oil sands mixture (the case M1).....	41
<b>Figure 3-1</b> Viscosity-temperature relationships of heavy oil sample and heavy oil samples mixed with solvents. As for heavy oil and solvent mixtures, points are measured data and lines are calculated by Lobe’s mixing rule. The viscosities of pure solvents are calculated by Eq. (3-3)..	58
<b>Figure 3-2</b> Measured refractive indexes for heavy oil diluted with different weight fractions of solvents. Solvent <i>n</i> -hexane and <i>n</i> -octane are used in these tests.....	59
<b>Figure 3-3</b> Schematic of the experimental setup used for conducting the combined EM heating and solvent assisted gravity drainage for heavy oil recovery.....	60
<b>Figure 3-4</b> Temperature profiles of bulk materials when they are exposed to microwave heating. The microwave power level is 100. ....	62
<b>Figure 3-5</b> Schematic of (a) combined EM heating and solvent-assisted gravity drainage, (b) fluid flow within EM excited zone.....	63
<b>Figure 3-6</b> Effect of microwave heating power level on (a) recovery factors and (b) temperature profiles (Experiments #1-3 in Table 3-2). When the heating power level is 10, the temperature rise is not sufficient to initiate gravity drainage of heavy oil.....	64
<b>Figure 3-7</b> Effect of initial water saturation on (a) recovery factors and (b) temperature profiles	

(Experiments #2, #4 and #5 in Table 3-2).....	66
<b>Figure 3-8</b> Effect of solvent types and EM heating powers on (a) recovery factors and (b) temperature profiles (Experiment #1, #2 and #6-11 in Table 3-2). In this Figure, black, blue, and red lines represent the cases without solvent, with solvent n-hexane, and solvent n-octane, respectively; the dotted, solid, and dash lines correspond to the experiments conducted at EM heating power levels of 10, 20, and 30, respectively. ....	69
<b>Figure 3-9</b> Oil recovery factors of heavy oil, heavy oil premixed with solvent n-hexane and n-octane at EM heating power levels of 10, 20, and 30 (Experiments #1-3, #6-11). In the Exp. #1-3, no solvent is premixed with heavy oil. In Exp. #6-8, 10wt% n-hexane is premixed with heavy oil. In Exp. #9-11, 10wt% n-octane is premixed with heavy oil. ....	70
<b>Figure 3-10</b> Effect of simultaneous and alternate EM heating and n-hexane injection on (a) recovery factors and (b) temperature profiles (Experiment #12-14 in Table 3-2). In Figure. 3-10a, the lines represent the recovered oil and solvent mixtures, while the points correspond to the final oil recovery factor after deducting solvent from the mixtures. ....	72
<b>Figure 3-11</b> Effect of simultaneous and alternate EM heating and n-octane injection on (a) recovery factors and (b) temperature profiles (Experimental #16-18 in Table 3-2). In Figure 3-11a, the lines represent the recovered oil and solvent mixtures, while the points correspond to the final oil recovery factors after deducting solvent from the mixtures. ....	73
<b>Figure 3-12</b> Digital images of sand pack taken after simultaneous EM heating and 1 PV of solvent injection: (a) n-hexane (Experiment #12 in Table 3-2), and (b) n-octane (Experiment #16 in Table 3-2).....	75
<b>Figure 3-13</b> Parity charts of the measured and calculated $S_{or}$ within the sand pack: (a) calculated $S_{or}$ is based on Eq. (3-11)-Cardwell and Parsons' equation, and (b) calculated $S_{or}$ is based on Eq. (3-12)-Kulkarni and Rao' correlation .....	81
<b>Figure 3-14</b> Energy utilization efficiency of the experimental runs carried out in this study. Alternate EM heating and continuous injection of 0.5 PV n-octane consumes the least energy for generating the same oil recovery among all the experimental schemes tested. ....	82
<b>Figure 4-1</b> Schematic of the experimental setup used for investigating the property variations of formation rocks under EM heating.....	97
<b>Figure 4-2</b> Temperature profiles of different types of rocks under EM heating. The shale sample used in this test is S1. ....	98
<b>Figure 4-3</b> SEM images of sample S1 and S4 taken before and after EM heating. ....	103
<b>Figure 4-4</b> SEM/EDX analyses of sample S1: (a) backscatter image of the sample S1 and (b) the corresponding chemical composition distributions.....	104
<b>Figure 4-5</b> SEM/EDX analysis of sample S4: (a) BSE image of the sample S4 and (b) the corresponding chemical composition distributions.....	105
<b>Figure 4-6</b> N <sub>2</sub> adsorption/desorption results: (a) adsorption/desorption isotherms and (b) pore size distributions of sample S5 before and after EM heating.....	107
<b>Figure 4-7</b> N <sub>2</sub> adsorption/desorption results: (a) adsorption/desorption isotherms and (b) pore size distributions of sample S6 before and after EM heating.....	109
<b>Figure 4-8</b> Photos of tight sandstone saturated with water: (a) before EM heating and (b) after EM heating. ....	111
<b>Figure 4-9</b> Schematic of the simulation model. The dimensions of the waveguide and oven cavity are 7.8cm×5cm×1.8cm and 26.7cm×27cm×18.8cm, respectively. The dimensions (radius × height) of the glass plate and core sample are 11.35cm×0.6cm and 1.27cm×3cm, respectively. ....	112

<b>Figure 4-10</b> Schematic of the core samples used in the numerical simulation study: (a) homogenous model and (b) layered model. The dashed line in Figure 4-10a is the cutting line AB which will be used to illustrate the simulation result in Section 4.5.5. In Fig 4-10b, the red, blue, cyan, green, yellow, and grey colors represent quartz, clay, dolomite, pyrite, organic content, and feldspar, respectively.....	113
<b>Figure 4-11</b> Illustration of different boundaries: (a) symmetric boundary (green part), (b) peripheral boundary (red part), and (c) contact boundary (blue part).....	117
<b>Figure 4-12</b> Mesh configuration of the simulation.....	117
<b>Figure 4-13</b> Comparison of the measured and simulated temperatures on S1.....	118
<b>Figure 4-14</b> Temperature profiles of the homogeneous core model after (a) 10s, (b) 20s, and (c) 30s of EM heating.....	119
<b>Figure 4-15</b> First principal stress distribution of the homogeneous core model after (a) 10s, (b) 20s, and (c) 30s of EM heating.....	120
<b>Figure 4-16</b> Third principal stress distribution of the homogeneous core model after (a) 10s, (b) 20s, and (c) 30s of EM heating.....	120
<b>Figure 4-17</b> Temperature profiles of the layered core model after (a) 10s, (b) 20s, and (c) 30s of EM heating.....	121
<b>Figure 4-18</b> First principal stress distribution of the layered core model after (a) 10s, (b) 20s, and (c) 30s of EM heating.....	122
<b>Figure 4-19</b> Third principal stress distribution of the layered core model after (a) 10s, (b) 20s, and (c) 30s of EM heating.....	122
<b>Figure 4-20</b> Simulation results of (a) temperature, (b) first principal stress, and (c) third principal stress along the cutline AB. In these figures, the Q, C, D, P, O, and F stand for quartz, clay, dolomite, pyrite, organic content, and feldspar, respectively.....	124
<b>Figure 5-1</b> Schematic of the dipole rotation and ion conduction under an alternating electric field.....	138
<b>Figure 5-2</b> Schematic of the combined EM heating and solvent-assisted gravity drainage with a SAGD-like well configuration.....	140
<b>Figure 5-3</b> Flow chart of the calculation procedure for the proposed semi-analytical model....	153
<b>Figure 5-4</b> Schematic of the experimental setup used for conducting the combined EM heating and solvent assisted gravity drainage for heavy oil recovery (Adapted from Hu <i>et al.</i> 2016a)..	154
<b>Figure 5-5</b> Experimental temperature data of the sandpack of the combined EM heating and <i>n</i> -hexane-assisted gravity drainage (Adapted from Hu <i>et al.</i> 2016a).....	156
<b>Figure 5-6</b> Comparison of the measured diluted-oil mass flow rates and the predicted ones by the proposed semi-analytical model.....	157
<b>Figure 5-7</b> Summary of the calculated oil rates (subplots a, c, and e), and cumulative oil productions (subplots b, d, and f) versus time for all the production scenarios.....	162
<b>Figure 5-8</b> Calculated (a) oil rate, (b) average chamber edge temperature, (c) solvent concentration at the chamber edge, and (d) solvent diffusion length versus time. Propane is injected at 1500 kPa, and EM heating is implemented with power levels of 15 kW, 30 kW, and 45 kW. The green circles in Figure 8a indicate what happens in the oil rates during the transition from the chamber spreading stage to the chamber falling stage.....	164
<b>Figure 5-9</b> Calculated (a) solvent concentration at the chamber edge, (b) solvent diffusion length and diffusivity, (c) solvent rate, and (d) average chamber edge temperature versus time for different cases. Propane and <i>n</i> -butane are injected at 1500 kPa and 2500 kPa, and EM heating is conducted at 45 kW. In Figure 9b, the solid lines represent the solvent diffusion length, while the	

dash lines represent the solvent diffusivity. ....	166
<b>Figure 5-10</b> Calculated (a) oil rates and (b) cumulative oil production versus time for different initial reservoir temperatures. Propane is injected at 1500 kPa and EM heating is conducted at 45 kW. $T_{res}$ is the initial reservoir temperature. ....	167
<b>Figure 5-11</b> Illustration of the evolution of the chamber-edge locations of the case of EM heating at 45 kW and butane injection at 1500 kPa. In this plot, the orange point represents the injector/heater, while the black point represents the producer. ....	167
<b>Figure 5-12</b> Comparison of average oil flow rates provided by different production scenarios. ....	168
<b>Figure 5-13</b> Comparison of the NPVs provided by different production scenarios. ....	170
<b>Figure 5A-1</b> Schematic showing how to calculate the EM excited zone width. ....	182
<b>Figure 5B-1</b> Schematic of how to transform the coordinate system from $(w, h)$ to $(\xi, \eta)$ . ....	184
<b>Figure 5C-1</b> Illustration of the drainage zone and its integrating range used in the oil flow rate integral calculation: (a) chamber spreading stage calculated by Eq. 5-19a, and (b) chamber falling stage calculated by Eq. 5-19b. The darker areas represent the drainage zones which are calculated by Eq. 5-19. ....	187

# CHAPTER 1 INTRODUCTION

## 1.1 Background

Heavy oil and bitumen account for about 70% of the world total oil reserves (Alboudwarej et al. 2006). The biggest challenge of heavy oil/bitumen recovery is their large viscosity. Various methods have been proposed to overcome this challenge; based on the viscosity-reduction mechanisms, these methods can be classified into two major categories: heat-based methods and solvent-based methods. The frequently used *in-situ* thermal recovery methods such as steam/hot water flooding, cyclic steam stimulation (CSS), and steam-assisted gravity drainage (SAGD) (Butler 1997), significantly reduce the viscosity of heavy oil/bitumen due to a temperature rise caused by the released latent heat of steam. However, these steam-based methods suffer from a high energy intensity, large water consumption, and great environmental footprint. For instance, a typical SAGD project has an energy oil ratio of about 7.5 GJ/m<sup>3</sup>, which will emit about 0.38 tonnes of CO<sub>2</sub> to provide the steam to recover 1 m<sup>3</sup> of oil (Hassanzadeh and Harding 2016). The common solvent-based methods include vapor extraction (VAPEX) (Butler and Mokrys 1989) and cyclic solvent injection (CSI) (Ivory et al. 2010) which reduces the viscosity by solvent dilution. These solvent approaches reduce the energy intensity and suit for the water-hostile reservoirs but suffer from a low recovery rate. To incorporate the merits of both approaches, several hybrid processes have been proposed such as expanding solvent-SAGD process (ES-SAGD) (Nasr et al. 2003), solvent aided process (SAP, SA-SAGD) (Gupta and Gittins 2006; Gupta et al. 2010), N-Solv (Nenniger and Nenniger 2008), and warm VAPEX (Rezaei et al. 2010). The hybrid approach is either co-injecting solvent with steam or injecting heated solvent into the reservoirs.

The combined electromagnetic (EM) heating and solvent injection provides another hybrid solution, which enhances the oil recovery through both EM heating and solvent dilution. EM heating, converting the electrical energy into heat, reduces carbon emission caused by steam generation, avoids excessive water usage, and can be applied to reservoirs where steam-based methods are less effective. Driven by these merits, the idea of using EM heating to recover heavy oil has been investigated since the 70s (Abernethy 1976). The previous investigations (Jha et al. 1999; Alomair et al. 2012) showed that EM heating was a promising technique to heat up the reservoir; but the resulting recovery factors were normally low, and the heated area of the reservoir was confined in the vicinity of the wellbore, which hindered the generalization of this technique. Solvent injection is recently proposed to combine with EM heating to enhance oil recovery (Trautman et al. 2013). The merits of using solvent in EM heating include diluting heavy oil and thereby increasing its mobility, serving as a heat carrier by reinforcing heat convection in porous media, forming a vapor chamber to facilitate the gravity drainage, and supplementing the natural energy in addition to the thermal expansion and the vaporization of connate water by EM heating (Hu et al. 2016a).

The combined EM heating and solvent-assisted gravity drainage is currently at its initial development stage, which can be manifested by the following aspects: (1) the fundamental electrical properties (permittivity) of oil sands with the presence of solvent are still unavailable; (2) the effects of EM heating on changing the properties of reservoir materials (formation rocks and heavy oil) remain unclear; (3) the recovery performances of this hybrid process are not experimentally examined; and (4) analytical or semi-analytical models capable of simulating this hybrid process are still lacking. In this dissertation, we conduct a systematic study of this hybrid

process in an attempt to fill the aforementioned knowledge gaps, which will lay a foundation for achieving better understanding, design, and optimization of this hybrid technique.

## 1.2 Literature Review

Based on the applied frequencies, EM heating can be classified into three classes: low-frequency heating, inductive heating, and high-frequency heating. The heating mechanisms of each classification are distinct. In this chapter, we introduce the theory and field applications of different classifications of EM heating. The detailed reviews of relevant literature about the electrical properties of oil sands, the effect of EM heating on changing the properties of reservoir materials, experimental investigation of heavy oil recovery by the combined EM heating and solvent injection, and modeling of this hybrid process are presented in the following chapters.

### 1.2.1 Maxwell's Equations

Unlike the heat conduction and convection, electromagnetic heating relies on the heat generated by the interactions between the materials and electromagnetic waves (field). The variations of the electric and magnetic field can be described by Maxwell's equations (Metaxas and Meredith 1983):

$$\begin{aligned}\nabla \cdot D &= \rho_e \\ \nabla \cdot B &= 0 \\ \nabla \times E &= -\frac{\partial B}{\partial t} \\ \nabla \times H &= J + \frac{\partial D}{\partial t}\end{aligned}\tag{1-1}$$

where  $D$  is the electric displacement field,  $\rho_e$  is the electrical charge density,  $B$  is the magnetic flux density,  $E$  is the electric field,  $H$  is the magnetic field strength, and  $J$  is the current density. Assuming the electromagnetic properties (permittivity, conductivity, and permeability) are

constant and the electromagnetic field is time-harmonic, we can obtain a simplified form of Maxwell's equations (Fanchi 1993; Carrizales 2010):

$$\begin{aligned}
 \nabla \times E &= -j\omega\mu_{EM}H \\
 \nabla \times H &= (\sigma + j\omega\varepsilon)E \\
 \nabla \cdot E &= 0 \\
 \nabla \cdot H &= 0
 \end{aligned}
 \tag{1-2}$$

where  $\sigma$  is the electrical conductivity,  $\varepsilon$  is the electrical permittivity,  $\mu_{EM}$  is the magnetic permeability,  $\omega$  is the angular frequency, and  $j = \sqrt{-1}$ . Next, by performing the curl operation of Eq. (1-2), the obtained  $E$  and  $H$  are (Fanchi 1991):

$$\begin{aligned}
 \nabla^2 H &= \gamma^2 H \\
 \nabla^2 E &= \gamma^2 E
 \end{aligned}
 \tag{1-3}$$

where  $\gamma$  is a complex number, which is in the form:

$$\gamma = \alpha + j\beta
 \tag{1-4}$$

$$\alpha = \omega\sqrt{\frac{\mu\varepsilon}{2}} \left[ \sqrt{1 + \left(\frac{\sigma}{\omega\varepsilon}\right)^2} - 1 \right]^{1/2}
 \tag{1-5}$$

$$\beta = \omega\sqrt{\frac{\mu\varepsilon}{2}} \left[ \sqrt{1 + \left(\frac{\sigma}{\omega\varepsilon}\right)^2} + 1 \right]^{1/2}
 \tag{1-6}$$

where  $\alpha$  is the attenuation coefficient (absorption coefficient), and  $\beta$  is the phase shift constant. The penetration depth describes how far the EM wave can penetrate into the medium before it falls to  $1/e$  (about 0.37) of its original energy level (Kaur 1993):

$$D_p = \frac{1}{2\alpha}
 \tag{1-7}$$

where  $D_p$  is the penetration depth.

## 1.2.2 Low-Frequency Heating

**Figure 1-1** shows the schematic of the low-frequency heating for heavy oil recovery. In the low-frequency heating (50 or 60 Hz), an electrical potential is established between wells by setting some wells as anodes and the others as cathodes; the reservoir materials serve as the resistance in this process. Resistive heating or joule heating dominates this process (Harvey et al. 1979; Lashgari et al. 2016); the generated heat of Joule heating can be calculated by:

$$Q_{joule} = \rho_e J^2 \quad (1-8)$$

where  $\rho_e$  is the resistivity,  $J$  is the current density, and  $Q_{joule}$  is the heating source for the low-frequency heating.

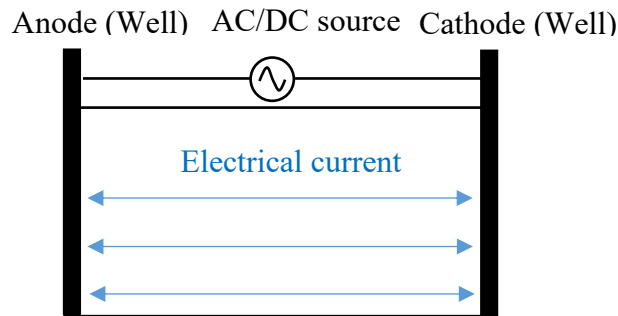


**Figure 1-1** Schematic of the low-frequency heating for heavy oil recovery (Adapted from Bera and Babadagli 2015). The blue arrows indicate the electrical current flow.

Pizarro and Trevisan (1990) conducted a low-frequency electrical heating field trial in Rio Panan field, Brazil. After 70 days of electrical heating with a power of 20 kW, the production rate increased from 1.2 bbl/d to 6.3 bbl/d. McGee (2008) conducted a pilot test of the ET-DSP™ (Electro-Thermal Dynamic Stripping Process); the reported recovery factor was about 75% and the equivalent steam-oil ratio was about 0.49. The inter-well connectivity is critical to this heating scheme. The water in the formation provides the main path for the electrical current to flow; hence, the formation temperature is constrained to be lower than the saturation temperature of water in order to maintain the circuit.

### 1.2.3 Inductive Heating

Inductive heating (from 1 to 200 kHz) uses a set of inductors to induce an alternating magnetic field which generates eddy current (Koolman et al. 2008; Wacker et al. 2011; Koch et al. 2013). The formation materials resist the flow of the eddy current, which produces heat. The heat generation of the inductive heating can be calculated by (Koch et al. 2013):

$$Q_{inductive} = \frac{1}{2}(J_r E_r + J_i E_i) \quad (1-9)$$

where  $J_r$  and  $E_r$  are the real parts of the current density and electric field, while  $J_i$  and  $E_i$  are the imaginary parts of the current density and electric field, and  $Q_{inductive}$  is the heating source for the inductive heating.

Siemens AG proposed the Electro Magnetic SAGD (EM-SAGD) which added inductor loops to the SAGD well pair (Koolman et al. 2008). **Figure 1-2** shows the schematic of the EM-SAGD process. The additional inductive heating could reduce the steam and water consumption as well as enhance the oil recovery, especially for reservoirs with a thick payzone (Koolman et al. 2008). The major obstacles for applying this technique are the drilling and completion difficulties caused by the utilization of the inductors (Ghannadi et al. 2016).

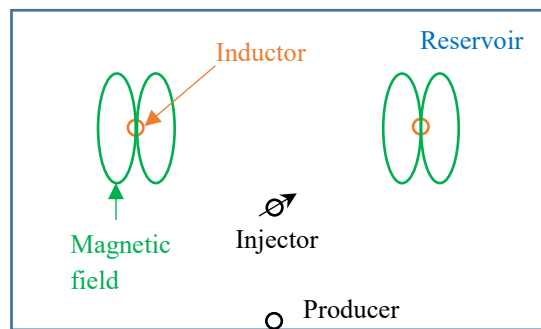


**Figure 1-2** Schematic of the inductive heating applied in a SAGD well pair (Adapted from Koolman et al. 2008).

#### 1.2.4 High-Frequency Heating

This thesis focuses on the high-frequency heating that could heat up a relatively large part of the reservoir to a high temperature within a short time. High-frequency heating (from 3 kHz to 300 GHz) generates heat through the dipole rotation and ion conduction under a high-frequency alternating electric field (Sresty et al. 1986; Trautman et al. 2013; Bera and Babadagli 2015). The polarized reservoir materials oscillate under an alternating electric field, generating frictional heat. The heat generation can be described by the Poynting theorem which is formulated as (Kaur 1993):

$$P_{avg} = \frac{1}{2} \text{Re}(E \times H^*) \quad (1-10)$$

where  $P_{avg}$  is the average power density,  $Re$  represents the real part of  $E \times H^*$ , and  $*$  indicates the complex conjugate. Then, the absorbed power per volume can be calculated by (Kaur 1993):

$$Q_{EM} = \frac{1}{2} \omega \epsilon_0 \epsilon'' |E|^2 \quad (1-11)$$

where  $Q_{EM}$  is the absorbed power per unit volume. Abernethy (1976) and Fanchi (1993) derived a simplified solution, employing Lambert's law to calculate the absorbed power distribution of EM heating:

$$P(r) = P_0 e^{-2\alpha r} \quad (1-12)$$

where  $P(r)$  is the absorbed power at  $r$ , and  $P_0$  is the incident power at the wellbore. This approximation significantly simplifies the calculation, which enables the evaluation of energy gain by EM heating without solving the complex Maxwell's equations.

Sresty et al. (1986) did a pilot test in a tar sand formation in Utah and an enhancement of 35% in oil recovery factor was achieved after three weeks of EM heating. Kasevich et al. (1994) tested the performance of the radio-frequency heating device which operated at 13.56 MHz and 25 kW for 99 hours; the efficiency of the radio-frequency applicator was reported to be 99%. Recently,

the enhanced solvent extraction incorporating EM heating (ESEIEH) was under pilot tests, where a SAGD-like well pair was adopted (Wise and Patterson 2016). **Figure 1-3** shows the schematic of the combined EM heating and solvent injection for heavy oil recovery.

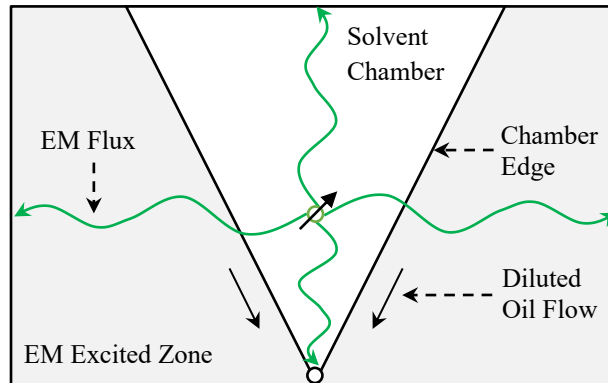


**Figure 1-3** Schematic of the combined EM heating and solvent injection for heavy oil recovery (Hu et al. 2018a).

### 1.3 Problem Statement and Objectives

Previous studies show that EM heating is a promising non-aqueous heating method for heavy oil recovery; recently, the combined EM heating and solvent injection is proposed to further enhance the heavy oil recovery. However, only limited studies have been conducted to examine this process, which leaves several key questions unaddressed:

- How to select a good candidate reservoir for this hybrid process? What are the major influential factors that affect the permittivity (electrical properties) of the oil sands? How does the injected solvent affect the permittivity of oil sands? How to calculate the reservoir permittivity that is required for the simulation of the EM heating process?
- What are the major mechanisms of this hybrid process? What are the individual roles of the EM heating and solvent injection in this hybrid process? What is the recovery performance of this technique? What are the major influential factors affecting the oil recovery? How to optimize the energy utilization of this process?

- Would formation rocks and heavy oil exhibit petrophysical and chemical property changes under EM heating? What types of formation rocks are more susceptible to EM heating? What are the responses of the formation rocks when being exposed to EM heating?
- How to analytically model this process? How to design the operational parameters that are needed for the effective application of the EM heating? How to properly select the solvent type, EM heating power, and frequency used in the hybrid process? How to increase the economic gain and reduce the energy consumption of this process?

The purpose of this research is to provide fundamental data, experimental design, and theoretical model for achieving better understanding, design, and optimization of the combined EM heating and solvent injection for heavy oil recovery. The detailed objectives of this research are listed below:

- Experimentally determine the permittivity of (normal alkane/) oil sands system; modify the current mixing rules to enhance their prediction accuracy of the permittivity for the normal alkane/oil sands mixtures;
- Conduct a series of experiments to examine the recovery performance; investigate the essential mechanisms that govern this process; understand the individual roles that the EM heating and solvent injection play in this hybrid process;
- Investigate the effect of EM heating on changing the petrophysical property of formation rocks; quantify the petrophysical-property changes of the formation rocks and chemical composition of heavy oil after EM heating; reveal the mechanisms leading to the possible property changes of the formation rocks by EM heating;
- Develop a semi-analytical model to simulate this hybrid process; apply the developed

model to simulate the oil recovery of this hybrid process by considering important process factors, including EM heating power, solvent type, and solvent injection pressure; optimize this process based on net present value and energy-consumption efficiency.

#### **1.4 Solution Methodology**

To achieve the above objectives, we conduct theoretical, experimental, and numerical studies in this research. The detailed tasks are divided into four phases; **Figure 1-4** shows the adopted solution methodology. In phase I, an open-ended co-axial probe method has been used to measure the permittivity of the constituents of oil sands, oil sands mixtures, solvent/bitumen, and solvent/oil sands mixtures along the frequency of 200 MHz to 10 GHz. The obtained relationships among the composition of oil sands, applied frequency, and permittivity of oil sands help to distinguish the essential factors that affect the permittivity of solvent/oil sands mixtures. Phase I provides fundamental data used for the design of the phase II work. Based on the measurement results, we evaluate and then modify the existing mixing rules to improve their prediction accuracy of the permittivity of the solvent/oil sands mixture.

In phase II, we propose an experimental workflow to investigate the essential mechanisms of this hybrid process and to study the effects of essential influential factors on the process efficiency. We conduct premixed experiments (the solvent is premixed with heavy oil in the sand pack) and dynamic flow experiments (solvent is injected into the sand pack) to examine the effects of EM heating power, solvent type, and water saturation on the recovery performance of this hybrid process. We then perform critical analyses on the viscosity reduction and the residual oil saturation to understand the mechanisms governing this hybrid process. Next, different ways of combining the EM heating and solvent injection, including simultaneous EM heating and solvent injection and alternate EM heating and solvent injection, are explored to find an efficient way to apply this technique. In addition, the compositions of the produced oil samples are characterized with SARA tests to study the *in-situ* upgrading effect of EM heating.

In phase III, we investigate the effect of EM heating on changing the petrophysical properties of formation rocks. Different types of formation rocks, including continental shale, Berea sandstone, tight sandstone, and Indiana carbonate, are exposed to EM heating for three minutes. Their petrophysical property changes by EM heating are quantified by SEM/EDX, N<sub>2</sub> adsorption/desorption, microscopic imaging, and core flooding experiments. Oven-heating experiments are also conducted to distinguish the effects of EM heating and conductive heating. Based on the obtained results, we examine the mechanisms leading to the variations in the petrophysical property of formation rocks under EM heating. Lab-scale simulations are performed to calculate the temperature and stress distributions of rock samples under EM heating.

In phase IV, we develop a semi-analytical model, incorporating the obtained measurement results and experimental observations, to simulate this hybrid process. The model first calculates the temperature distribution within the EM excited zone due to the radiation-dominated EM heating. By employing different attenuation coefficients within and beyond the vapor chamber, the model can properly describe the corresponding temperature responses in these regions. The previously obtained permittivity relationships are fed to the model to calculate the effective attenuation coefficients. Next, an average temperature of the chamber edge contributed by EM heating is used to estimate temperature-dependent properties, such as vapor/liquid equilibrium ratios (K-values), heavy-oil/solvent mixture viscosity, and solvent diffusivity. Subsequently, a 1-D diffusion equation is used to calculate the solvent-concentration distribution ahead of the chamber edge. Eventually, the Butler's SAGD model is used to evaluate the oil flow rate based on the calculated temperature and solvent distributions ahead of the chamber edge. The developed model is validated against the experimental results obtained in phase II. Applying the developed model, we investigate the effects of important influential factors on the performance of the combined EM heating and solvent-assisted gravity drainage. Different EM heating powers,

solvent types, and solvent injection pressures are examined via case studies. The net present value, solvent to oil ratio, and energy to oil ratio of different cases are used to optimize this hybrid process.

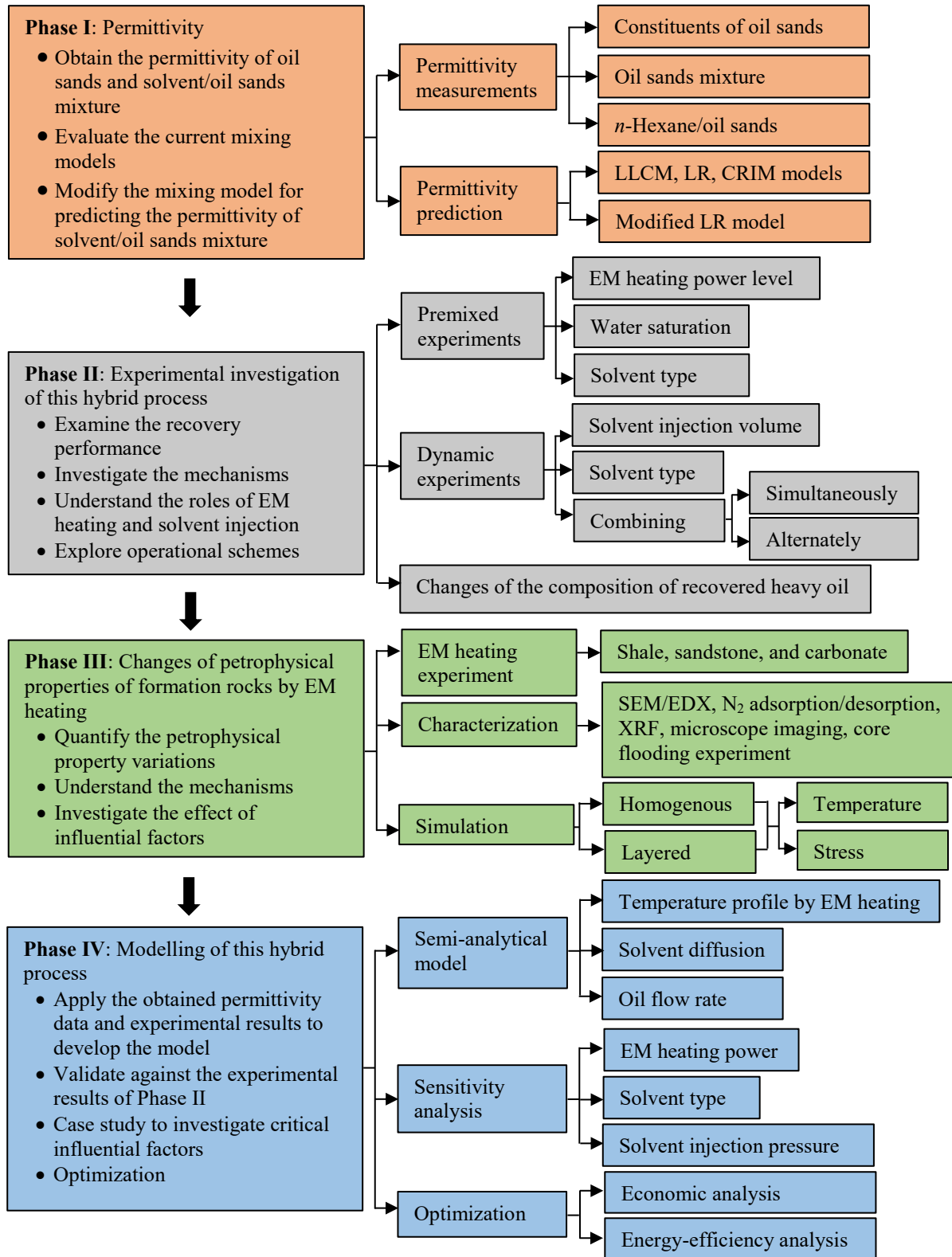


Figure 1-4 Overview of the methodology used in this study.

## 1.5 Thesis Structure

This paper-based thesis consists of six chapters. The introductory and conclusive chapters are presented in chapter 1 and chapter 6, respectively. Four papers correspond to the four chapters from chapter 2 to chapter 5; each of these chapters contains its own summary, introduction, results and discussion, conclusions, and references.

In **Chapter 1**, the background, literature review of the theory and the field applications of the EM heating methods, problem statements, objectives, solution methodology, and thesis structure are introduced. **Chapter 2** includes the results on the experimental determination of the permittivity of *n*-hexane/oil sands mixtures over the frequency range of 200 MHz to 10GHz. Also, various dielectric mixing models are evaluated, and a modified mixing model is proposed to enhance the prediction accuracy of the permittivity of solvent/oil sands mixtures. In **chapter 3**, the results on the experimental study of this hybrid process are shown. Influential factors including EM heating power, solvent type, water saturation, and manners of combining EM heating injection on the recovery performance of this process are investigated. The mechanisms of EM heating and solvent injection for heavy oil recovery are also revealed. **Chapter 4** presents the results on the petrophysical property changes of formation rocks by EM heating. The changes of petrophysical properties quantified by various characterization techniques are also presented. Experimental and numerical results are obtained to help understand the mechanisms of the petrophysical property changes of formation rocks under EM heating. In **Chapter 5**, the modeling work of this hybrid process is shown. A semi-analytical model for simulating the oil production of the combined EM heating and solvent injection in SAGD-liked wells is developed. Sensitivity analyses of EM heating, solvent type, and solvent injection pressure are performed via case studies. The

optimization of this hybrid process is conducted by the economic and energy-efficiency analyses.

**Chapter 6** shows the contributions and recommendations of this research.

## **1.6 References**

- Abernethy, E.R. 1976. Production increase of heavy oil by electromagnetic heating. *J. Can. Pet. Tech.* **15** (3): 91–97.
- Alboudwarej, H., Felix, J.J., Taylor, S., Badry, R., Bremner, C., Brough, B., Skeates, C., Baker, A., Palmer, D., Pattison, K., Beshry, M., Krawchuk, P., Brown, G., Calvo, R., Triana, J.A.C., Hathcock, R., Koerner, K., Hughes, T., Kundu, D., de Cárdenas, J.L., and West, C. 2006. Highlighting heavy oil. *Oilfield Review.* **18** (2): 34-53.
- Alomair, O.A., Alarouj, M.A., Althenayyan, A.A., Al Saleh, A.H., Mohammad, H., Altahoo, Y., Alhaidar, Y., Alansari, S., and Alshammari, Y. 2012. Improving heavy oil recovery by unconventional thermal methods. Paper SPE-163311-MS presented at the SPE Kuwait International Petroleum Conference and Exhibition, Kuwait City, Kuwait, 10-12 December.
- Bera A. and Babadagli, T. 2015. Efficiency of heavy-oil recovery by radio frequency EM heating: An experimental approach. Paper SPE-176113-MS presented at the SPE Asia Pacific Oil & Gas Conference and Exhibition, Bali, Indonesia, 20–22 October.
- Butler, R.M., and Mokrys, I.J. 1993. Recovery of heavy oils using vaporized hydrocarbon solvents: Further development of the VAPEX process. *J. Can. Pet. Technol.* **32**: 77–86.
- Butler, R.M. 1997. Thermal recovery of oil and bitumen. Calgary, Alberta: GravDrain Inc.
- Carrizales, M.A., Lake, L.W., and Johns, R.T. 2010a. Multiphase fluid flow simulation of heavy oil recovery by electromagnetic heating. Paper SPE-129730-MS presented at the SPE Improved Oil Recovery Symposium held in Tulsa, Oklahoma, USA, 24–28 April.
- Fanchi, J.R. 1993. Feasibility of reservoir heating by electromagnetic irradiation. *SPE Adv. Technol. Ser.* **1** (02): 161-169.
- Ghannadi, S., Irani, M., and Chalaturnyk, R. 2016. Overview of performance and analytical modeling techniques for electromagnetic heating and applications to steam-assisted-gravity-drainage process startup. *SPE J.* **21** (2): 311-333.
- Gupta, S.C., Gittins, S., Sood, A., and Zeidani, K. 2010. Optimal amount of solvent in Solvent Aided Process. Paper SPE-137543-MS presented at the Canadian Unconventional Resources and International Petroleum Conference, Calgary, 19-21 October.

- Gupta, S.C. and Gittins, S.D. 2006. Christina lake solvent aided process pilot. *J. Can. Pet. Tech.* **45** (9): 15-18.
- Harvey, A., Arnold, M.D., and El-Feky, S.A. 1979. Selective electric reservoir heating. *J. Can. Pet. Technol.* **18** (3): 47-57.
- Hassanzadeh, H. and Harding, T.G. 2016. Analysis of conductive heat transfer during *in-situ* electrical heating of oil sands. *Fuel* **178**: 290–299.
- Hu, L., Li, H.A., Babadagli, T., and Ahmadloo, M. 2016a. Experimental investigation of combined electromagnetic heating and solvent assisted gravity drainage for heavy oil recovery. Paper SPE-180747-MS presented at the SPE Heavy Oil Conference-Canada, Calgary, 7–9 June.
- Ivory, J., Chang, J., Coates, R., and Forshner, K. 2010. Investigation of cyclic solvent injection process for heavy oil recovery. *J. Can. Pet. Tech.* **49** (9): 22–33.
- Jha, K.N. and Chakma, A. 1999. Heavy-oil recovery from thin pay zones by EM heating. *Energy Sources* **21** (1-2): 63–73.
- Kasevich, R.S., Price, S.L., Faust, D.L., and Fontaine, M.F. 1994. Pilot testing of a radio frequency heating system for enhanced oil recovery from diatomaceous earth. Paper SPE-28619-MS presented at the SPE Annual Technical Conference and Exhibition, New Orleans, Louisiana, U.S.A., 25-28 September.
- Kaur, R., Newborough, M., and Probert, S.D. 1993. Multi-purpose mathematical model for electromagnetic-heating processes. *Appl. Energy* **44** (4): 337-386.
- Koch, A., Sotskiy, S., Mustafina D., and Danov, V. 2013. Mechanism of heavy oil recovery driven by electromagnetic inductive heating. Paper SPE-165507-MS presented at the SPE Heavy Oil Conference-Canada, Calgary, Alberta, Canada, 11–13 June.
- Koolman, M., Huber, N., Diehl, D., and Wacker, B. 2008. EM heating method to improve steam assisted gravity drainage. Paper SPE-117481-MS presented at the SPE International Thermal Operations and Heavy Oil Symposium, Calgary, Alberta, Canada, 20–23 October.
- Lashgari, H.R., Delshad, M., Sepehrnoori, K., and de Rouffignac, E. 2016. Development and application of electrical-joule-heating simulator for heavy-oil reservoirs. *SPE J.* **21** (1): 87-100.
- McGee, B.C. 2008. Electro-thermal pilot in the Athabasca oil sands: Theory versus performance. Paper PETSOC-2008-209 presented at the Canadian International Petroleum Conference,

Calgary, Canada, 17-19 June.

- Metaxas, A.C. and Meredith, R.J. 1983. Industrial microwave heating. London : Peter Peregrinus Ltd. on behalf of the Institution of Electrical Engineers, 1983.
- Nasr, T.N., Beaulieu, G., Golbeck, H., and Heck, G. 2003. Novel expanding solvent-SAGD process “ES-SAGD”. *J. Can. Pet. Technol.* **42** (1): 13–16.
- Nenniger, J. and Nenniger, E. 2008. Method and apparatus for stimulating heavy oil production. US Patent No. 7,363,973.
- Pizarro, J.O.S. and Trevisan, O.V. 1990. Electrical heating of oil reservoirs: Numerical simulation and field test results. *J. Pet. Technol.* **42** (10): 1320–1326.
- Rezaei, N., Mohammadzadeh, O., and Chatzis, I. 2010. Warm VAPEX: A thermally improved vapor extraction process for recovery of heavy oil and bitumen. *Energy Fuels* **24** (11): 5934-5946.
- Sresty, G.C., Dev, H., and Snow, R.H. 1986. Recovery of bitumen from Tar sand deposits with the radio frequency process. *SPE Res. Eng.* **1** (1): 85–94.
- Trautman, M., Ehresman, D., Edmunds, N., Taylor, G., and Cimolai, M. 2013. Effective solvent extraction system incorporating EM heating. U.S. Patent No. 8,616,273. Washington, DC.
- Wacker, B., Karmeileopardus, D., Trautmann, B., Helget, A., and Torlak, M. 2011. Electromagnetic heating for in-situ production of heavy oil and bitumen Reservoirs. Paper SPE-148932-MS presented at the Canadian Unconventional Resources Conference, Alberta, Canada, 15-17 November.
- Wise, S. and Patterson, C. 2016. Reducing supply cost with Esei<sup>TM</sup> pronounced easy. Paper SPE-180729-MS presented at the SPE Heavy Oil Conference-Canada, Calgary, 7–9 June.

**CHAPTER 2 DETERMINATION OF THE PERMITTIVITY OF  
N-HEXANE/OIL SANDS MIXTURES OVER THE FREQUENCY  
RANGE OF 200MHZ TO 10GHZ**

A version of this chapter has been accepted for publication in *The Canadian Journal of Chemical Engineering*.

## Summary

Combined electromagnetic (EM) heating and solvent injection has been recently proposed to recover bitumen from oil sands due to its great environmental friendliness. The permittivity of oil sands with the presence of solvent is a crucial property for the design, evaluation, and optimization of this process. In this study, we use the open-ended coaxial probe method to measure the permittivity of oil sands over the frequency range of 200 MHz to 10 GHz. Results of the permittivity of the constituents of oil sands reveal that water is a major dielectric contributor; no relaxation phenomenon has been found for bitumen, sand, and *n*-hexane over the tested frequency range. Also, the results for the oil sands mixtures show that water content is crucial for the permittivity of oil sands; both the dielectric constant and loss factor are enhanced with an increasing water content. With the addition of *n*-hexane, the permittivity of bitumen slightly changes and fluctuates between the dielectric values of pure bitumen and *n*-hexane. As for the *n*-hexane/oil sands mixtures, the added *n*-hexane induces the asphaltene aggregation/flocculation, affecting the interaction between water and asphaltene and leading to an enhanced free water content in the oil sands. Consequently, the permittivity of oil sands significantly increases after *n*-hexane addition. Based on the experimental data, we evaluate the prediction accuracy of commonly used mixing models. A modified Lichtenecker-Rother model considering effective water saturation is proposed to accurately characterize the permittivity of *n*-hexane/oil sands mixtures. The obtained data and correlations can be useful when experimental data are missing.

**Keywords:** permittivity, oil sands, *n*-hexane, electromagnetic heating, permittivity mixing model

## 2.1 Introduction

To meet the increasing energy demand, there is a growing interest in exploiting unconventional hydrocarbon resources such as heavy oil and bitumen. Due to the large oil viscosity, the

production of these resources is frequently accomplished through thermal recovery methods, which reduce the heavy oil viscosity by transferring heat into the reservoir. The most effective ways of in-situ recovery of oil sands are steam-based methods, such as steam flooding, cyclic steam stimulation (CSS), and steam-assisted gravity drainage (SAGD),<sup>[1]</sup> where the condensation of steam releases latent heat for raising the reservoir temperature. These steam-based processes consume a large amount of water and require a massive amount of energy to generate steam. For instance, the energy oil ratio of a SAGD project is about 7.5 GJ/m<sup>3</sup> corresponding to a typical steam oil ratio of 3; if burning natural gas is used to generate the required amount of steam, about 0.38 tonnes of CO<sub>2</sub> will be emitted to produce 1 m<sup>3</sup> of oil.<sup>[2]</sup> Furthermore, steam-based methods are less efficient for recovering heavy oil from thin payzones and deep formations, due to the large heat loss.<sup>[3]</sup>

EM heating, possessing the advantages of fast heating, environmental friendliness, and a water-less nature, provides a promising alternative method for heavy oil/bitumen recovery.<sup>[4-6]</sup> Based on the applied frequency, EM heating can be classified into three classes: low-frequency heating, inductive heating, and high-frequency heating. In the low-frequency heating (50 or 60 Hz), an electrical potential is established between wells by setting some wells as anodes and the others as cathodes; resistive heating or joule heating dominate this process.<sup>[7-8]</sup> Inductive heating (from 1 to 200 kHz) applies a coil around the heating objects and relies on the eddy current to generate heat.<sup>[9-11]</sup> High-frequency heating (from 3 kHz to 300 GHz), i.e., radio or microwave frequency heating, generates heat through dipole rotation and ion conduction under a high-frequency alternating electric field.<sup>[12-18]</sup> This study focuses on the classification of high-frequency heating that could heat up the reservoir to a high temperature within a short time.

Oil sands are complex mixtures of sand, clay, fine minerals, formation water, and bitumen.<sup>[19]</sup> Bitumen is also a mixture containing different types of hydrocarbons, normally characterized by the fractions of saturates, aromatics, resins, and asphaltenes (SARA); among these components, resins and asphaltenes are polarized, while saturates and aromatics are non-polarized or slightly polarized.<sup>[20]</sup> The permittivity of oil sands has been measured over a large frequency and temperature range (1 Hz to 1 GHz, 2.45 GHz; 20–500 °C) by the coaxial probe method, resonant cavity method, and parallel plate method,<sup>[21–23]</sup> the measured results are summarized in **Table 2-1**. However, the permittivity of oil sands at higher frequencies is still incomplete. In addition, the oil sands samples are normally characterized by their “grade” in the previous studies,<sup>[21–23]</sup> which distinguishes the oil sands samples mainly by their weight fractions of bitumen, while overlooking the properties of other components and the porous structure of oil sands. Although empirical correlations have been developed to approximate the measured permittivity of a given oil sands sample,<sup>[21]</sup> the efficiency of commonly used mixing models for predicting the permittivity of oil sands have not been fully examined.

**Table 2-1** Summary of previous measurements on dielectric properties of oil sands in the literature

Method	Sample	Frequency	Temperature	Dielectric constant	Loss tangent	Ref.
Coaxial probe method	Athabasca sample	10Hz-1GHz	24 °C	4–5@1GHz	-	Chute et al. <sup>[21]</sup>
Resonant cavity method	Alberta oil sands	2.45GHz	23 °C	2.8–3.2	0.01–0.07	Erdogan et al. <sup>[22]</sup>
Parallel plate method	Alberta oil sands	100Hz-1MHz	20–200 °C	3–4	0–55	Gaikwad <sup>[23]</sup>
Parallel plate method	N.W. Asphalt Ridge specimen (sample A)	200Hz-50kHz	50–500 °C	8–100	0–6	Das et al. <sup>[46]</sup>
	Circle Cliffs oil sands specimen	10Hz-1MHz	250–450 °C	7–240	0–5	
	Athabasca sample	10MHz-1GHz	25–350 °C	2.6–4.4	0–2	

Solvent injection was recently combined with EM heating to further enhance the oil recovery.<sup>[13,24]</sup> The normal alkanes are actively explored in this hybrid process because of their

effectiveness in reducing viscosity and enhancing the swelling effect of heavy oil.<sup>[25]</sup> Several studies have been conducted to measure the permittivity of crude oil and solvents,<sup>[26,27]</sup> however, the permittivity of oil sands mixture with the presence of normal alkane solvent is still elusive. It is of great importance to obtain the permittivity data of oil sands at high frequencies, to understand the effect of adding *n*-hexane on the permittivity of oil sands, and to evaluate the accuracy of existing mixing models for characterizing the permittivity of oil sands.

In this study, the permittivity of the synthesized oil sands samples has been measured by using the open-ended coaxial probe method within a frequency range of 200 MHz to 10 GHz. We first investigate the permittivity of constituents of oil sands. Subsequently, the permittivity measurement is performed to oil sands with different porosity and water saturation. To elucidate the effect of the *n*-hexane addition on the permittivity of oil sands, we first measure the permittivity of the *n*-hexane/bitumen mixture and then extend the measurement to *n*-hexane/oil sands mixtures. Based on the obtained permittivity data, we evaluate the prediction accuracy of the commonly-used mixing models, including the Lorentz-Lorenz and Clausius-Mossotti (LLCM) model, the Lichtenecker-Rother (LR) model, the logarithmic Lichtenecker (L-LN) model, and the complex refractive index method (CRIM), for characterizing the permittivity of oil sands.<sup>[28]</sup> Lastly, to enhance the permittivity prediction accuracy of *n*-hexane/oil sands mixtures, we empirically modify the LR model to capture the change in the free water content caused by the *n*-hexane addition.

## 2.2 Theory

The permittivity, characterizing the interaction between the electric field and materials, is a crucial factor for EM heating. The permittivity is a complex number, comprised of the real part and imaginary part, which is given by the following:<sup>[29,30]</sup>

$$\varepsilon_r^* = \frac{\varepsilon^*}{\varepsilon_0} = \varepsilon' - j\varepsilon'' \quad (2-1)$$

where  $\varepsilon_r^*$  is relative complex permittivity,  $\varepsilon^*$  is absolute complex permittivity (F/m),  $\varepsilon_0$  is permittivity of free space ( $8.854 \times 10^{-12}$  F/m),  $\varepsilon'$  is the real part of relative permittivity (i.e., dielectric constant), which reflects how much EM energy is stored in the material,  $\varepsilon''$  is the imaginary part of relative permittivity (i.e., the loss factor), which indicates the ability to dissipate stored energy into heat, and  $j = \sqrt{-1}$ .

The permittivity affects the penetration depth ( $D_p$ ) and absorbed power ( $P_d$ ), which play a pivotal role in affecting the performance of the EM heating process. The penetration depth describes how far the EM wave can penetrate into the reservoir before it falls to  $1/e$  (about 0.37) of its original energy level, while the absorbed power determines how much of the EM energy can be absorbed by the reservoir; the mathematical formula of the penetration depth and absorbed power are as follows:<sup>[30]</sup>

$$D_p = \frac{C}{2\pi f \sqrt{2\varepsilon'} \left[ \sqrt{1 + \left(\frac{\varepsilon''}{\varepsilon'}\right)^2} - 1 \right]^{1/2}} \quad (2-2)$$

$$P_d = 2\pi f \varepsilon_0 \varepsilon'' |E|^2 \quad (2-3)$$

where  $C$  is the speed of light in a vacuum (about  $3 \times 10^8$  m/s),  $f$  is frequency (Hz), and  $E$  is electric field (V/m). The absorbed power ( $P_d$ ) also can be approximated by the Beer-Lambert law when the calculation of the electric field becomes problematic, which is given as follows:<sup>[31]</sup>

$$P_d(r) = P_0 \cdot e^{-2\alpha(r-r_0)} \quad (2-4)$$

$$\alpha = 2\pi f \left\{ \mu_o \varepsilon_o \varepsilon' \left[ \left( 1 + \left( \frac{\varepsilon''}{\varepsilon'} \right)^2 \right)^{1/2} \right] - 1 \right\}^{1/2} \quad (2-5)$$

where  $P_d(r)$  is the absorbed power at  $r$  ( $\text{W}/\text{m}^3$ ),  $P_0$  is the incident power at the wellbore ( $\text{W}/\text{m}^3$ ),  $r_0$  is the radius of the wellbore (m),  $\alpha$  is the absorption coefficient ( $1/\text{m}$ ),  $\mu_o$  is the permeability (electromagnetism) of free space ( $1.26 \times 10^{-6}$  H/m). As we can see, both penetration depth and absorbed power are dependent on the permittivity. Therefore, accurate permittivity data and prediction models of the oil sands are critical for the design, evaluation, and optimization of EM heating recovery techniques.

## 2.3 Experimental Section

### 2.3.1 Materials

In this study, synthesized oil sands, composed of silica sand, distilled/salty water, and bitumen, are used in the measurements. Silica sand with three different mesh size ranges (40–45 Mesh, 40–70 Mesh, and 100 Mesh) and a grain density of  $1.305 \text{ g}/\text{cm}^3$  are used to make up the matrix of the oil sands mixture with different porosities. The main chemical composition of the sand particles is  $\text{SiO}_2$ , accounting for 92.5 g/g. Distilled water and sodium chloride are used to prepare the simulated formation water with certain salinity. The bitumen sample is from Alberta, of Canada, with a density of  $1.0006 \text{ g}/\text{cm}^3$  at room temperature ( $20 \text{ }^\circ\text{C}$ ) and atmospheric pressure. **Table 2-2** shows the results of gas-chromatography (GC) analysis as well as saturates, aromatics, resins, and asphaltenes (SARA) analysis of the bitumen sample. The solvent used in this study is *n*-hexane (99+ g/g purity, ACROS Organics™, Fisher Scientific, USA) with a density of  $0.659 \text{ g}/\text{cm}^3$ . A rotational viscometer (Brookfield DV-II+ Pro) is used to measure the viscosity of the bitumen sample from  $15.6 \text{ }^\circ\text{C}$  to  $-85.6 \text{ }^\circ\text{C}$ . **Table 2-3** shows the measured viscosity data of

bitumen as well as *n*-hexane/bitumen mixtures with 20 %, 50 %, and 80 % volume fractions of *n*-hexane.

**Table 2-2** GC and SARA analysis results of the bitumen sample

Carbon No.	Weight Fraction (%)
7	2.79
8	0.03
9	0.11
10	0.17
11-20	21.9
21-30	30.42
31-40	15.16
41-50	12.87
51-60	9.81
60+	6.77
SARA	Weight Fraction (%)
Saturates	16.74
Aromatics	31.56
Resins	31.62
Asphaltenes	20.03

**Table 2-3** Viscosity-temperature data for bitumen and *n*-hexane/bitumen mixtures

<i>T</i> (°C)	Bitumen Viscosity (cp)	Solvent/bitumen mixture (20vol% of <i>n</i> -hexane) viscosity (cp)	Solvent/bitumen mixture (50vol% of <i>n</i> -hexane) viscosity (cp)	Solvent/bitumen mixture (80vol% of <i>n</i> -hexane) viscosity (cp)
15.60	461352.30	623.50	8.31	3.11
25.60	107000.00	354.80	7.29	2.09
35.60	29853.00	222.10	6.44	1.53
45.60	9811.00	155.10	5.55	0.84
55.60	3892.00	104.40	4.68	0.76
65.60	1678.00	72.84	3.98	0.64
75.60	827.70	48.67	3.38	0.48
85.60	433.80	26.68	2.84	0.42

As for the preparation of the oil sands samples, we first mix the simulated formation water and sand particles to form a water-wet matrix. Then, the oleic mixture, (*n*-hexane)/bitumen, is gradually added into the water-wet sand particles to make up the oil sands samples; meanwhile, the mixture is stirred sufficiently to make sure that the samples are evenly mixed. At last, the prepared oil sands samples are placed into plastic containers with a volume of 60 mL for the permittivity measurements. **Table 2-4** lists the detailed experimental schemes.

**Table 2-4** Detailed experimental schemes used in this study

Exp. No.	Exp. category	Sample details
#1	Pure component	Distilled water
#2		Salty water (Salinity 10 000 ppm)
#3		Silica sand
#4		Bitumen
#5		<i>n</i> -Hexane
#6	Oil sands mixture	Porosity: 31 %
#7		Porosity: 25 %
#8		Porosity: 15 %
#9		$S_w = 0.0$
#10		$S_w = 0.2$
#11	$S_w = 0.4$	
#12	<i>n</i> -Hexane/bitumen mixture	<i>n</i> -Hexane weight fraction: 30 %
#13		<i>n</i> -Hexane weight fraction: 50 %
#14		<i>n</i> -Hexane weight fraction: 70 %
#15	<i>n</i> -Hexane/oil sands mixture	M0- $V_{sand} : V_{oil} : V_{water} : V_{sol} = 70 \% : 20 \% : 10 \% : 0 \%$ (water salinity 10 000 ppm)
#16		M1- $V_{sand} : V_{oil} : V_{water} : V_{sol} = 70 \% : 16 \% : 10 \% : 4 \%$ (water salinity 10 000 ppm)
#17		M2- $V_{sand} : V_{oil} : V_{water} : V_{sol} = 70 \% : 10 \% : 10 \% : 10 \%$ (water salinity 10 000 ppm)
#18		M3- $V_{sand} : V_{oil} : V_{water} : V_{sol} = 70 \% : 4 \% : 10 \% : 16 \%$ (water salinity 10 000 ppm)

### 2.3.2 Experimental Setup and Procedures

Figure 2-1 shows a schematic of the experimental setup, which consists of a probe (85070E Dielectric Probe Kit, Keysight Technologies, USA), network analyzer (PNA E8362B, Agilent Technologies, USA), cable, and computer with permittivity interpretation software (85070 software kit, Agilent Technologies, USA). Prior to the measurement, standard calibrations with air, short circuit, and distilled water have been carried out.<sup>[32,33]</sup> The permittivity of liquids (water, bitumen, *n*-hexane, *n*-hexane/bitumen mixtures) is measured by submerging the probe into the samples, while the permittivity of the oil sands mixture is measured by carefully mounting the probe at the top of the sample to ensure a good contact between the probe and samples.<sup>[33]</sup> A series of 980-points, linearly swept from 200 MHz to 10 GHz, are measured at room temperature (20 °C) and atmospheric pressure. Multiple measurements have been performed to reduce the systematic error.

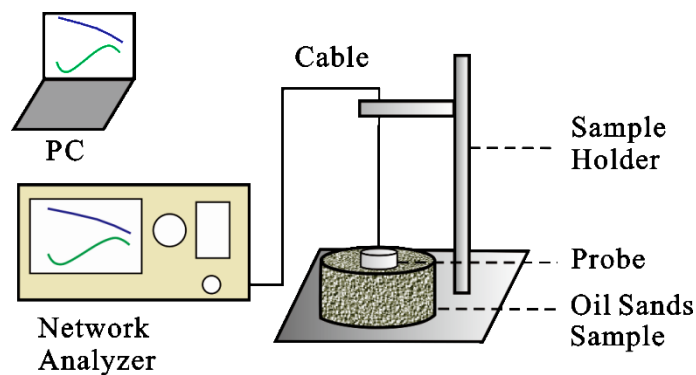
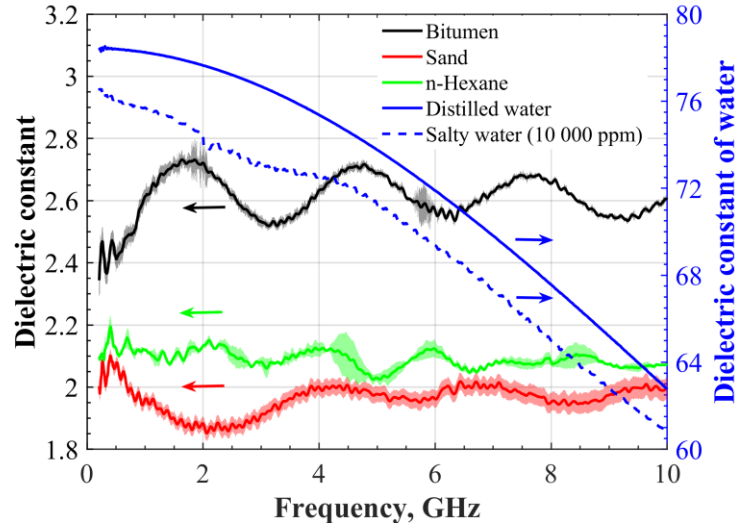


**Figure 2-1** Schematic of the experimental setup for conducting the permittivity measurements.

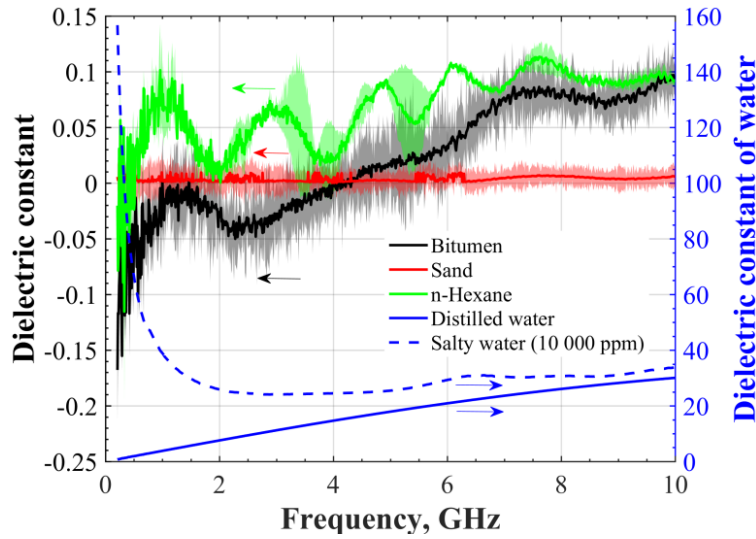
## 2.4 Results and Discussion

### 2.4.1 Permittivity of Constituents of Oil Sands

We first measure the permittivity of *n*-hexane and the constituents of the oil sands, including the silica sand, bitumen, distilled water, and salty water with a salinity of 10 000 ppm; **Figure 2-2** shows the measured dielectric constant and loss factor as a function of frequency. The average values of the measurements are plotted as solid lines, while the standard deviations are plotted as the corresponding shaded area adjacent to the line. At room temperature ( $20 \pm 2$  °C) and atmospheric pressure, distilled water has a dielectric constant of 78.45 at 200 MHz and decreases to 62.76 as the frequency increases to 10 GHz; the loss factor of water increases with an increase in frequency and reaches 30.30 at 10 GHz. With the addition of sodium chloride, the dielectric constant of simulated formation water (salinity of 10 000 ppm) slightly decreases, but the loss factor soars over the low frequencies, and then decreases with an increasing frequency. The added ions reduce the effective water concentration and restrain the water molecules' orientation,<sup>[34]</sup> leading to a decreased dielectric constant of water. As for the loss factor of the simulated formation water, the introduced extra ions can enhance the ion conduction, which increases the loss factor at low frequencies. At higher frequencies, the ions fail to align themselves with the fast alternating electric field, leading to a lessened enhancement in loss factor.<sup>[35,36]</sup>



(a)



(b)

**Figure 2-2** Permittivity of the constituents of oil sands: a) dielectric constant, and b) loss factor. The solid lines represent the average values of the measured permittivity, while the corresponding belts are error bars of the measurements (standard deviation).

Compared to water, other constituents are less polarized, which leads to much lower permittivity.

The dielectric constants and loss factors of bitumen, silica sand, and *n*-hexane remain almost constant along the tested frequency range, except with some fluctuations. Measurement results on the constituents of oil sands reveal that water is the major dielectric contributor in oil sands. Also, no relaxation phenomena have been found for bitumen, silica sand, and *n*-hexane over the tested frequency range. **Table 2-5** compares the measured permittivity with data from literature at

certain frequencies, and a good agreement has been found between the measured results and published data.

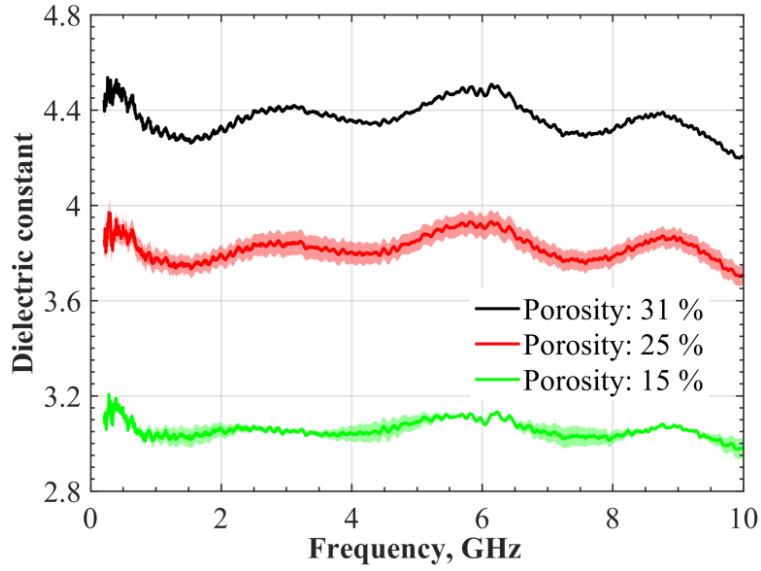
**Table 2-5** Comparison of the measured permittivity in this study and permittivity data from the literature

Sample	Frequency	Measured permittivity	Published data	Ref.
Bitumen	2.45 GHz	2.623–0.011j	2–0.002j	Okassa et al. <sup>[44]</sup>
<i>n</i> -Hexane	5.8 GHz	2.056 –0.082j	2.222–0.540j	Horikoshi et al. <sup>[45]</sup>
Sand	2.45 GHz	1.859 –0.005j	3.78–0.001j	Okassa et al. <sup>[44]</sup>
Brine (10 000 ppm)	200 MHz	76.599–156.709j	79.842–151.282j	Gadani et al. <sup>[36]</sup>
	1GHz	75.697–38.661j	73.544–35.897j	
Distilled water	2.45 GHz	77.256–9.256j	77.4–9.2j	Buffler <sup>[46]</sup>
Porosity: 31 %	2.45 GHz	4.367–0.061j	*(2.845–3.217)– (0.015–0.057)j	Erdogan et al. <sup>[22]</sup>
Porosity: 25 %		3.814–0.036j		
Porosity: 15 %		3.057–0.017j		
$S_w=0.2$		3.236–0.036j		
$S_w=0.4$		4.850–0.066j		

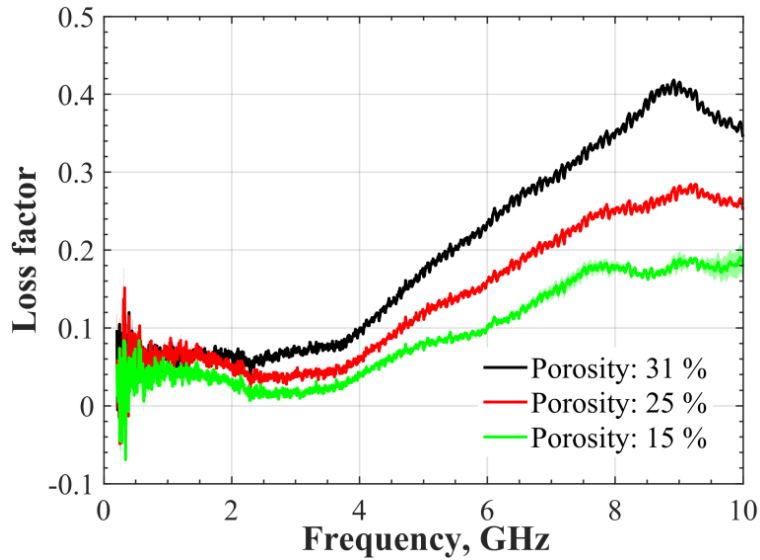
Note: \*The oil sands samples contain various water fractions.

#### 2.4.2 Effect of Water Content on Permittivity of Oil Sands

In the oil sands, water exists in the form of free water and bound water; the thin film of water on the surface of sand particles is characterized as bound water, which exhibits a lower mobility and permittivity compared to free water,<sup>[37,38]</sup> while the permittivity of the free water is similar to the properties of water in bulk. Also, the water content of oil sands is determined by the porosity and water saturation. To understand the effect of water content on the permittivity of oil sands mixtures, we first study the effect of porosity (31 %, 25 %, and 15 %) on the permittivity of oil sands formed by different sizes of sand particles, when the fluid saturations are fixed ( $S_w = 0.3$  and  $S_o = 0.7$ ); we then measure the permittivity of oil sands with different water saturation, when the porosity is fixed at 31 %. **Figures 2-3** and **Figure 2-4** show the measured results on the dielectric constant and loss factor of oil sand samples with different porosity and water saturation, respectively. Both an increasing porosity and an increasing water saturation enhance the water content in oil sands, leading to a boosted permittivity of oil sands.

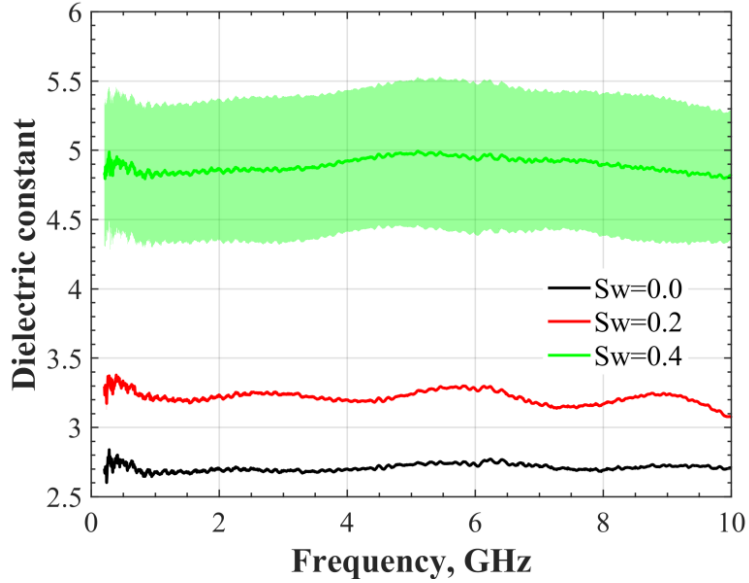


(a)

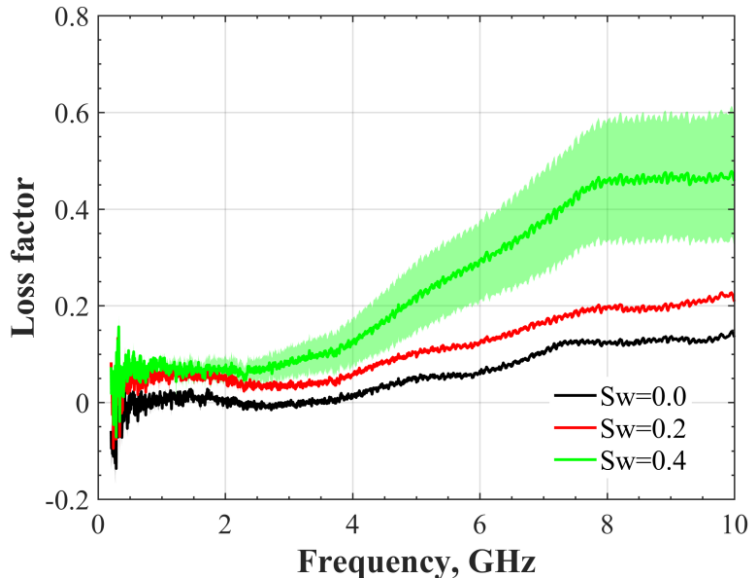


(b)

**Figure 2-3** Permittivity of oil sands with different porosity: a) dielectric constant, and b) loss factor. The solid lines represent the average values of the measured permittivity, while the corresponding belts are error bars of the measurements (standard deviation).



(a)



(b)

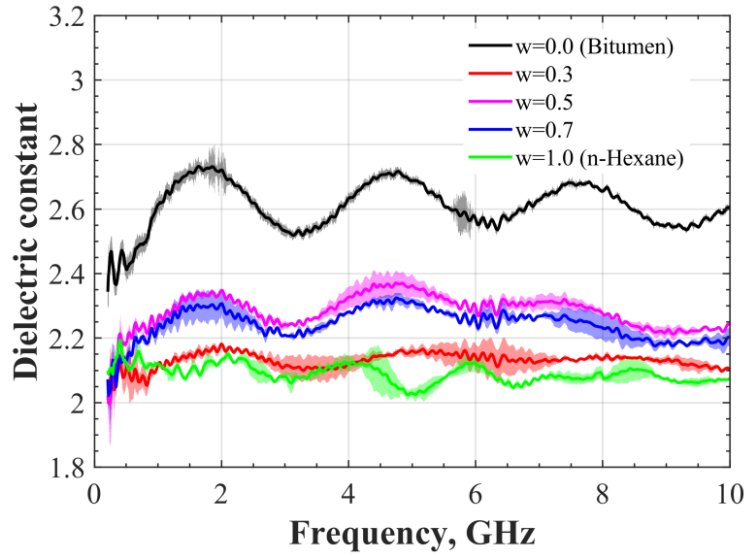
**Figure 2-4** Permittivity of oil sands with different water saturation: a) dielectric constant, and b) loss factor. The solid lines represent the average values of the measured permittivity, while the corresponding belts are error bars of the measurements (standard deviation).

The dielectric constants of oil sands slightly decrease as the frequency increases, while the loss factors of oil sands increase with an increasing frequency. The relationship between the permittivity of oil sands and frequency is similar to that of water's. However, the loss factors of oil sands reach the maximum values around 8 – 9 GHz, while the loss factor of bulk distilled water peaks at 10 GHz. The confinement of water molecules, exerted by other constituents of oil

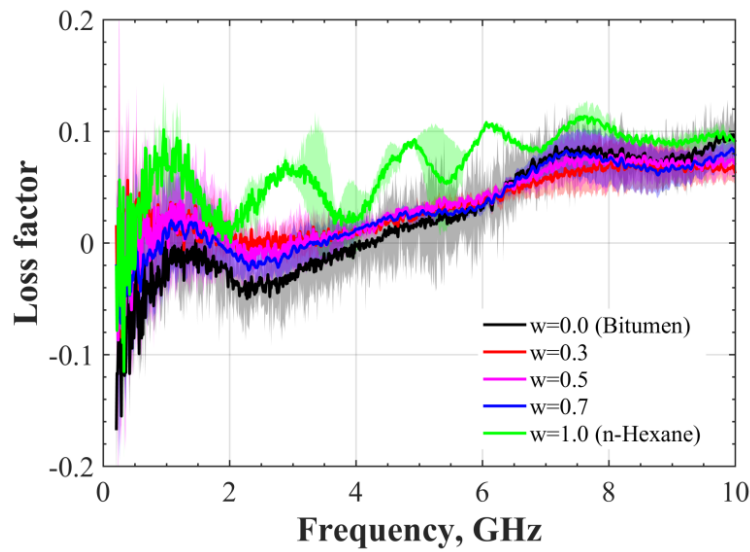
sands, causes the shift of relaxation frequency towards the lower frequencies; similar phenomena have also been found for the soil-water mixtures.<sup>[39]</sup> It is noted that a sudden jump occurs into the permittivity of oil sands for the case of water saturation of 0.4. A similar nonlinear relationship between water content and permittivity has been found in Hu and Liu's results.<sup>[40]</sup>

### **2.4.3 Effect of *n*-Hexane Addition**

We first investigate the effect of adding *n*-hexane on the permittivity of *n*-hexane/bitumen mixtures; **Figure 2-5** shows the permittivity of mixtures with different weight fractions of *n*-hexane. The dielectric constants of the mixtures fluctuate within a narrow range over the tested frequencies, while the loss factors rise with an increasing frequency. Results show that the permittivity of *n*-hexane/bitumen mixtures varies between the permittivity of *n*-hexane and bitumen. Also, the variations of the permittivity of *n*-hexane/bitumen mixture are not strictly proportional to the weight fraction of *n*-hexane. This is due to the complex interaction between bitumen and *n*-hexane when these two materials are mixed. Adding *n*-hexane reduces the viscosity of bitumen by dilution, which enhances the mobility of charge carriers in the mixture.<sup>[41]</sup> However, the addition of *n*-hexane addition also induces the self-aggregation/precipitation of asphaltene, which restrains the movement of the ions and causes a caging phenomenon.<sup>[27,42]</sup> Overall, adding *n*-hexane slightly reduces the dielectric constant of bitumen, while increasing the loss factor of bitumen.



(a)

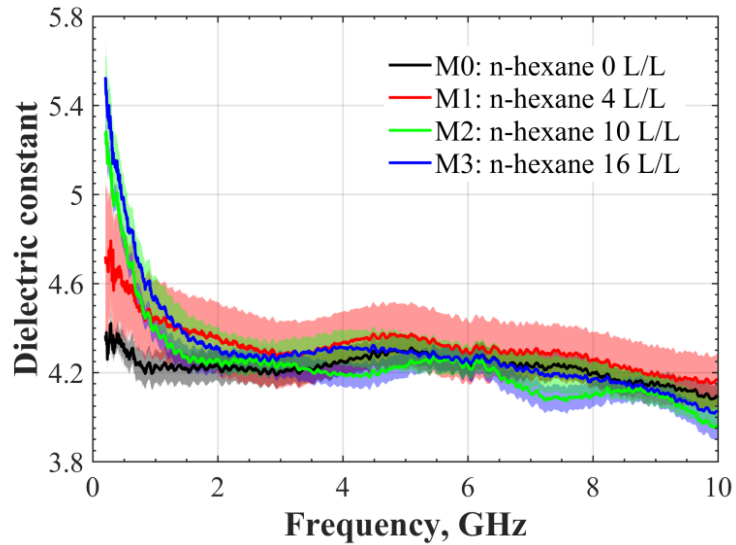


(b)

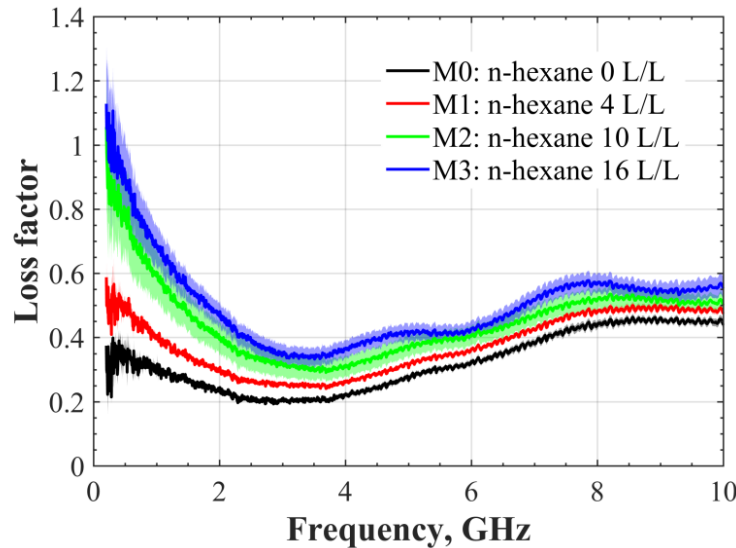
**Figure 2-5** Permittivity of *n*-hexane/bitumen mixtures: a) dielectric constant, and b) loss factor. The solid lines represent the average values of the measured permittivity, while the corresponding belts are error bars of the measurements (standard deviation).

We then examine the effect of *n*-hexane addition on the permittivity of the *n*-hexane/oil sands mixture. To simulate the real oil sands, the distilled water is changed to salty water with a salinity of 10 000 ppm. **Figure 2-6** shows the permittivity of the *n*-hexane/oil sands mixture: the volume fractions of solvent in mixtures M0, M1, M2, and M3 are 0, 4, 10, and 16 L/L, respectively. As the *n*-hexane fraction increases, the dielectric constant of the *n*-hexane/oil sands mixture

increases when the frequency is approximately below 2 GHz, while it reduces as the frequency continues to rise. Interestingly, the loss factor of the *n*-hexane/oil sands mixture significantly enhances with the addition of solvent addition, although *n*-hexane only marginally changes the permittivity of bitumen as shown in Figure 2-5.



(a)



(b)

**Figure 2-6** Permittivity of *n*-hexane/oil sands mixtures: a) dielectric constant, and b) loss factor. The solid lines represent the average values of the measured permittivity, while the corresponding belts are error bars of the measurements (standard deviation).

The interaction between the bitumen and water is a major mechanism that affects the permittivity of the *n*-hexane/oil sands mixture. Bitumen has a high viscosity and shows almost no mobility at room temperature, which may curb the charge movements in the oil sands. Also, water can bond with asphaltene since both of them are polar materials, which restrains the movement of water molecules at their interface and thereby reduces the overall free water content in oil sands. When adding *n*-hexane into the oil sands, the bitumen viscosity significantly decreases as shown in Table 2-3, which facilitates the mobility of charges in the oil sands.<sup>[27]</sup> Moreover, the asphaltene flocculation induced by the *n*-hexane addition affects the association between asphaltene and water, which frees the water molecule previously bonded by the asphaltenes.

**Figure 2-7** shows a schematic of the constituents' distribution of oil sands, describing the free water changes after the *n*-hexane addition. It shows that the *n*-hexane addition can enhance the free water content in the oil sands mixture. The previous investigations have proven that an increasing free water content could enhance the soil mixtures' permittivity.<sup>[35,38,40]</sup> Hence, the dynamic change of free water content induced by the addition of *n*-hexane addition provides an explanation for the permittivity behaviors of *n*-hexane/oil sands mixtures.

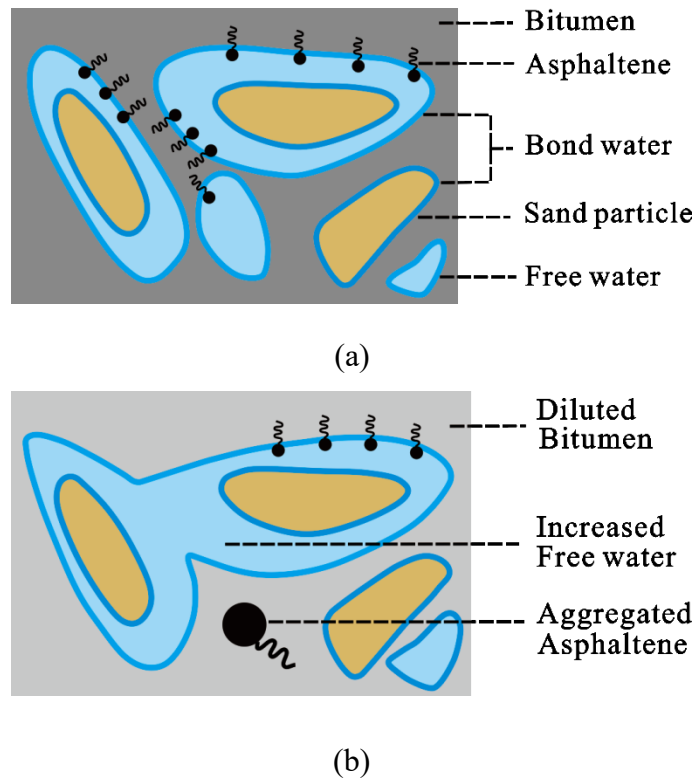


**Figure 2-7** Conceptual pictures of water distribution in oil sands: a) before *n*-hexane addition, and b) after *n*-hexane dilution.

The dielectric constant of the *n*-hexane/oil sands mixture is affected by both the free water content and solvent fraction. The addition of *n*-hexane reduces the dielectric constant of bitumen, while the induced free water enhances the dielectric constant of oil sands. Consequently, the final dielectric values of the *n*-hexane/oil sands mixtures are a balanced result between these two factors. The dielectric constant of *n*-hexane/oil sands first increases with the solvent addition, suggesting that enhanced free water is the dominant mechanism when the solvent fraction is low. As the solvent fraction increases, the dielectric constant of bitumen continuously reduces; meanwhile, the incremental amplitude of the induced free water content declines. Consequently, the dielectric constant of the *n*-hexane/oil sands mixture reduces at higher solvent fractions. The measured dielectric constants in Figure 2-6a exhibit large anomalous values below 2 GHz, which are caused by the frequency dispersion at initial frequencies.<sup>[27]</sup> The loss factors of the oil sands

get notably boosted after the solvent addition because both the *n*-hexane addition and free water content are beneficial to enhance the permittivity of oil sands. The augmentation of the free water content and the reduction of bitumen's viscosity lead to an enhanced permittivity of oil sands. As the volume fraction of solvent continuously increases, the amplitude of viscosity reduction and free water increment decrease, leading to a lessened enhancement in the permittivity of oil sands.

## 2.5 Evaluation of Mixing Models Used for the Permittivity Prediction of Oil Sands

The oil sands are complex mixtures consisted of polar materials (water, resins, and asphaltenes) and *non*-polar or slightly polarized materials (sand, saturates, and aromatics). The commonly - used mixing models for predicting the permittivity of soil and sandstone can be applied to predict the permittivity of oil sands.<sup>[28,43]</sup> In this section, the prediction accuracy of various mixing models is evaluated by assessing the average absolute relative deviation (AARD) between the measured values and the calculated ones.

### 2.5.1 Commonly-Used Mixing Models

The following mixing models, taking into account the porous structure of the mixture, are adopted to predict the dielectric properties permittivity of oil sands:, such as the Lorentz-Lorenz and Clausius-Mossotti (LLCM) model, complex refractive index method (CRIM), natural logarithmic Lichtenecker (L-LN) model, and Lichtnecker-Rother (LR) model.<sup>[28,42]</sup> The LLCM model calculates the permittivity of a mixture based on the permittivity of two of its components at each time. As for the oil sands, the permittivity of the liquid phase (bitumen/water mixture) is calculated first, and then the mixture's permittivity is assessed based on the permittivity of the sand and liquid phase. The LLCM model is given by the following: <sup>[28]</sup>

$$\frac{\varepsilon_{wb} - \varepsilon_w}{\varepsilon_{wb} + 2\varepsilon_w} = \frac{\varepsilon_b - \varepsilon_w}{\varepsilon_b + 2\varepsilon_w} (1 - S_w) \quad (2-6a)$$

$$\frac{\varepsilon_m - \varepsilon_{wb}}{\varepsilon_m + 2\varepsilon_{wb}} = \frac{\varepsilon_s - \varepsilon_{wb}}{\varepsilon_s + 2\varepsilon_{wb}}(1 - \phi) \quad (2-6b)$$

The L-LN model calculates the oil sands mixture's permittivity based on the natural logarithm of the permittivity of each constituent: [28]

$$\ln \varepsilon_m = (1 - \phi) \ln \varepsilon_s + \phi(1 - S_w) \ln \varepsilon_b + \phi S_w \ln \varepsilon_w \quad (2-7)$$

The LR model uses the power function to calculate the permittivity of oil sands, which is given as follows:[28,42]

$$\varepsilon_m^c = (1 - \phi) \varepsilon_s^c + \phi(1 - S_w) \varepsilon_b^c + \phi S_w \varepsilon_w^c \quad (2-8)$$

where  $c$  is a dimensionless fitting parameter or cementation factor. The range of  $c$  is between -1 and 1, corresponding to the harmonic-weighted average and direct-weighted average, respectively;[42] in general,  $c = 1/3$ . [39] When  $c = 0.5$ , the LR model reduces to the complex refractive index method (CRIM) model, which is given by the following:[28]

$$\sqrt{\varepsilon_m} = (1 - \phi) \sqrt{\varepsilon_s} + \phi(1 - S_w) \sqrt{\varepsilon_b} + \phi S_w \sqrt{\varepsilon_w} \quad (2-9)$$

In Equations (4)–(7),  $\varepsilon_m$  is the relative permittivity of the oil sands mixture,  $\varepsilon_s$  is the relative permittivity of bitumen,  $\varepsilon_b$  is the relative permittivity of water,  $\varepsilon_w$  is the relative permittivity of the water/bitumen mixture,  $\varepsilon_w$  is the relative permittivity of sand, and  $S_w$  and  $\phi$  are the water saturation and porosity of the oil sands sample, respectively. The above mixing models predict the permittivity of the oil sands mixture based on the composition and the permittivity of each constituent.

### 2.5.2 Evaluation of Prediction Accuracy of Various Mixing Models

The measured permittivities of the constituents of oil sands are used as input data in the aforementioned mixing models to predict the permittivity of different oil sands samples. The permittivities of bitumen,  $n$ -hexane, and sand are less dependent on the frequency compared to water. To lower the systematic error and large fluctuations at certain frequencies, the average

permittivity values evaluated along the tested frequency range of bitumen (2.609–0.022j), *n*-hexane (2.090–0.068j), and sand (1.963–0.004j) (where  $j = \sqrt{-1}$ ), are used in the calculation. The measured permittivity of water is directly fed into the mixing models due to its dependence on frequency. The AARD of these mixing models is calculated as follows:

$$AARD(\%) = \frac{100}{N_p} \sum_{k=1}^{N_p} \left| \frac{\mathcal{E}_{cal} - \mathcal{E}_{exp}}{\mathcal{E}_{exp}} \right| \quad (2-10)$$

where  $\mathcal{E}_{cal}$  is the calculated dielectric constant or loss factor,  $\mathcal{E}_{exp}$  is the measured dielectric constant or loss factor, and  $N_p$  is the number of data points in each measurement.

**Table 2-6** summarizes the AARDs yielded by different mixing models in predicting the permittivity of oil sands. The LLCM model, using a bi-phase mixing approach, results in large errors, making it is inappropriate for predicting the permittivity of oil sands. The L-LN model, employing the natural logarithm relationship, also shows huge deviations, which is deficient for predicting the permittivity of oil sands. The CRIM and LR models, applying the power relationship, exhibit higher accuracy for the prediction of the oil sands' permittivity. These mixing models can reasonably predict the dielectric constant of oil sands, while they inaccurately predict the loss factor of oil sands. Also, these mixing models show large errors for the permittivity prediction of oil sands with zero water saturation.

**Table 2-6** Summary of AARDs for predicting the permittivity of (*n*-hexane/) oil sands mixtures given by different mixing models

Exp. Case	AARDs of predictions of dielectric constants									
	LLCM		L-LN		LR ( $c=1/3$ )		CIRM ( $c=0.5$ )		$c=0.447$	
	Dielectric constant	Loss factor	Dielectric constant	Loss factor	Dielectric constant	Loss factor	Dielectric constant	Loss factor	Dielectric constant	Loss factor
Porosity:31 %	33.88 %	87.97 %	30.08 %	90.47 %	14.60 %	56.48 %	2.56 %	34.37 %	4.06 %	34.63 %
Porosity:25 %	29.42 %	85.93 %	29.22 %	90.61 %	12.95 %	56.58 %	2.51 %	48.75 %	3.59 %	47.36 %
Porosity:15 %	21.71 %	82.17 %	22.19 %	86.49 %	10.93 %	64.16 %	1.48 %	55.36 %	4.34 %	57.62 %
$S_w=0.0$	20.83 %	85.34 %	20.88 %	76.66 %	20.88 %	86.61 %	20.76 %	85.95 %	20.57 %	79.41 %
$S_w=0.2$	19.94 %	84.90 %	18.12 %	87.39 %	3.87 %	60.36 %	9.76 %	35.89 %	6.50 %	38.49 %
$S_w=0.4$	34.58 %	87.27 %	33.85 %	90.15 %	12.38 %	46.14 %	7.48 %	37.34 %	3.16 %	41.40 %
M0	32.99 %	99.96 %	14.99 %	29.30 %	10.27 %	71.30 %	8.28 %	15.80 %	5.75 % *(1.95 %)	36.44 % *(15.21 %)
M1	33.00 %	99.96 %	11.62 %	13.19 %	11.98 %	76.55 %	5.71 %	22.58 %	7.71 % *(2.09 %)	41.66 % *(10.54 %)
M2	32.96 %	93.86 %	13.46 %	11.34 %	10.77 %	77.98 %	7.75 %	29.97 %	5.58 % *(1.85 %)	50.93 % *(10.81 %)
M3	35.51 %	93.04 %	11.04 %	59.37 %	13.01 %	79.37 %	5.62 %	35.61 %	8.40 % *(1.88 %)	55.85 % *(11.26 %)

Note: \* The AARDs in the brackets are calculated with effective water saturation, while the values outside of brackets are evaluated with the original water saturation.

**Figure 2-8** illustrates the measured and predicted permittivity for the case of oil sands (porosity = 31 %) and the case of the *n*-hexane/oil sands mixture (M1). As we can see, the CRIM model slightly overestimates the permittivity of oil sands, while the LR model underestimates the permittivity of oil sands. Similar observations have been found for other oil sands cases. The only difference between the CRIM model and LR model lies in the parameter *c*, which can be treated as a fitting parameter. We tune the *c*-parameter to enhance the prediction accuracy for oil sands cases. When  $c = 0.447$ , the overall deviation for all the oil sands cases reaches the minimum. However, the prediction errors of loss factors are still high after such a correction. We conduct curve fitting for the loss factor data to obtain correlations for the loss factor of oil sands. A three terms Fourier series fit well for the measured loss factors, as shown in Figure 2-8. The coefficients and the coefficient of determination ( $R^2$ ) corresponding to each case are listed in **Table 2-7**.

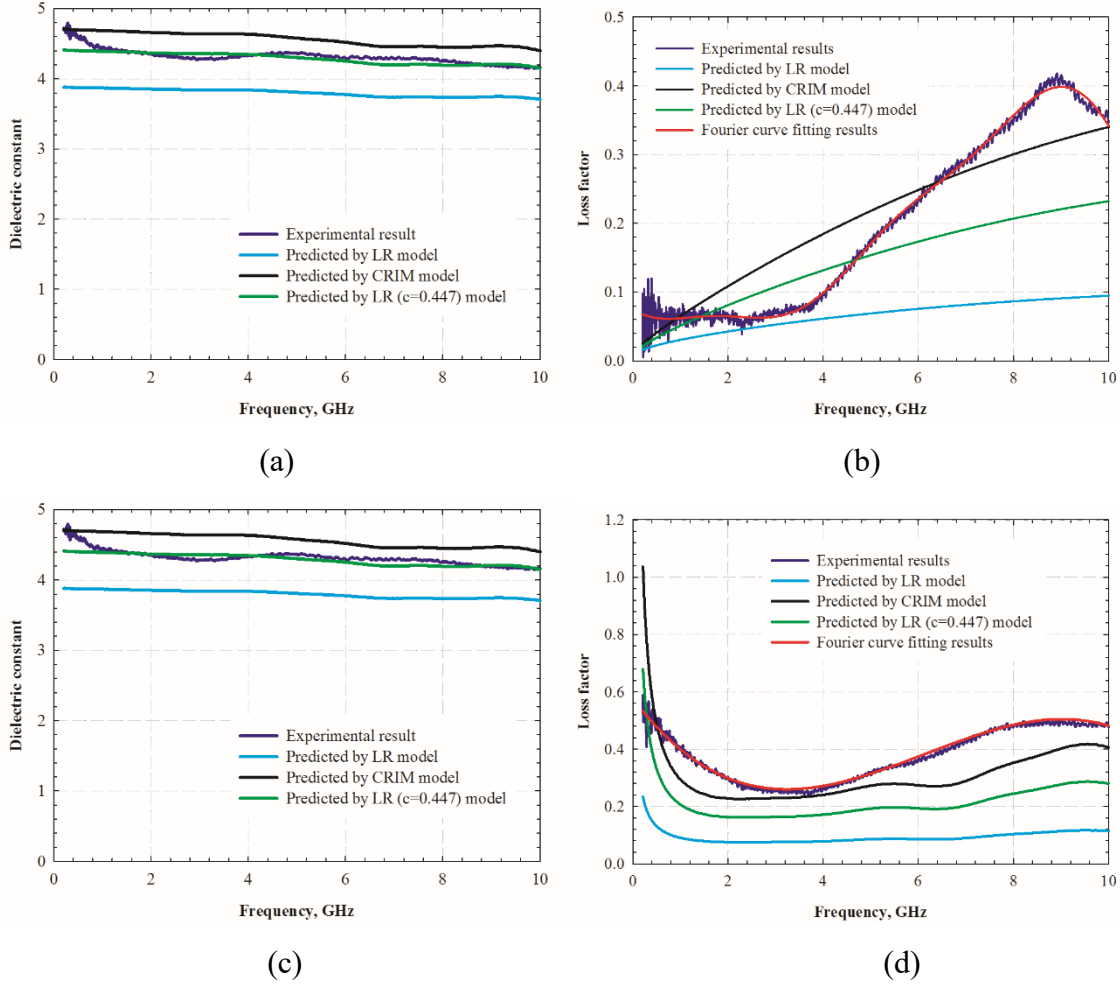


**Figure 2-8** Comparison of the measured permittivity and calculated ones by different mixing models: a) dielectric constant of oil sands (the case with a porosity of 31 %), b) loss factor of oil sands (the case with a porosity of 31 %), c) dielectric constant of *n*-hexane/oil sands mixture (the case M1), and d) loss factor of *n*-hexane/oil sands mixture (the case M1).

**Table 2-7** Coefficient values for calculating the loss factor of the (*n*-hexane/) oil sands mixtures

Property	Sample	$a_0$	$a_1$	$b_1$	$a_2$	$b_2$	$a_3$	$b_3$	$w(10^{-1})$	$R^2$
Loss factor	Porosity:31 %	$1.951 \times 10^{-1}$	$-7.210 \times 10^{-2}$	$-1.484 \times 10^{-1}$	$-3.563 \times 10^{-2}$	$4.591 \times 10^{-3}$	$1.222 \times 10^{-2}$	$1.727 \times 10^{-2}$	5.116	0.996
	Porosity:25 %	-3.148	2.050	4.764	1.586	-1.815	$-4.658 \times 10^{-1}$	$-1.909 \times 10^{-1}$	2.157	0.991
	Porosity:15 %	$-4.092 \times 10^5$	$6.063 \times 10^5$	$9.901 \times 10^4$	$-2.335 \times 10^5$	$-7.841 \times 10^4$	$3.645 \times 10^4$	$1.927 \times 10^4$	0.253	0.982
	$S_w = 0.0$	$-2.884 \times 10^7$	$4.311 \times 10^7$	$-3.668 \times 10^6$	$-1.707 \times 10^7$	$2.926 \times 10^6$	$2.796 \times 10^6$	$-7.279 \times 10^5$	-0.141	0.966
	$S_w = 0.2$	$-1.264 \times 10^6$	$1.878 \times 10^6$	$-2.695 \times 10^5$	$-7.301 \times 10^5$	$2.140 \times 10^5$	$1.159 \times 10^5$	$-5.284 \times 10^5$	-0.220	0.982
	$S_w = 0.4$	$-1.429 \times 10^6$	$2.124 \times 10^6$	$3.014 \times 10^5$	$-8.255 \times 10^5$	$-2.393 \times 10^5$	$1.310 \times 10^5$	$5.908 \times 10^4$	0.205	0.995
	M0	$3.373 \times 10^{-1}$	$4.946 \times 10^{-3}$	$-1.210 \times 10^{-1}$	$9.279 \times 10^{-3}$	$6.487 \times 10^{-3}$	$6.644 \times 10^{-3}$	$6.769 \times 10^{-3}$	5.090	0.987
	M1	$4.600 \times 10^{-1}$	$4.951 \times 10^{-2}$	$-1.614 \times 10^{-1}$	$6.002 \times 10^{-2}$	$-7.247 \times 10^{-2}$	$-5.270 \times 10^{-3}$	$-2.633 \times 10^{-2}$	3.970	0.991
M2	$1.913 \times 10^6$	$-2.847 \times 10^6$	$3.541 \times 10^5$	$1.113 \times 10^6$	$-2.810 \times 10^5$	$-1.784 \times 10^5$	$6.929 \times 10^4$	-0.214	0.991	
M3	$8.047 \times 10^{-1}$	$3.469 \times 10^{-1}$	$-4.524 \times 10^{-1}$	$3.947 \times 10^{-2}$	$-2.990 \times 10^{-1}$	$-6.560 \times 10^{-2}$	$-5.518 \times 10^{-2}$	3.836	0.985	

Note: The correlation is in the form of  $\varepsilon'' = a_0 + \sum_{i=1}^{i=3} a_i \cdot \cos(i \times f \times w) + b_i \cdot \sin(i \times f \times w)$ , where  $\varepsilon''$  is the loss factor,  $f$  is the frequency in GHz, and  $w, a, b$  are coefficients.

### 2.5.3 Modification of the LR Model for Predicting the Permittivity of *n*-Hexane/Oil Sands

As for the permittivity prediction of the *n*-hexane/oil sands mixture, these mixing models exhibit large error since they overlook the changes of bitumen properties due to the *n*-hexane addition and variations of free water content. Punase and Hascakir measured the dielectric properties of various crude oil samples; they also found that the permittivity prediction models, which neglect the interactions between the asphaltene and deasphaltene fraction, exhibit large deviations.<sup>[47]</sup> To capture the dynamic changes in free water content caused by asphaltene flocculation, an effective water saturation is proposed to replace the static water saturation in the LR model. The modified LR model is given as follows:

$$\varepsilon_m^c = (1 - \phi) \varepsilon_s^c + \phi(1 - S_w) \varepsilon_b^c + \phi S_{w-eff} \varepsilon_w^c \quad (2-11)$$

where  $c = 0.447$  (obtained from the cases of oil sands mixtures), and  $S_{w-eff}$  is the effective water saturation. We empirically tune the water saturation in the original mixing models, and the ones that yield the least AARDs are treated as the effective water saturation.

**Figure 2-9** plots the relationship of the differences between the effective water saturation and original water saturation ( $\Delta S_w = S_{w-eff} - S_w$ ) versus. the double logarithm viscosity of the diluted bitumen ( $\log[\log(\mu_d)]$ ); a good linear relationship ( $R^2 = 0.991$ ) has been found between these two parameters. Therefore, effective water saturation can be approximated by the obtained correlation and the viscosity of bitumen after the solvent addition:

$$\Delta S_w = -0.0936 \log[\log(\mu_d)] + 0.1585 \quad (2-12)$$

where  $\mu_d$  is the viscosity of the diluted bitumen. Table 2-6 shows the comparison of AARDs between the original LR models and the improved one in predicting the permittivity of *n*-hexane/oil sands mixtures. It can be seen that the modified LR model with effective water

saturation provides much more accurate predictions for the *n*-hexane/oil sands mixtures. This also confirms that the effective water saturation should be considered if one wants to apply these mixing models when the miscible solvent is present. Also, the modified LR model can be conveniently applied to estimate the permittivity of *n*-alkane solvent/oil sands mixtures when experimental data are lacking.

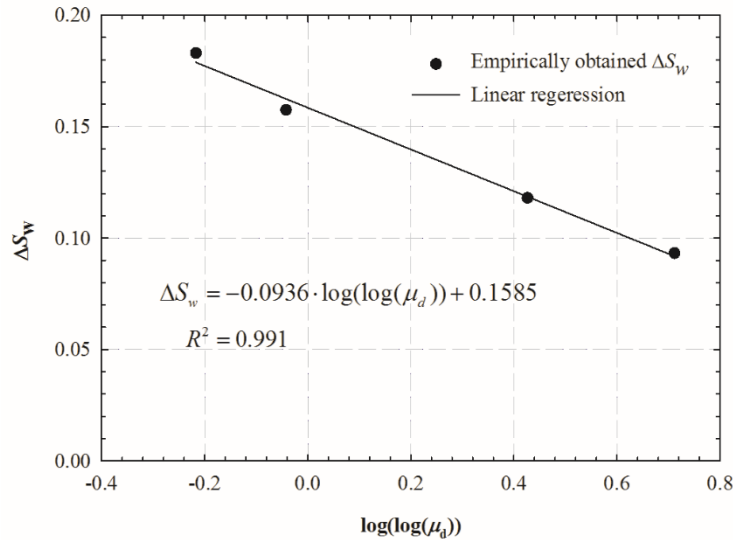


**Figure 2-9** Linear correlation between the double logarithm viscosity of solvent-diluted bitumen ( $\log_{10}[\log_{10}(\mu_d)]$ ) and the difference of the effective water saturation and original water saturation ( $\Delta S_w = S_{w-eff} - S_w$ ).

## 2.6 Conclusions

In this experimental study, the open-ended coaxial probe method is utilized to measure the permittivity of the constituents of oil sands, oil sands with different water saturation and porosity, *n*-hexane/bitumen mixtures, and *n*-hexane/oil sands mixtures. The permittivity data over a large frequency range of 200 MHz to 10 GHz are obtained. Results show that water is a major dielectric contributor to the oil sands. Consequently, water content plays a critical role in affecting the permittivity of oil sands. Both the dielectric constant and loss factor increasing with an increasing water content. No relaxation phenomena have been found for bitumen, *n*-hexane, and silica sand within the tested frequency range. When *n*-hexane is mixed with bitumen, the

dielectric constant of bitumen decreases, while the loss factor of bitumen increases. Meanwhile, a significant viscosity reduction and asphaltene flocculation happen when *n*-hexane is added into the bitumen, which causes nonlinear changes in the permittivity of *n*-hexane/bitumen mixtures. As for the oil sands, the addition of *n*-hexane significantly enhances the loss factor of oil sands due to the viscosity reduction and the increment in free water content. Among the tested mixing models, the LR model reasonably predicts the dielectric constant of the oil sands mixture. However, it fails to accurately characterize the loss factor of oil sands. Empirical correlations have been developed between the loss factors and frequency for circumstances where the mixing models are inefficient. To capture the variation of free water content induced by the *n*-hexane addition, an effective water saturation is proposed to replace the original water saturation in the LR model (when  $c=0.447$ ). The modified LR model significantly improves the prediction accuracy for the *n*-hexane/oil sands mixtures, which provides a quick estimation for the permittivity of the *n*-alkane/oil sands mixtures when experimental data are missing.

## Nomenclature

$c$	dimensionless fitting parameter in Equation (2-8)
$C$	speed of light in a vacuum (about $3 \times 10^8$ m/s)
$D_p$	penetration depth (m)
$E$	electric field (V/m)
$f$	frequency (Hz)
$P_d$	absorbed power (W)
$P_0$	incident power at the wellbore ( $\text{W/m}^3$ )
$r$	distance to wellbore (m)

- $r_0$  radius of the wellbore (m)
- $S_w$  water saturation (dimensionless)
- $S_{w-eff}$  effective water saturation in Equation (2-11) (dimensionless)
- $\Delta S_w$  difference between effective water saturation and original water saturation
- $N_p$  number of data points

#### Greek Letters

- $\alpha$  absorption coefficient (1/m)
- $\varepsilon^*$  absolute complex permittivity (F/m)
- $\varepsilon'$  real part of relative permittivity (dimensionless)
- $\varepsilon''$  imaginary part of relative permittivity (dimensionless)
- $\varepsilon_b$  relative permittivity of bitumen (dimensionless)
- $\varepsilon_{cal}$  calculated relative permittivity (dimensionless)
- $\varepsilon_{exp}$  measured relative permittivity (dimensionless)
- $\varepsilon_m$  relative permittivity of oil sands mixture (dimensionless)
- $\varepsilon_r^*$  relative complex permittivity (dimensionless)
- $\varepsilon_s$  relative permittivity of sand (dimensionless)
- $\varepsilon_w$  relative permittivity of water (dimensionless)
- $\varepsilon_{wb}$  relative permittivity of water/bitumen mixture (dimensionless)
- $\phi$  porosity (dimensionless)
- $\mu_o$  permeability (electromagnetism) of free space ( $1.26 \times 10^{-6}$  H/m)

$\mu_d$  viscosity of the diluted bitumen (mPa·s)

## 2.7 References

- [1] R. M. Butler, *Thermal Recovery of Oil and Bitumen*, GravDrain Inc., Calgary **1997**.
- [2] H. Hassanzadeh, T. G. Harding, *Fuel* **2016**, *178*, 290.
- [3] J. R. Fanchi, *SPE Advanced Technology Series* **1993**, *1*, 161.
- [4] H. Gill, *J. Microwave Power E.E.* **1983**, *18*, 107.
- [5] Y. M. Cheng, C. Z. Guo, L. Gong, “A Mathematic Model of Electrical Heating in Hollow Pump Rod and Its Application,” *SPE International Heavy Oil Symposium*, Society of Petroleum Engineers, Calgary, 19–21 June **1995**.
- [6] R. S. Kasevich, S. L. Price, D. L. Faust, M. F. Fontaine, “Pilot Testing of a Radio Frequency Heating System for Enhanced Oil Recovery from Diatomaceous Earth,” *SPE Annual Technical Conference and Exhibition*, Society of Petroleum Engineers, New Orleans, 25–28 September **1994**.
- [7] A. Harvey, M. D. Arnold, S. A. El-Feky, *J. Can. Petrol. Technol.* **1979**, *18*, 47.
- [8] H. R. Lashgari, M. Delshad, K. Sepehrnoori, E. de Rouffignac, *SPE J.* **2016**, *21*, 87.
- [9] M. Koolman, N. Huber, D. Diehl, B. Wacker, “EM Heating Method to Improve Steam Assisted Gravity Drainage,” *SPE International Thermal Operations and Heavy Oil Symposium*, Society of Petroleum Engineers, Calgary, 20–23 October **2008**.
- [10] B. Wacker, D. Karmeileopardus, B. Trautmann, A. Helgetet, M. Torlak, “Electromagnetic Heating for In-Situ Production of Heavy Oil and Bitumen Reservoirs,” *Canadian Unconventional Resources Conference*, Society of Petroleum Engineers, Calgary, 15–17 November **2011**.
- [11] A. Koch, S. Sotskiy, D. Mustafina, V. Danov, “Mechanism of Heavy Oil Recovery Driven by EM Inductive Heating,” *SPE Heavy Oil Conference-Canada*, Society of Petroleum Engineers, Calgary, 11–13 June **2013**.
- [12] G. C. Sresty, H. Dev, R. H. Snow, J. E. Bridges, *SPE Reservoir Eng.* **1986**, *1*, 85.
- [13] US. 8, 616273 B2 (**2013**), M. Trautman, D. Ehresman, N. Edmunds, G. Taylor, M. Cimolai.
- [14] A. Bera, T. Babadagli, *Appl. Energ.* **2015**, *151*, 206.
- [15] A. Sadeghi, H. Hassanzadeh, T. G. Harding, *Int. J. Heat Mass Tran.* **2017**, *111*, 908.
- [16] A. Sadeghi, H. Hassanzadeh, T. G. Harding, *J. Petrol. Sci. Eng.* **2017**, *154*, 163.

- [17] A. Sadeghi, H. Hassanzadeh, T. G. Harding, *Chem. Eng. Sci.* **2017**, *172*, 13.
- [18] L. Hu, H. A. Li, T. Babadagli, M. Ahmadloo, *SPE J.* **2018**, In Press.
- [19] J. Czarnecki, B. Radoev, L. L. Schramm, R. Slavchev, *Adv. Colloid Interfac.* **2005**, *114–115*, 53.
- [20] L. Goual, A. Firoozabadi, *AIChE J.* **2002**, *48*, 2646.
- [21] F. S. Chute, F. E. Vermeulen, M. R. Cervenak, F. J. McVea, *Can. J. Earth Sci.* **1979**, *16*, 2009.
- [22] L. Erdogan, C. Akyel, F. M. Ghannouchi, *J. Microwave Power E.E.* **2011**, *45*, 15.
- [23] R. Gaikwad, *Electrical properties estimation of oil sands*, MSc thesis, University of Alberta, Edmonton, AB, **2014**.
- [24] L. Hu, H. A. Li, T. Babadagli, M. Ahmadloo, *J. Petrol. Sci. Eng.* **2017**, *154*, 589.
- [25] H. Li, S. Zheng, D. Yang, *SPE J.* **2013**, *8*, 695.
- [26] C. Lesaint, Ø. Spets, W. R. Glomm, S. Simon, J. Sjöblom, *Colloid. Surface A* **2010**, *369*, 20.
- [27] E. Y. Sheu, S. Acevedo, *Fuel* **2006**, *85*, 1953.
- [28] K. Hu, C. R. Liu, *IEEE T. Geosci. Remote* **2000**, *38*, 1328.
- [29] A. C. Metaxas, R. J. Meredith, *Industrial microwave heating*, Peter Peregrinus, London, **1983**.
- [30] M. Al-Harashseh, S. Kingman, A. Saeid, J. Robinson, G. Dimitrakakis, H. Alnawafleh, *Fuel Process. Technol.* **2009**, *90*, 1259.
- [31] J. R. Fanchi, *SPE Advanced Technology Series* **1993**, *1*, 161.
- [32] Keysight Technology, Keysight (Agilent) 85070E dielectric probe kit 200MHz to 50GHz, USA, **2012**.
- [33] Keysight Technology, *Basics of measuring the dielectric properties of materials*, Application Note, USA, November 19, **2014**.
- [34] J. M. Donadille, O. Faivre, “Water Complex Permittivity Model for Dielectric Logging,” *SPE Middle East Oil & Gas Show and Conference*, Society of Petroleum Engineers, Manama, 8–11 March **2015**.
- [35] Y. Lasne, P. Paillou, A. Freeman, T. Farr, K. C. McDonald, G. Ruffiè, J. M. Malèzieux. B. Chapman, F. Demontoux, *IEEE T. Geosci. Remote* **2008**, *46*, 1674.
- [36] D. H. Gadani, V. A. Rana, S. P. Bhatnagar, A. N. Prajapati, A. D. Vyas, *Indian J. Pure Ap. Phys.* **2012**, *50*, 405.

- [37] W. A. Jury, R. Horton, *Soil Physics*, 6th edition, Wiley, **2004**.
- [38] J. R. Wang, T. J. Schmugge, *IEEE T. Geosci. Remote* **1980**, *GE-18*, 288.
- [39] P. Hoekstra, A. Delaney, *J. Geophys. Res.* **1974**, *79*, 1699.
- [40] C. Lesaint, S. Simon, C. Lesaint, W. R. Glomm, G. Berg, L. E. Lundgaard, J. Sjöblom, *Energ. Fuel.* **2012**, *27*, 75.
- [41] E. Y. Sheu, D. A. Storm, M. B. Shields, *Energ. Fuel.* **1994**, *8*, 552.
- [42] T. P. Leão, E. Perfect, J. S. Tyner, *T. ASABE* **2014**, *58*, 83.
- [43] F. D. Okassa, A. Godi, M. De Simoni, M. Manotti, M. Misenta, G. Maddinelli, “A Nonconventional EOR Technology Using RF/MW Heating Coupled with a New Patented Well/Reservoir Interface,” *SPE Annual Technical Conference and Exhibition*, Society of Petroleum Engineers, Florence, 22–23 Sept **2010**.
- [44] S. Horikoshi, S. Matsuzaki, T. Mitani, N. Serpone, *Radiat. Phys. Chem.* **2012**, *81*, 1885.
- [45] C. R. Buffler, *A new, low power 915 MHz microwave system for efficient industrial scale-up prototyping*, Microwave Industrial Food Processing, Chicago, **1998**.
- [46] M. Das, R. Thapar, K. Rajeshwar, J. Dubow, *Can. J. Earth Sci.* **1981**, *18*, 742.
- [47] A. Punase, B. Hascakir, *Energ. Fuel.* **2017**, *31*, 65.

## **CHAPTER 3 EXPERIMENTAL INVESTIGATION OF COMBINED ELECTROMAGNETIC HEATING AND SOLVENT ASSISTED GRAVITY DRAINAGE FOR HEAVY OIL RECOVERY**

A version of this chapter was presented at the SPE Heavy Oil Conference-Canada held on 7–9 June 2016 in Calgary, Alberta, Canada and has been accepted for publication in *Journal of Petroleum Science and Engineering* **154**: 589-601.

## Summary

Electromagnetic (EM) heating holds a significant potential for heavy oil recovery since it can reduce carbon emission and avoid excessive water usage, and is applicable for water hostile reservoirs. Combining solvent injection with EM heating might further reduce the energy intensity of the process. The merits of using solvent in EM heating include diluting heavy oil and thereby increasing its mobility, serving as a heat carrier by reinforcing heat convection in porous media and facilitating gravity drainage by forming a vapor chamber. In this study, we conduct a series of laboratory experiments to investigate the performances and mechanisms of combined EM heating and solvent assisted gravity drainage for heavy oil recovery.

During experiments, sand pack samples contained in Buchner filter funnel are placed in a microwave oven. Solvent injection can be initiated together with EM heating to simulate this hybrid process. Temperatures of the sand pack and oil recoveries are simultaneously recorded. We investigate the effects of influential factors on the process performances, including EM heating power, initial water saturation, solvent types (*n*-hexane and *n*-octane), and combination strategies of EM heating and solvent injection (simultaneous or alternate means). Experimental results show that combined EM heating and solvent assisted gravity drainage could effectively enhance heavy oil recovery; the recovery factors of EM heating only, alternate EM heating and *n*-hexane injection, and alternate EM heating and *n*-octane injection are 12.37%, 61.18%, and, 83.59%, respectively. Moderate initial water saturation increases the heating speed and provides a higher oil recovery. The effect of solvent addition, affected by the solvent concentration in heavy oil, varies at different EM heating powers. Alternate EM heating and solvent injection is more cost effective due to the lower energy consumption and higher oil recovery compared to the

simultaneous EM heating and solvent injection. A lowered asphaltene fraction in recovered oil has also been found in this hybrid process.

**Keywords:** Electromagnetic heating, Solvent concentration, Asphaltenes, Residual oil saturation

### **3.1 Introduction**

Thermal methods are the most effective ways for heavy oil recovery. Conventional in-situ thermal methods, such as hot water/steam flooding, cyclic steam stimulation (CSS), and steam-assisted gravity drainage (SAGD), raise the reservoir temperature and increase the mobility of heavy oil by injecting hot water or steam. These steam-based methods are less effective in thin pay zones and deep reservoirs (Sahni et al., 2000) due to the large heat loss to adjacent formations or through the wellbore. Electromagnetic (EM) heating, overcomes some of these difficulties and possesses the merits of fast heating speed and environmental friendliness. Based on the frequency, EM heating could be classified into three classes: (1) low-frequency heating, (2) inductive heating, and (3) high-frequency heating.

In the (1) low-frequency heating, an electrical potential is established between wells by setting some wells as anodes and the others as cathodes; resistive heating or joule heating dominates this process. Harvey et al. (1979) experimentally tested the feasibility of this process. Pizarro and Trevisan (1990) conducted a low-frequency electrical heating field trial in the Rio Panan field, Brazil. After 70 days of heating, production rate increased from 1.2 bbl/d to 6.3 bbl/d at a heating power of 20 kW. Recently, Lashgari et al. (2016) developed an electrical-joule-heating simulator with the consideration of phase change of water and combined with fractures saturated with fluids. The inter-well connectivity is critical to this heating scheme, and formation temperature is limited below the water saturation temperature to maintain the circuit. (2) Inductive heating applies coil around the heating objects and relies on the eddy current to generate heat. Koolman

et al. (2008) studied the inductive heating by inserting an inductor loop into the sandbox and measured the temperature changes and found that inductive heating could help the chamber expansion and increase the heating speed of SAGD. Koch et al. (2013) investigated the mechanisms of inductive heating and found that operational pressure played a major role in the oil recovery. (3) High-frequency heating (from 3 kHz to 300 GHz), also known as radio or microwave frequency heating, generates heat through dipole rotation and ion conduction under a high-frequency alternating electric field. Sresty et al. (1986) conducted a pilot test in a tar sand formation in Utah where 35% of oil in place was recovered after three weeks' heating. Bera and Babadagli (2015) conducted an exhaustive review of experimental works, simulation studies, and field applications of the radio-frequency heating. Recently, the enhanced solvent extraction incorporating EM heating (ESEIEH) is under pilot tests, where a SAGD-like well pair was adopted, with antennas and solvent injection implemented at the upper well and the oil produced at the lower well (Pasalic et al., 2015).

To heat up a large part of the reservoir, field application is usually carried out at the radio-frequency ranges because of the greater penetration depths. Yet, experimental studies are generally conducted at the microwave frequency range because of the trade-off between sample size and wavelength affected by the applied frequency. Despite the large frequency difference between radio-frequency and microwave-frequency, both frequencies are classified as high-frequency heating and share a similar heating mechanism. Jha et al. (1999) built a model to study the combination of gas injection and EM heating. They observed that injecting N<sub>2</sub> at 41.3 kPa could recover about 20% of original oil in place (OOIP), EM heating at 10 MHz could recover about 24% OOIP, and combined EM heating and N<sub>2</sub> injection could recover 45% of OOIP. Alomair et al. (2012) investigated the performance of three methods including EM induction

heating, electrical resistance heating, and microwave heating in recovering oil from sand packs. The three methods provided incremental recoveries of 17.80%–34.00%, 24.80%–29.40% and 10.34%–20.79%, respectively. They also found that microwave heating exhibited the fastest heating speed and could reduce the heating time, and concluded that microwave heating was the most economical recovery method regarding recovery and power consumption. Bientinesi et al. (2013) used a dipole antenna to heat a sandbox containing 2000 kg oil sands sample. They reported that EM heating could heat the sample up to 200°C, but they found that the gravity drainage effect was unobservable in their experiment. Hascakir et al. (2009) conducted experiments in a commercial microwave oven to study the influencing parameters on the process efficiency, such as heating time, waiting period, porosity, permeability, wettability, and water saturation. They concluded that high initial water saturation results in high oil recovery, water-wetness is more favorable to EM heating, and high porosity and permeability could provide a higher oil recovery. Kovaleva et al. (2011) compared the effects of electrical and radio-frequency EM heating on the mass transfer in a solvent flooding scheme. They concluded that radiofrequency heating exhibits a higher oil recovery and less asphaltene precipitation, because of the better oil property after being exposed to EM radiation. Greff and Babadagli (2013) studied the effectiveness of using nanoparticles in EM heating and found that nanoparticles generate a catalytic effect on heavy oil, reducing its viscosity and that a higher concentration of nanoparticles yields a higher temperature and recovery factor. Bera and Babadagli (2015) further tested the effect of different EM heating power and the use of Ni and Fe nanoparticles. They concluded that high power leads to a faster heating speed and a higher temperature, Ni nanoparticles are more effective than Fe, and the oil with nanoparticle addition exhibits a significant reduction in viscosity after being exposed to microwave heating.

It is noted that using electromagnetic heating to recover heavy oil could heat up the reservoir to a high temperature within a short time, but the resulting oil recovery factor is normally not high. Due to the low reservoir pressure of heavy oil formations, gravity drainage tends to be a more feasible approach for producing heavy oil compared with flooding methods. Yet, the effect of gravity drainage on heavy oil recovery when electromagnetic heating is applied solely is not prominent, as shown in previous studies (Jha et al., 1999; Alomair et al., 2012; Bientinesi et al., 2013). Combined electromagnetic heating and solvent assisted gravity drainage could increase the mobility of heavy oil through both heat and solvent dilution. The large density difference between (vapor) solvent and heavy oil is also beneficial to gravity drainage. An enhanced oil recovery is expected from this hybrid process. The oil recovery governed by gravity drainage when EM heating and solvent are both present has seldom been studied in previous research. It is still of critical importance to evaluate the performance and examine the important mechanisms of this hybrid method, and hence optimize the efficiency of such a process.

In this study, laboratory experiments are conducted to investigate the combined EM heating and solvent assisted gravity drainage. A sand pack saturated with heavy oil is vertically placed in a microwave oven, while solvent can be injected from the top and oil can be recovered from the bottom of the sand pack. Temperatures of the sand pack and oil recoveries are recorded continuously, and these data are analyzed to clarify the conditions that can improve heating and oil recovery efficiency. We investigate the effect of influential factors on the performance of this hybrid process, including EM heating power, initial water saturation, types of solvent, and combining strategies of EM heating and solvent injection. To elucidate the effect of combined EM heating and solvent addition on oil recovery, we calculate the viscosity of diluted heavy oil based on the liquid phase composition obtained from the flash calculation and temperature of the

sand pack after EM heating. And saturates, aromatics, resins, and asphaltenes (SARA) analysis of recovered oil sample is carried out to clarify the property changes of recovered oil in this process. To study the residual oil saturation of this hybrid process, experimental residual oil saturations are compared with estimated residual oil saturations calculated with gravity drainage models. Finally, we compare the energy utilization of two operation strategies: simultaneous EM heating and solvent injection, and alternate EM heating and solvent injection.

### **3.2 Statement of Problem**

Unlike conventional heating methods where heat is transferred from outside, EM heating could generate heat within the materials and significantly accelerate the heating process. Dipoles and ions, characterized by their dielectric properties, align themselves with a high-frequency alternating electric field, generating frictional heat (Tang et al., 2001). Based on this mechanism, reservoirs exposed to EM radiation will be simultaneously heated to a high temperature within a short time. During the heating process, formation fluids will vaporize once reaching their saturation temperatures. Because of the low dielectric properties of vapor phase, EM waves could penetrate deeper into the reservoir. Together with the effect of heat conduction and convection, a large portion of the reservoir will eventually be heated up. However, only the near antenna part will initially be heated due to the shorter wavelength at a high frequency; effective ways to further expand the heated zone is necessary. Meanwhile, although thermal expansion and connate water vaporization could provide some degrees of driving force for the oil flow, a large vapor chamber is needed to provide sufficient gravity drainage for heavy oil towards the production well.

Implemented with EM heating, solvent injection could bring along several benefits including enhancing viscosity reduction and swelling effect (Li et al., 2013) of heavy oil, serving as a heat

carrier by reinforcing heat convection, and providing a vapor chamber once heated above saturated temperature. Further experiments are drastically needed to clarify these mechanisms of the combined EM heating and solvent injection, as well as the effects of influential factors on such hybrid process.

### 3.3 Experimental

#### 3.3.1 Materials

The heavy oil sample used in this study is from Alberta, Canada. Its API gravity is 8.6°API. Silica sands (provided by Sil Mineral Industry, Canada) with a mesh range of 40–70 are used to make the sand pack. The sand pack has an average porosity of 32% and permeability of 40 Darcy. Distilled water is used to prepare formation water. The solvents employed in this study are *n*-hexane and *n*-octane with 99+ wt% purity, provided by ACROS Organics™ (Fisher Scientific, USA).

A rotational viscometer (Brookfield DV-II+ Pro, Brookfield Engineering, USA) is used to measure the viscosity of heavy oil as well as solvent/heavy oil mixtures. A two-parameter double-logarithm relation has been applied to fit the measured heavy oil viscosity data ( $R^2=0.99996$ ):

$$\log_{10}[\log_{10}(\mu_o)] = -3.6337 \log_{10}(T) + 9.6888 \quad (3-1)$$

where  $\mu_o$  is the heavy oil viscosity in cp and  $T$  is the temperature in K. A linear relationship is found to hold well for the measured heavy oil density data ( $R^2=0.99940$ ):

$$\rho_o = -0.6551 \times T + 1199.9 \quad (3-2)$$

The viscosity and density of *n*-hexane and *n*-octane can be determined from the following correlations (Yaws, 2003):

$$\log_{10}(\mu_s) = A + \frac{B}{T} + CT + DT^2 \quad (3-3)$$

$$\rho_s = E \cdot F^{-\left(1 - \frac{T}{T_c}\right)^N} \quad (3-4)$$

where  $\rho_o$  is the density of heavy oil sample in  $\text{kg/m}^3$ ,  $\mu_s$  and  $\rho_s$  are viscosity and density of solvents in cp and  $\text{g/cm}^3$ ,  $T$  is the temperature in K,  $T_c$  is the critical temperature of solvent in K, and  $A, B, C, D, E, F$ , and  $N$  are the coefficients with their corresponding values listed in **Table 3-1**. The densities of solvents/heavy oil mixtures are calculated based on the weight fraction of solvents. The viscosity of solvents/heavy oil mixtures can be calculated with the following Lobe's mixing rule (Lobe, 1973), based on the viscosity and volume fraction of solvent and heavy oil:

$$\rho_{mix} = \frac{1}{\sum \frac{w_i}{\rho_i}} \quad (3-5)$$

$$v_{mix} = \phi_s v_s \exp(\phi_o \alpha_o) + \phi_o v_o \exp(\phi_s \alpha_s) \quad (3-6)$$

$$\alpha_o = 0.27 \ln\left(\frac{v_o}{v_s}\right) + \left[1.3 \ln\left(\frac{v_o}{v_s}\right)\right]^{0.5} \quad (3-7)$$

$$\alpha_s = -1.7 \ln\left(\frac{v_o}{v_s}\right) \quad (3-8)$$

where  $w_i$  is the weight fraction of  $i$ th component,  $\rho_i$  is the density of  $i$ th component,  $\phi$  is volume fraction,  $v$  is kinematic viscosity, the subscripts of  $o$ ,  $s$  and  $mix$  represent heavy oil, solvent, and mixture, respectively. **Figure 3-1** shows the measured viscosity of solvent/heavy oil mixtures as a function of temperature, together with the pure solvents' viscosity. Solvent  $n$ -hexane has a lower viscosity than  $n$ -octane at the same temperature, resulting in a more viscosity reduction effect when used for diluting the heavy oil. **Figure 3-1** also shows the calculated

mixture viscosity with the Lobe's mixing rule, which indicates that the calculated ones are in a reasonably good agreement with the measured data.

To clarify the solvent fraction in the recovered oil, the refractive index ( $RI$ ) (Moreno and Babadagli, 2014) of oil samples with different solvent fractions have been measured and plotted as base data in **Figure 3-2**. The following two equations can fit well to the measured  $RI$  for  $n$ -hexane/heavy oil mixtures and  $n$ -octane/heavy oil mixtures ( $R^2=0.9946$  and  $0.9949$ ), respectively:

$$RI_{n\text{-hexane}} = 0.0450w_s^2 - 0.2505w_s + 1.5779 \quad (3-9)$$

$$RI_{n\text{-octane}} = 0.0593w_s^2 - 0.2395w_s + 1.5717 \quad (3-10)$$

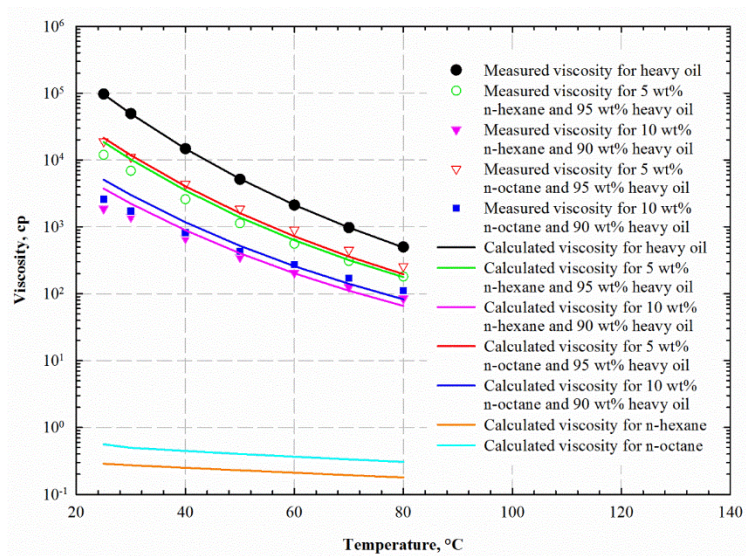


**Figure 3-1** Viscosity-temperature relationships of heavy oil sample and heavy oil samples mixed with solvents. As for heavy oil and solvent mixtures, points are measured data and lines are calculated by Lobe's mixing rule. The viscosities of pure solvents are calculated by Eq. (3-3).

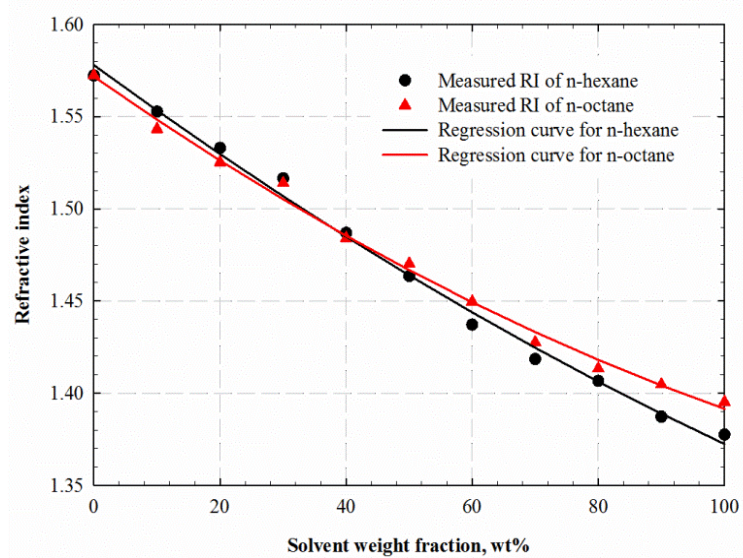


**Figure 3-2** Measured refractive indexes for heavy oil diluted with different weight fractions of solvents. Solvent n-hexane and n-octane are used in these tests.

**Table 3-1** Coefficients values in Equations (3-3) and (3-4)

Solvent	<i>A</i>	<i>B</i>	<i>C</i>	<i>D</i>	<i>E</i>	<i>F</i>	<i>T<sub>c</sub></i>	<i>N</i>
<i>n</i> -Hexane	-5.0715	655.36	0.0123	-0.000015042	0.2324	0.265	507.43	0.2781
<i>n</i> -Octane	-5.9245	888.09	0.0130	-0.000013596	0.2281	0.2548	568.83	0.2694

### 3.3.2 Experimental Setup and Procedures

**Figure 3-3** shows the schematic of the experimental setup. A microwave oven (Danby DMW111KBLDB), operating at a frequency of 2.45 GHz and power of 700 watts (with ten power levels) is used to generate microwave waves. A glass Buchner filter funnel with a pore size of 25  $\mu\text{m}$ , I.D. of 4 cm and height of 5 cm is used to contain the sand pack media considering that glass is transparent to microwave waves. Two holes have been drilled at the top and bottom of the microwave oven to accommodate the installation of injection inlet and production outlet. The solvent is injected from the upper part with a high precision ISCO syringe pump (Model 260D, Teledyne, USA), and oil is recovered from the bottom. A fiber optic temperature probe (Neoptix, Canada), with a diameter of 1.15 mm and a temperature range of  $-270\text{ }^{\circ}\text{C}$  to  $250\text{ }^{\circ}\text{C}$  has been placed in the middle of the sand pack to monitor the temperature change. Oil produced is

weighed through an electronic scale (Setra BL-4100S) and the data are transferred to a personal computer.

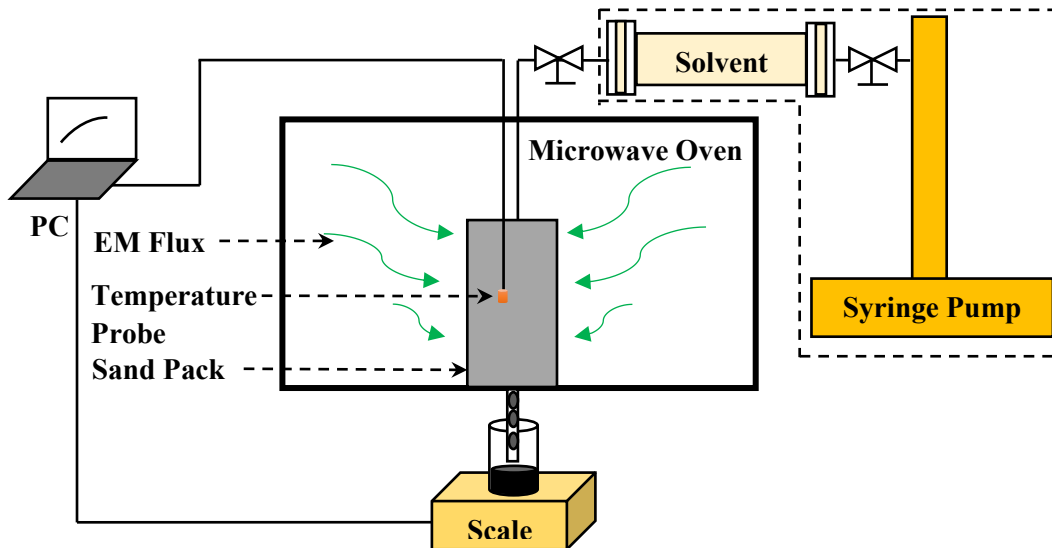


**Figure 3-3** Schematic of the experimental setup used for conducting the combined EM heating and solvent assisted gravity drainage for heavy oil recovery.

The sand particles are mixed with water at first to create a water-wet condition, then, the oil sample is added followed by a vigorous stirring of the mixture. During the packing process, the temperature probe is pre-installed to the middle of the sand pack. The funnel containing the sand pack is then placed into the microwave oven. The top of the funnel is capped while its bottom is open for collecting the produced oil. The solvent is injected by a syringe pump to the top of the sand pack through a plastic tube. The injected solvent is mixed with heavy oil by gravity force and diffusion; no injecting pressure is applied. Each experiment lasts for three hours, and the temperature changes of the sample and oil recovery are continuously recorded. The oil recovery factor is calculated by dividing the weight of recovered oil by the weight of the original oil in place at room temperature. The *RIs* of recovered oil are measured to determine the fraction of solvent in the recovered oil based on the aforementioned *RI* correlations.

**Table 3-2** shows the detailed experimental schemes. As for the pre-mixed cases, solvents are pre-mixed with oil and then saturated in the sand pack, while solvents are injected at the top via a syringe pump for the solvent injection cases.

**Table 3-2** Experimental schemes employed in this study

Exp. No.	Sample detail	Power level	Scheme
1	$S_w=0.00$	10	EM heating only
2	$S_w=0.00$	20	EM heating only
3	$S_w=0.00$	30	EM heating only
4	$S_w=0.25$	20	EM heating only
5	$S_w=0.50$	20	EM heating only
6	$S_w=0.00$	10	EM heating power level 10 and 10wt% <i>n</i> -hexane premixed with oil
7	$S_w=0.00$	10	EM heating power level 10 and 10wt% <i>n</i> -octane premixed with oil
8	$S_w=0.00$	20	EM heating power level 20 and 10wt% <i>n</i> -hexane premixed with oil
9	$S_w=0.00$	20	EM heating power level 20 and 10wt% <i>n</i> -octane premixed with oil
10	$S_w=0.00$	30	EM heating power level 30 and 10wt% <i>n</i> -hexane premixed with oil
11	$S_w=0.00$	30	EM heating power level 30 and 10wt% <i>n</i> -octane premixed with oil
12	$S_w=0.00$	20	Simultaneous EM heating and 1.0 PV of <i>n</i> -hexane injection
13	$S_w=0.00$	20	Simultaneous EM heating and 0.5 PV of <i>n</i> -hexane injection
14	$S_w=0.00$	20	Alternate EM heating and 0.5 PV of <i>n</i> -hexane injection
15	$S_w=0.00$	-	Continuous 1PV of <i>n</i> -hexane injection
16	$S_w=0.00$	20	Simultaneous EM heating and 1.0 PV of <i>n</i> -octane injection
17	$S_w=0.00$	20	Simultaneous EM heating and 0.5 PV of <i>n</i> -octane injection
18	$S_w=0.00$	20	Alternate EM heating and 0.5 PV of <i>n</i> -octane injection
19	$S_w=0.00$	-	Continuous 1PV of <i>n</i> -octane injection

### 3.4 Results and Discussion

#### 3.4.1 Microwave's Selective Heating

In the electromagnetic heating, heat is generated by the interaction between reservoir polarizable fluids, matrix, and electromagnetic waves, which heavily depends on the dielectric properties of reservoir materials. At the microwave oven operating frequency (2.45 GHz) and room temperature (20°C), distilled water has the highest relative dielectric constant (about 80) among the components of the formed sand pack (Komarov, 2012). Heavy oil, sand, *n*-hexane, and *n*-octane are less polarized with lowered relative dielectric constants between 2–4 (Komarov, 2012; Godard and Bethbeder, 2011). In order to test the interactions between microwave and materials used in the experiments, the same amount (10 mL) of experimental materials, namely, heavy oil,

distilled water, silica sand, solvent *n*-hexane and *n*-octane, have been heated in the microwave oven at a power of 700W. **Figure 3-4** shows the temperature profiles, and selective heating phenomena have been observed. After 20 s heating, water has reached its saturation temperature and starts to vaporize, while other components are still at a relatively low temperature. Both heavy oil and alkane solvents are hydrocarbons; their dielectric properties are close to each other, which leads to a similar temperature change under the EM heating.

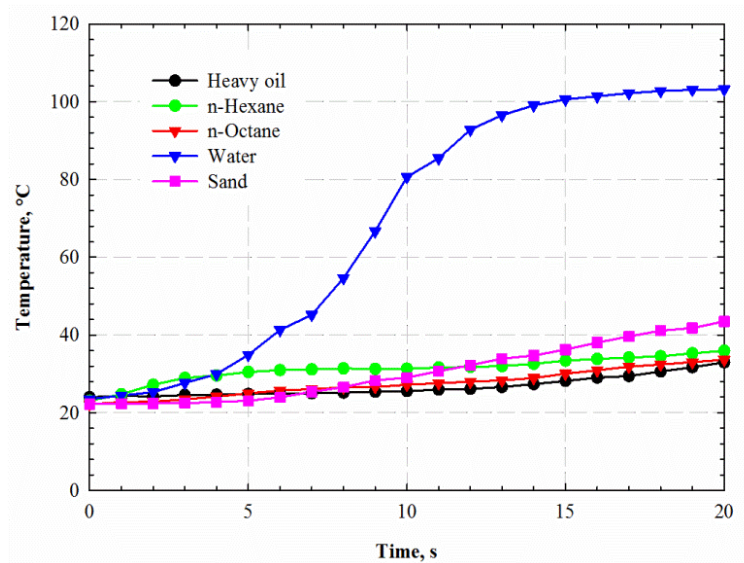


**Figure 3-4** Temperature profiles of bulk materials when they are exposed to microwave heating. The microwave power level is 100.

As for the combined EM heating and solvent assisted gravity drainage, because of the features of fast and selective heating of electromagnetic waves, connate water and injected solvent will vaporize, creating a desiccated region and a solvent chamber; solvent-diluted heavy oil will flow along the solvent chamber (Trautman et al., 2013). **Figure 3-5** shows schematics of combined EM heating and solvent-assisted gravity drainage and fluid flow within the EM excited zone. EM excited zone is a part of the reservoir, where both EM heating and solvent dilution will increase the mobility of heavy oil. As it is indicated in Figure 3-5, EM flux controlled by heating power, initial water saturation, and solvent dilution are important factors that affect the performance of the

combined EM heating and solvent assisted gravity drainage, which deserves detailed investigation.

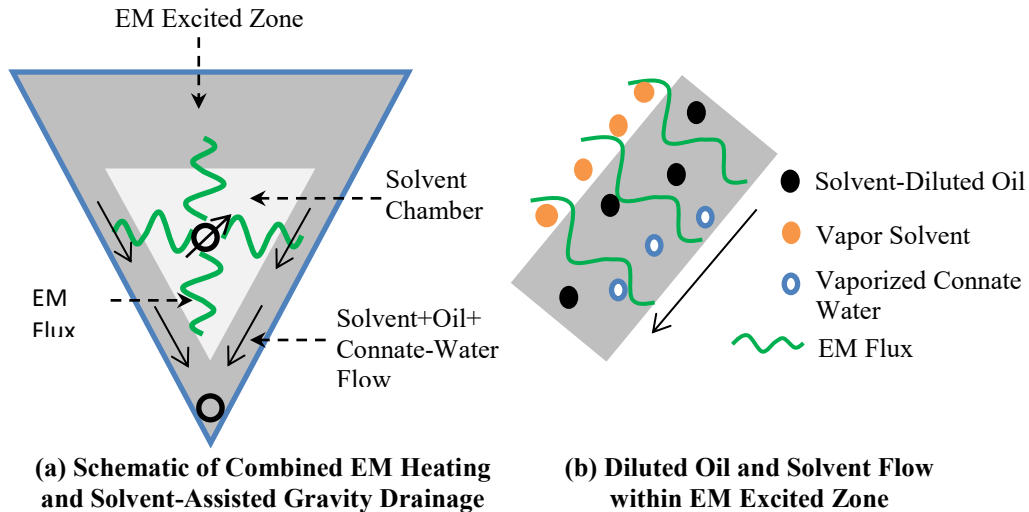
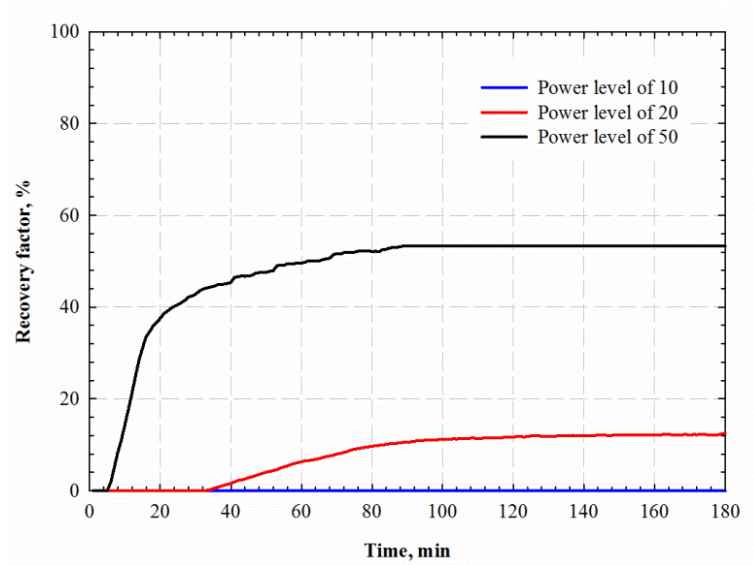


**Figure 3-5** Schematic of (a) combined EM heating and solvent-assisted gravity drainage, (b) fluid flow within EM excited zone.

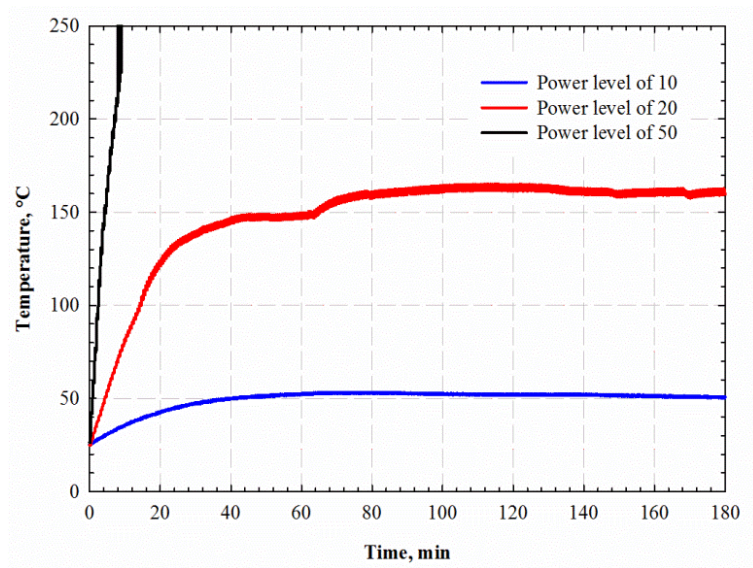
### 3.4.2 Effects of Influencing Factors on the Performance of This Hybrid Process

#### 3.4.2.1 EM Heating Power

Three EM heating power levels, 10, 20 and 30, have been tested, and **Figure 3-6** shows the resulting recovery factors and temperature profiles. It is found that a higher EM heating power level provides a faster heating speed, a higher temperature, and an earlier oil production. In this experiment, the EM heating power is tuned by the feature of power level in the microwave oven. The power level controls the microwave oven heating time and waiting time; i.e., power level 10 means that the microwave oven works 10% of its full duty and idles for 90% of the time in every heating cycle. Increasing EM heating power level is equivalent to increasing the total radiated power which leads to a higher temperature of the sample under EM heating (Abernethy, 1976).



(a)



(b)

**Figure 3-6** Effect of microwave heating power level on (a) recovery factors and (b) temperature profiles (Experiments #1-3 in Table 3-2). When the heating power level is 10, the temperature rise is not sufficient to initiate gravity drainage of heavy oil.

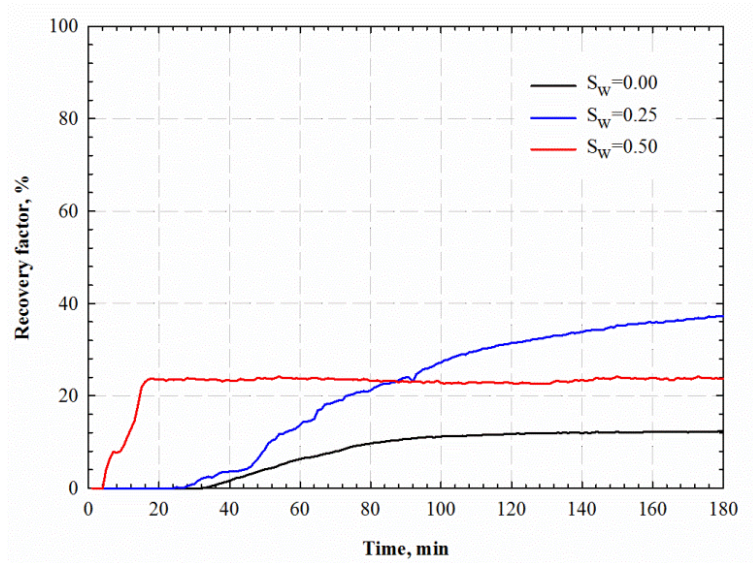
During the microwave heating process, samples absorb EM energy and generate heat resulting in the raising part in temperature profiles. The dielectric properties of sand pack reduce as temperature increases (Das et al., 1981), leading to less absorption of EM energy; meanwhile, the

produced oil also carries away parts of the heat. These two factors attribute to the slowing-down part in the temperature profile. At last, the sample temperature becomes stabilized when the heat generation rate is equal to the heat loss rate.

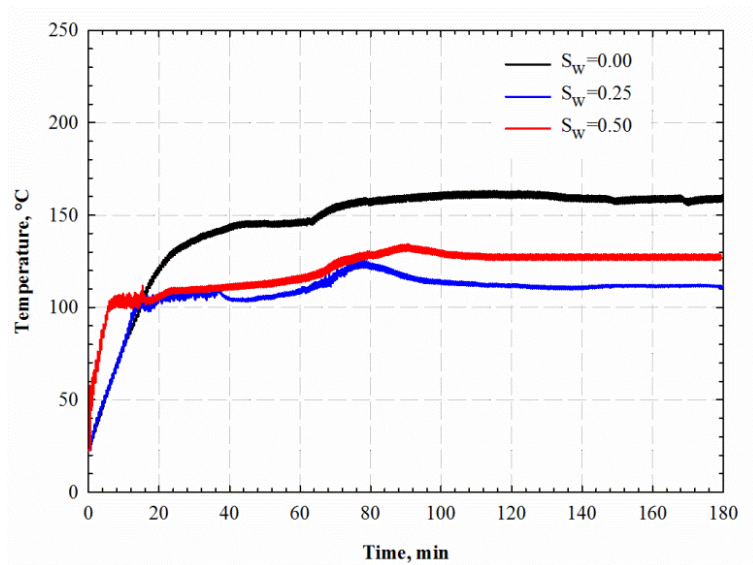
As for the case of power level 10, the sample could be heated up to 51°C and then stabilized at this temperature. Because the viscosity of this oil sample is approximately 4754.1 cP at this experimental temperature, which is still too viscous to allow for oil flow, no oil was produced after 3 hours of heating. As for the case of power level 20, temperature rising speed increases and the temperature stabilizes around 165°C; a total of 12.37% of OOIP has been recovered. As for the power level 30, the temperature reaches 250°C (upper bound of the temperature probe) within 11 min, and 53.40% of the oil has been recovered after 3 hours of heating. Based on the above experimental observations, the power level 20, which can heat up the sample to a desired temperature range and provide sufficient time for oil production, has been adopted for the remaining experiments.

### **3.4.2.2 Initial Water Saturation**

Higher initial water saturation accelerates the heating and recovery process by using EM heating, but moderate initial water saturation provides the highest oil recovery factor. **Figure 3-7** shows the oil recovery factors and temperature profiles for experimental tests with different initial water saturations. The times for the samples to reach the saturation temperature of water are 880s, 858s, and 326s when the initial water saturations are:  $S_w = 0.00$ ,  $S_w = 0.25$  and  $S_w = 0.50$ , respectively. The faster heating speed, achieved with higher initial water saturation, significantly expedites the oil recovery process. The oil production starts after 33 min, 25 min, and 5 min of EM heating corresponding to cases of  $S_w = 0.00$ ,  $S_w = 0.25$ , and  $S_w = 0.50$ ; and resulted oil recovery factors are 12.37%, 37.24%, and 23.73% for  $S_w = 0.00$ ,  $S_w = 0.25$ , and  $S_w = 0.50$ , respectively.



(a)



(b)

**Figure 3-7** Effect of initial water saturation on (a) recovery factors and (b) temperature profiles (Experiments #2, #4 and #5 in Table 3-2).

The phase change of water plays an important role in affecting the temperature profile of the sand pack in the EM heating. Before water vaporizes, sample with higher initial water saturation exhibits a larger water content, which leads to an enhanced bulk dielectric property (Chute et al., 1979) and results in a better EM energy absorption. Once reaching the saturation temperature,

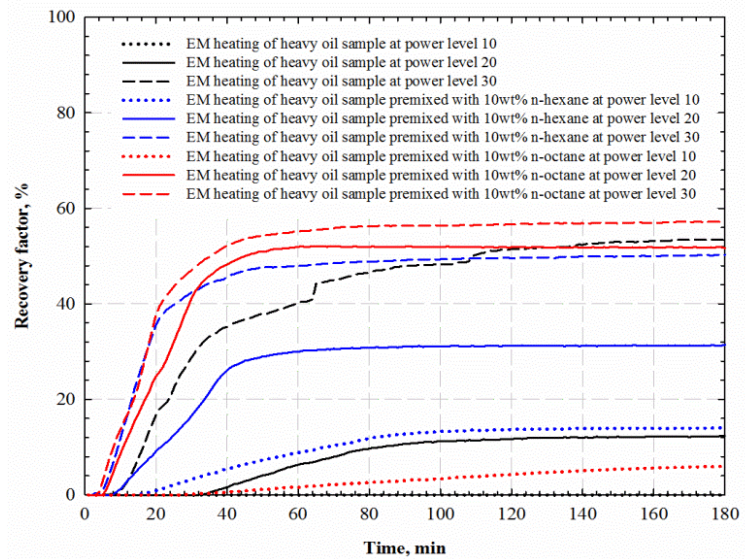
water becomes steam which could only absorb a small amount of EM energy because of the low dielectric properties of gasses. Due to the effect of selective heating, surrounding sand may still be at a relatively low temperature, so the vaporized steam condenses inside the sand pack and gets heated up again. This continuous phase change phenomenon results in the fluctuations of the temperature profile around the water saturation temperature, while the temperature tends to increase steadily for the case of  $S_w = 0.00$ . Because water is an excellent absorber of EM energy, connate water will be heated rapidly within the EM excited zone. The generated steam, even with a small quantity, can store the latent heat and release it to the reservoir when it becomes condensed.

Although a higher initial water saturation accelerates the heating and recovery process, the case of  $S_w=0.25$  exhibits the highest recovery factor. Similar phenomena have also been observed by Al-Farsi et al. (2016) in their microwave assisted gravity drainage experiments; they found that the oil recovery reached its peak at  $S_w=0.30$  and then decreases with increasing water saturation. An explanation is that these beneficial effects due to higher water saturation are more prominent before water vaporizes. Because of the large heat capacity of water, the condensation of evaporated water will continue to absorb EM energy and inhibit the temperature rise, which leads to a lowered stabilized temperature. This phenomenon has also been reported by Lowe et al. (2000) and Bera and Babadagli (2015); they found that wet soil/sand exhibited a lower temperature compared with dry soil/sand under radio frequency heating. Another explanation for the lowered stabilized temperature is that the early oil production and the vaporization of water leave a less amount of EM absorber in the sand pack. Nevertheless, a higher initial water saturation does not necessarily provide a higher recovery factor. The interfacial tension and capillary force also restrain oil recovery. The recovery factors obtained in the experimental cases

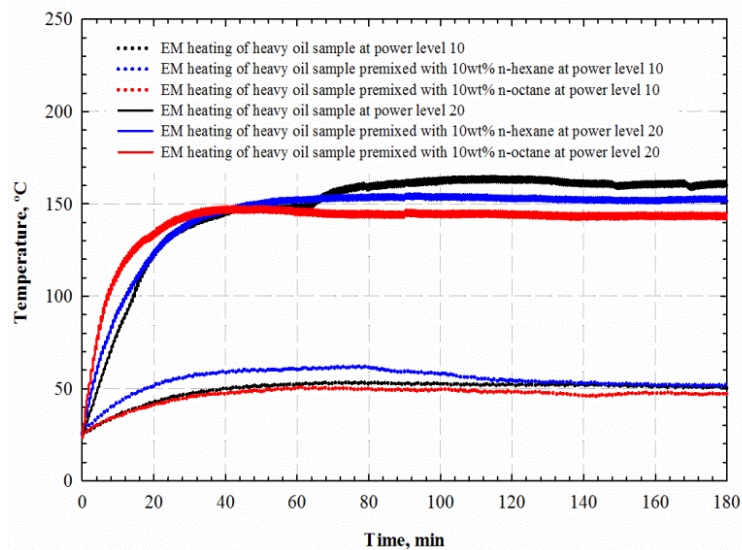
with only EM heating are not very promising, which motivates us to combine EM heating with solvent injection to enhance oil recovery.

### 3.4.2.3 Solvent Types and EM Heating Power

For comparative purposes, pre-mixed mixtures with 10wt% of each solvent (*n*-hexane and *n*-octane) and 90wt% heavy oil are saturated in the sand pack; subsequently, EM heating experiments are conducted at three power levels (10, 20, and 30) for each solvent. **Figure 3-8** shows the results of recovery factors and temperature profiles. With the addition of solvent, diluted oil is produced at an earlier stage and a faster rate; most of the heavy oil in place has been recovered only after one hour of heating. On the other hand, adding solvent exert fewer influences on the temperature profiles of the sand pack. The temperature profiles of experiments conducted at EM heating power level of 30 are not included since the sand pack's temperature is higher than the upper limit (250 °C) of the temperature probe.



(a)



(b)

**Figure 3-8** Effect of solvent types and EM heating powers on (a) recovery factors and (b) temperature profiles (Experiment #1, #2 and #6-11 in Table 3-2). In this Figure, black, blue, and red lines represent the cases without solvent, with solvent *n*-hexane, and solvent *n*-octane, respectively; the dotted, solid, and dash lines correspond to the experiments conducted at EM heating power levels of 10, 20, and 30, respectively.

The recovery factors presented in Figure 3-8a are calculated based on the recovered mixtures that contain both heavy oil and solvents. The *RI* measurements have been conducted on the recovered mixture to indicate the weight fractions of solvents in the recovered oil. Results show that *n*-hexane weight fractions are 7.33 wt%, 3.60 wt%, and 1.21 wt% corresponding to the EM heating power levels of 10, 20, and 30, respectively. And weight fractions of *n*-octane in recovered oil are 8.79 wt%, 7.29 wt%, and 2.37 wt% corresponding to the EM heating power levels of 10, 20, and 30, respectively. **Figure 3-9** shows the final oil recovery that deducted with solvent fraction in the recovered oil for each solvent at three EM heating power levels.

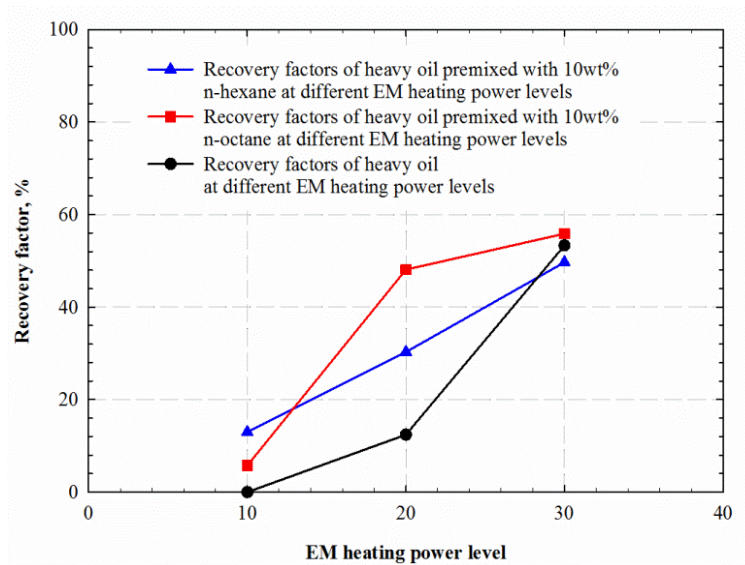


**Figure 3-9** Oil recovery factors of heavy oil, heavy oil premixed with solvent *n*-hexane and *n*-octane at EM heating power levels of 10, 20, and 30 (Experiments #1-3, #6-11). In the Exp. #1-3, no solvent is premixed with heavy oil. In Exp. #6-8, 10wt% *n*-hexane is premixed with heavy oil. In Exp. #9-11, 10wt% *n*-octane is premixed with heavy oil.

The effect of adding solvents on oil recovery varies with EM heating power levels due to the changes in solvent concentration in heavy oil. As for the cases conducted at EM heating power level of 10, both solvent *n*-hexane and *n*-octane stay in the liquid phase due to the relatively low temperature of samples. Solvent *n*-hexane has a better diluting effect compared with *n*-octane, which leads to a higher oil recovery.

Due to a higher temperature of sand packs obtained at higher EM heating powers, oil recovery factors are significantly enhanced for the experiments conducted at EM heating power level of 20 compared with experiments carried out at EM heating power level of 10 for both *n*-hexane and *n*-octane. And this enhancing effect is more prominent for solvent *n*-octane although *n*-hexane provides more oil viscosity reduction. Because of the elevated temperature of sand pack, most of the solvent *n*-hexane vaporizes, as confirmed by the lower fraction of *n*-hexane in the recovered oil. The low concentration of *n*-hexane in the oleic phase weakens the viscosity reduction effect from *n*-hexane dilution. In comparison, solvent *n*-octane, exhibiting higher saturation

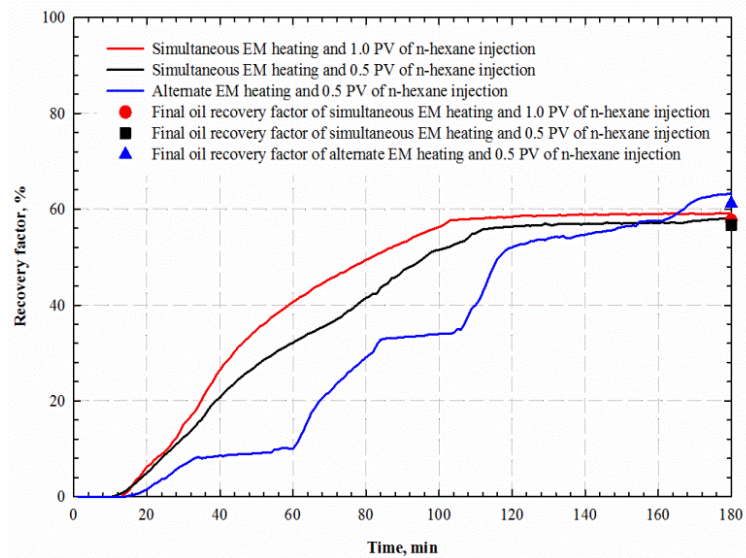
temperature, stays in the liquid phase at the EM heating power level of 20, confirmed by the higher *n*-octane fraction in recovered oil. Hence, *n*-octane gives more viscosity reduction and consequently provides a better recovery performance.

As for the cases conducted at EM heating power level of 30, the temperatures of sand packs become much higher and larger than the upper limit of the temperature probe (250 °C), which causes most of the solvents to vaporize, as demonstrated by the low solvent fractions in the recovered oil from *RI* measurements. Due to the low concentrations of solvent *n*-hexane and *n*-octane in heavy oil at higher temperatures, the viscosity reduction is mainly from the temperature rise by EM heating. As a result, solvent *n*-hexane and *n*-octane provide similar oil recovery factors, and the recovery factors of heavy oil samples with or without solvent addition are also close to each other.

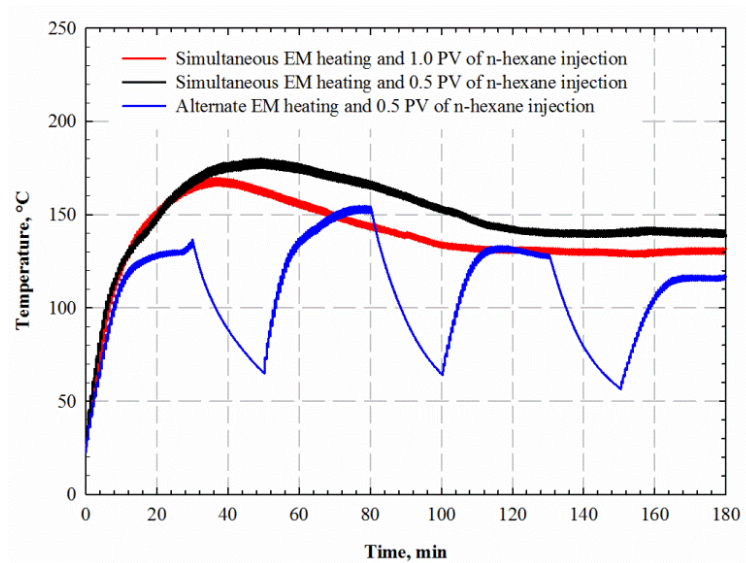
#### **3.4.2.4 Combining Strategies of EM Heating and Solvent Injection**

Combining strategies of EM heating and solvent injection, affecting the temperature of sand pack and solvent concentration in heavy oil, also play important roles in this hybrid process. Simultaneous/alternate EM heating and solvent injection are carried out at the EM power level of 20, and 0.5 pore volume (injection rate: 0.083 mL/min) and 1.0 pore volume (injection rate: 0.166 mL/min) of solvents are injected in the simultaneous EM heating and solvent injection schemes. Alternate EM heating and solvent injection has been conducted with the following procedure: EM heating for 30 min, injecting cold solvent for 15 min, and soaking for 5 min; this cycles repeats for three times and then ends up with another 30 min of EM heating. In the alternate process, a total of 0.5 pore volume (injection rate: 0.333 mL/min) of solvents is injected. These experiments are conducted at a gravity-drainage dominated condition where no injection pressure is applied; the injected solvents mix with heavy oil by gravity force and diffusion. **Figures 3-10 and 3-11** show the experimental results on recovery factors and temperature

profiles conducted with simultaneous/alternate schemes for solvent *n*-hexane and *n*-octane, respectively. We also perform two experimental runs with only solvent injection at the room temperature (22°C). Due to the large viscosity of heavy oil and slow diffusion rate of solvents, no oil is recovered after injecting 1.0 pore volume of solvents (3 hours).

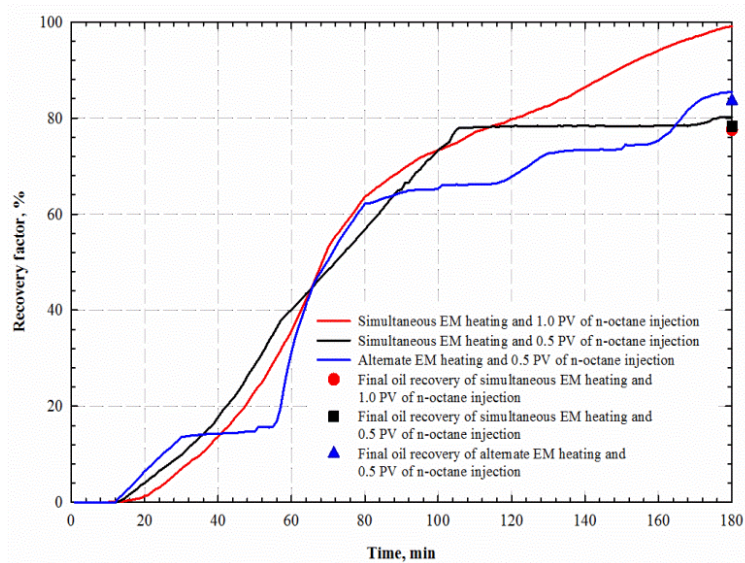


(a)

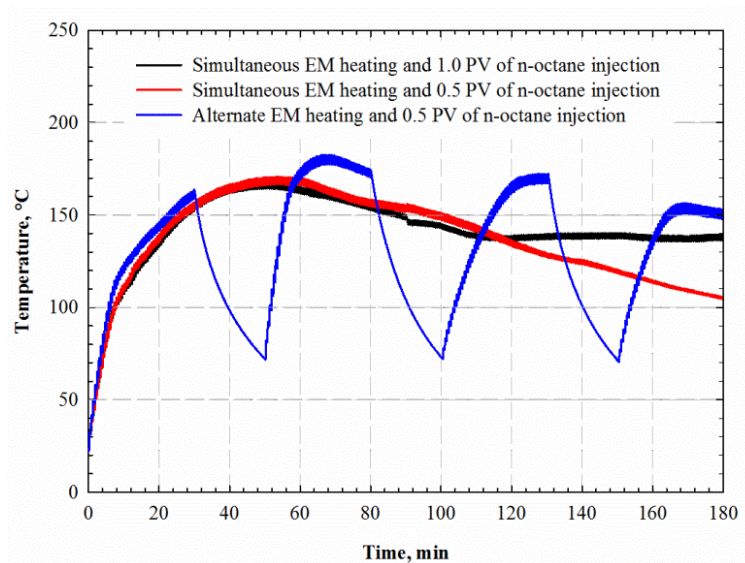


(b)

**Figure 3-10** Effect of simultaneous and alternate EM heating and *n*-hexane injection on (a) recovery factors and (b) temperature profiles (Experiment #12-14 in Table 3-2). In Figure. 3-10a, the lines represent the recovered oil and solvent mixtures, while the points correspond to the final oil recovery factor after deducting solvent from the mixtures.



(a)



(b)

**Figure 3-11** Effect of simultaneous and alternate EM heating and n-octane injection on (a) recovery factors and (b) temperature profiles (Experimental #16-18 in Table 3-2). In Figure 3-11a, the lines represent the recovered oil and solvent mixtures, while the points correspond to the final oil recovery factors after deducting solvent from the mixtures.

The *RI* measurements show that *n*-hexane fractions in recovered oil are 2.2wt%, 2.3wt%, and 3.5wt%, respectively, corresponding to three experimental schemes: (1) simultaneous EM heating and 0.5 PV of *n*-hexane injection, (2) simultaneous EM heating and 1.0 PV of *n*-hexane injection,

and (3) alternate EM heating and 0.5 PV of *n*-hexane injection. And the final oil recovery factors are 56.72%, 57.64%, and 61.18% corresponding to the schemes above. Due to the low saturation temperature of *n*-hexane, most of the injected *n*-hexane vaporizes at the experimental condition, as confirmed by the *RI* measurements, which leads to a low concentration of *n*-hexane in heavy oil. Hence, the oil recovery only slightly increases although the doubled pore volume of *n*-hexane has been injected in the simultaneous schemes. Due to the use of alternating approach and soaking period, the alternate strategy enables the better diluting effect of *n*-hexane on heavy oil; hence a higher oil recovery has been achieved even with a shorter heating time.

*n*-Octane gives a higher recovery factor compared with *n*-hexane. *n*-Octane breakthrough happens in the case of simultaneous EM heating and 1.0 PV of *n*-octane injection, which is reflected by the constant drop in the temperature. The *RI*s of recovered oil after 90 min and 180 min injection had been measured and results show that *n*-octane's weight fractions in the recovered oil are 7.7wt% and 53.7wt%, respectively. As for the case of simultaneous EM heating and 0.5 PV *n*-octane injection, *n*-octane's weight fractions are found to be 1.2wt% and 7.3wt% after 90 and 180 min injection, respectively. On the alternate scheme, the *n*-octane fraction experiences a gradual increase as the cycle number increases; *n*-octane fractions are found to be 0.8wt%, 3.0wt%, and 8.7wt% after the first, second, and third solvent-injection cycle, respectively. The final oil recovery factors after removing the recovered *n*-octane are found to be 78.34%, 77.62%, and 83.59% when the three schemes are used: (1) simultaneous EM heating and 0.5 PV of *n*-octane injection, (2) simultaneous EM heating and 1.0 PV of *n*-octane injection and (3) alternate EM heating and 0.5 PV of *n*-octane injection. *n*-Octane breakthrough in simultaneous EM heating and 1.0 PV of *n*-octane injection results in a lowered temperature and less contact with oil, which leads to a less increase in oil recovery compared with simultaneous

EM heating and 0.5 PV of *n*-octane injection. The alternate scheme also gives a higher oil recovery compared with the simultaneous schemes for *n*-octane. Unlike *n*-hexane, *n*-octane exhibits higher concentrations in heavy oil at higher temperatures, which is confirmed by the *RI* measurements. Instead of the better diluting effect achieved by the alternating approach, the enhanced oil recovery is attributed to the higher temperature of sand pack obtained at each heating stage in the alternate scheme. **Figure 3-12** shows the digital images of sand pack taken after simultaneous EM heating and 1 PV of solvent injection when *n*-hexane and *n*-octane are used. It can be seen that solvent *n*-octane provides a better vertical displacement efficiency of heavy oil than *n*-hexane based on the visual observation made on the sand pack.

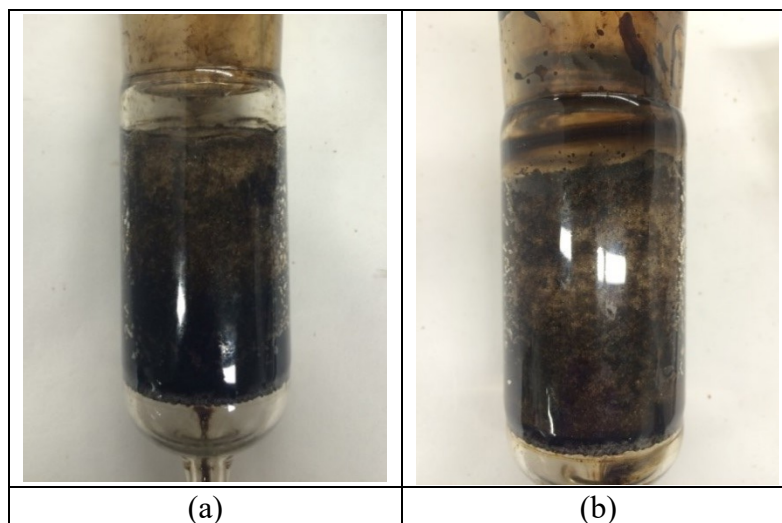


**Figure 3-12** Digital images of sand pack taken after simultaneous EM heating and 1 PV of solvent injection: (a) *n*-hexane (Experiment #12 in Table 3-2), and (b) *n*-octane (Experiment #16 in Table 3-2)

### 3.4.3 Further Analyses of the Experimental Results

#### 3.4.3.1 Solvent Concentration in Heavy Oil

Two-phase flash calculations for the experiments of heavy oil premixed with 10wt% of solvents at different power levels are carried out at experimental conditions based on PR EOS (Peng and Robinson, 1978). The critical properties of the heavy oil are calculated from Twu's (1984) and

Lee-Kesler's (1975) correlations. **Table 3-3** lists the critical properties of each component involved in the flash calculations. The two-phase flash calculations are performed at atmospheric pressure and the temperature of the sand pack after EM heating. Because the temperature of the sand pack is beyond the upper limit of the temperature probe for the experiments conducted at the EM heating power level of 30, we assume the experimental temperature is 250 °C. The viscosity of the diluted heavy oil is calculated by the Lobe's (1973) mixing rule by estimated liquid phase composition. **Table 3-4** shows the calculated viscosity.

**Table 3-3** Critical properties of *n*-hexane, *n*-octane and heavy oil and their binary interaction parameters used in the PR EOS model

Component	Critical pressure, kPa	Critical temperature, K	Acentric factor	Binary interaction parameter		
<i>n</i> -Hexane	3012.00	507.43	0.305	0	0.00135	0.03931
<i>n</i> -Octane	2486.00	568.83	0.396	0.00135	0	0.02653
Heavy oil	852.18	1056.71	1.290	0.03931	0.02653	0

**Table 3-4** Flash calculation results for premixed solvent/heavy oil mixtures under elevated temperatures and atmospheric pressure

EM heating power level	Feeds	<i>P</i> , kPa, <i>T</i> , °C	Solvent distribution, mol%		Calculated liquid-phase viscosity, cP
			Liquid	Vapor	
10	10wt% <i>n</i> -hexane 90wt% heavy oil	<i>P</i> : 101.33 <i>T</i> : 52.00	45.02 54.98	-	349.12
10	10wt% <i>n</i> -octane 90wt% heavy oil	<i>P</i> : 101.33 <i>T</i> : 47.00	38.18 61.82	-	665.71
20	10wt% <i>n</i> -hexane 90wt% heavy oil	<i>P</i> : 101.33 <i>T</i> : 153.40	10.10 89.90	100.00 0.00	18.29
20	10wt% <i>n</i> -octane 90wt% heavy oil	<i>P</i> : 101.33 <i>T</i> : 145.20	38.23 61.77	-	8.75
30	10wt% <i>n</i> -hexane 90wt% heavy oil	<i>P</i> : 101.33 <i>T</i> : 250.00	3.12 96.88	100.00 0.00	4.19
30	10wt% <i>n</i> -octane 90wt% heavy oil	<i>P</i> : 101.33 <i>T</i> : 250.00	7.55 92.45	100.00 0.00	3.84

Overall, the calculation results from the flash exercise are consistent with the aforementioned experimental observations. As for the experiments conducted at the EM heating power level 10, both *n*-hexane and *n*-octane stay in the liquid phase. Compared with *n*-octane, lighter solvent *n*-hexane provides more viscosity reduction of heavy oil because of the better diluting effect; hence,

higher oil recovery has been achieved at EM heating power level of 10 for solvent *n*-hexane. As for the experiments conducted at the EM heating power level 20, *n*-hexane exhibits a lower concentration in heavy oil due to the raised temperature, while heavier solvent *n*-octane shows a higher concentration of heavy oil and gives more viscosity reduction; consequently, *n*-octane provides a higher oil recovery. As for the experiments conducted at the EM heating power level 30, most of the *n*-hexane and *n*-octane vaporize, leaving less solvent in the liquid phase to dilute the heavy oil. As a result, solvent dilution contributes less to the viscosity reduction; hence, the oil recovery factors are close to each other for both solvents.

### 3.4.3.2 Asphaltene Precipitation and Breakage

To investigate the effect of this hybrid process on the properties of recovered heavy oils, we conduct saturates, aromatics, resins and asphaltenes (SARA) analyses on the original heavy oil and the recovered heavy oils, respectively. Because the presence of solvent will affect the measured SARA fractions of the recovered oils, we deduct the solvent fraction from the recovered oil samples as indicated by the *RI* measurements, and then recalculate the SARA fractions. **Table 3-5** shows the SARA results that eliminate the influence of solvent fraction in the recovered oils.

**Table 3-5** Results on saturates, aromatics, resins and asphaltenes (SARA) tests for the original heavy oil and recovered oils that eliminate the influence of the solvent presence

EM heating power level	Solvent	Saturates, %	Asphaltenes, %	Resins, %	Aromatics, %
-	-	28.60	18.00	23.60	30.70
20	-	27.60	15.69	31.71	25.00
30	-	28.70	15.66	31.26	24.40
20	10 wt% <i>n</i> -hexane premixed with oil	38.76	12.53	29.06	19.64
20	10 wt% <i>n</i> -octane premixed with oil	29.54	13.94	26.47	30.05
30	10 wt% <i>n</i> -hexane premixed with oil	33.36	14.05	30.19	22.40
30	10 wt% <i>n</i> -octane premixed with oil	27.03	13.81	33.34	25.82
20	1.0 PV of <i>n</i> -hexane injection (simultaneous)	30.80	14.32	31.67	23.21
20	0.5 PV of <i>n</i> -hexane injection(simultaneous)	33.79	15.26	27.26	23.68
20	0.5 PV of <i>n</i> -hexane injection (alternate)	31.29	16.04	30.56	22.11
20	1.0 PV of <i>n</i> -octane injection (simultaneous)	25.38	15.33	26.51	32.78
20	0.5 PV of <i>n</i> -octane injection(simultaneous)	33.96	15.19	26.12	24.74
20	0.5 PV of <i>n</i> -octane injection (alternate)	31.61	15.78	33.03	19.58

Compared with the original heavy oil, the combined the EM heating and solvent assisted gravity drainage could reduce the asphaltene fractions in the recovered oil samples. When hot solvents contact with heavy oil, asphaltene precipitation may occur in the sand pack (James et al., 2008; Leyva-Gomez and Babadagli, 2014). What's more, EM heating could affect the structure of asphaltene or even break the chains of asphaltene when exposed to a high-frequency alternating electric field (Kovaleva et al. 2011; Bera and Babadagli, 2015). These two possible factors attribute to the decrease of the asphaltenes fraction. SARA results show that the asphaltene fractions reduce by 2.31% and 2.34% in the recovered oils after 3 hours of EM heating at power levels of 20 and 30, respectively. A further reduction of asphaltene fractions in the recovered oil has been found for the cases with the presence of solvents, which implies the asphaltene precipitation occurs in the sand pack. And the asphaltene precipitation is more pronounced for solvent *n*-hexane compared with *n*-octane. The alternate scheme exhibits a less decrease in asphaltene fraction compared to the simultaneous manner, which is caused by the shortened EM heating time. These results imply that the combined EM heating and solvent assisted gravity drainage could reduce the asphaltene fraction in the recovered oils and alleviate the potential formation damage problem caused by asphaltene precipitation due to solvent use.

### **3.4.3.3 Residual Oil Saturation**

As mentioned above, EM heating and solvent dilution can help to reduce the viscosity of heavy oil. The vaporized solvent can form a vapor chamber, also promoting the gravity drainage process. Both mechanisms give a higher ultimate oil recovery. And all the experiments are conducted at a gravity drainage dominated scenario. To study the residual oil saturation of this hybrid process, the experimental residual oil saturations are compared with estimated residual oil saturation by Cardwell and Parsons' equation and Kulkarni and Rao's correlation. The Cardwell

and Parsons' equation, generally used to evaluate the residual oil saturation in the steam chamber, is given by (Cardwell and Parsons, 1949):

$$\overline{S_{or}} = \frac{(b-1)}{b} \left( \frac{\nu\phi Z}{bkgt} \right)^{1/(b-1)} \quad (3-11)$$

where  $\overline{S_{or}}$  is the average residual oil saturation after time  $t$ ,  $Z$  is drainage height,  $\phi$  is porosity,  $k$  is permeability,  $g$  is gravitational acceleration,  $9.8 \text{ m/s}^2$ ,  $\nu$  is the kinematic viscosity of diluted oil,  $\text{m}^2/\text{s}$  and  $b$  (typically 3.5) is the exponent in Cardwell and Parson's equation for relative permeability.

The Kulkarni and Rao's correlation, obtained empirically from miscible gas-assisted gravity drainage experiments and field data, is given by (Kulkarni and Rao, 2006):

$$R_{miscible} (\%) = 4.57 \ln(N_{GD}) + 55.39 \quad (3-12)$$

$$N_{GD} = N_G + \left[ \frac{\rho_g}{\rho_o} (N_C + N_B) \right] \quad (3-13)$$

$$N_G = \frac{\Delta\rho gk}{\Delta\mu u} \quad (3-14)$$

$$\overline{S_{or}} = 1 - R_{miscible} \quad (3-15)$$

where  $R_{miscible}$  is the oil recovery rate of miscible gas-assisted gravity drainage,  $N_{GD}$  is gravity drainage number,  $N_B$  is bond number,  $N_C$  is capillary number,  $N_G$  is the gravity number,  $\rho_g$  is the density of gas in  $\text{kg/m}^3$ ,  $\rho_o$  is the density of heavy oil in  $\text{kg/m}^3$ ,  $\Delta\rho$  is the density different between gas and oil in  $\text{kg/m}^3$ ,  $k$  is permeability in  $\text{m}^2$ ,  $g$  is gravitational acceleration,  $9.8 \text{ m/s}^2$ ,  $\mu$  is viscosity in  $\text{Pa}\cdot\text{s}$ , and  $u$  is Darcy velocity in  $\text{m/s}$ ,  $\overline{S_{or}}$  is the average residual oil saturation.

In our experiment,  $Z = 0.04 \text{ m}$ ,  $\phi = 0.32$ ,  $k = 3.95 \times 10^{-11} \text{ m}^2$  (40 Darcy),  $A_c = 1.26 \times 10^{-3} \text{ m}^2$  (cross-section area of sand pack) and  $t = 10800 \text{ s}$ . The kinematic viscosity of the heavy oil is calculated based on Eq. (1) and Eq. (2) for the cases of EM heating only. As for the cases with

solvent, the kinematic viscosity of the diluted heavy oil is calculated by using Lobe's mixing rule by the liquid composition obtained from two phase flash calculations. And the Darcy velocity is estimated by the average flow rate divided by the cross-section area of the sand pack. Our calculations show that both the bond number and capillary number are several orders smaller than the gravity number; hence the gravity drainage number in Eq. (13) can be approximated by only the gravity number. The density of gas can also be neglected in the calculation since it is much smaller the density of heavy oil.

**Figure 3-13** shows the parity chart of the measured residual oil saturations versus the estimated residual oil saturations by Eq. (3-11) and Eq. (3-15). Figure 3-13 show that the residual oil saturations calculated by the Cardwell and Parsons' equation fit well with those obtained in the experimental cases of  $S_w=0.25$  and  $S_w=0.50$  (Experiment #4 and #5 in Table 3-2), where the condition is typically a gas-liquid gravity drainage scenario. But the estimated residual oil saturations by Cardwell and Parsons' equation provide large errors for the cases with solvent addition. As for combined EM heating and solvent assisted gravity drainage, part of the solvent will vaporize under EM heating, which can be partially considered as a miscible gas-assisted gravity drainage process. Hence, the Kulkarni and Rao's correlation exhibits better agreement with the experimental results and can be potentially used to estimate the residual oil saturations for this hybrid process.

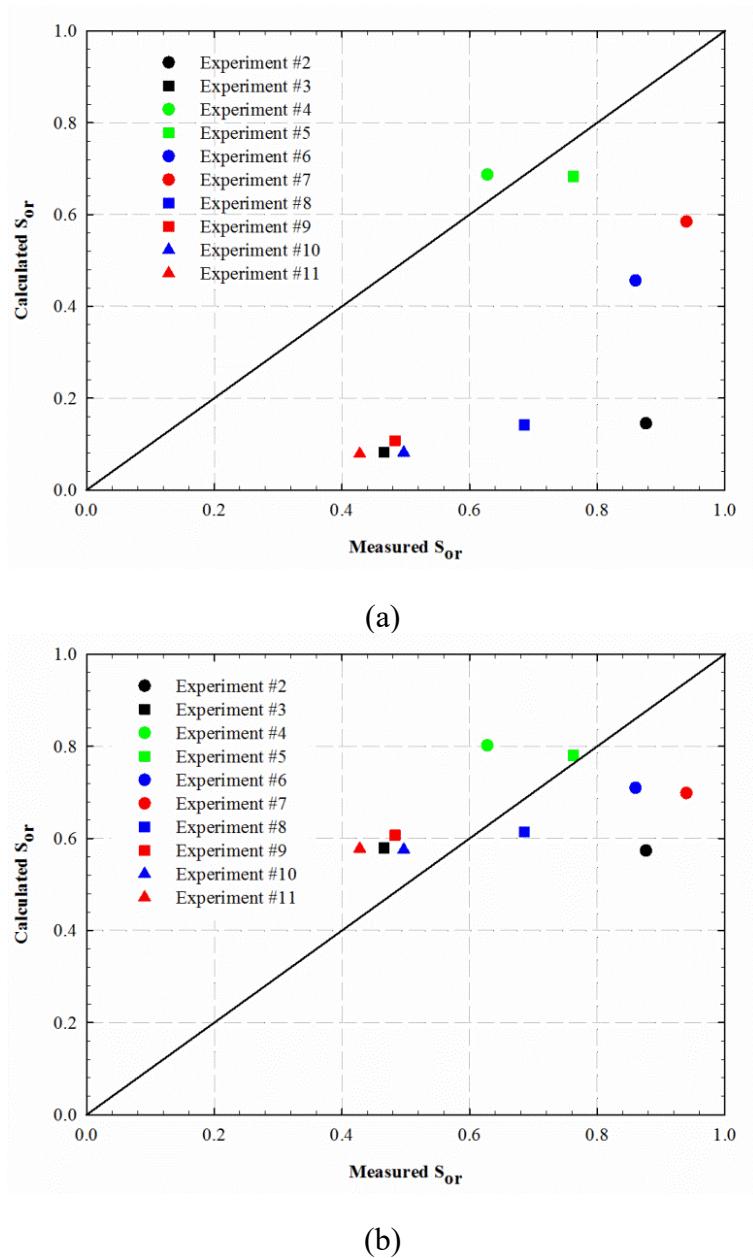


**Figure 3-13** Parity charts of the measured and calculated  $S_{or}$  within the sand pack: (a) calculated  $S_{or}$  is based on Eq. (3-11)-Cardwell and Parsons' equation, and (b) calculated  $S_{or}$  is based on Eq. (3-12)-Kulkarni and Rao' correlation.

### 3.4.3.4 Analysis on the Energy Utilization

Energy utilization of the combined process is critical for assessing the economic feasibility of such process. In this study, we convert the amount of injected solvent to an equivalent amount of energy that is required to heat the heavy oil to a temperature at which could yield the same viscosity of heavy oil by solvent addition. The typical microwave oven has an average heating

efficiency of about 64% ([https://en.wikipedia.org/wiki/Microwave\\_oven](https://en.wikipedia.org/wiki/Microwave_oven)). EM energy consumption is calculated by multiplying the microwave oven working power, power level percentage, heating time, and heating efficiency. **Figure 3-14** compares the energy utilization efficiencies of different schemes. At the same level of energy consumption, solvent *n*-octane provides a higher recovery than *n*-hexane. The alternate scheme is more efficient than the simultaneous approach for combining EM heating and solvent injection. This benefit can be attributed to the factors including a shorter EM heating time and better diluting effect provided by the alternate manner.

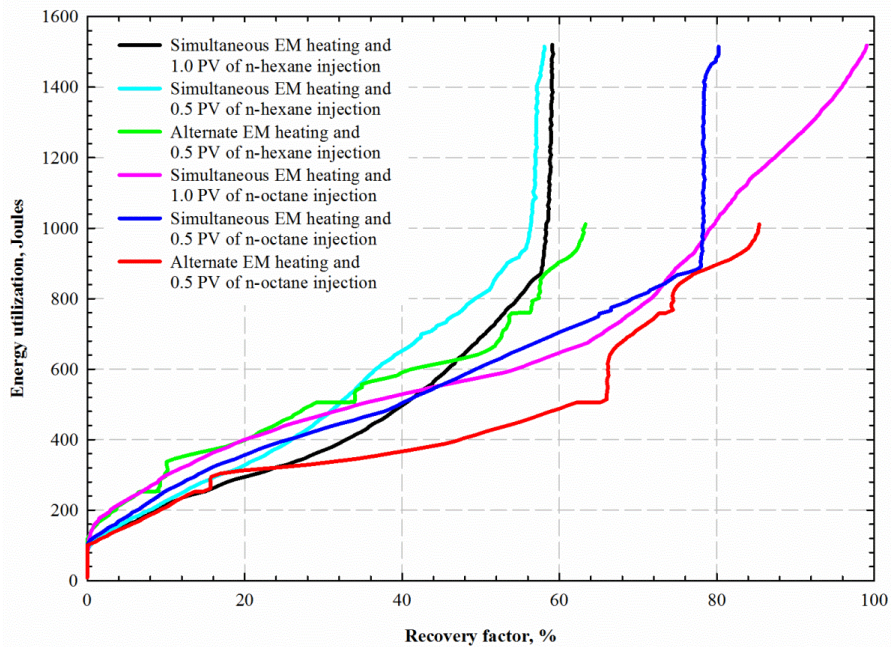


**Figure 3-14** Energy utilization efficiency of the experimental runs carried out in this study. Alternate EM heating and continuous injection of 0.5 PV *n*-octane consumes the least energy for generating the same oil recovery among all the experimental schemes tested.

### 3.5 Conclusions

In this study, we experimentally investigate the mechanisms governing the combined EM heating and solvent-assisted gravity drainage. The following conclusions can be drawn from our experimental observations and analyses:

1. Higher heating power accelerates the heating and recovery process. Moderate initial water saturation provides faster heating and better oil recovery. The combined scenario can significantly enhance oil recovery. The recovery factors of different scenarios of EM heating only, alternate EM heating and *n*-hexane injection, and alternate EM heating and *n*-octane injection are 12.37%, 61.18% and, 83.59%, respectively.
2. Depending on the solvent concentration in the heavy oil, the effect of adding solvents on oil recovery varies with EM heating power in such hybrid processes. Solvent *n*-hexane exhibits better performance at lower EM heating powers, while *n*-octane tends to be more effective at higher EM heating powers.
3. There is a significant reduction in asphaltene fraction of the recovered oil in this process. Both the asphaltene property alternation caused by EM heating and asphaltene precipitation in the sand pack induced by solvent contribute to the decrement of asphaltene in this process.
4. Alternate EM heating and solvent injection is a more efficient operational strategy since it reduces energy consumption by shortening heating time and achieves an even higher oil recovery factor with a similar amount of solvent usage than the simultaneous heating and solvent injection process.

## Nomenclature

$A, B, C, D$  = Coefficients in Eq. (3)

$A_c$  = Cross-section area of sand pack,  $m^2$

$b$  = Exponent in Eq. (3-11) defined by Cardwell and Parson's equation [35]  
for relative permeability

$E, F, N$  = Coefficients in Eq. (3-3)

$g$  = Gravitational acceleration,  $9.8 \text{ m/s}^2$

$k$  = Permeability,  $m^2$

$N_B$  = Bond number

- $N_C$  = Capillary number  
 $N_{GD}$  = Gravity drainage number  
 $N_G$  = Gravity number  
 $R_{miscible}$  = Oil recovery factor of miscible gas-assisted gravity drainage  
 $RI$  = Refractive index  
 $\overline{S_{or}}$  = Average residual oil saturation  
 $S_w$  = Water saturation  
 $T$  = Temperature, K  
 $T_c$  = Critical temperature, K  
 $t$  = Time, s  
 $u$  = Darcy velocity, m/s  
 $w_i$  = Weight fraction of  $i$ th component  
 $\alpha_s$  = Exponent of solvent in Eq. (6)  
 $\alpha_o$  = Exponent of heavy oil in Eq. (6)  
 $\rho_o$  = Density of heavy oil, kg/m<sup>3</sup>  
 $\rho_g$  = Density of gas, kg/m<sup>3</sup>  
 $\rho_s$  = Density of solvent, g/cm<sup>3</sup>  
 $\Delta\rho$  = Density different between gas and oil, kg/m<sup>3</sup>  
 $\rho_i$  = Density of  $i$ th component, kg/m<sup>3</sup>  
 $\rho_{mix}$  = Density of mixture, kg/m<sup>3</sup>  
 $\mu_o$  = Viscosity of heavy oil, cP  
 $\mu_s$  = Viscosity of solvent, cP  
 $\mu$  = Viscosity in Eq.(3-13), Pa·s  
 $\nu_{mix}$  = Kinematic viscosity of mixture, m<sup>2</sup>/s  
 $\nu$  = Kinematic viscosity of diluted oil, m<sup>2</sup>/s  
 $\nu_s$  = Kinematic viscosity of solvent, m<sup>2</sup>/s  
 $\nu_o$  = Kinematic viscosity of heavy oil, m<sup>2</sup>/s

$\phi$  = Porosity

$\phi_s$  = Volume fraction of solvent

$\phi_o$  = Volume fraction of heavy oil

### 3.6 References

- Abernethy, E.R., 1976. Production Increase of Heavy Oils by Electromagnetic Heating. *J. Can. Pet. Technol.* 15 (03), 91-97. <http://dx.doi.org/10.2118/76-03-12>.
- Al-Farsi, H., Pourafshary, P., and Al-Maamari, R.S., 2016. Application of Nanoparticles to Improve the Performance of Microwave Assisted Gravity Drainage (MWAGD) as a Thermal Oil Recovery Method. SPE-179764-MS presented at the SPE EOR Conference at Oil and Gas West Asia, Muscat, Oman, March 21-23. <http://dx.doi.org/10.2118/179764-MS>.
- Alomair, O.A., Alarouj, M. A., Althenayyan, A.A. et al., 2012. Improving Heavy Oil Recovery by Unconventional Thermal Methods. SPE-163311-MS presented at the SPE Kuwait International Petroleum Conference and Exhibition, Kuwait City, Kuwait, December 10–12. <http://dx.doi.org/10.2118/163311-MS>.
- Bera, A., and Babadagli, T., 2015. Status of EM Heating for Enhanced Heavy Oil/Bitumen Recovery and Future Prospects: A Review. *Appl. Energy.* 151, 206-226. <http://dx.doi.org/10.1016/j.apenergy.2015.04.031>.
- Bera A., and Babadagli, T., 2015. Efficiency of Heavy-Oil Recovery by Radio Frequency EM Heating: An Experimental Approach. SPE-176113-MS presented at the SPE Asia Pacific Oil & Gas Conference and Exhibition, Bali, Indonesia, October 20–22.
- Bientinesi, M., Petarca, L., Cerutti, A. et al., 2013. A Radiofrequency/Microwave Heating for Thermal Heavy Oil Recovery Based on A Novel Tight-Shell Conceptual Design. *J. Pet. Sci. Eng.* 107, 18–30. <http://dx.doi.org/10.1016/j.petrol.2013.02.014>.
- Cardwell, W.T., and Parsons, R.L., 1949. Gravity Drainage Theory. *Trans. AIME.* 179 (1), 199-215. <http://dx.doi.org/10.2118/949199-G>.
- Chute, F.S., Vermeulen, F.E., Cervenak, M.R., and Mcvea, F.J., 1979. Electrical Properties of Athabasca Oil Sands. *Can. J. Earth Sci.* 16 (10), 2009- 2021. <http://dx.doi.org/10.1139/e79-187>.

- Das, M., Thapar, R., Rajeshwar K., and Dubow, J., 1981. Thermophysical Characterization of Oil Sands: 3. Electrical Properties. *Can. J. Earth Sci.* 18 (4), 742-750. <http://dx.doi.org/10.1139/e81-068>.
- Godard, A., and Bethbeder, F.R., 2011. Radio Frequency Heating, Oil Sand Recovery Improvement. SPE-15056-MS presented at the SPE Heavy Oil Conference and Exhibition, Kuwait City, Kuwait, December 12-14. <http://dx.doi.org/10.2118/150561-MS>.
- Greff, J., and Babadagli, T., 2013. Use of Nano-Metal Particles as Catalyst under EM Heating for In-Situ Heavy Oil Recovery. *J. Pet. Sci. Eng.* 112, 258–265. <http://dx.doi.org/10.1016/j.petrol.2013.11.012>.
- Harvey, A., Arnold, M.D., and El-Feky, S.A., 1979. Selective Electric Reservoir Heating. *J. Can. Pet. Technol.* 18 (3), 47–57. <http://dx.doi.org/10.2118/170173-PA>.
- Hascakir, B., Acar, C., and Akin, S., 2009. Microwave-Assisted Heavy Oil Production: An Experimental Approach. *Energy Fuels.* 23(12), 6033–6039. <http://dx.doi.org/10.1021/ef9007517>.
- James, L.A., Rezaei, N., and Chatzis, I., 2008. VAPEX, Warm VAPEX and Hybrid VAPEX - The State of Enhanced Oil Recovery for In Situ Heavy Oils in Canada. *J. Can. Pet. Technol.* 47(04), 1-7. <http://dx.doi.org/10.2118/08-04-12-TB>.
- Jha, K.N., and Chakma, A., 1999. Heavy-Oil Recovery from Thin Pay Zones by EM Heating. *Energy Sources.* 21 (1-2), 63–73. <http://dx.doi.org/10.1080/00908319950014966>.
- Koch, A., Sotskiy, S., Mustafina D., and Danov, V., 2013. Mechanism of Heavy Oil Recovery Driven by EM Inductive Heating. SPE-165507-MS presented at the SPE Heavy Oil Conference-Canada, Calgary, Alberta, Canada, June 11–13. <http://dx.doi.org/10.2118/165507-MS>.
- Komarov, V.V., 2012. Handbook of Dielectric and Thermal Properties of Materials at Microwave Frequencies. Artech House, Boston, London. ISBN: 9781608075294.
- Koolman, M., Huber, N., Diehl, D., and Wacker, B., 2008. EM Heating Method to Improve Steam Assisted Gravity Drainage. SPE-117481-MS presented at the SPE International Thermal Operations and Heavy Oil Symposium, Calgary, Alberta, Canada, October 20–23. <http://dx.doi.org/10.2118/117481-MS>.

- Kovaleva, L., Davletbaev, A., Babadagli, T., and Stepanova, Z., 2011. Effects of Electrical and Radio-Frequency EM Heating on the Mass-Transfer Process during Miscible Injection for Heavy-Oil Recovery. *Energy Fuels*. 25(2), 482–486. <http://dx.doi.org/10.1021/ef1009428>.
- Kulkarni, M.M., and Rao, D.N., 2006. Characterization of Operative Mechanisms in Gravity Drainage Field Projects through Dimensional Analysis. SPE-103230-MS presented at the SPE Annual Technical Conference and Exhibition, San Antonio, Texas, USA, September 24–27. <http://dx.doi.org/10.2118/103230-MS>.
- Lashgari, H.R., Delshad, M., Sepehrnoori, K., and de Rouffignac, E., 2016. Development and Application of Electrical-Joule-Heating Simulator for Heavy-Oil Reservoirs. *SPE J.* 21 (1), 87–100. <http://dx.doi.org/10.2118/170173-PA>.
- Lee, B.I., and Kesler, M.G., 1975. A Generalized Thermodynamic Correlation Based on Three-Parameter Corresponding States. *AIChE J.*, 21(3), 510–527. <http://dx.doi.org/10.1002/aic.690210313>.
- Leyva-Gomez, H., and Babadagli, T., 2014. Optimal Application Conditions of Steam-Solvent Injection for Heavy Oil/Bitumen Recovery from Fractured Reservoirs: An Experimental Approach. SPE-172901-MS presented at the SPE International Heavy Oil Conference and Exhibition, Mangaf, Kuwait, December 8–10. <http://dx.doi.org/10.2118/172901-MS>.
- Li, H., Zheng, S., and Yang, D., 2013. Enhanced Swelling Effect and Viscosity Reduction of Solvent(s)/CO<sub>2</sub>/Heavy-Oil Systems. *SPE J.* 18 (4), 695–707. <http://dx.doi.org/10.2118/150168-PA>.
- Lobe, V.M., 1973. A Model for the Viscosity of Liquid-Liquid Mixtures. MSc thesis, University of Rochester, Rochester, New York.
- Lowe, D.F., Oubre, C.L., and Ward, C.H., 2000. Soil Vapor Extraction Using Radio Frequency Heating: Resource Manual and Technology Demonstration. Boca Raton, FL, Lewis Publishers. ISBN: 1-56670-464-2.
- Moreno, L., and Babadagli, T., 2014. Asphaltene Precipitation, Flocculation and Deposition during Solvent Injection at Elevated Temperatures for Heavy Oil Recovery. *Fuel*. 124, 202–211. <http://dx.doi.org/10.1016/j.fuel.2014.02.003>.
- Pasalic, D., Vaca, P., Okoniewski, M., and Diaz-Goano, C., 2015. EM heating: A SAGD Alternative Strategy to Exploit Heavy Oil Reservoirs. WHOC15-150 presented at the World Heavy Congress, Edmonton, Alberta, Canada, March 24–26.

- Peng, D.Y., and Robinson, D.B., 1978. The Characterization of the Heptanes and Heavier Fractions for the GPA Peng-Robinson Programs. GPA Research Report RR-28.
- Pizarro, J.O.S., and Trevisan, O.V., 1990. Electrical Heating of Oil Reservoirs: Numerical Simulation and Field Test Results. *J. Pet. Technol.* 42 (10), 1320–1326. <http://dx.doi.org/10.2118/19685-PA>.
- Sahni, A., Kumar, M., and Knapp, R.B., 2000. EM Heating Methods for Heavy Oil Recovery. SPE-62550-MS presented at the SPE/AAPG Western Regional Meeting, Long Beach, California, June 19–23. <http://dx.doi.org/10.2118/62550-MS>.
- Sresty, G.C., Dev, H., Snow, R.H., and Bridges, J.E., 1986. Recovery of Bitumen from Tar Sand Deposits with the Radio Frequency Process. *SPE Res. Eng.* 1 (1), 85–94. <http://dx.doi.org/10.2118/10229-PA>.
- Tang, J., Feng, H., and Lau, M., 2001. Microwave Heating in Food Processing. *Advances in Agricultural Engineering*, World Scientific Publisher, New York, Chap. 1. ISBN: 978-981-270-658-4.
- Trautman, M., Ehresman, D., Edmunds, N., Taylor, G., and Cimolai, M., 2013. Effective solvent extraction system incorporating EM heating. US Patent 8,616,273 B2.
- Twu, C.H., 1984. An Internally Consistent Correlation for Predicting the Critical Properties and Molecular Weights for Petroleum and Coal-Tar Liquids. *Fluid Phase Equilibria.* 16(2), 137–150. [http://dx.doi.org/10.1016/0378-3812\(84\)85027-X](http://dx.doi.org/10.1016/0378-3812(84)85027-X).
- Yaws, C.L., 2003. *Yaws' Handbook of Thermodynamic and Physical Properties of Chemical Compounds*. Knovel Corporation, ISBN: 978-1-59124-444-8.

## **CHAPTER 4 EFFECT OF ELECTROMAGNETIC HEATING ON THE CHANGES IN PETROPHYSICAL PROPERTY OF FORMATION ROCKS**

A version of this chapter was presented at the SPE Trinidad and Tobago Section Energy Resources Conference held on 25–26 June 2018, in Port of Spain, Trinidad and Tobago.

## Summary

Electromagnetic (EM) heating has been proposed to recover heavy oil, bitumen, and shale oil due to its great environmental friendliness. Previous studies have mainly focused on investigating the oil recovery efficiency of such non-aqueous method as well as its technical and economic feasibilities. However, the role that EM heating plays in affecting the petrophysical property of formation rocks is not well understood although it could significantly affect the reservoir deliverability and performance of the EM heating. Detailed investigations are required for a better understanding, design, and application of this technique.

In this study, we conduct a comprehensive study in an attempt to elucidate the petrophysical property changes of formation rock under EM heating. First, a commercial microwave oven is used to conduct the EM heating experiments; different types of formation rocks including continental shale, Berea-sandstone, tight sandstone, and Indiana-carbonate are tested. Next, scanning electron microscopy (SEM), energy dispersive X-ray (EDX), N<sub>2</sub> adsorption/desorption, X-Ray fluorescence (XRF), and core flooding experiments are used to characterize the petrophysical properties of rock samples before and after EM heating experiments. Moreover, oven-heating experiments are conducted to distinguish the effects of conductive-heating and EM heating on changing the properties of rock samples. Lastly, experimental-scale simulations are conducted to verify the experimental results and to further understand the mechanisms of variations in the petrophysical properties of formation rocks under EM heating.

Results show that different types of rocks exhibit distinct responses to EM heating due to a different dielectric property. Shale samples exhibit a higher temperature compared with sandstone and carbonate because of the abundance of good EM energy absorbance (i.e. clays and pyrite) in shale. The shale samples are crumbled into pieces or fractured after EM heating, while

the sandstone and carbonate samples remain almost unchanged when exposed to EM heating. The SEM results reveal that EM heating induces micro-fractures, shrinkage of clay, decomposition and release of organic content to the shale sample. Also, the N<sub>2</sub> adsorption/desorption measurements demonstrate that the pore volume of shale sample significantly increases due to clay shrinkage, while part of the pore can be blocked by the converted bituminous kerogen after EM heating. On the contrary, EM heating has almost no effect on the pore-structures of Berea sandstone and Indiana carbonate due to the transparency of quartz and calcite to EM waves. However, the EM heating can fracture the tight sandstone that is saturated with water because of the rapid rise of pore pressure under EM heating. Furthermore, a finite element simulation is conducted to simulate the temperature profile and stress distribution of shale sample under EM heating; results show that the heterogeneous expansion of shale sample under EM heating induces a large tension which causes tensile failure of the shale sample. The visual observations, quantitative results, and simulation results obtained in this study provide insights into the design and application of EM heating for the purpose of oil recovery from unconventional reservoirs.

**Keywords:** Electromagnetic heating, formation rock, petrophysical property, thermal stress, fracture.

#### **4.1 Introduction**

To meet the increasing energy demand, there is a growing interest in exploiting the unconventional hydrocarbon resources such as heavy oil, bitumen, and shale oil. Steam-based methods, such as cyclic steam stimulation (CSS) and steam assisted gravity drainage (SAGD), have proved to be effective for heavy oil and bitumen recovery, but suffer from a high energy intensity, large water consumption, and great environmental footprint [1-3]. A typical SAGD

project has an energy oil ratio of about 7.5 GJ/m<sup>3</sup>, which will emit about 0.38 tonnes of CO<sub>2</sub> to provide the steam to recover 1 m<sup>3</sup> of oil [4]. The steam-based methods and gas injection are inefficient for shale oil recovery due to the interaction of clay and steam-condensed water and low injectivity of shale [5-6].

EM heating, converting the electrical energy into heat, reduces carbon emission caused by steam generation, avoids excessive water consumption, and can be applied in water-hostile reservoirs [2]. These features of EM heating make it attractive to recover heavy oil, bitumen, and shale oil. Previous studies discussed the recovery performance, technical feasibility, and economic efficiency of EM heating [7-9], demonstrating a great potential of using EM heating to recover heavy oil and bitumen. However, the effects of EM heating on affecting the petrophysical property of formation rocks have been seldom discussed. The petrophysical property of formation rock affects the reservoir deliverability, fluid flow, and final oil recovery, justifying that the property variations of formation rocks under EM heating requires detailed investigation.

Jamaluddin et al. [10] first proposed the idea of formation heat treatment (FHT) and summarized the mechanisms of thermal treatment as follows: vaporization of blocked water, dehydration of clays, partial destruction of clay minerals, and possible micro-fracturing due to the thermally induced stresses. Since then, researchers have conducted various investigations about the formation rocks under heat treatment. Previous studies which employed an oven or a furnace to heat the shale samples showed that the enlargement in the pore volume under heating is caused by the evaporation of saturated water and light organic components, decomposition of kerogen and inorganic minerals [11-13], which leads to a significant enhancement to the permeability of formation rocks. Kang et al. [13] studied the permeability changes of shale samples by heat treatment and found that permeability significantly increases when the temperature is above

400°C. Compared with shale, sandstone and carbonate exhibit high thermal stability; the sandstone and carbonate became unstable when the temperature is approximately above 600°C [14-15].

Several attempts have been conducted to investigate the interactions of EM heating and water-saturated formation rocks. Li et al. [16] proposed using microwave (MW) heating to remediate the water blocking in the gas reservoir and found that the gas permeability of sandstone increases after the vaporization of trapped water by EM heating. Moreover, their SEM results show that the dehydration of clays causes a volume shrinkage, which cracks some mineral wafers, while the heterogeneous swelling of grains under EM weakens the cementation and induces microfractures. Chen et al. [17] proposed using MW to fracture tight rocks and concluded the major fracturing mechanism of this method is the tensile breakage caused by rapid pressurization of saturated water in confined pores. Wang et al. [18] studied the petrophysical properties of sandstone under MW heating and investigated the feasibility of using MW heating to lower the water saturation in the near-wellbore region. They found that the dehydration and decomposition of minerals under EM heating enhances both the porosity and permeability of sandstone. Hassani et al. [19] investigated the effect of MW irradiation on rocks and found that both the tensile and compressive strengths of rocks (nortie, granite, and basalt) are reduced after being exposed to MW irradiation.

In this study, we conducted a systematic study to investigate the roles EM heating plays in altering the petrophysical properties of formation rocks (including sandstone, carbonate, and shale). A commercial microwave oven was used to conduct the EM heating experiment and an infrared thermometer was used to measure the surface temperature of rock samples. Various characterization techniques, including SEM, EDX, N<sub>2</sub> adsorption/desorption, and XRF were

employed to investigate the effect of EM heating on shales. Core flooding experiments were performed to quantify the effect of EM heating on influencing the porosity and permeability of Berea sandstone, tight sandstone, and carbonate. Furthermore, an experimental-scale simulation work was done to calculate the stress distribution of core samples and understand the mechanisms of induced changes to formation rocks caused by EM heating.

## 4.2 Theory

Unlike the conventional heating method, EM heating relies on the fractional heating generated by dipole rotation and ion conduction under an alternating electric field, which provides the features of rapid heating, volumetric heating, and selective heating [20]. Because of these merits, EM heating has frequently been proposed in mineral separation, ore emollienting, enhancement of the grindability of coals [21], remediate the oil-contaminated soil and cuttings [22], break water-oil emulsion [23], and heavy oil/bitumen recovery.

The permittivity, characterizing the interaction between the electric field and a material, plays a pivotal role in EM heating process. The permittivity is composed of real and imaginary parts [24]:

$$\varepsilon^* = \varepsilon_0(\varepsilon' - j\varepsilon'') \quad (4-1)$$

where  $\varepsilon^*$  is the complex permittivity,  $\varepsilon_0$  is the permittivity of free space ( $8.85 \times 10^{-12}$  F/m),  $\varepsilon'$  is the real part of relative permittivity (i.e., dielectric constant, indicating how much energy can be stored in the material), and  $\varepsilon''$  is the imaginary part of the relative permittivity (i.e., loss factor, indicating the ability of turning the stored energy into heat).

Based on the loss factor, the materials can be classified into three categories: good absorber ( $\varepsilon'' > 0.2$ ), intermediate absorber ( $0.1 \leq \varepsilon'' \leq 0.2$ ), and weak absorber ( $0.1 < \varepsilon''$ ) [24]. **Table 4-1** lists the dielectric properties of common materials in the formation rocks. Among them, quartz, calcite,

dolomite, mica, and bitumen are characterized as weak absorbers, which are almost transparent to EM waves; feldspar is an intermediate absorber; clays, pyrite, distilled water, brine, and n-paraffin are good absorbers [9, 22, 25-28]. Because water is an excellent absorber to EM waves, allowing EM heating to effectively dehydrate the formation rocks, previous studies have demonstrated great advantages of using EM heating to remedy the water blockage and pressurize the rocks by water vaporization. However, how the clays, pyrite, and organic content behave under EM heating is not fully understood. Moreover, formation rocks have complex mineralogical compositions and high heterogeneity, and contain both good and weak absorbers. It is of critical importance to further study how EM heating would alter the petrophysical properties of formation rocks as the induced petrophysical property changes of the formations rocks could significantly affect the oil recovery efficiency and process efficiency of EM heating in the reservoir.

**Table 4-1** Dielectric properties of common materials in the formation rocks.

Material	Dielectric constant	Loss factor	Category	Ref
Quartz	3.8	0.001	Weak absorber	[25]
Mica	1.6	0.005	Weak absorber	
Calcite	8.94	0.0004	Weak absorber	
Feldspar	2.6	0.02	Intermediate absorber	
Pyrite	79	7.1	Good absorber	[27]
Dolomite	5.7	0.009	Weak absorber	[28]
Bitumen	2.62	0.011	Weak absorber	[9]
Distilled Water	77.27	9.22	Good absorber	
Brine	73.68	24.57	Good absorber	
Smectite	76.14	15.34	Good absorber	[26]
Illite	48.56	4.11	Good absorber	
Kaolinite	42.13	3.10	Good absorber	
n-Paraffin	8	2	Good absorber	[22]

## 4.3 Experimental

### 4.3.1 Materials

In this study, we collected shale, Berea sandstone, tight sandstone, and Indiana carbonate samples for the EM heating experiments. The rock samples were cut to the standard cylindrical cores with a diameter of 2.54 cm. The shale samples are continental shale retrieved from the Ordos Basin, China. **Table 4-2** summarizes the mineral compositions of these core samples obtained by XRF and the measured total organic contents (TOC). The shale samples are composed of clay, quartz, feldspar, pyrite, dolomite, and calcite, while the sandstone and carbonate rocks are mainly composed of quartz and calcite, respectively.

**Table 4-2** Mineral compositions and TOCs of the core samples used in this study.

Sample	Mineral composition (wt%)						TOC (wt%)	Ref
	Quartz	Feldspar	Calcite	Dolomite	Pyrite	Clay		
Shale sample #1 (S1)	22	13	0	11	27	27	2.63	
Shale sample #2 (S2)	29	26	0	6	9	30	1.12	
Shale sample #3 (S3)	22	39	3	5	6	25	4.81	
Shale sample #4 (S4)	17	23	3	3	0	54	4.53	
Shale sample #5 (S5)	30	8	0	2	4	56	0.52	
Shale sample #6 (S6)	18	33	3	0	8	38	6.60	
Shale sample #7 (S7)	24	25	3	4	9	35	6.70	
Shale sample #8 (S8)	28	21	2	26	5	18	1.30	
Berea Sandstone	90							[29]
Tight Sandstone	92							
Indiana Carbonate			97					[29]

#### 4.3.2 Characterization of Core Samples

The surface morphology, chemical compositions, and petrophysical properties of formation rock samples were measured before and after EM heating experiments. The pore size distributions of shale samples were quantified by Autosorb Quantachrome 1MP (Quantachrome Instruments, USA). A Zeiss EVO M10 scanning electron microscopy (Carl Zeiss Microscopy GmbH, Germany) coupled with energy dispersive X-ray (SEM/EDX) was used to characterize the surface morphology and chemical composition distribution of shale samples. Also, a Zeiss Stemi 2000C microscope (Carl Zeiss Microscopy GmbH, Germany) was used to visualize the surface of

rock samples. The porosity and permeability of Berea sandstone, tight sandstone, and Indiana carbonate were measured by typical core flooding experiments.

### 4.3.3 Experimental Setup and Procedures

A microwave oven, operating at a frequency of 2.45 GHz and a power of 1000 W, was used to conduct the EM heating experiments. **Figure 4-1** shows the schematic of the experimental setup. The microwave was generated by a magnetron and then transmitted to the oven cavity through a waveguide; the core sample, placed at the center of the oven, was heated by the generated EM flux. Before the experiment, all the core samples were dried in an oven at 105°C for 24 h to eliminate the residual water. Then, the characterizations were performed to obtain the original properties of the samples. Next, the samples were subjected to EM heating for 3 min; an infrared thermometer was used to measure the surface temperature of the sample. SEM/EDX and N<sub>2</sub> adsorption/desorption were performed to investigate the pore-structure changes of shale samples after EM heating, while the permeability of Berea sandstone, tight sandstone, and Indiana carbonate was measured by core flooding experiments. Based on the final temperatures of samples under EM heating, selected samples were heated in an oven at the same temperature to compare the effects of EM heating and conductive heating.

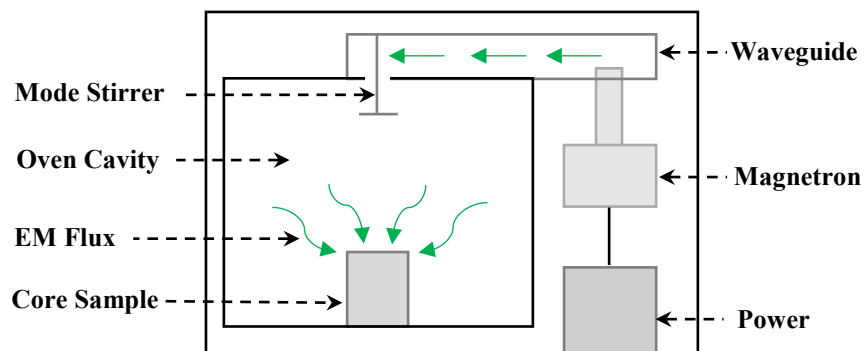


**Figure 4-1** Schematic of the experimental setup used for investigating the property variations of formation rocks under EM heating.

## 4.4 Experimental Results

### 4.4.1 Temperature Responses of Different Types of Formation Rocks

Figure 4-2 shows the temperature responses of different types of formation rocks. After 3 min of EM heating, the surface temperatures of shale (S1), Berea sandstone, tight sandstone, and Indiana carbonate were 214°C, 46°C, 47°C, and 49°C, respectively. Due to the heterogeneity of formation rocks, the surface temperature varies from spot to spot; the values above are the measured highest temperatures. The sandstone and carbonate rocks exhibit a low-temperature response under EM heating because quartz and calcite, the main components of sandstone and carbonate, are weak absorbers to EM waves. On the contrary, the large content of clays and pyrite in shale provides abundant ions, which significantly enhances the absorption of EM energy and leads to a higher temperature.

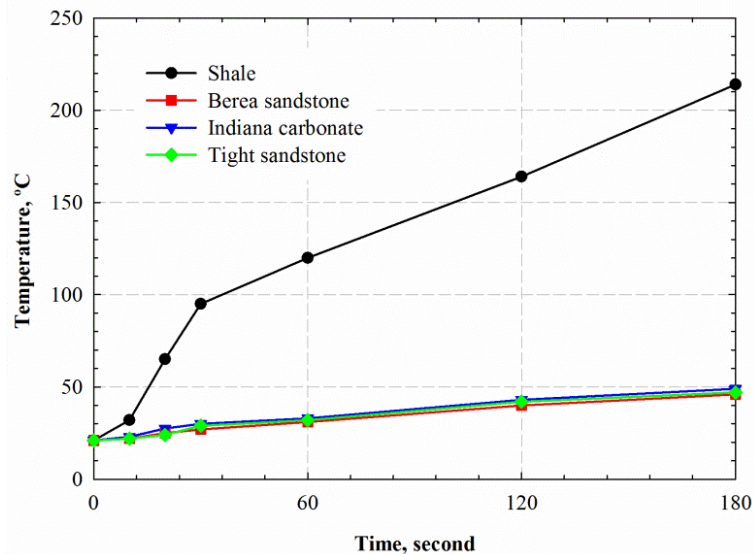


Figure 4-2 Temperature profiles of different types of rocks under EM heating. The shale sample used in this test is S1.

### 4.4.2 Effect of EM Heating on Shale Samples

The shale sample exhibited a notable response to EM heating, which showed a high temperature and fast temperature rise under EM heating. In this section, we investigate the effect of EM

heating on changing the petrophysical properties of shale samples. Samples with different clay contents, pyrite contents, and organic content were tested.

#### **4.4.2.1 Pyrite Content**

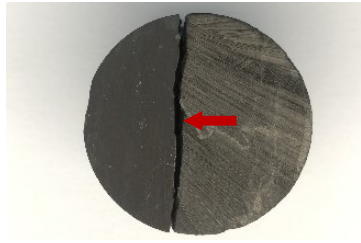
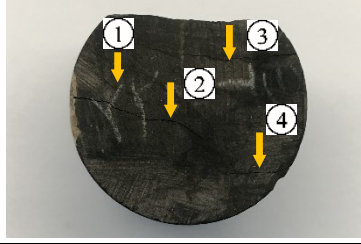
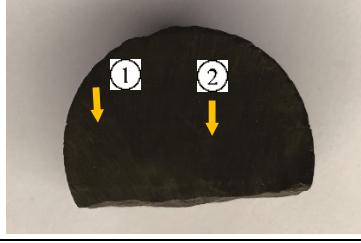
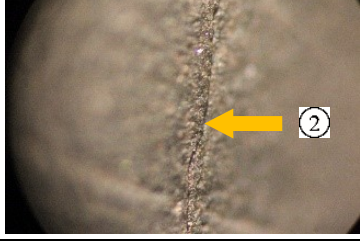
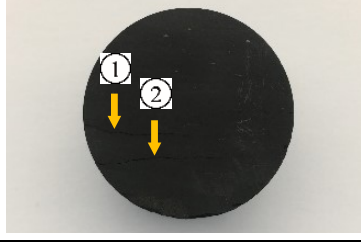
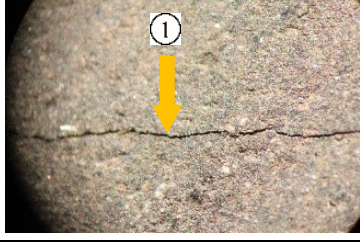
The pyrite exhibits a large loss factor value, as shown in **Table 4-2**, which makes it an excellent EM energy absorber. Samples S1, S2, S3, and S4, exhibiting various pyrite content, were used to illustrate the effect of pyrite. **Table 4-3** summarizes the surface temperatures of samples as well as the photos taken before and after EM heating. The measured surface temperatures of samples were similar to each other; however, the internal temperatures were expected to be higher than the surface temperature due to the heating mechanism of EM heating (Detailed analysis will be presented in Section 4.5.5).

Comparing the appearances of the samples after EM heating, we found that a higher pyrite content provides more significant changes to the sample. The sample S1 fractured into two pieces due to the crumbling of the rock matrix; the samples S2, S3, and S4 were still intact but axial and tangential fractures were generated. The pyrite is an excellent EM energy absorber, which exhibits a high temperature under EM heating. Also, the pyrite has a high thermal expansion coefficient of about  $8.87 \times 10^{-6} \text{ K}^{-1}$  [30]. On the contrary, the weak absorber (i.e., quartz) only slightly expands due to a low-temperature rise and a low thermal expansion coefficient; the thermal expansion coefficient of quartz is about  $5.5 \times 10^{-7} \text{ K}^{-1}$  [31]. This heterogeneous thermal expansion induces a tensile stress which can break the shale sample. (Detailed stress analysis will be shown in Section 5.5.) Fractures were also generated in sample S4 after EM heating, albeit S4 contains no pyrite. This is because S4 possesses a large fraction of clay, which also plays a critical role in this process.

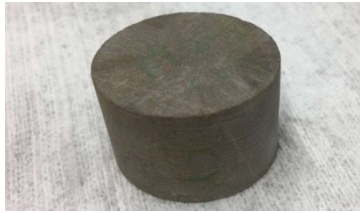
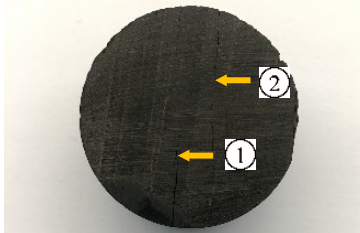
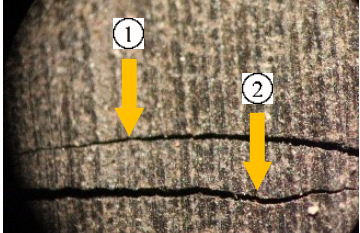
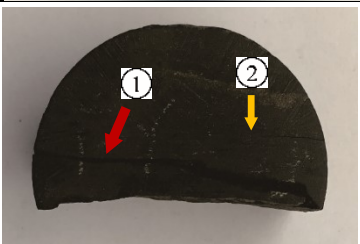
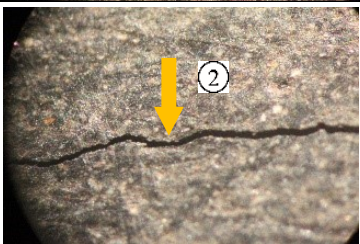
#### **4.4.2.2 Clay Content**

Clays are also good EM energy absorber, which has been applied as an additive to enhance loss factor of materials in EM heating [24]. Samples S4, S5, S6, S7, and S8, which possessed different fractions of clay, were used to study the effect of clay content in this process. **Table 4-4** summarizes the surface temperatures of the samples as well as the photos taken before and after EM heating. Similar to the experimental results on the pyrite effect, the surface temperatures of samples containing different clay contents were close to each other.

**Table 4-3** Images of shale samples with different pyrite contents taken before and after EM heating experiments.

Sample	Before heating	After heating	<sup>c</sup> Microscope image
S1 <sup>a</sup> PC: 27wt% <sup>b</sup> T: 214°C			N/A
S2 PC: 9 wt% T: 216°C			
S3 PC: 6 wt% T: 236°C			
S4 PC: 0 wt% T: 227°C			
Notes: <sup>a</sup> PC is the pyrite content; <sup>b</sup> T is the highest surface temperature measured after 3 min of EM heating; <sup>c</sup> The microscope image is obtained under 5X magnification. The red arrow points to a fracture that has been generated due to the crumbling of the shale samples, while the yellow arrows point to the intact fractures that are generated in the samples.			

**Table 4-4** Images of shale samples with different clay contents taken before and after EM heating experiments.

	Before heating	After heating	<sup>c</sup> Microscope image
S5 <sup>a</sup> CC: 56 wt% <sup>b</sup> T: 212°C			N/A
S6 CC: 38 wt% T: 209°C			
S7 CC: 35 wt% T: 199°C			
S8 CC: 18 wt% T: 220 °C			

Notes: <sup>a</sup>CC is the clay content; <sup>b</sup>T is the highest surface temperature measured after 3 min of EM heating; <sup>c</sup>The microscope image is obtained under 5X magnification. The red arrow points to fractures that have been generated due to the crumbling of the shale samples, while the yellow arrows point to the intact fractures that are generated in the samples.

The sample S5 had a large clay content, which crumbled into pieces after about 40s of EM heating, and the S7 sample fractured into 2 pieces after about 1 min of EM heating. The sample S8 cracked into three pieces after 3 min EM heating, while axial and tangential fractures were generated in the sample S6. The effect of EM heating on clays involves both expansion and shrinkage. The high temperature of clays under EM heating leads to thermal expansions; meanwhile, the dehydration of clay causes the shrinkage. Such shrinkage can crack the minerals

and decrease the cementation between grains [16]. Moreover, the clay-confined water will vaporize into steam under EM heating, which can fracture the shale sample due to a larger pore pressure caused by the vaporization of water [17]. The aforementioned factors contribute to the breakage of shale samples with large clay content.

#### **4.4.2.3 SEM/EDX Characterization**

We investigated the macroscopic changes of shale core samples under EM heating; the shale samples could crumble into pieces, crack into several parts, or form axial and tangential fractures. To further examine the morphology changes of the shale samples, SEM/EDX characterizations were performed on sample S1 and S4 before and after EM treatment. **Figure 4-3** compares the SEM test results on samples S1 and S4 made before and after EM heating. The surfaces of the original samples were smooth and flat, while the surfaces became coarse and rough after 3 min of EM heating. Also, new pore spaces were created, and the intrapores became enlarged after EM heating. These observations verify the hypothesis that shrinkage of clay and vaporization of clay-confined water can generate additional pore spaces in shale.

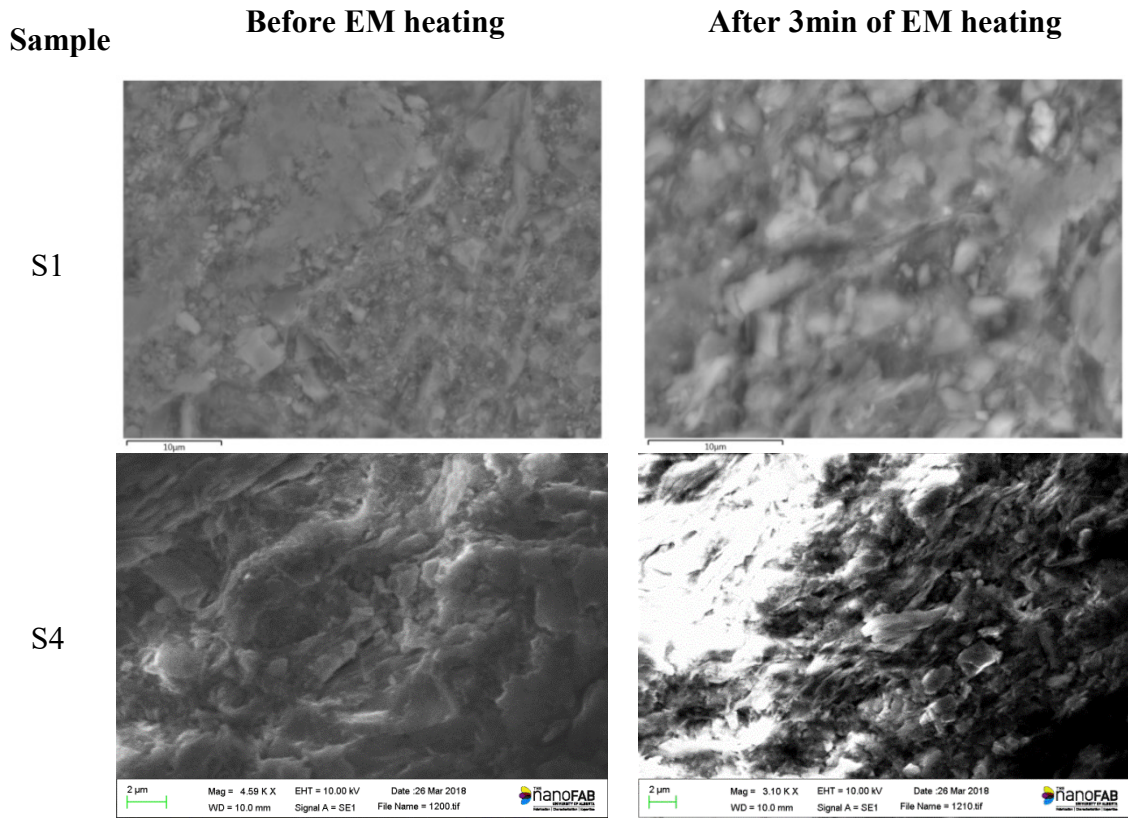


**Figure 4-3** SEM images of sample S1 and S4 taken before and after EM heating.

We also observed micro-fractures in the samples and SEM/EDX tests were performed to understand the mechanisms that generated these fractures. **Figure 4-4** shows the backscatter image of the sample S1 and the corresponding chemical composition distributions. A micro-fracture was generated (shown at the top right of the picture), and the element analyses showed that this part was mainly Si (quartz), while the right corner parts were abundant with Fe (pyrite). This observation verifies that the selective heating of EM waves leads to a heterogeneous expansion of pyrite and quartz, which eventually creates fractures near the boundary of pyrite and quartz-rich area.

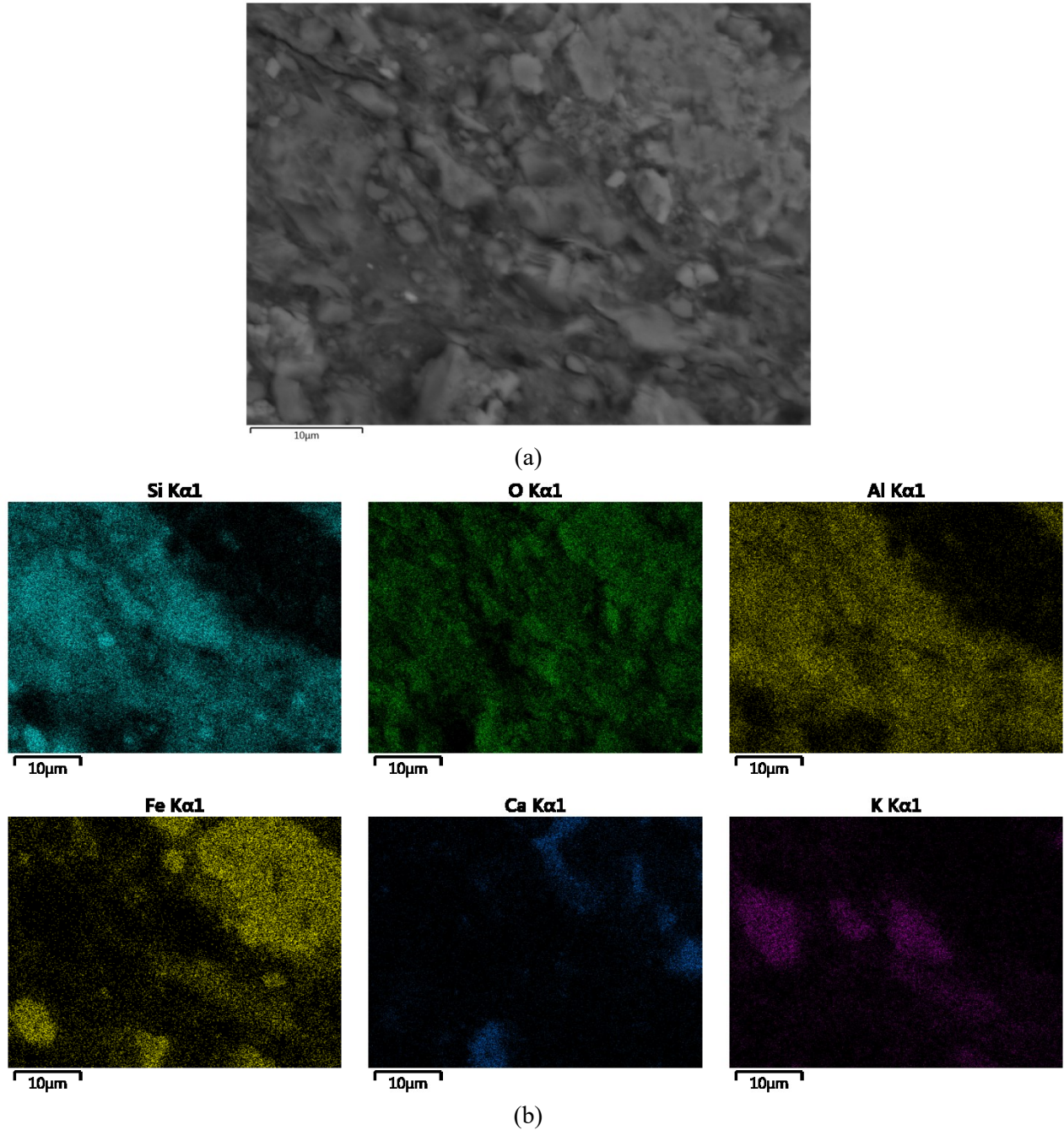


**Figure 4-4** SEM/EDX analyses of sample S1: (a) backscatter image of the sample S1 and (b) the corresponding chemical composition distributions.

**Figure 4-5** shows the backscatter image of the sample S4 and the corresponding chemical composition distributions. Careful examination of Figure 4-5 indicates that fractures were created in the organic-rich area where the carbon intensity is high. This result indicates that the

decomposition of organic content creates new pore space and fractures. Similar CT-scan results were found by Tiwari et al. [11].

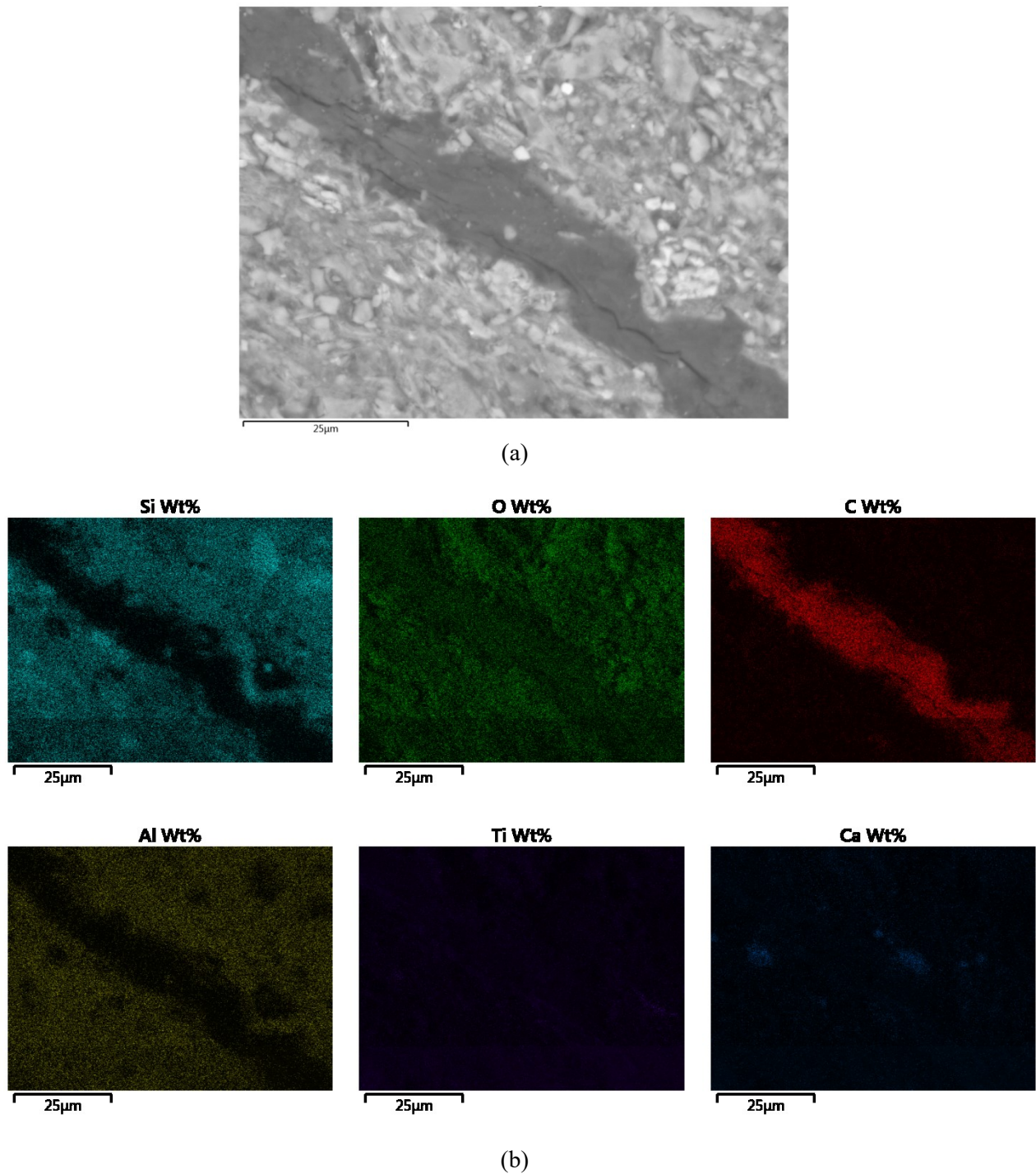
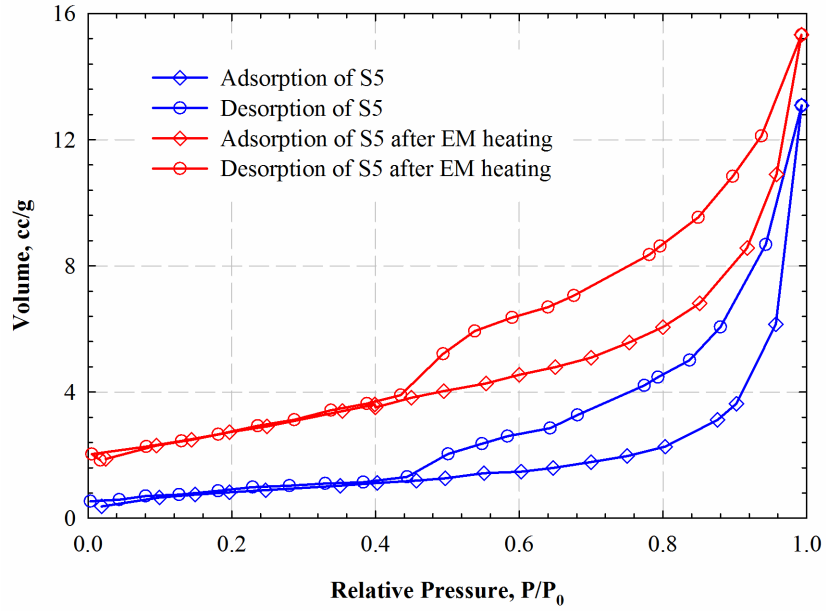


**Figure 4-5** SEM/EDX analysis of sample S4: (a) BSE image of the sample S4 and (b) the corresponding chemical composition distributions.

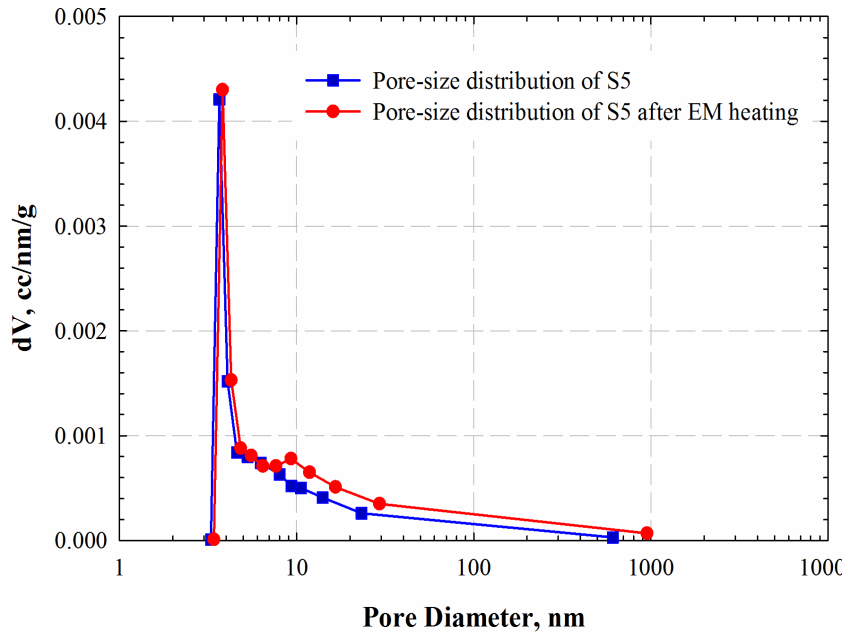
#### 4.4.2.4 N<sub>2</sub> Adsorption and Desorption Characterization

To quantify the effect of EM heating on the pore-structures of shale samples, N<sub>2</sub> adsorption/desorption tests were performed on S5 and S6. Samples S5 and S6 were outgassed at 212°C and 209°C (measured surface temperature after EM heating), respectively; the outgas processes last for 2-4 h. After the adsorption/desorption tests, desorption data and Barrett-Joyner-Halenda (BJH) method were used to calculate the pore-size distributions [32]. The pores had diameters ranging from 2 to 1000 nm, covering both the mesopores (2-50 nm) and macropores (>50 nm).

**Figure 4-6** shows the isotherms of shale sample S5 as well as the pore-size distributions before and after EM heating. Sample S5 had a large content of clay and showed significant changes after EM heating. The isotherms showed that the adsorption volume significantly increased after EM heating and the pore diameters increased after EM heating as well. As illustrated in Figure 4-3, the clay shrinkage and clay-confined water vaporization created new pore spaces. Consequently, the additional pore spaces increased the total surface area, boosting the adsorption volume. Also, the shrinkage of clays enlarged the intrapore space and increased the pore volume of the pores that were larger than 8 nm.



(a)

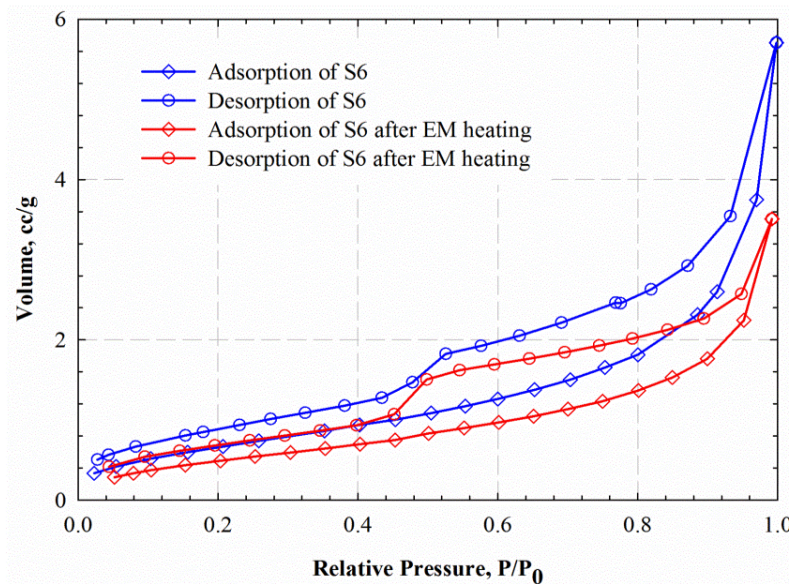


(b)

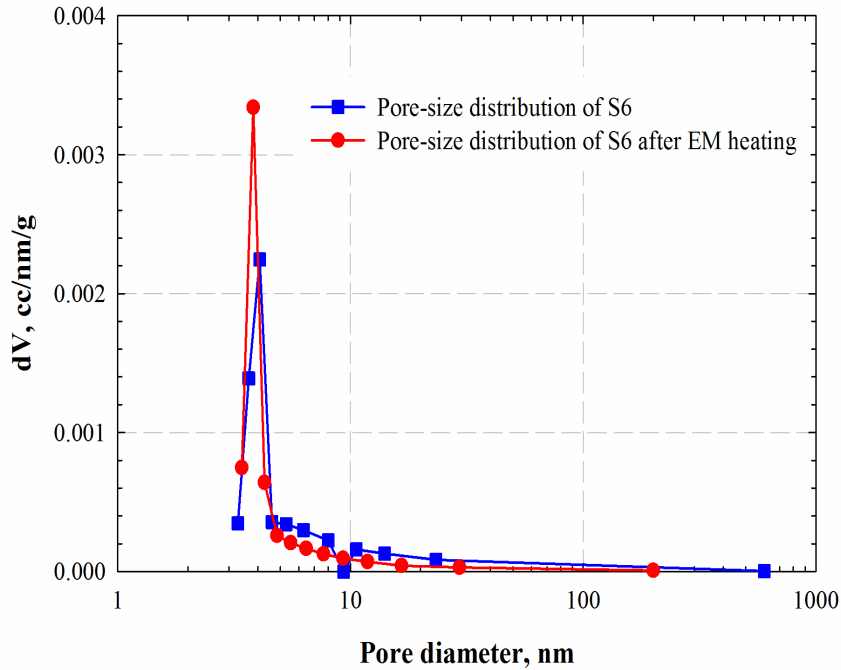
**Figure 4-6** N<sub>2</sub> adsorption/desorption results: (a) adsorption/desorption isotherms and (b) pore size distributions of sample S5 before and after EM heating.

**Figure 4-7** shows the isotherms and pore-size distributions of sample S6 before and after EM heating. It can be seen from Figure. 4-7 that the adsorption volume decreased after EM heating; the number of small pores (less than 4.5 nm) increased while the numbers of larger pores (larger

than 4.5 nm) decreased after EM heating. Such different observation made on S6 can be attributed to its low clay content but large organic content. Compared with sample S5 (its clay content is 56 wt% and its TOC is 0.52 wt%), the sample S6 possessed a much lower clay content (18 wt%) but a higher organic content (6.59 wt%). The increase in the small pores was organic pores created by the release of volatile organic content. However, the decrement in the large pores was caused by the fact that the large pores were blocked by the converted bituminous kerogen upon EM heating. Similar observations were also reported in the study conducted by Saidian et al. [33]. The shale samples used in this study were continental shales, which were thermally immature; also, the EM heating only lasted for 3 min, which failed to sufficiently convert the kerogen to light hydrocarbons.



(a)



(b)

**Figure 4-7** N<sub>2</sub> adsorption/desorption results: (a) adsorption/desorption isotherms and (b) pore size distributions of sample S6 before and after EM heating.

#### 4.4.3 Comparison with Oven Heating Experiments

To compare the effect of EM heating and heat conduction/convection, samples S1 and S4 were heated by a conventional oven at 227°C (the highest measured surface temperature of S1 and S4 after EM heating) for 12 h. The weight of samples S1 and S4 decreased about 0.0034 wt% and 0.0039 wt% after oven heating, which was caused by vaporization of confined water and light organic content. Apart from this, no significant changes were found in the shale samples that were treated by the conventional oven heating. However, the shale samples experienced significant changes under EM heating. Although it is difficult to measure the permeability changes of shales under EM heating, an enhancement of the overall permeability in shale is expected due to the generated fractures.

##### 4.4.3.1 Effect of EM Heating on the Porosity and Permeability of Berea Sandstone, Tight Sandstone, and Indiana Carbonate

We quantified the effect of EM heating on Berea sandstone, tight sandstone, and Indiana carbonate by measuring the permeability changes before and after EM heating. The detailed procedures used were as follows: (1) we first measured the original permeability and porosity of these samples; (2) these samples were then dried in an oven at 105°C for 12 h; (3) we conducted 3 min EM heating experiments on these samples; (4) we measured the permeability and porosity of samples again after EM heating; (5) we repeated the EM heating experiment again using the same samples, but saturated with water; (6) the permeability and porosity of these samples were measured for the last time. Steps 1-4 first examined the effect of EM heating on changing the properties of dry cores, while steps 5-6 examined the effect of EM heating on changing the properties of water-saturated cores. The confining pressure used during the core flooding experiment was 200 psi.

**Table 4-5** summarizes the permeability and porosity of Berea sandstone, Indiana carbonate, and tight sandstone measured before and after EM heating. By comparing the original porosity/permeability and those measured after EM heating of the dry samples, we can see that the porosity and permeability of these samples almost remained unchanged. This is because the main components of these samples (either quartz or calcite) are transparent to EM waves; hence, the EM heating has an insignificant effect on the petrophysical-property changes of Berea sandstone, tight sandstone, and Indiana carbonate.

**Table 4-5** Porosity and permeability of Berea sandstone, tight sandstone, and Indiana carbonate measured before and after EM heating.

Sample	Original		EM heating after drying the samples		EM heating after saturating the samples with water	
	Porosity, %	Permeability, mD	Porosity, %	Permeability, mD	Porosity, %	Permeability, mD
Berea Sandstone	15.10	25.63	15.06	25.25	15.02	25.52
Indiana Carbonate	19.84	26.02	19.36	25.34	19.52	25.86
Tight Sandstone	2.35	0.04	2.13	0.05	*	
Note: *The tight sandstone crumbles into pieces; hence, no permeability and porosity measurements have been performed.						

We then conducted EM heating experiments on saturated samples to examine the effect of elevated pore pressure due to water vaporization caused by EM heating. The permeability and porosity of Berea sandstone and Indiana carbonate remained almost unchanged after EM heating, while the tight sandstone crumbled into pieces after about 2 min of EM heating. **Fig 3-8** shows the tight sandstone saturated with water before and after EM heating. Water is a good absorber to EM waves because its temperature soars under EM heating and quickly vaporizes [8]. Hence, EM heating rapidly increased the pore pressure in cores that were saturated with water [17]. Because the permeability of the tight sandstone is quite low, the elevated pore pressure caused by EM heating could not be promptly released, which started to accumulate and eventually cracked the sample. However, the water or steam could easily escape from the Berea sandstone and Indiana carbonate due to their higher permeability.

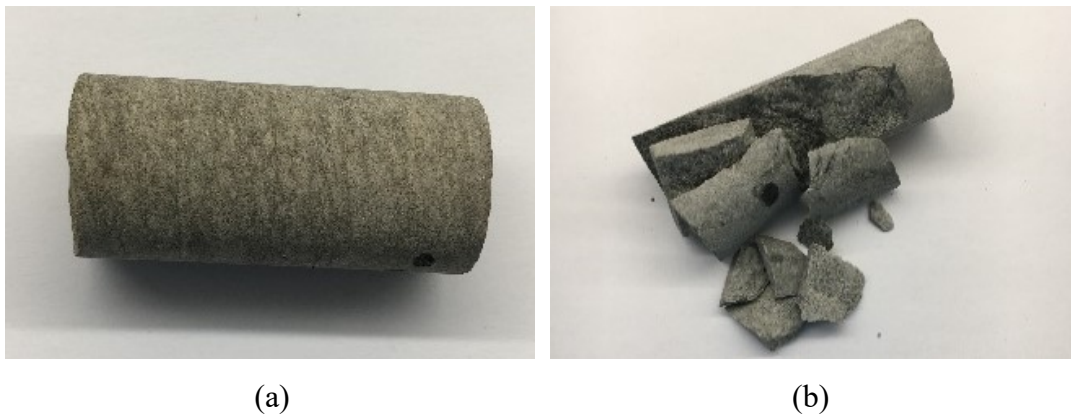


**Figure 4-8** Photos of tight sandstone saturated with water: (a) before EM heating and (b) after EM heating.

#### 4.5 Numerical Analyses

In this section, we numerically investigated the temperature and stress distributions of the shale samples under EM heating. A commercial finite element simulator, COMSOL Multiphysics, was used to analyze this process. The simulation consisted of three major parts: (1) evaluation of the

electric field provided by EM heating, (2) computation of the temperature profiles of the core sample, and (3) calculation of the stress distribution of the core sample.

#### 4.5.1 Model Description

**Fig 4-9** shows the schematic of the simulation model. An experimental scale simulation model was built, and only a half of the model was simulated to save the computational time. The model consisted of a waveguide, an oven cavity, a glass plate, and a core sample. Similar to the experimental process, the core sample was placed at the center of the plate and heated by the generated microwaves.

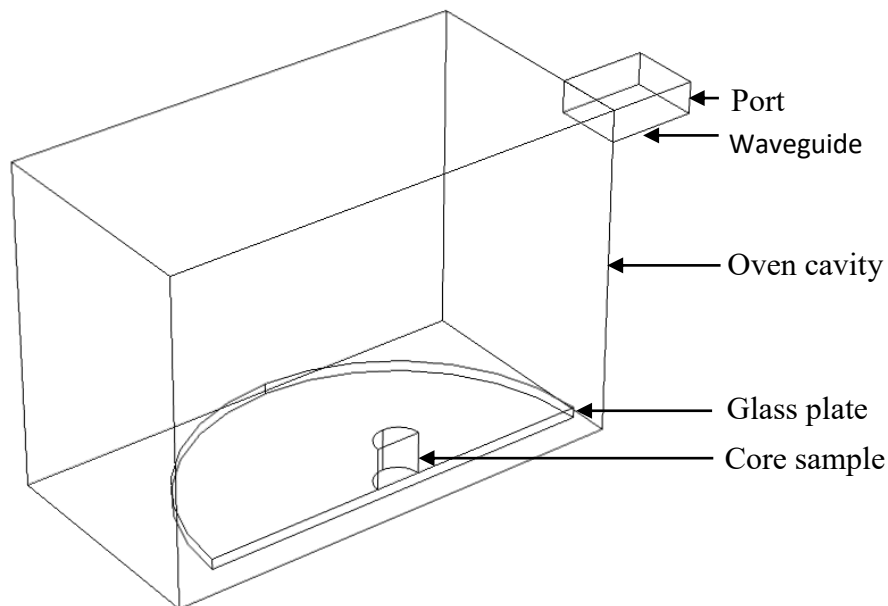


**Figure 4-9** Schematic of the simulation model. The dimensions of the waveguide and oven cavity are  $7.8\text{cm}\times 5\text{cm}\times 1.8\text{cm}$  and  $26.7\text{cm}\times 27\text{cm}\times 18.8\text{cm}$ , respectively. The dimensions (radius  $\times$  height) of the glass plate and core sample are  $11.35\text{cm}\times 0.6\text{cm}$  and  $1.27\text{cm}\times 3\text{cm}$ , respectively.

Two types of core samples, homogenous and layered ones, were simulated. **Figure 4-10** shows the schematic of these two models used to represent the two types of core samples. The homogeneous model assumed the minerals were uniformly distributed, and the material properties of the homogeneous model were determined by taking the volumetric averages of the properties of each mineral component. The layered model assumed that each mineral formed a

layer in the core sample, and the volume of each layer was determined by the mineral's volume fraction. The mineral composition of S1 was applied to the layered model. Also, the minerals were distributed in the core sample in a manner that two good absorbers were separated by a weak absorber. All the material properties used in the simulation are listed in **Table 4-6**.

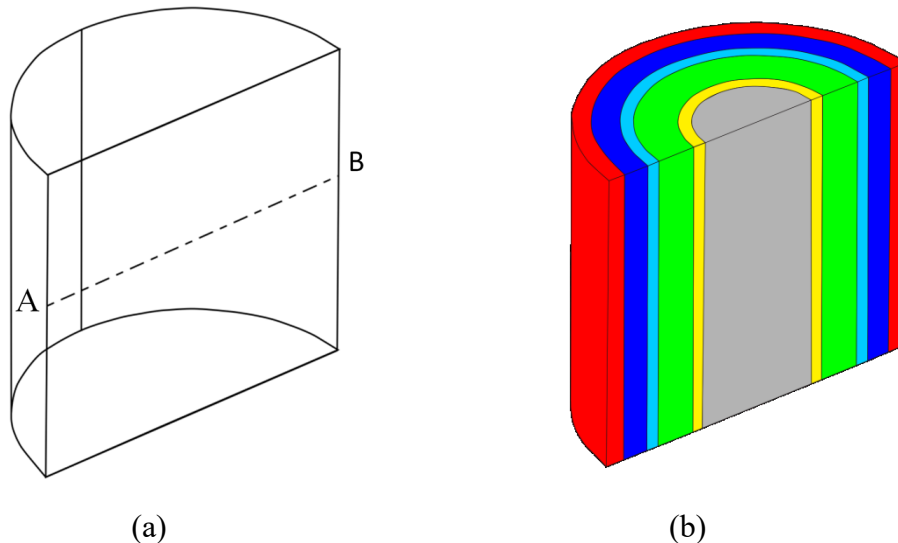


**Figure 4-10** Schematic of the core samples used in the numerical simulation study: (a) homogenous model and (b) layered model. The dashed line in Figure 4-10a is the cutting line AB which will be used to illustrate the simulation result in Section 4.5.5. In Fig 4-10b, the red, blue, cyan, green, yellow, and grey colors represent quartz, clay, dolomite, pyrite, organic content, and feldspar, respectively.

#### 4.5.2 Assumptions

To simplify the numerical simulation studies, we have made the following key assumptions:

- 1) The core sample is homogeneous and isotropic; as for the layered model, each layer is homogeneous and isotropic;
- 2) The phase changes during EM heating process are neglected;
- 3) The material properties of the core sample are independent of temperature;
- 4) The core sample is assumed to be linear elastic;
- 5) The thermal stress can get accumulated even when it reaches the ultimate strength of rock samples;

6) The generated microwave is assumed to be a standing wave with a TE<sub>10</sub> mode in the Z direction [38].

**Table 4-6** Material properties used in the numerical simulations

Property	Layered model						<sup>a</sup> Homogeneous model
	Clay	Feldspar	Organic	Pyrite	quartz	dolomite	
Permittivity	55.61-7.51j [26]	2.6-0.02j [25]	<sup>b</sup> 2.62-0.011j [9]	79-7.1j [27]	3.8-0.001j [25]	5.7-0.009j [28]	<sup>c</sup> 37.39-6.57j
Electrical conductivity, S/m	8×10 <sup>-4</sup> [34]	3.16 [35]	0.012 [36]	3.16×10 <sup>-5</sup> [37]	1×10 <sup>-12</sup> [38]	1×10 <sup>-6</sup> [39]	0.00075
Density, kg/m <sup>3</sup>	2788 [40]	2640 [40]	1180 [40]	2640 [40]	2650 [40]	2753 [40]	2632
Thermal conductivity, W/(m×K)	0.49 [41]	2.1 [42]	1.5 [43]	20.5 [44]	1.5 [45]	2.11 [46]	6.35
Heat Capacity, J/(kg×K)	1000 [47]	1145 [48]	1170 [49]	1051 [44]	1000 [50]	802 [46]	1021
Shear Moduli, GPa	20.19 [40]	27.54 [40]	1.75 GPa [40]	27.54 [40]	41.77 [40]	35.29 [40]	27.87
Bulk Moduli, GPa	35.31 [40]	52.87 [40]	3.5 GPa [40]	65.41 ([40])	35.94 [40]	91.76 [40]	49.45
Expansion coefficient, K <sup>-1</sup>	<sup>d</sup> 0	9.7×10 <sup>-6</sup> [51]	<sup>d</sup> 0	8.87×10 <sup>-6</sup> [30]	5.5×10 <sup>-7</sup> [31]	1.95 ×10 <sup>-6</sup> [52]	3.28×10 <sup>-5</sup>

Note: <sup>a</sup> The material properties ( $x$ ) for the homogeneous model are determined by taking the volumetric averages of the properties of each mineral component. ( $x = \sum x_i \times v_i$ ). <sup>b</sup> The permittivity of bitumen is used to approximate the permeability of organic content. <sup>c</sup> The permittivity of the homogeneous model is calculated by Lichtnecker-Rother model [9]. <sup>d</sup> The thermal treatment of clay and organic content is a complex process, which involves decomposition, transformation, shrinkage and expansion, which makes it difficult to obtain the thermal expansion coefficient of these samples. Hence, the thermal expansion of clay and organic content is not considered in this study by setting their coefficients to be zero.

### 4.5.3 Governing Equations

The Maxwell equation is used to evaluate the electric field distribution under EM heating [38]:

$$\nabla \times (\mu_r^{-1} \nabla \times E) - k_0 (\epsilon_r - j\sigma_e / \omega \epsilon_0) E = 0 \quad (4-2)$$

where  $\mu_r$  is the relative permeability (electromagnetics),  $E$  is the electric field,  $k_0$  is the wave

number ( $k_0 = \frac{\omega}{c_0}$ ),  $\omega$  is the angular frequency,  $c_0$  is the speed of light in free space,  $\epsilon_r$  is the

relative permeability (Eq. 1),  $\epsilon_0$  is the permeability of free space ( $8.85 \times 10^{-12}$  F/m), and  $\sigma_e$  is the

electric conductivity, and  $j = \sqrt{-1}$ .

Knowing the electric field distribution, the EM heating source and temperature profiles can be calculated by [54]:

$$P_d = 2\pi f \varepsilon_0 \varepsilon'' E^2 \quad (4-3)$$

$$\nabla \cdot (k \nabla T) + P_d = C_p \rho \frac{\partial T}{\partial t} \quad (4-4)$$

In Eqs. 4-4,  $P_d$  is the absorbed power,  $f$  is frequency (Hz),  $k$  is the thermal conductivity,  $\rho$  is density,  $C_p$  is heat capacity, and  $T$  is temperature.

Lastly, for linear elastic material, the stress distribution with the consideration of EM heating can be evaluated by [54]:

$$\{\sigma\} = [D] \{\varepsilon_{el} - \alpha(T - T_0)\} \quad (4-5)$$

$$\begin{bmatrix} \sigma_x \\ \sigma_y \\ \sigma_z \end{bmatrix} = \frac{E}{(1+\nu)(1-2\nu)} \begin{bmatrix} 1-\nu & \nu & \nu \\ \nu & 1-\nu & \nu \\ \nu & \nu & 1-\nu \end{bmatrix} \begin{bmatrix} \varepsilon_x \\ \varepsilon_y \\ \varepsilon_z \end{bmatrix} - (1+\nu)\alpha(T - T_0) \quad (4-5a)$$

where  $\sigma$  is stress,  $\varepsilon_{el}$  is elastic strain,  $D$  is the constitutive tensor,  $E$  is Young's modulus,  $\nu$  is Poisson's ratio,  $\alpha$  is thermal expansion coefficient, and  $T_0$  is the reference temperature (21°C).

#### 4.5.4 Boundary Conditions and Mesh

For the calculation of the electric field, the walls of the microwave oven are treated as the impedance boundary [38]:

$$\sqrt{\frac{\mu_0 \mu_r}{\varepsilon_0 \varepsilon_r - \frac{j\sigma_e}{\omega}}} n \times H + E - (n \cdot E)n = 0 \quad (4-6)$$

where  $\mu_0$  is the permeability (electromagnetics) of free space,  $H$  is the magnetic field, and  $n$  is the normal direction to the surface.

The symmetric boundary, as shown in **Figure 4-11a**, was set as a perfect magnetic conductor:

$$n \times H = 0 \quad (4-7)$$

A port boundary was used to represent the generated microwaves. The port was working at the same condition (i.e., 2.45 GHz and 1000 W) as the microwave oven. However, only half of the model was simulated; hence, the working power of the port reduced to 500 W.

In the heat transfer part, the convective boundary (as illustrated in **Figure 4-11b**) condition has been applied to the peripherals of the core sample:

$$q = h \cdot (T_{ext} - T) \quad (4-8)$$

where  $q$  is the heat flux,  $h$  is heat transfer coefficient (40 W/(m<sup>2</sup>×K) borrowed from [55]), and  $T_{ext}$  is the external temperature which is assumed to be the same as the initial temperature ( $T_0$ ). The insulation condition, ( $-n \cdot q = 0$ ), was applied to the symmetric boundary and contact boundary (as shown in **Figure 4-11c**).

Similarly, at the symmetric boundary,  $n \cdot u = 0$ , for the stress analyses ( $u$  is displacement). The contact surface (Figure 4-11c) between the core sample and the glass plate was set as a fixed constraint:  $u=0$ , while the others boundaries were set as free.

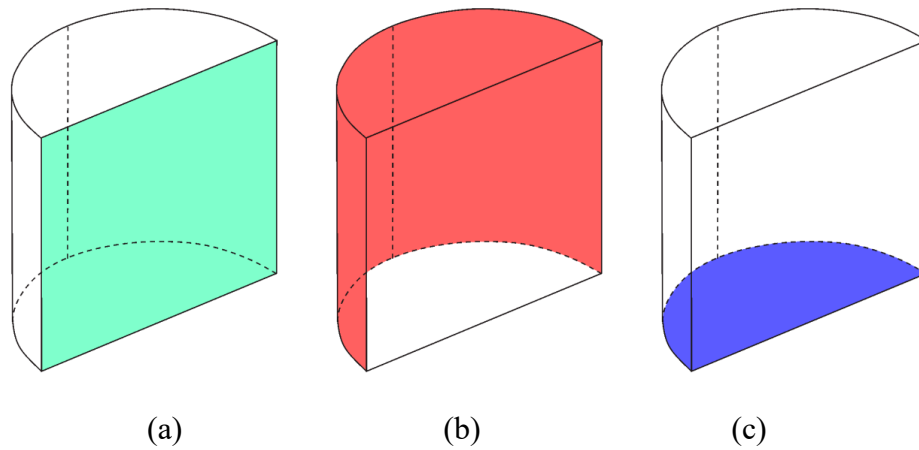


**Figure 4-11** Illustration of different boundaries: (a) symmetric boundary (green part), (b) peripheral boundary (red part), and (c) contact boundary (blue part).

The tetrahedron mesh was adopted in all domains in this simulation work. To obtain robust results and save computational time, different mesh sizes were chosen for the different physics simulated. For the electric field calculation, the maximum element size was set to the  $1/10^{\text{th}}$  of the wavelength [56]. However, the mesh was refined at the core sample for the heat transfer and stress analysis; the maximum element size was set to 1mm to avoid numerical dispersion [57].

**Figure 4-12** shows the mesh configuration; a number of 182641 tetrahedral elements were generated.

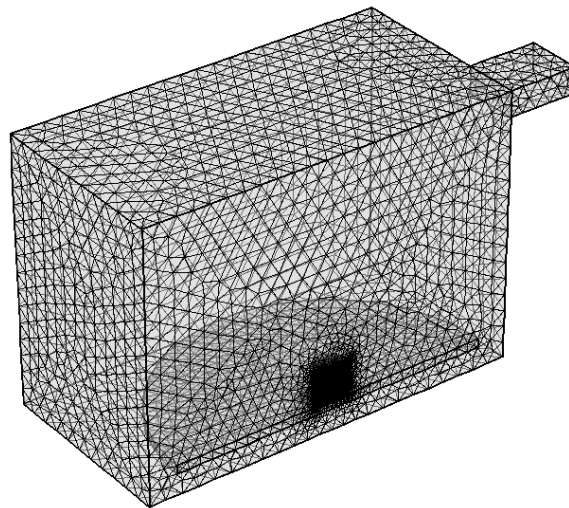


**Figure 4-12** Mesh configuration of the simulation.

#### 4.5.5 Simulation Results

**Figure 4-13** shows the measured temperatures of S1 and simulated temperatures of the layered core model. The inferred thermometer measured the surface temperature of the core sample; hence, the average temperature of the side of the core was evaluated and compared with experimental results. The simulated temperature is only slightly higher than the experimental temperatures; although the layered core model is a simplified case for the real distribution of the minerals, the simulated temperatures agree well with the measured ones.

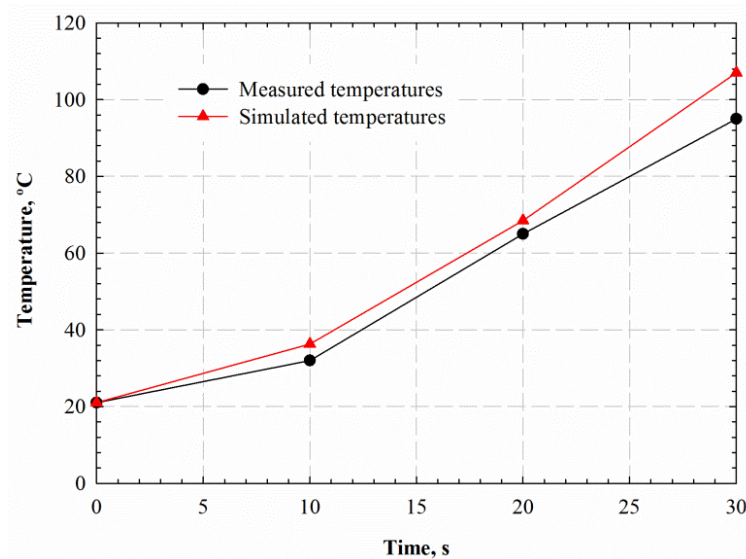


**Figure 4-13** Comparison of the measured and simulated temperatures on S1.

We simulated the first 30s of the experiment (just before the core samples are fractured). We first investigated the effect of EM heating on a homogenous core. **Figure 4-14** shows the temperature profiles after 10s, 20s, and 30s of EM heating. The temperature is higher at the center and decreases towards the peripheral. EM waves penetrate into the samples and accumulate inside the sample, while the heat loss occurs at the surface; these two factors produce a temperature gradient pointing outside in the sample [20]. **Figure 4-15** shows the evolution of the first principal stress (maximum tensile stress) distribution of the core sample. The temperature increases as the EM heating continues, which leads to an increment in the thermal stress. At the

center of the core sample, the higher temperature provides a higher degree of expansion, rendering the hot spot under compression. Consequently, the outside region of the core sample is under tension. Hence, the first principal stress decreases from the center to the peripherals. **Figure 4-16** shows the third principal stress (maximum compressive stress) distribution at different times; in spite of the higher temperature at the center, the largest compression happens at the contact surface between the core sample and the glass plate, which is corresponding to the fixed boundary. For the homogeneous core model, the thermal stresses were mainly induced by the temperature gradient. The maximum thermally induced tensile and compressive stresses are  $4.45 \times 10^{-7}$  MPa and  $-2.91 \times 10^{-6}$  MPa, which are below the tensile strength (about 9.1 MPa) and compressive strength (about 47.9 MPa) of shale sample [58].

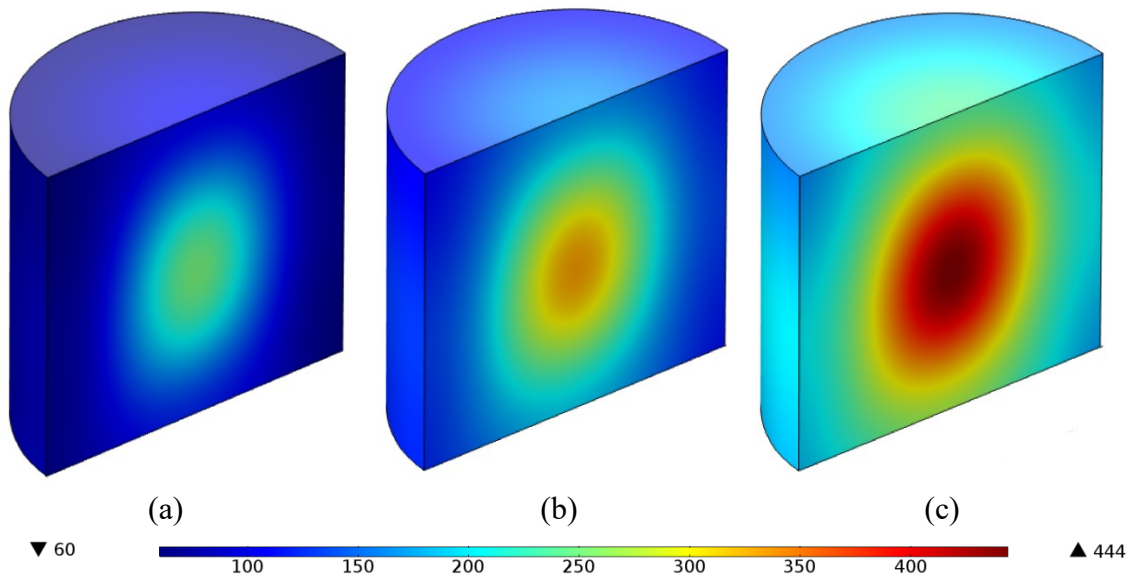


**Figure 4-14** Temperature profiles of the homogeneous core model after (a) 10s, (b) 20s, and (c) 30s of EM heating.

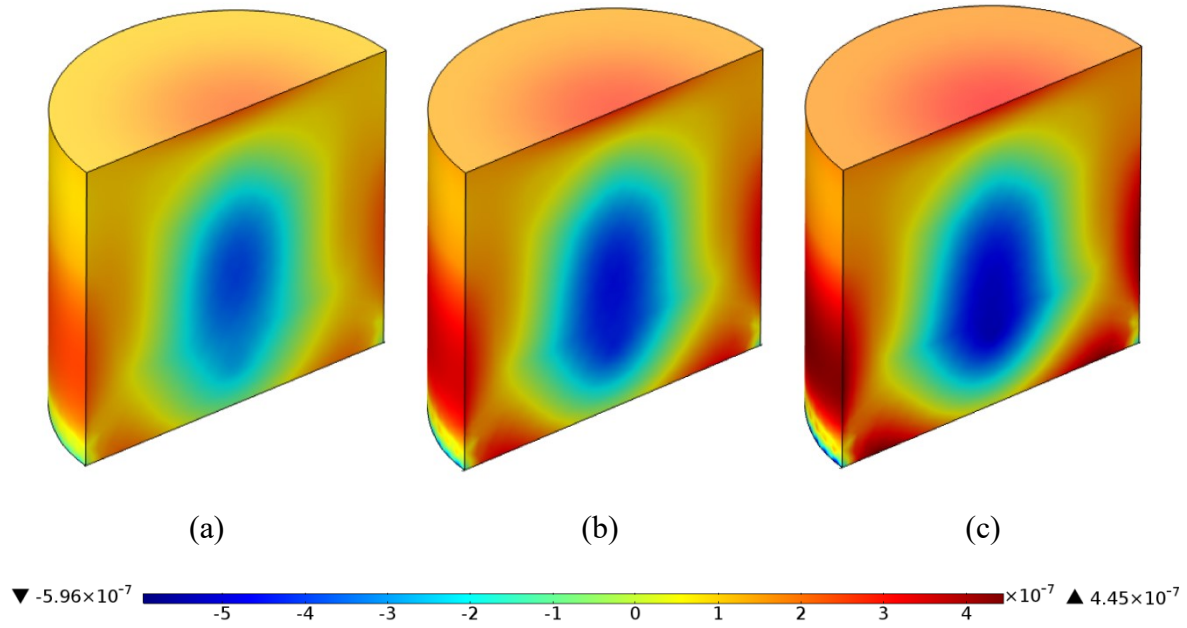


**Figure 4-15** First principal stress distribution of the homogeneous core model after (a) 10s, (b) 20s, and (c) 30s of EM heating.

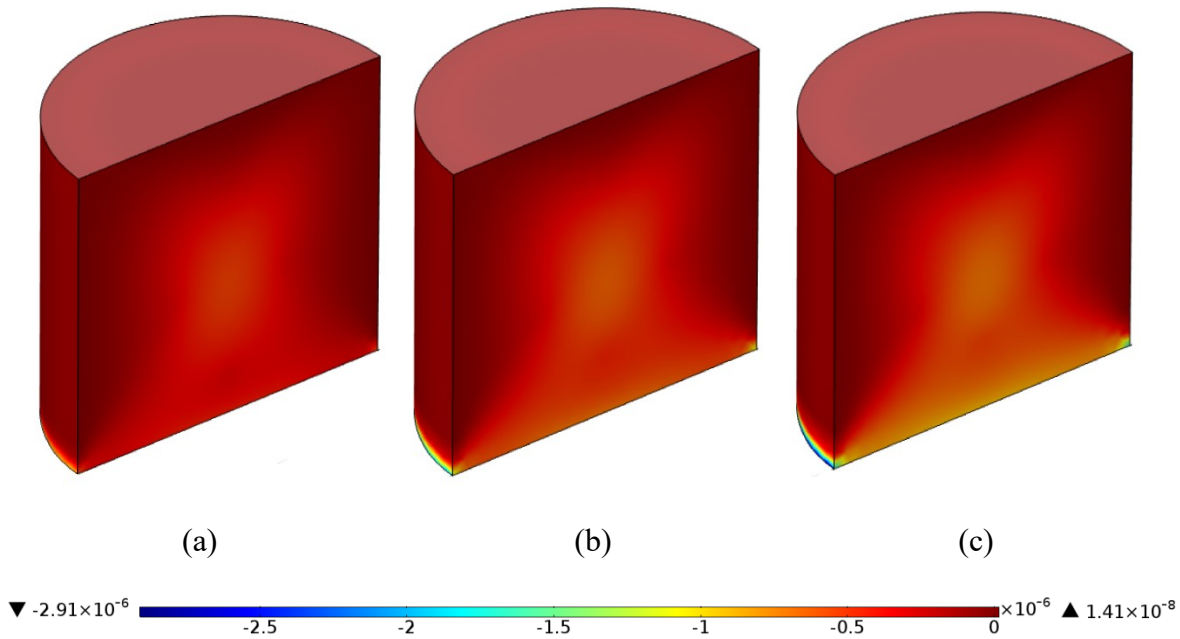


**Figure 4-16** Third principal stress distribution of the homogeneous core model after (a) 10s, (b) 20s, and (c) 30s of EM heating.

**Figure 4-17—Figure 4-19** show the temperature, first principal stress, and third principal stress distributions of the layered core model. Due to the distinct dielectric properties of each mineral,

the temperature of the layered model varies significantly from one layer to another. Moreover, the thermal expansion coefficients are different for different minerals. These factors contribute to a heterogeneous expansion, inducing a large thermal stress; the maximum tensile and compressive stresses are 308 MPa and -434 MPa, respectively. The tensile and compressive strength of common formation rocks are in the range of 7-70MPa and 40-400MPa [59], respectively; hence, the shale rock can be broken under EM heating.

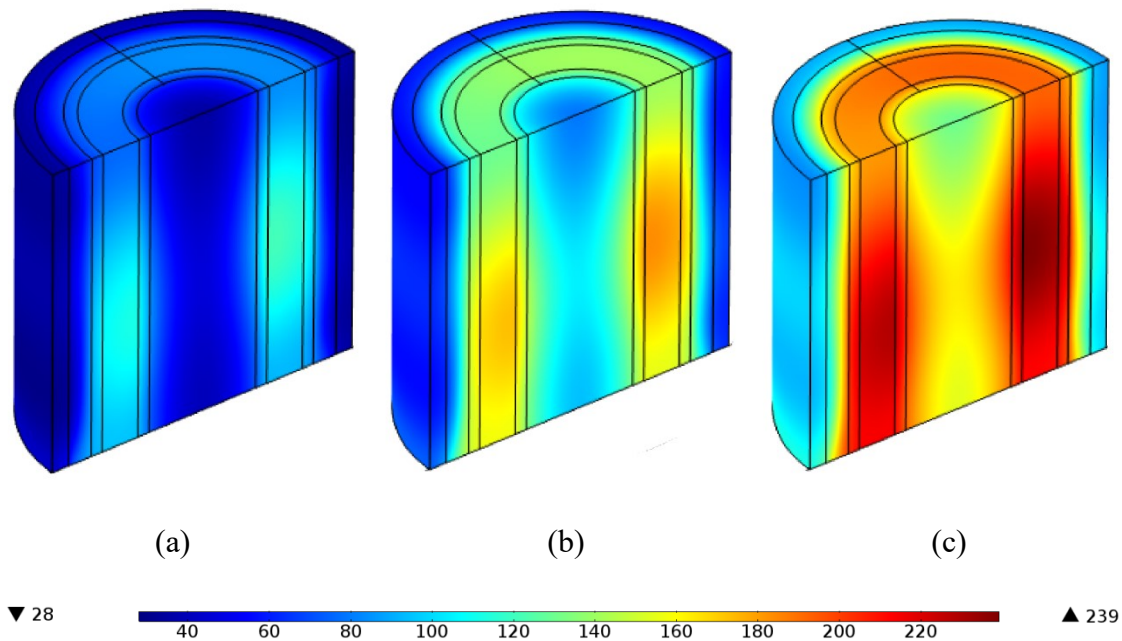


**Figure 4-17** Temperature profiles of the layered core model after (a) 10s, (b) 20s, and (c) 30s of EM heating.

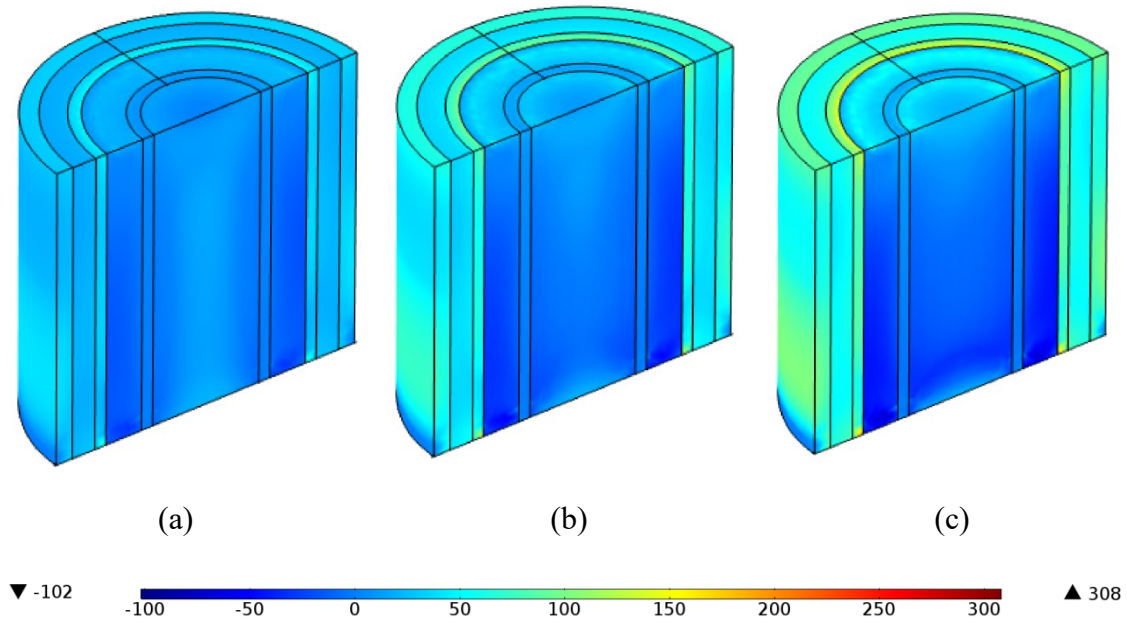


**Figure 4-18** First principal stress distribution of the layered core model after (a) 10s, (b) 20s, and (c) 30s of EM heating.

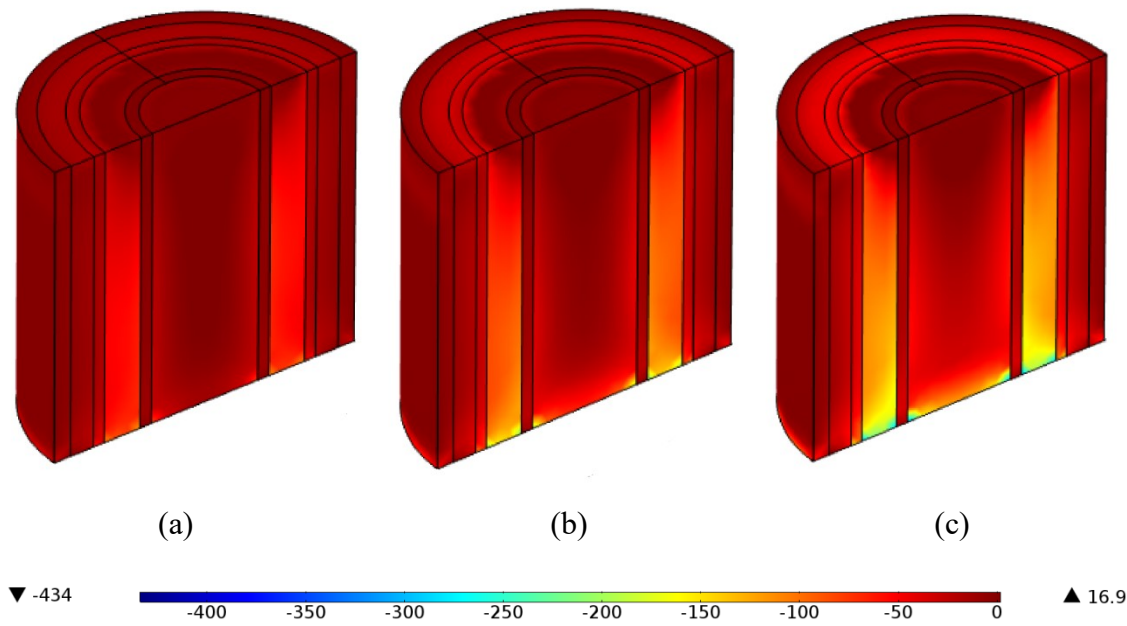
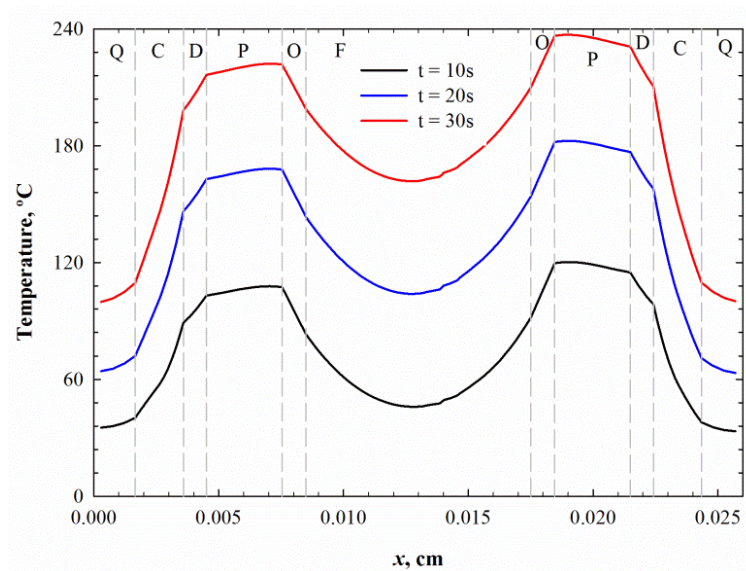
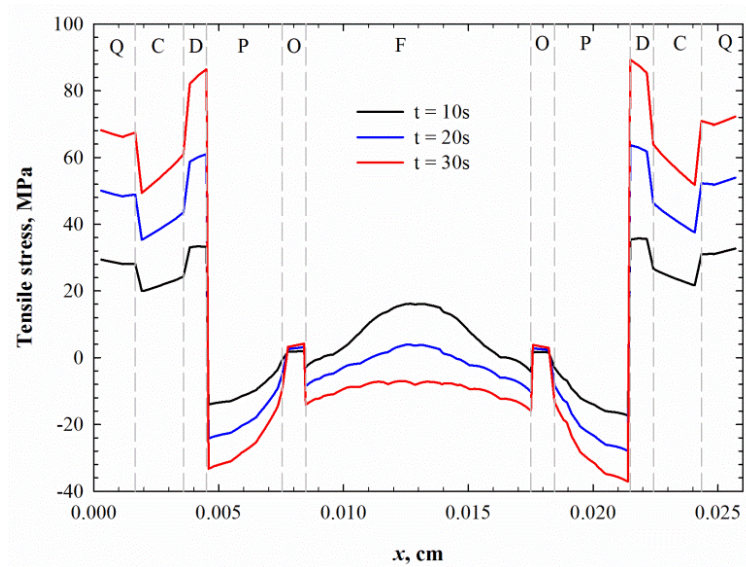


**Figure 4-19** Third principal stress distribution of the layered core model after (a) 10s, (b) 20s, and (c) 30s of EM heating.

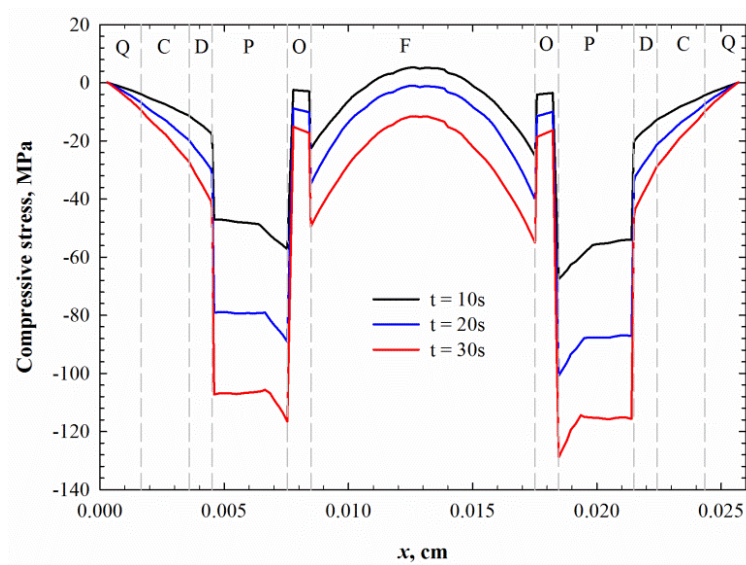
**Figure 4-20** shows the detailed temperature profile, tensile and compressive stresses for each mineral along the cutline AB (shown in Figure 4-10a). Because the EM wave source was located at the right side, the temperature was slightly higher on the right than the left. The pyrite exhibits a higher temperature and thermal expansion coefficient than other components, which leads to a significant expansion under EM heating. The expansion of pyrite induces a large tensile stress to its adjacent minerals (dolomite), which reaches about 86MPa after 30s of EM heating. Such a high tension causes tensile failures in the rock sample. The simulation results show that the mechanisms of breakage of shale rocks under EM heating is the tensile failure caused by a heterogeneous thermal expansion. The results of stress analyses verify the experimental observation that EM heating can cause tensile failure in the shale sample.



(a)



(b)



(c)

**Figure 4-20** Simulation results of (a) temperature, (b) first principal stress, and (c) third principal stress along the cutline AB. In these figures, the Q, C, D, P, O, and F stand for quartz, clay, dolomite, pyrite, organic content, and feldspar, respectively.

#### 4.6 Conclusions and Further Remarks

In this study, we experimentally and numerically investigated the petrophysical property changes of formation rocks under EM heating. The following conclusions can be drawn:

- 1) Different types of formation rocks exhibit distinct responses to EM heating. The surface temperatures of shale, Berea sandstone, tight sandstone, and Indiana carbonate, after 3 min of EM heating, are 214°C, 46°C, 47°C, and 49°C, respectively.
- 2) Shale samples tend to be more susceptible to EM treatment than other types of rocks due to its high pyrite content, clay content, and organic content. Shale samples with a higher pyrite or clay content can be crumbled into pieces under EM heating.
- 3) The SEM/EDX results indicate the stimulating mechanisms of EM heating on shale are tensile failure induced by heterogenous thermal expansion, clay shrinkage by dehydration, and enlargement of the organic pore by decomposition and releasing of the volatile organic content.
- 4) The N<sub>2</sub> adsorption/desorption analyses show that the EM heating can increase the pore volume through clay shrinkage and vaporization of organic content. However, the converted bituminous kerogen can block part of the pores if the shale sample is thermally immature.
- 5) The EM heating has negligible influence on the property of Berea sandstone and Indiana carbonate because their major chemical components are transparent to EM heating. However, EM heating can quickly heat up the saturated water and thereby raises the pore pressure in tight sandstone. Due to the low permeability of tight sandstone, the accumulated pore pressure can eventually fracture the tight sandstone.
- 6) An experimental scale simulation is built to further understand and verify the experimental results. The calculated stress distributions show that the heterogeneous expansion of minerals under EM heating can induce a large tension which can cause failures to the shale sample.

- 7) Our study shows that EM heating can be a promising green technique for stimulating the shale rock. For the shale oil recovery, EM heating can generate fractures in minerals and organic content, helping to achieve an enhanced the oil recovery. For the heavy oil and bitumen recovery, EM heating is usually combined with solvent injection. Careful design is required if the over/under-burdens are shale because EM heating can damage the integrity of these over/under-burdens. However, as for the shale barriers staying inside the payzone, EM heating can dilate them and facilitate the propagation of the solvent chamber. In the future, we will investigate the effect of EM heating on changing the petrophysical property of formation rocks under in-situ stress conditions.

#### 4.7 References

- [1] Butler, R.M. 1997. Thermal recovery of oil and bitumen. Calgary, Alberta: GravDrain Inc.
- [2] Hu, L., Li, H.A., Babadagli, T. et al. 2018a. A semi-analytical model for simulating the combined electromagnetic heating and solvent-assisted gravity drainage. *SPE J.*, Preprint.
- [3] Zhou, W., Chen, S., and Dong, M. 2016. Novel insights on initial water mobility: Its effects on steam-assisted gravity drainage performance. *Fuel* **174**: 274-286.
- [4] Hassanzadeh, H. and Harding, T.G. 2016. Analysis of conductive heat transfer during *in-situ* electrical heating of oil sands. *Fuel* **178**: 290–299.
- [5] Sahni, A., Kumar, M., and Knapp, R.B. 2000. EM heating methods for heavy oil recovery. Paper SPE 62550 presented at the SPE/AAPG Western Regional Meeting, Long Beach, California, June 19–23.
- [6] Egboga, N.U., Mohanty, K.K., and Balhoff, M.T. 2017. A feasibility study of thermal stimulation in unconventional shale reservoirs. *J. Petr. Sci. Eng.* **154**: 576-588.
- [7] Bera, A. and Babadagli, T. 2015. Status of EM heating for enhanced heavy oil/bitumen recovery and future prospects: A review. *Appl. Energy.* **151**: 206–226.
- [8] Hu, L., Li, H.A., Babadagli, T. et al. 2017. Experimental investigation of combined electromagnetic heating and solvent assisted gravity drainage for heavy oil recovery. *J. Petr. Sci. Eng.* **154**: 589–601.

- [9] Hu, L., Li, H.A., Ahmadloo, M. 2018b. Determination of the permittivity of n-hexane/oil sands mixtures over the frequency range of 200 MHz to 10 GHz. *Can. J. Chem. Eng.*, Preprint.
- [10] Jamaluddin, A.K.M., Vandamme, M., and Mann, B.K. 1995. Formation heat treatment (FHT): A state-of-the-art technology for near-wellbore formation damage treatment. 46th Annual Technical Meeting, Calgary, Alberta, Canada, 7-9 June. PETSOC-95-67.
- [11] Tiwari, P., Deo, M., Lin, C.L. et al. 2013. Characterization of oil shale pore structure before and after pyrolysis by using X-ray micro CT. *Fuel* **107**: 547–554.
- [12] Bai, F., Sun, Y., Liu, Y. et al. 2017. Evaluation of the porous structure of Huadian oil shale during pyrolysis using multiple approaches. *Fuel* **187**: 1–8.
- [13] Kang, Y., Chen, M., Chen, Z. et al. 2016. Investigation of formation heat treatment to enhance the multiscale gas transportability of shale. *J. Nat. Gas Sci. Eng.* **35**: 265–275.
- [14] Yang, L., Marshall, A.M., Wanatowski, D. et al. 2017. Effect of high temperatures on sandstone - A computed tomography scan study. *Int. J. Phys. Modell. Geotech.* **17** (2):75–90.
- [15] Popescu, M. A., Isopescu, R., Matei, C. et al. 2014. Thermal decomposition of calcium carbonate polymorphs precipitated in the presence of ammonia and alkylamines. *Adv. Powder Technol.* **25**: 500–507.
- [16] Li, G., Meng, Y., Tang, H. et al. 2006. Clean up water blocking in gas reservoirs by microwave heating: laboratory studies. SPE International Oil & Gas Conference and Exhibition, Beijing, China, 5–7 December. SPE-101072-MS.
- [17] Chen, J.H., Georgi, D., Liu, H.H. et al. 2015. Fracturing tight rocks by elevated pore-water pressure using microwaving and its applications. SPWLA 56th Annual Logging Symposium, Long Beach, California, USA, 18-22 July. SPWLA-2015-RRR.
- [18] Wang, H., Rezaee, R., and Saeedi, A. 2016. Preliminary study of improving reservoir quality of tight gas sands in the near wellbore region by microwave heating. *J. Nat. Gas Sci. Eng.* **32**: 395–406.
- [19] Hassani, F., Nekoovaght, P. M., and Gharib, N. (2016). The influence of microwave irradiation on rocks for microwave-assisted underground excavation. *J. Rock Mech. Geotech. Eng.* **8** (1): 1-15.
- [20] Zhang, Y., Chen, P., Liu, S. et al. 2017. Effects of feedstock characteristics on

- microwave-assisted pyrolysis - A review. *Bioresour. Technol.* **230**: 143–151.
- [21] Prokopenko, A. 2011. Microwave heating for emolliating and fracture of rocks. *Advances in Induction and Microwave Heating of Mineral and Organic Materials*, InTech.
- [22] Junior, I.P., Pereira, M.S., dos Santos, J.M., et al. 2015. Microwave remediation of oil well drill cuttings. *J. Petr. Sci. Eng.* **134**: 23-29.
- [23] Kar, T., and Hascakir, B. 2015. The role of resins, asphaltenes, and water in water–oil emulsion breaking with microwave heating. *Energy Fuels* **29** (6): 3684-3690.
- [24] Majdzadeh-Ardakani, K. and Holl, M.M.B. 2017. Nanostructured materials for microwave receptors. *Prog. Mater Sci.* **87**: 221–245.
- [25] Robinson, J.P., Kingman, S.W., and Onobrakpeya, O. 2008. Microwave-assisted stripping of oil contaminated drill cuttings. *J. Environ. Manage.* **88**: 211–218.
- [26] Josh, M. and Clennell, B. 2015. Broadband electrical properties of clays and shales: Comparative investigations of remolded and preserved samples. *Geophysics* **80** (2): 129–143.
- [27] Peng, Z., Hwang, J., Kim, B., et al. 2014. Microwave permittivity, permeability, and penetration depth of pyrite. *Characterization of Minerals, Metals, and Materials 2014*, John Wiley & Sons, Inc.
- [28] Hasmaliza, M., Zainal, A.A., and Norfadhulah, I. 2015. Dolomite addition in non-stoichiometric cordierite glass-ceramic: effects on dielectric constant. *J. Solid State Sci. Technol.* **23** (1-2):20-25.
- [29] Churcher, P.L., French, P.R., Shaw, J.C. et al. 1991. Rock properties of Berea sandstone, Baker dolomite, and Indiana limestone. SPE International Symposium on Oilfield Chemistry, Anaheim, California, USA, 20-22 February. SPE-21044-MS.
- [30] Hussain, M., Ansari, M. 2017. X-Ray determination of thermal expansion of Iron Sulphide. *IOSR J. Appl. Phys.* **9** (5): 61-63.
- [31] Luque, A., Leiss, B., Alvarez-Lloret, P. et al. 2011. Potential thermal expansion of calcitic and dolomitic marbles from Andalusia (Spain). *J. Appl. Crystallogr.* **44** (6): 1227-1237.
- [32] Barrett, E.P., Joyner, L.G., and Halenda, P.P. 1951. The determination of pore volume and area distributions in porous substances. I. Computations from nitrogen isotherms. *J. Am. Chem. Soc.* **60** (2): 309–319.
- [33] Saidian, M., Godinez, L.J., and Prasad, M. 2016. Effect of clay and organic matter on

- nitrogen adsorption specific surface area and cation exchange capacity in shales (mudrocks). *J. Nat. Gas Sci. Eng.* **33**: 1095–1106.
- [34] Wagner, N., Bore, T., Robinet, J. C. et al. 2013. Dielectric relaxation behavior of Callovo-Oxfordian clay rock: A hydraulic-mechanical-electromagnetic coupling approach. *J. Geophys. Res: Solid Earth.* **118** (9): 4729-4744.
- [35] Hu, H., Dai, L., Li, H. et al. 2014. Electrical conductivity of K-feldspar at high temperature and high pressure. *Miner. Petro.* **108** (5): 609-618.
- [36] Shabro, V., Kelly, S., Torres-Verdín, C. et al. 2014. Pore-scale modeling of electrical resistivity and permeability in FIB-SEM images of organic mudrock. *Geophys.* **79**(5): 289-299.
- [37] Schieck, R., Hartmann, A., Fiechter, S. et al. 1990. Electrical properties of natural and synthetic pyrite (FeS<sub>2</sub>) crystals. *J. Mater. Res.* **5** (7):1567-1572.
- [38] COMSOL Multiphysics Reference Manual, version 5.3, COMSOL, Inc, [www.comsol.com](http://www.comsol.com)
- [39] Ono, S., and Kenji M. 2015. Influence of pressure and temperature on the electrical conductivity of dolomite. *Phys. Chem. Miner.* **42** (9): 773-779.
- [40] PetroWiki. 2015. *Isotropic elastic properties of minerals*. [http://petrowiki.org/index.php?title=Isotropic elastic properties of minerals&oldid=48038](http://petrowiki.org/index.php?title=Isotropic_elastic_properties_of_minerals&oldid=48038) (accessed 25 June 2015)
- [41] Dondi, M., Mazzanti, F., Principi, P. et al. 2004. Thermal conductivity of clay bricks. *J. Mater. Civ. Eng.* **16** (1): 8-14.
- [42] Sass, J.H. 1965. The thermal conductivity of fifteen feldspar specimens. *J. Geophys. Res.* **70** (16): 4064-4065.
- [43] Ilozobhie, A.J., Obi, D. A., George, A.M. et al. 2016. Determination of thermal conductivity of some shale samples in Awi formation and its geophysical implications, Cross River State, Nigeria. *J. Environ. Earth Sci.* **6** (8):102-111.
- [44] Wang, Y. and Djordjevic, N. 2014. Thermal stress FEM analysis of rock with microwave energy. *Int. J. Miner. Process.* **130**: 74–81.
- [45] Abdulagatov, I.M., Emirov, S.N., Tsomaeva, T.A. et al. 2000. Thermal conductivity of fused quartz and quartz ceramic at high temperatures and high pressures. *J. Phys. Chem. Solids.* **61** (5): 779-787.

- [46] Eppelbaum, L., Kutasov, I., Pilchin, A. Applied geothermics. Springer: Heidelberg. 2014.
- [47] Skauge, A., Fuller, N., and Hepler, L.G. 1983. Specific heats of clay minerals: sodium and calcium kaolinites, sodium and calcium montmorillonites, illite, and attapulgite. *Thermochim. Acta.* **61** (1-2): 139-145.
- [48] Hemingway, B.S., Krupka, K.M., and Robie, R.A. 1981. Heat capacities of the alkali feldspars between 350 and 1000 K from differential scanning calorimetry, the thermodynamic functions of the alkali feldspars from 298. 15 to 1400 K, and the reaction quartz+ jadeite= analbite. *Am. Mineral.* **66**:1202-1215.
- [49] Ungerer, P., Collell, J., and Yiannourakou, M. 2014. Molecular modeling of the volumetric and thermodynamic properties of kerogen: Influence of organic type and maturity. *Energy & Fuels* **29** (1): 91-105.
- [50] Baumann, T., and Zunft, S. 2015. Properties of granular materials as heat transfer and storage medium in CSP application. *Sol. Energy Mater. Sol. Cells.* **143**: 38-47.
- [51] Huotari, T., and Kukkonen, I. 2004. Thermal expansion properties of rocks: Literature survey and estimation of thermal expansion coefficient for Olkiluoto mica gneiss. Posiva Oy, Olkiluoto, Working Report 4.
- [52] Harvey, R.D. 1967. Thermal expansion of certain Illinois limestones and dolomites. Illinois State Geological Survey. *Circular no. 415*.
- [53] Kaur, R., Newborough, M., and Probert, S. D. 1993. Multi-purpose mathematical model for electromagnetic-heating processes. *Appl. Energy* **44** (4): 337-386.
- [54] Molaro, J.L., Byrne, S., and Le, J.L. 2017. Thermally induced stresses in boulders on airless body surfaces, and implications for rock breakdown. *Icarus* **294**: 247-261.
- [55] Datta, A.K. and Rakesh, V. 2013. Principles of microwave combination heating. *Compr. Rev. Food Sci. Food Saf.* **12** (1): 24-39.
- [56] Lin, B.Q., Li, H., Dai, H.M. et al. 2016. Three-dimensional simulation of microwave heating coal sample with varying parameters. *Appl. Therm. Eng.* **93**: 1145-1154.
- [57] Toifl, M., Meisels, R., Hartlieb, P. et al. 2016. 3D numerical study on microwave induced stresses in inhomogeneous hard rocks. *Miner. Eng.* **90**: 29-42.
- [58] Gao, Q., Tao, J., Hu, J. et al. 2015. Laboratory study on the mechanical behaviors of an anisotropic shale rock. *J. Rock Mech. Geotech. Eng.* **7** (2): 213-219.
- [59] Johnson, R.B., and DeGraff, J.V. 1988. *Principles of engineering geology* **497**. New York, Wiley.

## **CHAPTER 5 A SEMI-ANALYTICAL MODEL FOR SIMULATING THE COMBINED ELECTROMAGNETIC HEATING AND SOLVENT- ASSISTED GRAVITY DRAINAGE**

A version of this chapter was presented at the World Heavy Oil Congress held on 7–9 September 2016 in Calgary, Alberta, Canada and has been accepted for publication in *SPE Journal*.

## Summary

Solvent/thermal hybrid methods are recently proposed to enhance heavy oil recovery and to overcome the shortcomings that are encountered when either method is solely applied. One of the ways for this hybridization is to combine electromagnetic (EM) heating and solvent injection to facilitate heavy-oil production by gravity drainage. This approach has several advantages including reduced carbon dioxide emissions, decreased water consumption, and appropriateness for water-hostile reservoirs. We are currently lacking any mathematical model for better understanding, designing, and optimization of this hybrid technique, which is partly attributed to this technique still being in its infancy.

We propose a semi-analytical model to predict the oil flow rate resulted from the combined EM heating and solvent-assisted gravity drainage. The model first calculates the temperature distribution within the EM excited zone due to the radiation-dominated EM heating. By employing different attenuation coefficients within and beyond the vapor chamber, the model can properly describe the corresponding temperature responses in these regions. Next, an average temperature of the chamber edge contributed by EM heating is used to estimate the temperature-dependent properties, such as vapor/liquid equilibrium ratios (*K-values*), heavy-oil/solvent mixture viscosity, and solvent diffusivity. Subsequently, a 1-D diffusion equation is used to calculate the solvent-concentration distribution ahead of the chamber edge. Eventually, the oil flow rate is evaluated with the calculated temperature and solvent distributions ahead of the chamber edge. The proposed model is validated against the experimental results as obtained in our previous study, and the predicted oil flow rate agrees reasonably well with the experimental data.

The proposed model can efficiently predict the oil flow rate of this hybrid process. We conduct sensitivity analyses to examine the effect of major influential factors on the performance of this hybrid technique, including EM heating powers, solvent types, solvent injection pressures, and initial reservoir temperatures. The modeling results demonstrate that a higher EM heating power, a heavier solvent, and a higher solvent injection pressure could accelerate the oil recovery rate, but tend to lower the net present value (NPV) and increase the energy consumption. In summary, the newly proposed model provides an efficient tool to understand, design, and optimize the combined EM heating and solvent-assisted gravity drainage technique.

## **5.1 Introduction**

The large viscosity and low mobility of heavy oil pose the biggest challenge in its recovery. Aiming to overcome this challenge, many methods have been proposed recently. Based on the viscosity-reduction mechanisms, these methods can be classified into two major categories: (1) heat-based methods and (2) solvent-based methods. In the thermal approaches, a significant viscosity reduction of heavy oil is achieved by raising the reservoir temperature through transferring heat into the reservoir. The common ways are through injecting hot water or steam, such as steam/hot water flooding, cyclic steam stimulation (CSS), and steam-assisted gravity drainage (SAGD) (Butler 1997). These methods consume a significant amount of water as well as a massive amount of energy for generating steam. Despite the considerable amount of latent heat that steam can carry, the steam-based methods are less effective for recovering heavy oil from thin pay zones, deeper reservoirs, and water-hostile reservoirs (Sahni et al. 2000). The solvent-based methods take advantage of the mixing of solvent and heavy oil to reduce the viscosity of heavy oil (Allen and Redford 1978). The conventional solvent-based methods include vapor extraction (VAPEX) (Butler and Mokrys 1989) and cyclic solvent injection (CSI)

(Ivory et al. 2010). These methods exhibit a lower oil recovery rate compared with thermal approaches, albeit their reduced energy intensity and appropriateness for the steam-hostile reservoirs.

To overcome the disadvantages of the high energy intensity of heat-based methods and the low recovery rate of solvent-based methods, several hybrid processes have been proposed such as expanding solvent-SAGD process (ES-SAGD) (Nasr et al. 2003), solvent aided process (SAP, SA-SAGD) (Gupta and Gittins 2006; Gupta et al. 2010), N-Solv (Nenniger and Nenniger 2008), and warm VAPEX (Rezaei et al. 2010). These hybrid methods reduce the viscosity of heavy oil through both heating and solvent diluting. Most of them adopt a SAGD-like well configuration to incorporate the merits of both SAGD and VAPEX. The methods of combining heat and solvent are either co-injecting solvent with steam or injecting heated solvent into the reservoirs. Many analytical models have been developed to examine the mechanisms and performances of these hybrid methods (Gupta and Gittins 2012; Keshavarz et al. 2014; Faradonbeh et al. 2017; Liu et al. 2017; Irani and Cokar 2016; Haghghat and Maini 2013). The previous investigations suggested that co-injecting solvent with steam would, to some extent, lead to a reduced chamber-edge temperature because of a lowered steam pressure caused by the partial pressure effect of the injected solvent (Dong 2012; Keshavarz et al. 2014). In addition, the accumulation of solvent at the vapor/liquid interface might create an insulation layer that tends to block heat conduction if improper solvents and injecting strategies were implemented (Gupta and Gittins 2012; Keshavarz et al. 2014). These aspects would cause a less enhancement or even a decrement in the oil recovery. As for injecting heated solvent, the latent heat that solvent can carry is limited, which may lead to an insufficient temperature rise and make it less effective in recovering certain heavy oils.

The combined electromagnetic (EM) heating and solvent-assisted gravity drainage provides another hybrid solution, which enhances the oil recovery through both EM heating and solvent dilution. EM heating, converting the electrical energy into heat, reduces carbon emission caused by steam generation, avoids excessive water usage, and can be applied to reservoirs where steam-based methods are less effective. Further, the reservoir temperature rise provided by EM heating can be much higher than that caused by the injection of superheated solvents. Solvent injection also plays an important role in this hybrid process, which further thins the heavy oil by dilution, forms a vapor chamber to facilitate the gravity drainage once heated above its saturation temperature, and supplement the natural energy in addition to the thermal expansion and the vaporization of connate water by EM heating (Hu et al. 2016a).

Based on the applied frequency, EM heating can be classified into three categories: resistive heating (low-frequency), inductive heating, and dielectric heating (radio-frequency and microwave-frequency). This study focuses on the class of dielectric heating that could heat up a relatively large part of the reservoir to a high temperature within a short time. Many authors have derived analytical solutions, investigated the feasibilities, and evaluated the performances of using EM heating for heavy oil recovery with or without solvent. Abernethy (1976) firstly developed the mathematical solution of electromagnetic heating in heavy oil recovery with a single well serving as both heater and producer. The Beer-Lambert's law (Bird et al. 2002), relating the attenuation of light to the properties of the material when it travels through, was used to describe the relationship between the radiation power and distance in his model. Fanchi (1993) later verified the feasibility of using Beer-Lambert's law to simplify the calculation by solving the radiation power distribution, instead of solving the complex Maxwell equation to calculate the electric field distribution. Carrizales et al. (2010a) developed a multi-phase model to study the

enhanced heavy oil production using EM heating in vertical wells. Davletbaev et al. (2008) conducted numerical simulations to study the heat and mass transfer of injecting solvent with simultaneous electromagnetic heating in vertical wells. However, they solved the mass transfer and heat transfer separately and neglected the temperature effect on the solvent concentration in heavy oil. Ghannadi et al. (2016) developed mathematical solutions to the temperature profiles by resistive heating, inductive heating, and radio-frequency heating. Based on the calculated temperature at the midpoint between the injector and producer as well as the assumption of a threshold temperature, they evaluated the performance of applying different heating strategies to the startup process in a SAGD scenario. However, they treated the reservoir as static and neglected the effect of variations of the attenuation coefficients on EM heating. Bogdanov et al. (2016) coupled commercial simulators of CMG and COMSOL to simulate the heavy oil recovery via the combination of radio-frequency heating and solvent injection with a SAGD-like well configuration. Their simulation results on the saturation distributions and local fluid fluxes showed that the injected solvent formed a vapor chamber and the oil flow mainly happened in the vapor/liquid interface and drained along the interface. Hu et al. (2016b) proposed a semi-analytical model to simulate the oil rates during the combined EM heating and solvent-assisted gravity drainage, but this model can be only used to calculate the oil rates during the chamber-spreading stage. Recently, Wise and Patterson (2016) conducted economic analyses for different scenarios of enhanced solvent extraction incorporating EM heating (ESEIEH<sup>TM</sup>) (Trautman et al. 2013). Their marginal supply cost analyses indicate that the application of ESEIEH is an economical choice when oil price sustains around \$60 /barrel.

The combined EM heating and solvent-assisted gravity drainage is a multi-physics process involving the electromagnetic waves' propagation and absorption, the frictional heat generated by

the interaction of the polarized reservoir materials and electromagnetic waves, and the heat/mass transfer in porous media. Due to the complexity of solving Maxwell equations in porous media and the coupling of different physics, numerical simulations of the combined EM heating and solvent injection tend to be very time-consuming. What's more, the change of reservoir permittivity is crucial for the evaluation of the absorbed power by EM heating. But, there are few attempts to discuss this effect on the temperature rise of the reservoir by using EM heating in the literature. It is of great importance to develop an analytical model that can lower the computational complexity but preserve the essential mechanisms.

In this study, a semi-analytical model is developed to predict the oil flow rate of the combined EM heating and solvent-assisted gravity drainage process. The model first estimates the temperature distribution by EM heating, and then calculates the solvent distribution ahead of the chamber edge. Lastly, the oil flow is evaluated based on the obtained temperature and solvent distributions. The experimental results of the combined EM heating and solvent-assisted gravity drainage conducted by Hu et al. (2016a) are used to validate the proposed model. We then perform sensitivity, economic, and energy-consumption analyses on the major influential factors, including EM heating powers, solvent types, solvent injection pressures, and initial reservoir temperatures.

## **5.2 Theory**

Unlike conventional heating methods that transfer heat into reservoirs by injecting heated fluids, EM heating relies on the frictional heat generated by the dipole rotation and ion conduction under a high-frequency alternating electric field. **Figure 5-1** shows a schematic of the movement of dipoles and ions under an oscillating electric field. The permittivity, characterizing the interaction between the electric field and reservoir materials, plays a pivotal role in the performance of EM

heating. It is a function of composition and applied frequency, composed of real and imaginary parts (Metaxas and Meredith 1983; Al-Harashseh et al. 2009):

$$\varepsilon^* = \varepsilon_0(\varepsilon' - j\varepsilon'') \quad (5-1)$$

where  $\varepsilon^*$  is the complex permittivity,  $\varepsilon_0$  is the permittivity of free space ( $8.85 \times 10^{-12}$  F/m),  $\varepsilon'$  is the real part of relative permittivity (i.e. dielectric constant, indicating how much energy can be stored in the material),  $\varepsilon''$  is the imaginary part of the relative permittivity (i.e. loss factor, indicating the ability of turning the stored energy into heat), and  $j = \sqrt{-1}$ .

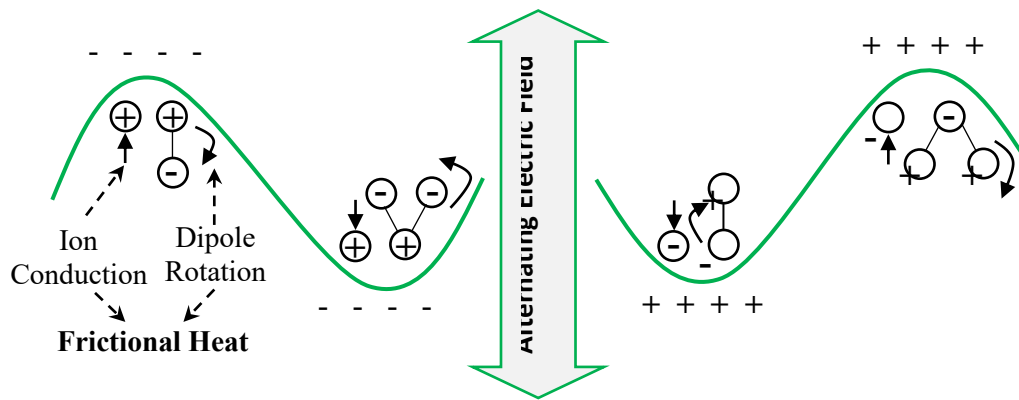


**Figure 5-1** Schematic of the dipole rotation and ion conduction under an alternating electric field. Based on this heating mechanism, the reservoir materials will absorb EM energy when exposed to EM field, leading to an elevated temperature of the reservoir. Among the reservoir materials and injected solvents, formation water is a polar material, which will be vaporized first and then create a desiccated region (Trautman et al. 2013; Hu et al. 2016a). Because of the low loss factor of steam in the desiccated zone, the EM waves penetrate deeper into the reservoir. The reduced attenuation of EM energy in the lowered permittivity regions is beneficial to expand the heated zone further, and the generated steam can store the latent heat and release it to the reservoir once condensed. Eventually, a large part of the reservoir can be heated up.

In some cases, the cyclic vaporization and condensation of connate water is a desirable factor to EM heating due to the storage and release of the latent heat. However, this factor might be detrimental if an “insulating layer” is formed where the constant phase change of connate water blocks the EM wave to penetrate deeper and inhibits the temperature rise (Lowe et al. 2000; Bera and Babadagli 2017; Hu et al. 2016a). Injecting solvent can not only mitigate this unfavorable effect by redistributing the generated steam but also dilute the heavy oil, reduce the interfacial tension, enhance swelling effect (Li et al. 2013), and supplement the natural energy depletion caused by production. Meanwhile, the lowered heavy oil viscosity at an elevated temperature provided by EM heating could enhance the solvent diffusivity, which improves the solvent diffusion and provides a better diluting effect. As a result, both EM heating and solvent dilution could enhance the oil recovery for this hybrid process. However, it is difficult to handle the cyclic phase change of formation fluids analytically. To simplify the calculation, the model assumes the vapor chamber is desiccated, and the connate water could be either vaporized or produced within the chamber. And the effect of temperature change on the reservoir pressure is not considered in this study.

**Figure 5-2** shows a schematic of the combined EM heating and solvent-assisted gravity drainage with a SAGD-like well configuration. The antenna used to generate EM flux is located in the upper well (injector) where the solvent injection is also implemented. The heated and diluted heavy oil flows out of the reservoir through the lower well (producer). The EM excited zone is a part of the reservoir that EM radiation dominates the heating process. Once outside the EM excited zone, EM heating is ineffective to heat up the reservoir; another heater or well pair can be implemented to recover oil outside this region. The chamber edge refers to the edge of the vapor chamber, while the drainage zone refers to the region between the chamber edge and the

boundaries of EM excited zone. In this study, the proposed model focuses on predicting the oil recovery within the EM excited zone.

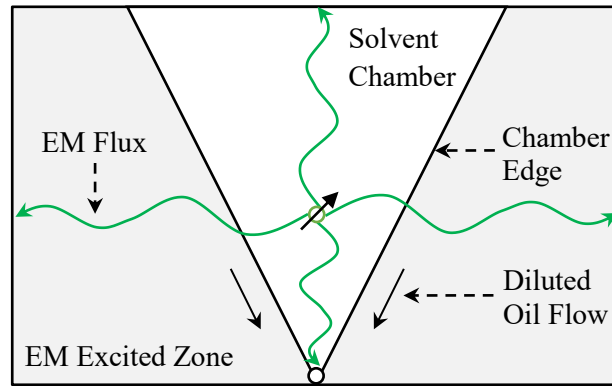


**Figure 5-2** Schematic of the combined EM heating and solvent-assisted gravity drainage with a SAGD-like well configuration.

### 5.3 Semi-Analytical Model

#### 5.3.1 Model Description

A semi-analytical model is proposed to predict the oil flow rate of the combined EM heating and solvent-assisted gravity drainage. The model consisted of three major parts: estimation of the temperature distribution of EM heating, calculation of the solvent distribution, and evaluation of the oil flow rate based on the temperature and solvent distributions. The major assumptions of this analytical model are as follows: (1) Reservoir is homogeneous and isotropic; (2) Heat loss to the overburden and underburden formations is neglected; (3) EM heating is dominated by radiation in the EM excited zone, and the effects of heat conduction and convection are neglected; (4) An inverted triangle is assumed as the shape of the vapor chamber, where the production well is located at the bottom vertex (Reis 1992), and the direction of oil flow is parallel to the chamber edge; (5) The pressure at the chamber edge is constant and equals to the injection pressure; (6) The inter-well connectivity has been established, and the solvent chamber has reached the top of the reservoir and spread sideways; (7) The evolution of the formed

chamber follows the manner of the angularly expanding chamber; (8) The solvent chamber is desiccated and the connate water inside the chamber is either vaporized or produced; (9) The effect of steam generated by the connate water on the partial pressure of injected solvent is neglected; (10) The effect of solvent convection is not considered; (11) Heat capacity and EM attenuation coefficient are assumed to be independent of temperature; (12) The effects of thermal expansion and latent heat are not considered.

### 5.3.2 Temperature Distribution by EM Heating

The model first calculates the temperature distribution of the radiation-dominated EM heating within the EM excited zone. The EM waves travel through the formation and attenuate as the reservoir materials absorb the EM energy. A simplified solution, employing Lambert's law to approximate the relationship between radiation and distance, is used to calculate the absorbed EM heating power distribution (Abernethy 1976; Fanchi 1993):

$$P(r) = P_0 e^{-\alpha(r-r_0)} \quad (5-2)$$

$$\alpha = 2\omega \left\{ \frac{\mu_0 \epsilon_0 \epsilon'}{2} \left[ \left( 1 + \left( \epsilon'' / \epsilon' \right)^2 \right)^{1/2} \right] - 1 \right\}^{1/2} \quad (5-3)$$

The penetration depth of EM radiation defines the distance at which the intensity of radiation falls to 1/e (about 37%) of its original level (Carrizales 2010b), given by:

$$\delta_p = \frac{1}{\alpha} \quad (5-4)$$

In Eqs. 5-2-4,  $r_0$  is the radius of wellbore in m (0.05 m),  $r$  is the distance to the radiation source (antenna) in m,  $\alpha$  is the attenuation coefficient in 1/m,  $\omega$  is the angular frequency,  $\mu_0$  is the permeability (electromagnetism) of free space ( $1.26 \times 10^{-6}$  H/m),  $\delta_p$  is the penetration depth in m,  $P_0$  is the incident power at the wellbore ( $r_0$ ) in W, and  $P(r)$  is the absorbed power at  $r$  in W. In the

following calculations made for different scenarios, the EM heating powers of 15 kW, 30 kW and 45 kW correspond to the different values of  $P_0$ .

The reservoir permittivity changes as oil is gradually produced in the hybrid process, which is crucial to the calculation of the distribution of the absorbed EM heating power. To capture this effect in the analytical model, we treat the permittivity differently for the reservoir inside and ahead of the vapor chamber. The complex refractive index method (Wharton et al. 1980), which estimates the reservoir's bulk permittivity with the volume fraction of each composition and its corresponding permittivity, is used to calculate the relative permittivity of the reservoir inside and ahead of the vapor chamber:

$$\sqrt{\varepsilon_r} = (1-\phi)\sqrt{\varepsilon_g} + \phi(1-S_w)\sqrt{\varepsilon_o} + \phi S_w\sqrt{\varepsilon_w} \quad (5-5a)$$

$$\sqrt{\varepsilon_c} = (1-\phi)\sqrt{\varepsilon_g} + \phi S_{or}\sqrt{\varepsilon_o} + \phi(1-S_{or})\sqrt{\varepsilon_v} \quad (5-5b)$$

where  $\varepsilon$  is the relative permittivity, subscript  $g$ ,  $w$ ,  $o$ , and  $v$  represent formation rock, water, heavy oil, and vapor phase,  $\varepsilon_r$  is the calculated relative permittivity of reservoir outside the vapor chamber,  $\varepsilon_c$  is the calculated relative permittivity of reservoir within the vapor chamber,  $\phi$  is the porosity,  $S_w$  is the water saturation, and  $S_{or}$  is the residual oil saturation. To simplify the calculation, the model neglects the effect of solvent dissolution in heavy oil on the bulk permittivity. This is reasonable for alkane-like solvents, propane and  $n$ -butane, because of the low concentrations of solvent, which only account for a small volume fraction of the oil sands. Meanwhile, the dielectric constants of solvent (1-3) are relatively small compared with water (about 80) (Younglove and Ely 1987; Gadani et al. 2012). The attenuation coefficients for the reservoir inside and outside the vapor chamber can thereby be obtained by substituting Eq. 5-5a

and Eq. 5-5b into Eq. 5-3, respectively. The distribution of the absorbed power (Eq. 5-2) with the consideration of the varying permittivity of reservoir becomes:

$$P(r) = \begin{cases} P_0 e^{-\alpha_c(r-r_0)}, & r < r_c \\ P_0 e^{-\alpha_c(r_c-r_0)-\alpha_r(r-r_c)}, & r \geq r_c \end{cases} \quad (5-6)$$

where  $\alpha_c$  is the attenuation coefficient for the reservoir inside the vapor chamber,  $\alpha_r$  is the attenuation coefficient for reservoir outside the vapor chamber, and  $r_c$  is the distance of chamber edge to the antenna.

According to the industrial, scientific, and medical (ISM) frequency allocation, the available frequencies for EM heating within the radio-frequency range are 6.78 MHz, 13.56 MHz, 27.12 MHz, and 40.68 MHz. For these available frequencies, the attenuation coefficient of the reservoir decreases with an increasing frequency, because the imaginary permittivity of salty water decreases with an increasing frequency (Gadani et al. 2012). Hence, a higher frequency could provide a deeper penetration but tend to lower the absorption of the EM energy. We perform example calculations of the proposed model at the frequency of 13.56 MHz, and we find that such frequency provides a sufficient temperature rise and appropriate penetration depth under the reservoir conditions given in **Table 5-1**. Table 5-1 shows the reservoir and fluid properties employed in the semi-analytical model, while **Table 5-2** shows the permittivity of each component and the calculated bulk permittivity at 13.56 MHz. Based on the obtained permittivity, the calculated attenuation coefficients for reservoir inside and ahead of the vapor chamber are 0.060 ( $\alpha_r$ ) and 0.001 ( $\alpha_c$ ), respectively. The geometry of the EM excited zone is set to 22×20 m for this given reservoir condition, applied frequency, and well configuration (Appendix 5A shows the detailed calculation of the range of the EM excited zone). The

boundaries of the EM excited zone are adiabatic and serve as no-flow boundaries for the proposed model.

**Table 5-1** Reservoir and fluid properties used in the semi-analytical model.

Property	Value	Unit
Reservoir height	20	m
Initial water saturation	0.20	Dimensionless
Initial oil saturation	0.80	Dimensionless
Residual oil saturation	0.35	Dimensionless
Initial oil viscosity	1024.36	kg/(m×s)
Initial solvent concentration in heavy oil	$1 \times 10^{-5}$	vol%
Absolute permeability	$5 \times 10^{-12}$	m <sup>2</sup>
Porosity	0.30	Dimensionless
Gravitational acceleration	9.8	m/s <sup>2</sup>
Initial reservoir temperature	10	°C
Volumetric reservoir heat capacity	2527	kJ/(m <sup>3</sup> ×°C)

**Table 5-2** Reservoir electrical properties at 13.56 MHz and room temperature.

Property	Real part of relative permittivity	Imaginary part of relative permittivity
Formation water	80.21 <sup>a</sup>	80.0000 <sup>a</sup>
Heavy oil	2.61 <sup>b</sup>	0.0216 <sup>b</sup>
Formation rock	1.96 <sup>c</sup>	0.0083 <sup>c</sup>
Vapor	1 <sup>d</sup>	0.0000 <sup>d</sup>
Reservoir outside the vapor chamber	3.63 <sup>e</sup>	0.4041 <sup>e</sup>
Reservoir inside the vapor chamber	1.81 <sup>f</sup>	0.0063 <sup>f</sup>

<sup>a</sup> Godard, A. and Rey-Bethbeder, F. (2011) and Gadani *et al.* (2012).  
<sup>b</sup> The properties are measured in this study with an open-ended coaxial probe at the room temperature; the oil sample has an API gravity of 8.6 °API.  
<sup>c</sup> The permittivity of silica sand is used to approximate the permittivity of formation rock; the properties are also measured in this study with an open-ended coaxial probe at the room temperature.  
<sup>d</sup> To simplify the calculation, the vapor phase is treated as a vacuum whose complex permittivity is approximated with  $1-0.0000j$ . Younglove and Ely (1987) measured the dielectric constants of the vapor propane and *n*-butane and found that they are slightly higher than 1.  
<sup>e</sup> Calculated by Eq. 5a.  
<sup>f</sup> Calculated by Eq. 5b.

The temperature distribution by EM heating is affected by radiation, convection, and conduction (Abernethy 1976):

$$\frac{\partial T}{\partial t} = \frac{1}{2\pi r h \rho_f C_{pt}} \left\{ \underbrace{\alpha P(r)}_{\text{Radiation}} + \underbrace{\rho_o q_o C_{po}}_{\text{Convection}} \left( \frac{\partial T}{\partial r} \right) + \underbrace{2\pi h k}_{\text{Conduction}} \frac{\partial}{\partial r} \left( r \frac{\partial T}{\partial r} \right) \right\} \quad (5-7)$$

where  $T$  is temperature,  $t$  is time,  $h$  is the height of payzone,  $\rho_i$  is the volumetric density of the reservoir,  $C_{pt}$  is the volumetric heat capacity of the reservoir,  $\rho_o$  is the density of heavy oil,  $q_o$  is the oil flow rate,  $C_{po}$  is the heat capacity of heavy oil, and  $k$  is the effective thermal conductivity of reservoir. We evaluated the heat fluxes of steady-state heat conduction and EM radiation in the EM excited zone; results show that, as for the applied EM heating powers, the heat flux of heat conduction is much smaller than the heat fluxes of EM radiation. Because the adequate EM heating power is provided to the targeted reservoir located within the penetration depth of the EM radiation, the conduction term is negligible compared with the radiation term. Meanwhile, neglecting the conduction and convection could help to greatly reduce the complexity of the semi-analytical model. The transient temperature profile approximated based on the radiation term and accumulation for a horizontal well is given by:

$$T(r,t) = \frac{\alpha(r)P(r)}{2\pi r l \rho_i C_{pt}} t + T_{res} \quad (5-8)$$

where  $T_{res}$  is the initial reservoir temperature and  $l$  is the lateral well length ( $l=1$  m). The calculated temperature profile of Eq. 5-8 follows a 1-D radial pattern, but the fluid flow is taking place in a 2-D domain. To obtain the 2-D temperature profile by EM heating, we first generate a 2-D Cartesian mesh to calculate the distances of each grid in the EM excited zone to the antenna. Then, the obtained temperature  $T(w, h)$  is transformed to the directions that are normal and parallel to the chamber edge  $T(\xi, \eta)$ . Next, we use the correlation, obtained based on the average temperature of  $T_\xi$ , to approximate the temperature distribution ahead of the chamber edge, given by:

$$T(\xi) = C_1 \exp(C_2 \xi) + C_3 \exp(C_4 \xi) \quad (5-9)$$

where  $\xi$  is the perpendicular distance to the chamber edge in m and  $C_1$ ,  $C_2$ ,  $C_3$ , and  $C_4$  are coefficients with their values being assessed during the calculation. The coefficients of determination ( $r^2$ ) yielded by Eq. 5-9 are about above 0.95. Appendix 5B shows the detailed approximation of the temperature distribution ahead of the chamber edge. Eventually, Eq. 5-9 can be used to approximate the temperature distribution by EM heating in the drainage zone.

### 5.3.3 Solvent Concentration Distribution Ahead of the Chamber Edge

In this section, the 1-D diffusion equation is used to calculate the solvent concentration ahead of the chamber edge, given by Das and Butler (1998):

$$C = C_r + (C_i - C_r)e^{-\frac{U\xi}{D_s}} \quad (5-10)$$

where  $C$  is the solvent concentration ahead of the chamber edge,  $C_r$  is the initial solvent concentration in heavy oil (a small value of  $1 \times 10^{-5}$  vol%, borrowed from Gupta and Gittins (2012), is used in this study),  $C_i$  is the solvent concentration at the chamber edge,  $D_s$  is the solvent diffusivity, and  $U$  is the chamber edge moving velocity ( $U_m$ , the chamber moving velocity at the top, is used to approximate  $U$ ).

The average temperature of the chamber edge is used to estimate the temperature-related properties, such as the vapor/liquid equilibrium ratio ( $K_{value}$ ), the viscosity of heavy oil/solvent mixture, and the solvent diffusivity. The  $K_{value}$  of solvent is evaluated by the following correlation (Reid et al. 1997; CMG 2013):

$$K_{value} = \left( \frac{k_{v1}}{P_{inj}} + k_{v2}P_{inj} + k_{v3} \right) e^{\frac{k_{v4}}{T_{ave} - k_{v5}}} \quad (5-11)$$

where  $K_{value}$  is the vapor-liquid equilibrium ratio,  $k_{v1}$ ,  $k_{v2}$ ,  $k_{v3}$ ,  $k_{v4}$ , and  $k_{v5}$  are coefficients listed in **Table 5-3**,  $P_{inj}$  is the solvent injection pressure, and  $T_{ave}$  is the average temperature of the

chamber edge. By neglecting the steam generated by the connate water and assuming the vapor fraction of solvent as 1, the volumetric solvent concentration in heavy oil can be calculated by:

$$C_i = \frac{x_s M_s}{\rho_s} \bigg/ \frac{x_s M_s}{\rho_s} + \frac{(1-x_s)M_o}{\rho_o} \quad (5-12)$$

$$x_s = 1/K_{value} \quad (5-13)$$

where  $x_s$  is the solvent mole fraction in the liquid phase,  $\rho_s$  is the density of the solvent,  $\rho_o$  is the density of the heavy oil,  $M_s$  is the molecular weight of solvent, and  $M_o$  is molecular weight of heavy oil. Table 5-3 summarizes the molecular weights of solvents and heavy oil as well as the correlations and coefficients for calculating the densities of solvents and heavy oil.

The solvent diffusivity is evaluated based on the heavy oil/solvent mixture's viscosity at the average chamber edge temperature provided by EM heating, given by:

$$D_s = L \times \mu_m (T_{ave})^M \quad (5-14)$$

where  $L$  and  $M$  are coefficients used to calculate the solvent diffusivity, and  $\mu_m$  is the viscosity of the diluted heavy oil. The mixture's viscosity is calculated by Lobe's (1973) mixing rule and mixture's density:

$$v_{mix} = f_s v_s \exp(f_o \alpha_o) + f_o v_o \exp(f_s \alpha_s) \quad (5-15a)$$

$$\alpha_o = 0.27 \ln\left(\frac{v_o}{v_s}\right) + \left[1.3 \ln\left(\frac{v_o}{v_s}\right)\right]^{0.5} \quad (5-15b)$$

$$\alpha_s = -1.7 \ln\left(\frac{v_o}{v_s}\right) \quad (5-15c)$$

$$\rho_{mix} = 1 \bigg/ \left(\frac{x_s}{\rho_s} + \frac{x_o}{\rho_o}\right) \quad (5-16)$$

where  $v$  is the kinematic viscosity,  $f$  is the volume fraction, and subscripts  $o$ ,  $s$ , and  $mix$  represent heavy oil, solvent, and mixture, respectively.

**Table 5-3** Summary of the correlations used in the calculations and the corresponding parameters appearing in the correlations.

Property	Equation/Correlation	Constants					
Heavy oil viscosity <sup>a</sup>	$\log_{10}[\log_{10}(\mu_o)] = A \log_{10}(T) + B$		<i>A</i>	<i>B</i>			
			-3.6337	9.6888			
Heavy oil density <sup>a</sup>	$\rho_o = C \times T + D$		<i>C</i>	<i>D</i>			
			-0.6551	1199.9			
Solvent viscosity <sup>b</sup>	$\log_{10}(\mu_s) = E + \frac{F}{T} + GT + HT^2$		<i>E</i>	<i>F</i>	$G \times 10^2$	$H \times 10^5$	
		Propane	-3.1759	297.12	0.95	-1.8781	
		<i>n</i> -Butane	-6.859	673.93	2.2	-3.0686	
		<i>n</i> -Hexane	-5.0715	805.87	1.23	-1.5	
Solvent density <sup>b</sup>	$\rho_s = 1000 \times 10^{-3} \times \left(\frac{T}{T_c}\right)^N$		<i>I</i>	<i>J</i>	<i>N</i>	<i>T<sub>c</sub></i>	
		Propane	0.2215	0.2774	0.287	369.82	
		<i>n</i> -Butane	0.2283	0.2724	0.2863	425.18	
		<i>n</i> -Hexane	0.2324	0.2654	0.2781	507.43	
<i>K-values</i> <sup>c</sup>	Eq. 5-11		$k_{v1} \times 10^5$	$k_{v2}$	$k_{v3}$	$k_{v4}$	$k_{v5}$
		Propane	9.0085	0	0	-1872.46	25.16
		<i>n</i> -Butane	8.5881	0	0	-2154.90	34.42
		<i>n</i> -Hexane	10.062	0	0	-2697.55	48.78
Molecular weight	-	Heavy oil <sup>a</sup>	635				
		Propane <sup>b</sup>	44.1				
		<i>n</i> -Butane <sup>b</sup>	58.1				
		<i>n</i> -Hexane <sup>b</sup>	86.2				
Solvent diffusivity	$D_s = L \times \mu_m(T_{ave})^M$		$L \times 10^{-9}$	<i>M</i>			
		Propane <sup>d</sup>	1.306	-0.46			
		<i>n</i> -Butane <sup>d</sup>	0.413	-0.46			
		<i>n</i> -Hexane <sup>e</sup>	9.91	-0.46			
Vapor solvent density	$\rho_{vs} = V_1 \times T_{c-ave}^{V_2}$		<i>V<sub>1</sub></i>	<i>V<sub>2</sub></i>			
		Propane (1500 kPa) <sup>f</sup>	204.68	-0.461			
		Propane (2500 kPa) <sup>f</sup>	797.02	-0.612			
		<i>n</i> -Butane (1500 kPa) <sup>f</sup>	663.14	-0.619			
		<i>n</i> -Butane (2500 kPa) <sup>f</sup>	4326.4	-0.856			
<p>Note: Properties in this table have the units of <i>T</i> in K, <math>\mu</math> in cP, and <math>\rho</math> in kg/m<sup>3</sup>.</p> <p><sup>a</sup> Hu et al. (2016a)</p> <p><sup>b</sup> Yaws (2003)</p> <p><sup>c</sup> Reid et al. (1997) and CMG (2013)</p> <p><sup>d</sup> Das and Butler (1996)</p> <p><sup>e</sup> Faradonbeh et al. (2017)</p> <p><sup>f</sup> Correlations obtained based on the regression of the vapor density data calculated by WINPROP CMG 2013)</p>							

### 5.3.4 Oil Flow Rate

In this hybrid process, both EM heating and solvent dilution could reduce the viscosity of heavy oil, thus leading to an enhanced oil flow rate. The fluid flow is assumed to be a single-phase flow, and the effect of capillary pressure is neglected. Darcy's law for gravity drainage and

material balance are used to calculate the oil flow rate. Darcy's law gives (Gupta and Gittins 2012):

$$q_o = Kg \sin \theta \int (1-C) \left( \frac{1}{\nu} - \frac{1}{\nu_r} \right) d\xi \quad (5-17a)$$

$$I_o = \int (1-C) \left( \frac{1}{\nu} - \frac{1}{\nu_r} \right) d\xi \quad (5-17b)$$

where  $q_o$  is the oil flow rate,  $K$  is the absolute permeability,  $g$  is the gravitational acceleration ( $9.8 \text{ m/s}^2$ ),  $\theta$  is the angle between the chamber edge and the horizontal axis,  $C$  is the solvent concentration,  $\nu$  is the kinematic viscosity of heavy oil (which is a function of both solvent concentration and temperature distributions) as evaluated by Lobe's mixing rule,  $\nu_r$  is the kinematic viscosity of the heavy oil at the initial reservoir condition, and  $I_o$  is the oil flow rate integral integrating over the entire EM excited zone. Considering the geometry relationship and material balance, the oil flow rates at the chamber spreading and falling stages can be calculated by:

$$q_{os} = \sqrt{\frac{1}{2} Kg \phi \Delta S_o U_m I_1} \quad (5-18a)$$

$$q_{of} = \sqrt{\frac{(Kg I_2)^2 \pm \sqrt{(Kg I_2)^4 - [Kg \phi \Delta S_o U_m I_3]^2}}{2}} \quad (5-18b)$$

where

$$I_1 = \int_0^{W \sin \theta} H (1-C) \left( \frac{1}{\nu} - \frac{1}{\nu_R} \right) d\xi - \int_{(W-w_i) \sin \theta}^{W \sin \theta} \left( \frac{\xi - (W-w_i) \sin \theta}{\cos \theta} \right) (1-C) \left( \frac{1}{\nu} - \frac{1}{\nu_R} \right) d\xi \quad (5-19a)$$

$$I_2 = \int_0^{W \sin \theta} (1-C) \left( \frac{1}{\nu} - \frac{1}{\nu_R} \right) d\xi \quad (5-19b)$$

$$I_3 = \int_0^{W \sin \theta} \left( W - \frac{\xi}{\sin \theta} \right) (1 - C) \left( \frac{1}{v} - \frac{1}{v_R} \right) d\xi \quad (5-19c)$$

where  $q_{os}$  is the oil flow rate of one-half of the reservoir per unit well length at the chamber spreading stage,  $q_{of}$  is the oil flow rate of one-half of the reservoir per unit well length at the chamber falling stage,  $\Delta S_o$  is the difference between the original and the residual oil saturation,  $W$  is the width of the EM excited zone,  $w_i$  is the chamber edge location at the top,  $I_1$ ,  $I_2$ , and  $I_3$  are integrals used in the calculation of oil flow rate. Appendix 5C describes the detailed calculation of the oil flow integral as well as the mathematical derivations of Eq. 5-18. The mass flow rate of the heavy oil is calculated by the multiplication of calculated oil flow rate and heavy oil density at the initial reservoir conditions, while the mass flow rate of the solvent is calculated with the consideration of the varying density of solvent in the drainage zone (Gupta and Gittins 2012):

$$m_o = q_o \times \rho_o \quad (5-20a)$$

$$m_s = Kg \sin \theta \int \rho_s C \left( \frac{1}{v} - \frac{1}{v_r} \right) d\xi \quad (5-20b)$$

where  $m_o$  is the calculated oil mass flow rate, and  $m_s$  is the calculated solvent mass flow rate. The solvent distribution  $C$  in Eq. 5-20 is evaluated with the converged  $U$ .

### 5.3.4 Calculation Procedure

In this hybrid process, the EM heating provides a transient temperature profile increasing with time. Hence, the oil flow rate is also time-dependent and is calculated using the finite time step method and the oil flow is assumed to be constant within each time step. **Figure 5-3** shows the flowchart for calculating the oil flow rate of the proposed semi-analytical model. The following steps are used in the calculation:

1. For given reservoir conditions and applied EM heating configuration, the model first calculates the range of EM excited zone ( $W$ ,  $H$ ) using Eqs. 5-A1 and 5-A2. Then, the model evaluates the temperature distribution within the EM excited zone by Eqs. 5-6 and 5-7. Next, the model transforms the temperature distribution to the directions that are normal and parallel to the chamber edge. Last, the approximated temperature distribution ahead of the chamber edge ( $T(\xi)$ ) is obtained by using Eq. 5-9;
2. The solvent distribution ( $C$ ) is calculated by solving Eq. 5-10 based on the chamber edge conditions ( $K_{\text{value}}$ ,  $C_i$ ,  $D_s$ , and  $\mu_m$ ) that are estimated using the average chamber edge temperature ( $T_{\text{ave}}$ ). These calculations are carried out with Eqs. 5-11—5-16 and 5B1;
3. The oil flow rate is evaluated based on the obtained temperature and solvent distributions. The chamber edge's moving velocity affects the solvent distribution, which in turn has an impact on the kinematic viscosity of heavy oil and, consequently, the oil flow rate. Hence, the chamber edge's moving velocity is solved iteratively by satisfying both Eq. 5-17 and Eq. 5-18, and the corresponding oil flow rate is calculated with the converged chamber edge moving velocity;
4. The chamber edge location is renewed at each time step. The effective attenuation coefficients ( $\alpha_r$  and  $\alpha_c$ ) of the reservoir are also updated based on the chamber edge location to calculate the absorbed power distribution by Eq. 5-6. Then the time step is updated to continue the calculation in the next time step;
5. Steps 1-4 are repeated until the production enters the chamber falling stage. If the production enters the chamber falling stage, the calculations are switched correspondingly by changing the equations and conditions to those at the chamber falling stage. After switching, the new steps 1-4 are repeated until the end of the production.

This procedure is repeated to obtain the oil flow rate at each time step until the entire EM excited zone under consideration has been swept. The time step used in the calculation is 1 day. Table 5-3 summarizes the correlations and the parameters involved in the calculations.

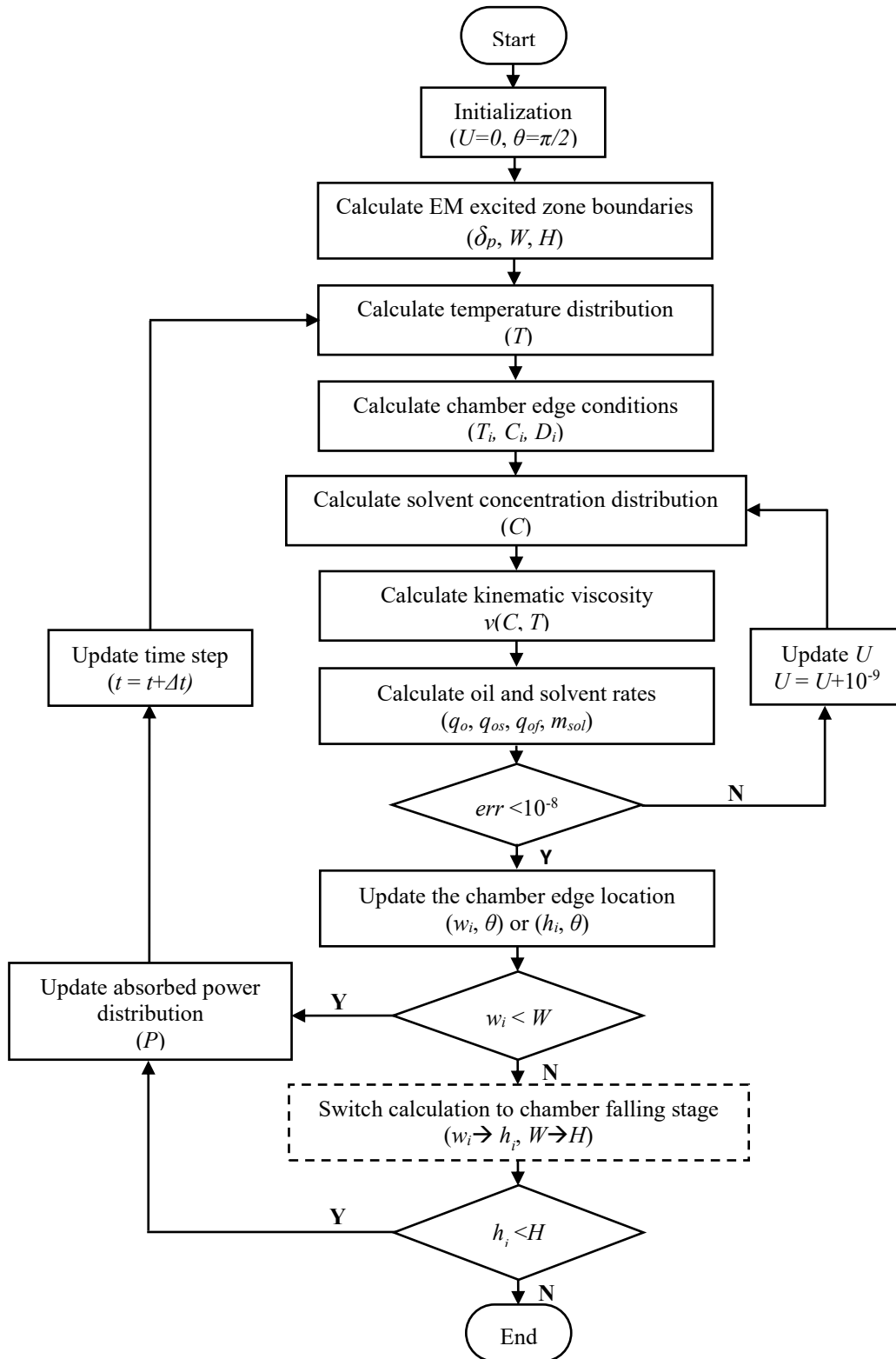


**Figure 5-3** Flow chart of the calculation procedure for the proposed semi-analytical model.

#### 5.4 Model Validation

We use the experimental results of the combined EM heating and *n*-hexane-assisted gravity drainage conducted by Hu et al. (2016a) to validate the proposed semi-analytical model. A microwave oven, generating the microwaves to heat the sandpack, was used in the experiments. **Figure 5-4** shows the schematic of the experimental setup; the solvent is injected at the top of the sandpack, while oil is produced at the bottomed. The temperature probe is installed at the center of the sandpack, 2.5 cm away from the top of the sandpack. **Table 5-4** lists the detailed geometry of the sandpack, properties of experimental materials, and experimental conditions. In the microwave oven heating, EM flux tends to be reflected by the oven walls, continuously heating the sandpack. The reflection of the EM flux inside the oven can form a hot spot in the middle of the sample where the highest temperature is observed, and the temperature of the sample decreases from the center to the peripheries (Hong et al. 2016). Due to this feature of the microwave oven heating, the formed hotspot can be treated as an imaginary antenna. We also assume that the injected solvent first spreads sideways and then spread downwards. Based on the above consideration, the proposed model can be applied to predict the flow rates of diluted oil during the sandpack experiment.

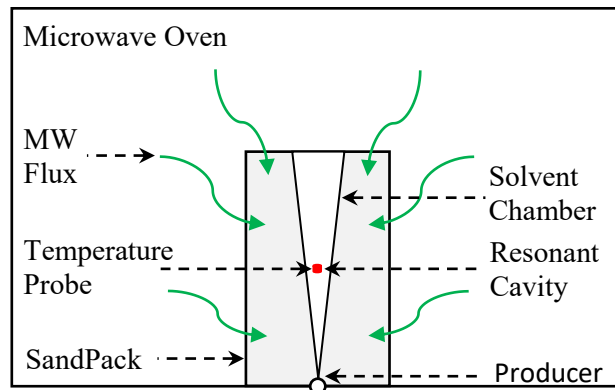


**Figure 5-4** Schematic of the experimental setup used for conducting the combined EM heating and solvent assisted gravity drainage for heavy oil recovery (Adapted from Hu *et al.* 2016a).

**Table 5-4** Detailed properties of the sandpack used in the experimental tests (Hu et al. 2016a).

Property	Value	Unit
Height of the sandpack	5	cm
I.D. of the sandpack	4	cm
Water saturation	0	Dimensionless
Oil saturation	1	Dimensionless
Residual oil saturation	0.4285	Dimensionless
Average porosity	0.32	Dimensionless
Experimental initial temperature	25.00	°C
Experimental pressure	101.33	kPa
Note: These properties are taken from Hu <i>et al.</i> (2016a).		

Another distinct feature of the experiments is the pulse-heating of the microwave oven, which cyclically heats the sandpack. We used this feature to control the temperature of sandpack within the measurement limit of the temperature probe. But it is difficult to capture this feature by the proposed model; alternatively, we feed the measured temperatures of the sandpack, as shown in **Figure 5-5**, to the model to calculate the oil flow rates. We then tune the permeability of sandpack to match the experimental data. The experiment recorded the mass flow rate of the solvent/heavy-oil mixture; accordingly, we use the proposed analytical model to calculate the mass flow rate of diluted heavy oil:

$$m_{mix} = m_o + m_s \quad (5-21)$$

where  $m_{mix}$  is the calculated diluted oil mass flow rate,  $m_o$  is the calculated oil mass flow rate at room temperature, and  $m_s$  is the solvent flow rate calculated by Eq. 5-20b.

At the initial stage of the experiment, the sandpack remains at a relatively low temperature that is below the saturation temperature of the injected solvent. The model is not applicable to this stage and tends to overestimate the solvent flow rate; hence, we apply the model to predict the mixture's mass flow rate when the temperature is above the saturation temperature of the injected solvent. The sandpack is cylindrical in the experiment, while the geometry of sandpack is approximated to be rectangular in the calculation. The mass flow rate integral of diluted oil,

calculated by Eq. 5-21, is then upscaled by multiplying a volume factor that yields the same volume as the cylindrical sandpack. **Figure 5-6** shows the measured diluted-oil mass flow rates and the predicted ones with the proposed semi-analytical model. Results show that the sandpack with a permeability of 8 Darcy yields the least deviation between the predicted and measured mass flow rates; the yielded  $r^2$  between the calculated and measured mass flow rates is 0.71.

As shown in Figure 5-6, the predicted mass flow rate curve slightly shifts to the left of the measured rates because the model neglects the pre-heating stage. The measured flow rates exhibit large fluctuations, while the predicted flow rates are smoother. In general, the predicted rates share the same trend as the measured ones. Our model predicts the solvent's weight fraction in the recovered mixture to be 2.23 wt% which is almost identical to the measured value of 2.3 wt% (Hu et al. 2016a).

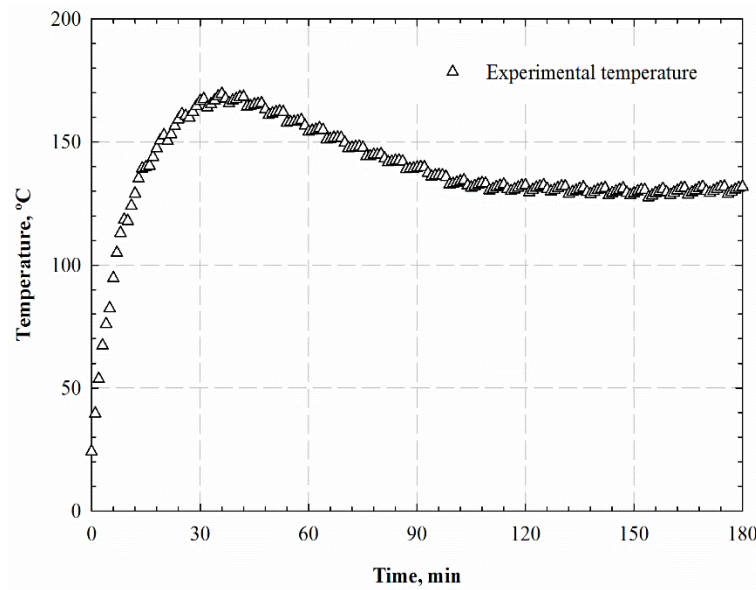


**Figure 5-5** Experimental temperature data of the sandpack of the combined EM heating and *n*-hexane-assisted gravity drainage (Adapted from Hu et al. 2016a).

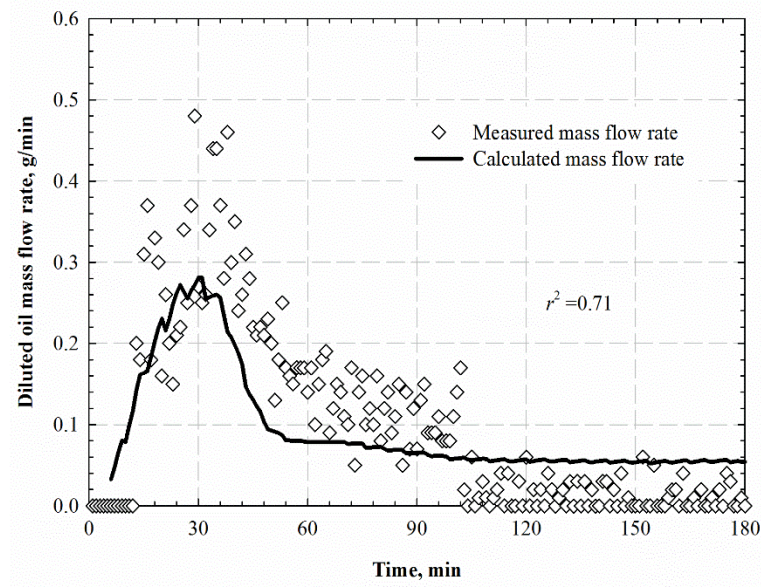


**Figure 5-6** Comparison of the measured diluted-oil mass flow rates and the predicted ones by the proposed semi-analytical model.

## 5.5 Results and Discussion

Applying the abovementioned semi-analytical model, we investigate the effects of important influential factors on the performance of the combined EM heating and solvent-assisted gravity drainage. Different EM heating powers (15 kW, 30 kW, and 45 kW), solvent types (propane and *n*-butane), solvent injection pressures (1500 kPa and 2500 kPa), and initial reservoir temperatures (10 °C, 15 °C, and 20 °C) are examined via case studies. Table 5-1 shows the reservoir and fluid properties used in the semi-analytical model.

### 5.5.1 Residual Oil Saturations

Due to the lack of experimental data measured for the residual oil saturations generated by this hybrid process, we use the Cardwell and Parsons (1949) equation to estimate the residual oil saturation:

$$\overline{S_{or}} = \frac{(b-1)}{b} \left( \frac{v_{ave} \phi H}{bKgt} \right)^{1/(b-1)} \quad (5-22)$$

where  $\overline{S_{or}}$  is the average residual oil saturation,  $H$  is drainage height,  $K$  is permeability,  $\phi$  is porosity,  $b$  (equals to 3.5) is the exponent in Cardwell and Parsons equation for relative permeability,  $V_{ave}$  is the average kinematic viscosity of the diluted oil, and  $t$  is the recovery time. The average temperatures of the EM excited zone at the end of production are used to evaluate the average kinematic viscosity of the diluted oil, and the solvent dissolution at this temperature and solvent injection pressure is also considered in the calculation. The duration spent on sweeping the whole EM excited zone is used as the recovery time in Eq. 5-22. A lower residual oil saturation, leading more oil to be produced, corresponds to a longer recovery time. The recovery time, which is equal to the heating time, affects the average reservoir temperature and thus affects the residual oil saturation. Hence, we first make a series of guesses for the residual oil saturation that appears in Eq. 5-18. For each guessed value, the analytical model is applied once to obtain the necessary information that can be input into Eq. 5-22. A new residual oil saturation is then calculated with Eq. 5-22. Finally, we select the residual oil saturation that gives an absolute error of  $<0.01$  between the guessed residual oil saturations and the updated one.

**Table 5-5** summarizes the key parameters used in Eq. 5-22 and the calculated residual oil saturations for different cases. Results show that the residual oil saturation increases with an increasing EM heating power, while decreases with an increasing solvent injection pressure. As for the solvent, a higher solvent injection pressure boosts the dissolution of solvent, further reducing the kinematic viscosity of the heavy oil and leading to a lower residual oil saturation. Likewise, a heavier solvent exhibits a higher concentration in heavy oil, which results in a decreased residual oil saturation. This is consistent with our previous experimental results that a heavier solvent provides a higher recovery factor (Hu et al. 2017). The residual oil saturations yielded by the different initial reservoir temperature are also listed in Table 5-5. A higher initial

reservoir temperature shortens the recovery/heating time, which lowers the reservoir temperature and leads to an increased residual oil saturation. Substituting the obtained residual oil saturations into the analytical model, the oil rates and cumulative oil productions for all the tested cases are calculated and summarized in **Figure 5-7**. The calculated oil-rate results correspond to one-half of the EM excited zone per unit well length.

**Table 5-5** Calculated residual oil saturations for different production scenarios. Eq. 5-22 is used to perform these calculations.

Heating Power (kW)	Solvent type	Initial reservoir temperature (°C)	Solvent injection pressure (kPa)	Average reservoir temperature (°C)	Solvent concentration in heavy oil (vol%)	Recovery Time (Day)	Kinematic Viscosity ( $\times 10^{-5} \text{m}^2/\text{s}$ )	Calculated $S_{or}$ (Dimensionless)
15	Propane	10	1500	116.849	0.104	1562	2.502	0.095
		10	2500	117.472	0.205	1557	0.850	0.062
	<i>n</i> -Butane	10	1500	118.332	0.352	1572	0.123	0.028
		10	2500			*		
30	Propane	10	1500	134.201	0.078	914	1.969	0.107
		10	2500	134.933	0.146	918	0.998	0.082
	<i>n</i> -Butane	10	1500	135.704	0.201	922	0.379	0.055
		10	2500			*		
45	Propane	10	1500	145.248	0.066	658	1.655	0.114
		15		146.454	0.064	660	1.642	0.114
		20		141.156	0.070	516	1.777	0.129
	<i>n</i> -Butane	10	2500	145.913	0.121	661	0.981	0.092
		10	1500	146.756	0.162	664	0.463	0.068
		10	2500	148.171	0.415	668	0.049	0.028

\*Note: The solvent at these EM heating powers and solvent injection pressure is in the liquid phase which is not applicable to the model.

### 5.5.2 Effect of EM Heating Power

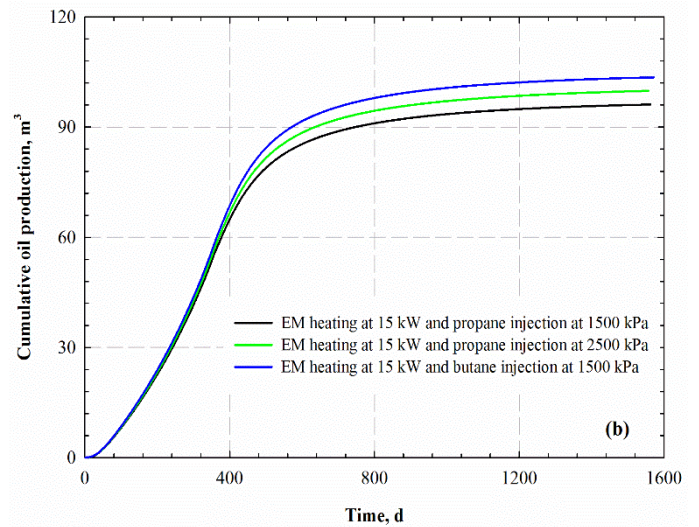
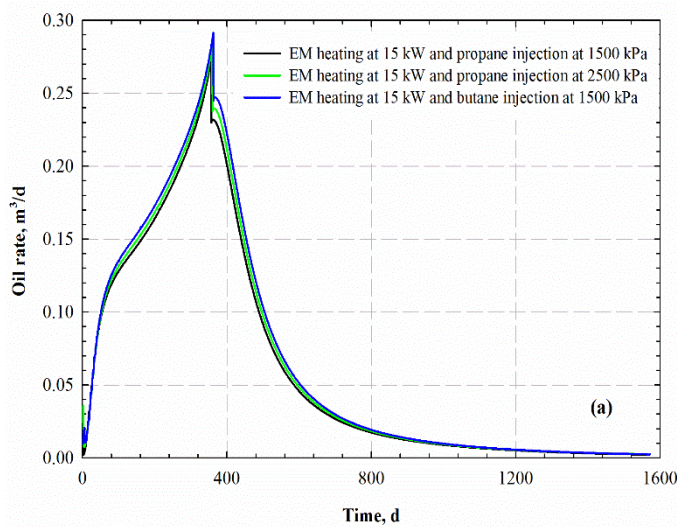
**Figure 5-8** shows the calculated oil rates, average chamber edge temperature, solvent concentration at the chamber edge, and solvent diffusion length ( $D/U$ ) versus time; in these calculations, propane is injected at 1500 kPa, and EM heating powers of 15 kW, 30 kW, and 45 kW are simulated. These example calculations are made to illustrate the effect of EM heating power on the recovery performance of the hybrid process. Results show that the reservoir temperature rises to a higher peak value with a faster speed as the EM heating power increases.

Consequently, a higher EM heating power could enhance oil flow rate and accelerate the recovery process, shown in **Figure 5-8a**. In comparison, the reduced reservoir temperature at a lower heating power prolongs the recovery time, which results in a lower residual oil saturation and higher cumulative oil production (See Table 5-5). Similar observations have been made for other cases using different solvents and injection pressures.

The oil production process can be divided into two stages: the chamber spreading and falling stages. At the chamber spreading stage, the reservoir temperature continuously increases as the EM heating goes on, leading to an increased oil flow rate. As the chamber propagates, the drainage zone moves away from the antenna, resulting in a reduced chamber edge temperature as demonstrated in **Figure 5-8b**. But the temperature in the entire drainage zone still increases; hence, the oil production continues to ramp up. As the production enters the chamber falling stage, the oil flow rate constantly declines although the temperature of the drainage zone increases continuously. This is because of the reduced drainage height and the less gravity drive caused by the decreased slanted angle. Some discontinuities (i.e., the sudden jumps in the oil rate curves as marked by the green circles) exist in the curves because of the calculation errors that are caused when the model switches from the chamber spreading stage to the chamber falling stage.

As for the same solvent and injection pressure, the oil recovery of the hybrid cases is a balanced result between EM heating and solvent dilution. A higher EM heating power provides a higher temperature, which in turn reduces the solvent concentration in heavy oil, as illustrated in **Figure 5-8c**. **Figure 5-8d** shows the variation of the solvent diffusion length versus time; it can be seen that the solvent diffusion length first starts with a high value, then decreases over time and finally picks up again in the later stage. The higher solvent concentration and lower chamber moving

velocity attributed to a higher solvent diffusion length at the early and late stage, respectively. Hence, one can infer that the effect of solvent dilution on the oil recovery is more notable in the early stage when the reservoir temperature is relatively low, as well as in the late stage when the drainage zone moves farther away from the antenna. The solvent diffusion length, with a maximum value of about 0.04 m, is much shorter than the EM excited zone of about 22 m. Although the solvent penetration into the drainage zone is shallow, it is very effective in enhancing the heavy oil mobility within the penetration length. In addition, the solvent can provide other benefits including replenishing the reservoir pressure and further reducing the residual oil saturation.



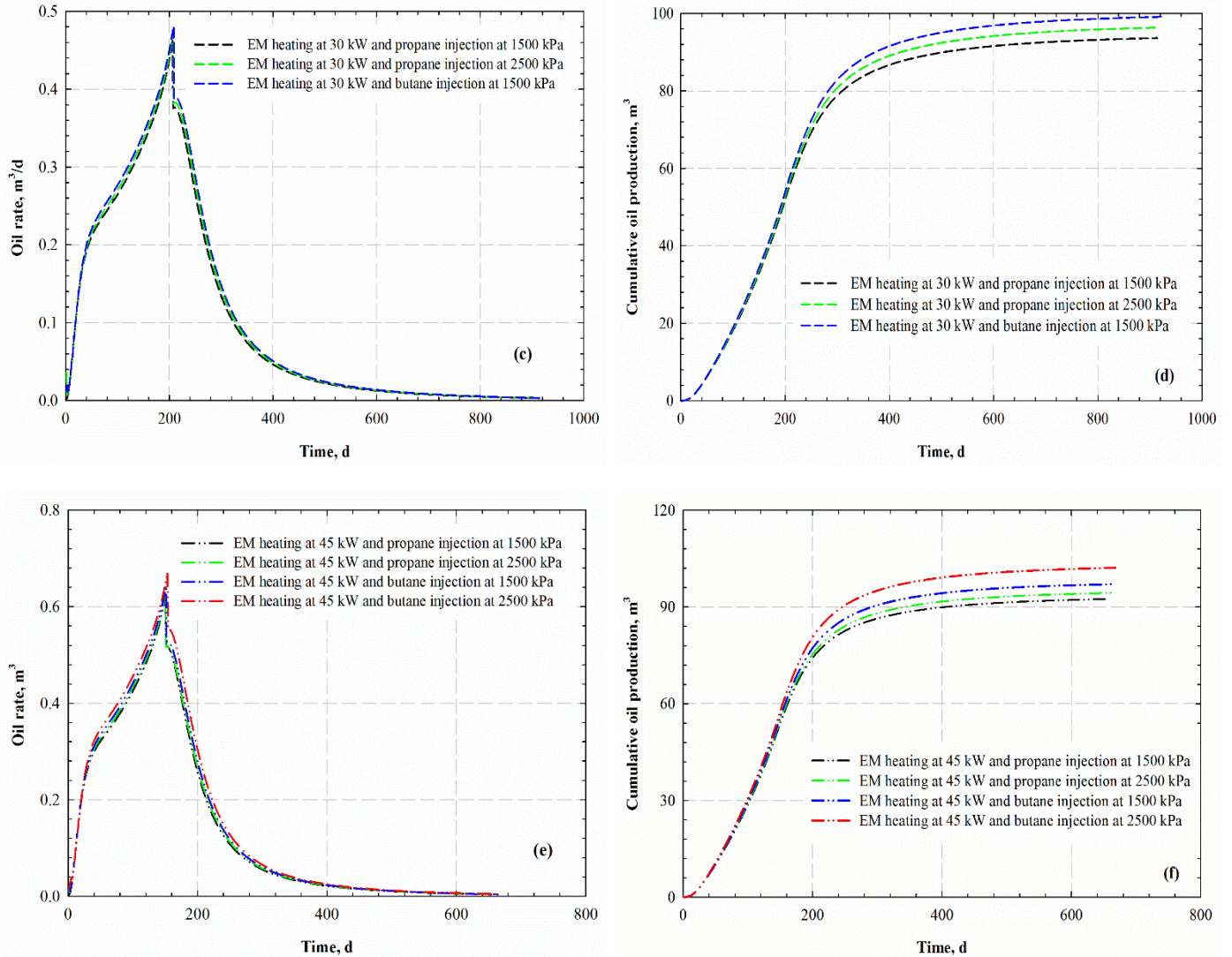


**Figure 5-7** Summary of the calculated oil rates (subplots a, c, and e), and cumulative oil productions (subplots b, d, and f) versus time for all the production scenarios.

### 5.5.3 Effect of Solvent Type and Solvent Injection Pressure

**Figure 5-9** illustrates the calculated average chamber edge temperature, solvent concentration at the chamber edge, solvent diffusion length ( $D/U$ ), solvent diffusivity, and solvent mass rate of the tested cases where EM heating is conducted at 45 kW and solvent (propane or *n*-butane) is injected at two pressures of 1500 kPa and 2500 kPa. In the recovery process, the average temperature of the chamber edge increase as EM heating continues while reduces as the chamber edge moves away from the antenna. Due to this feature of EM heating, the temperature profiles

exhibit two cycles of rising and dropping. The solvent concentration in heavy oil and solvent diffusivity are a function of the average temperature of the chamber edge, which exhibits curvature changes because of the temperature variations. **Figure 5-9a** plots the solvent concentration in heavy oil at chamber edges as a function of time. At the same EM heating power (i.e., 45 kW), the higher solvent injection pressure and heavier solvent could increase the solvent concentrations in heavy oil, which enhances the solvent diffusion as seen in **Figure 5-9b**. Although propane has a higher diffusivity in heavy oil indicated by Figure 9b, the diluting effect of *n*-butane is superior to propane, leading to a reduced residual oil saturation and an enhanced oil recovery. This result echoes well with our experimental observations heavier solvent leads to a better recovery performance for this hybrid method (Hu et al. 2017). **Figure 5-9c** shows that a higher solvent injection pressure and heavier solvent could also entail a larger solvent usage, particularly at the chamber falling stage when the effect of solvent diffusion is more prominent. But, the solvent rate is several orders of magnitude smaller than the oil rate, suggesting that only a limited amount of solvent is required in this hybrid method. The detailed solvent-oil ratios of different cases will be evaluated in the economic analysis section. **Figure 5-9d** shows an interesting phenomenon wherein the production scheme yielding a faster oil rate also exhibits a higher temperature of the drainage zone. At a given time, the scenario with a higher oil rate could create a larger vapor chamber. This leads to a less attenuation of the EM energy as the EM wave travels through the vapor chamber, eventually results in a higher temperature in the drainage zone.

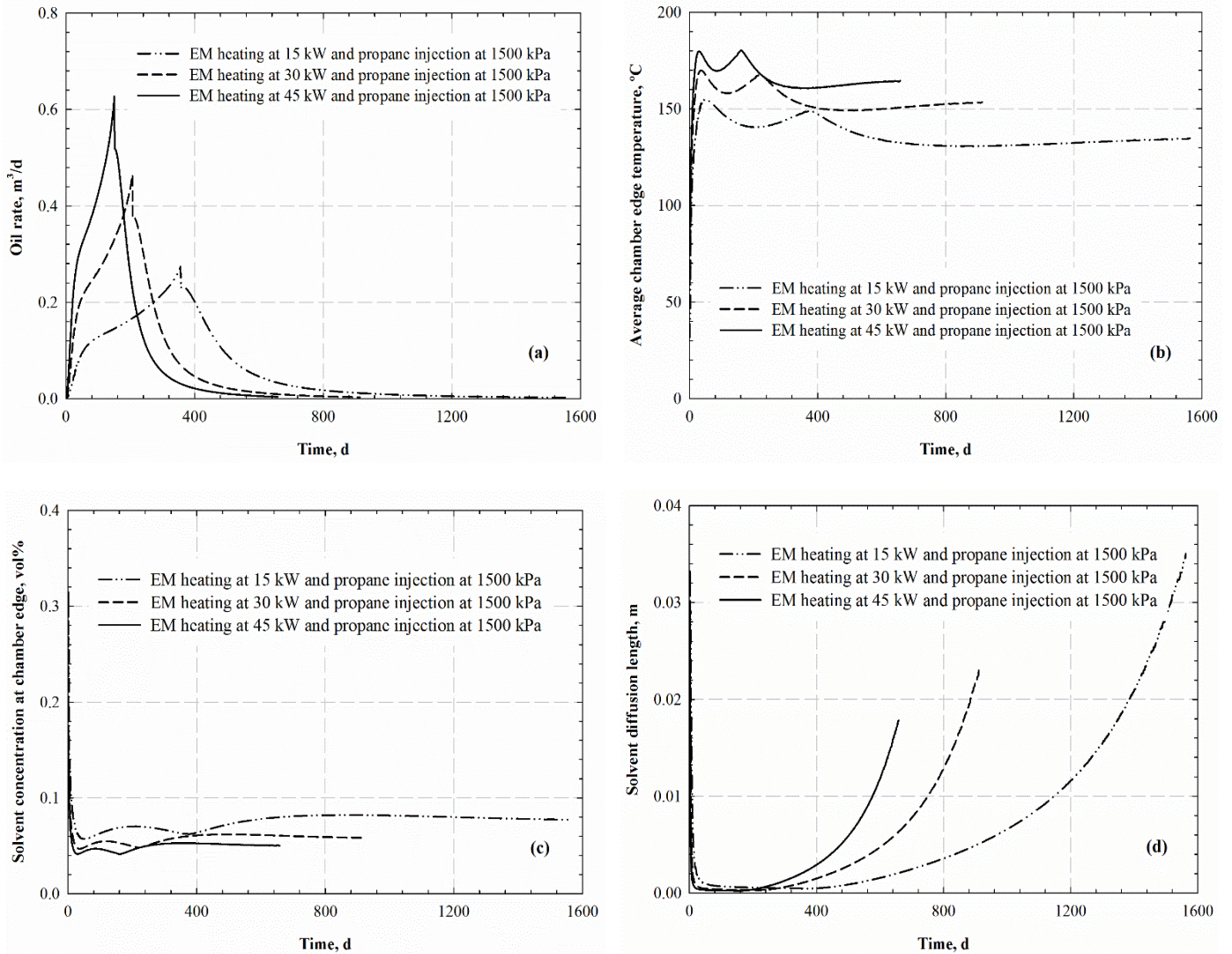


**Figure 5-8** Calculated (a) oil rate, (b) average chamber edge temperature, (c) solvent concentration at the chamber edge, and (d) solvent diffusion length versus time. Propane is injected at 1500 kPa, and EM heating is implemented with power levels of 15 kW, 30 kW, and 45 kW. The green circles in Figure 8a indicate what happens in the oil rates during the transition from the chamber spreading stage to the chamber falling stage.

### 5.5.4 Effect of Initial Reservoir Temperature

**Figure 5-10** shows the oil rates and cumulative oil productions obtained from different initial reservoir temperatures (10 °C, 15 °C, and 20 °C) which are in the typical initial reservoir temperature range of Athabasca oil sands (Rottenfusser and Ranger 2004). The propane is injected at 1500 kPa and EM heating is conducted at 45 kW to exemplify the calculation. Figure

10a shows the oil rates which slightly shift to the left as the initial reservoir temperature increases. Figure 10b compares the cumulative oil productions, which exhibit marginal variations when the initial reservoir temperature changes from 10 °C to 15 °C; however, the cumulative oil production slightly reduces when the initial reservoir temperature reaches 20 °C due to a shortened recovery time. The effect of initial reservoir temperature is similar to that of the EM heating power; a higher initial reservoir temperature can accelerate the oil production due to a lowered *in-situ* oil viscosity, but the cumulative oil production will be slightly reduced due to a shortened recovery time. Overall, the initial reservoir temperature only slightly affects the oil recovery of this hybrid process, which is a less dominant factor compared with EM heating and solvent injection.

### 5.5.5 Chamber Edge Location and Average Oil Flow Rate

The propagation of the chamber edge as a function of time can vividly indicate how the reservoir has been gradually produced by this hybrid recovery method. **Figure 5-11** illustrates the calculated chamber edge positions as a function of time for the case of EM heating at 15 kW and butane injection at 1500 kPa. The height of the EM excited zone ( $H$ ) is 20 m and the width of the drainage zone ( $W$ ) is 22m. The results shown in Figure 11 are normalized by dividing  $h$  by  $H$  and dividing  $w$  by  $W$ . The solvent chamber first spreads sideways and then falls downwards as the oil production goes on. Once entering the chamber-falling stage, the propagation rate of the chamber edge slows down. **Figure 5-12** further compares the average flow rates provided by different production schemes. A lateral well length of 500 m, the reservoir properties in Table 5-1 and the residual oil saturations in Table 5-5 are used to upscale the calculated results. The results show that a higher heating power, a heavier solvent, and a higher injection pressure could enhance the oil flow rates.

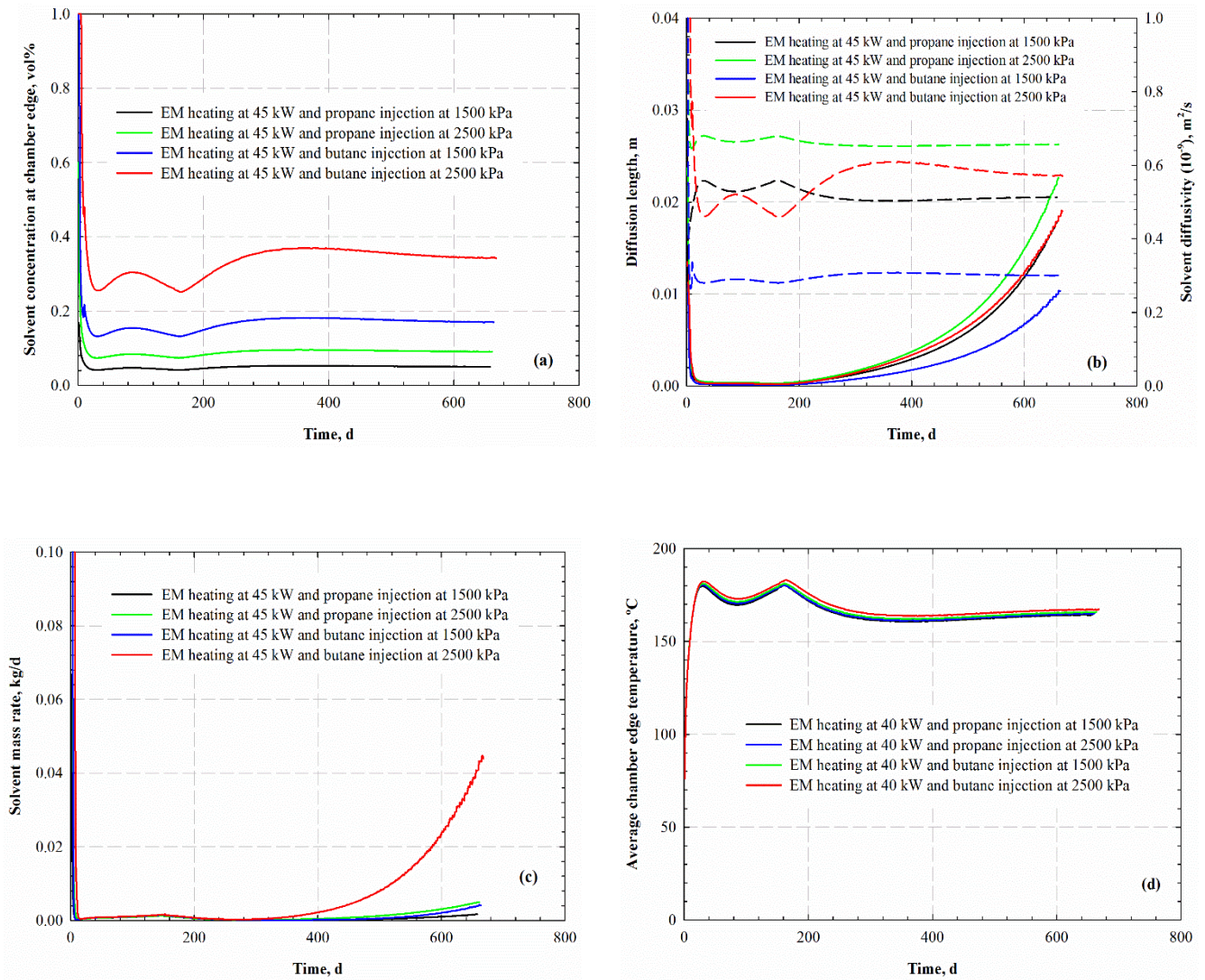


**Figure 5-9** Calculated (a) solvent concentration at the chamber edge, (b) solvent diffusion length and diffusivity, (c) solvent rate, and (d) average chamber edge temperature versus time for different cases. Propane and n-butane are injected at 1500 kPa and 2500 kPa, and EM heating is conducted at 45 kW. In Figure 9b, the solid lines represent the solvent diffusion length, while the dash lines represent the solvent diffusivity.

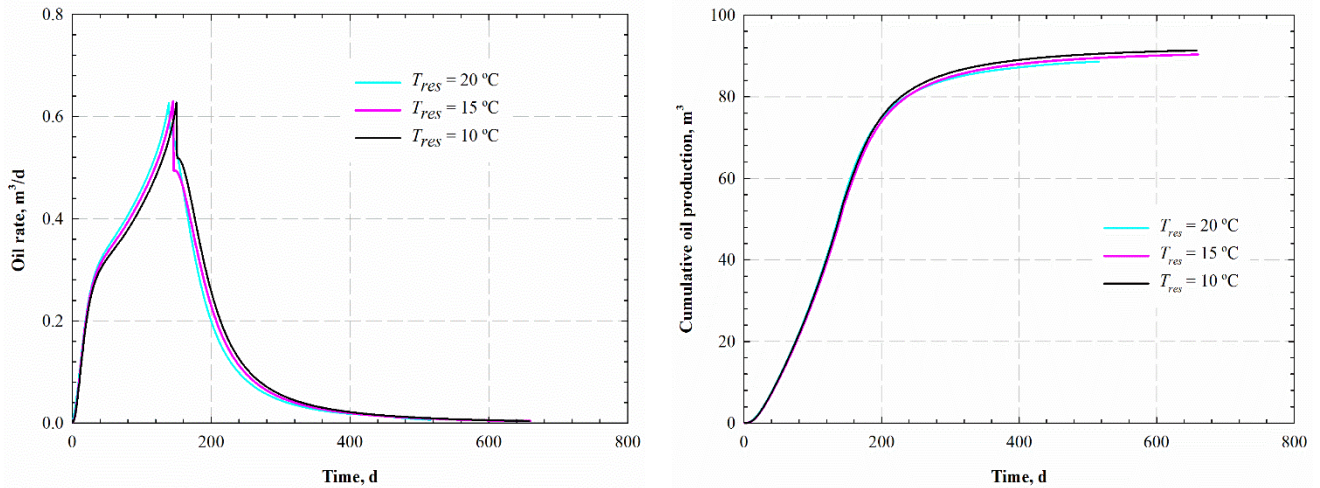


**Figure 5-10** Calculated (a) oil rates and (b) cumulative oil production versus time for different initial reservoir temperatures. Propane is injected at 1500 kPa and EM heating is conducted at 45 kW.  $T_{res}$  is the initial reservoir temperature.

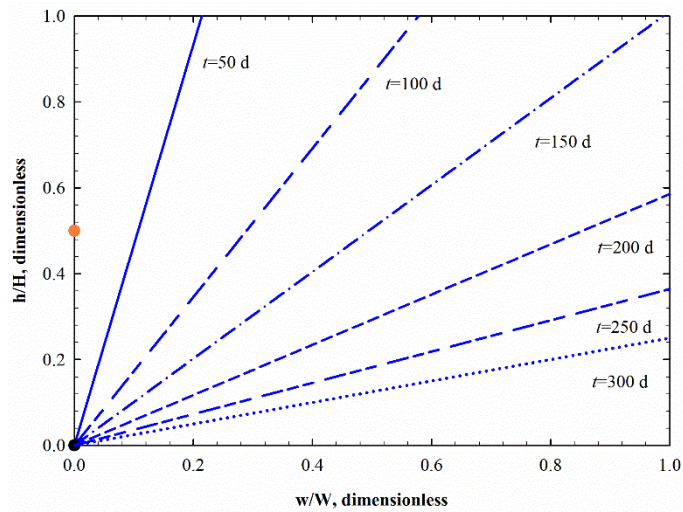


**Figure 5-11** Illustration of the evolution of the chamber-edge locations of the case of EM heating at 45 kW and butane injection at 1500 kPa. In this plot, the orange point represents the injector/heater, while the black point represents the producer.

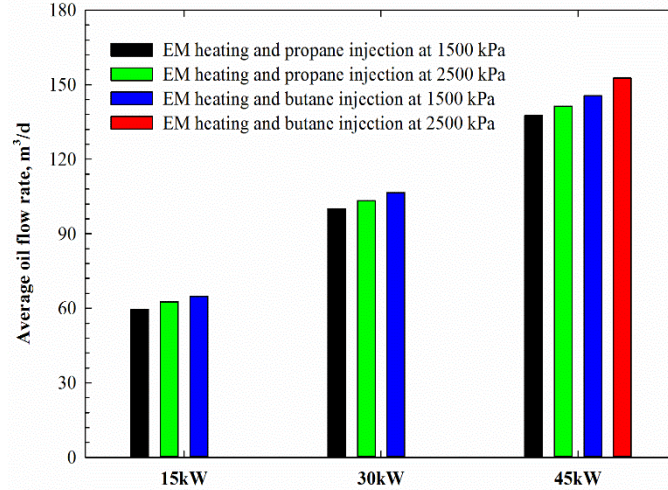


**Figure 5-12** Comparison of average oil flow rates provided by different production scenarios.

### 5.6 Economic Analysis

Operational strategies with a higher heating power, the injection of a heavier solvent and a higher injection pressure can provide an enhanced production rate, but a higher cost might also ensue.

We calculate the net present value (*NPV*) in an attempt to demonstrate how to use the proposed semi-analytical model to evaluate the economic feasibility of this hybrid EM heating and solvent injection method. The main costs associated with this hybrid process are comprised of the electricity fee and solvent retention, while the major revenue is contributed by the oil production.

The largest capital investment is due to the purchasing, installation, and maintenance of the EM heating device in the horizontal well, which is assumed to \$10,000/m in this study. We also assume that the antenna is fully functioning during the entire simulation period. **Table 5-6** shows the detailed prices used in the economic analysis. The *NPV* is calculated by:

$$NPV = \sum NCF - C_a \quad (5-23)$$

$$NCF = (REV - OPEX)/(1+i)^m \quad (5-24a)$$

$$REV = Q_m \times PX_o \quad (5-24b)$$

$$OPEX = EX_e + EX_s \quad (5-24c)$$

$$EX_e = HP \times t \times PX_e \quad (5-24d)$$

$$EX_s = W \times H \times \phi \times T_{c-ave} \times \rho_{vs} \times PX_s \quad (5-24e)$$

where  $NCF$  is the net cash flow,  $C_a$  is the capital cost of purchasing and installing the antenna,  $REV$  is the monthly revenue,  $OPEX$  is the monthly operational expenditure,  $i$  is the monthly interest,  $m$  is the months used to recover the oil in the EM excited zone,  $Q_m$  is the monthly oil production,  $PX_o$  is the oil price,  $EX_e$  is the expenditure of EM heating,  $EX_s$  is the expenditure of residual vapor solvent in the EM excited zone,  $HP$  is the EM heating power,  $t$  is the time,  $PX_e$  is the electricity fee,  $PX_s$  is the solvent price,  $\rho_{vs}$  is the density of the vapor solvent, and  $T_{c-ave}$  is the average chamber temperature.

**Table 5-6** Parameters used in the economic analysis.

Property	Value	Unit
Monthly interest rate	0.8333	%
Oil price	50	\$/barrel
Solvent price	20	\$/barrel
Electricity fee	0.06	\$(/kWh)
EM heating device	10,000	\$/m

**Figure 5-13** shows the calculated  $NPVs$  for various production schemes. The calculated results represent the  $NPVs$  of a unit well length; the oil flow rate is also doubled to consider the oil production from the whole EM excited zone. The results show that a higher EM heating power could provide a higher oil flow rate but accompanied by a significant increase in the electricity charges. Among the tested cases, the EM heating at 15 kW and  $n$ -butane injection at 1500 kPa offers the largest  $NPV$ . **Table 5-7** lists the solvent-oil ratios (SORs) that are calculated based on the mass ratios (mass/mass) of the consumed solvent to the produced oil. The solvent usage includes both the produced and retained solvent. The amount of retained solvent is calculated by multiplying the chamber volume and the solvent vapor density; the solvent vapor density is

estimated at the conditions of the average chamber temperature and solvent injection pressure. The cumulative solvent production can be obtained by summing up the daily solvent mass rates as calculated by Eq. 20b. The mass of the produced oil is calculated by multiplying the cumulative oil production and heavy oil density; the heavy oil density is evaluated at the initial reservoir condition.

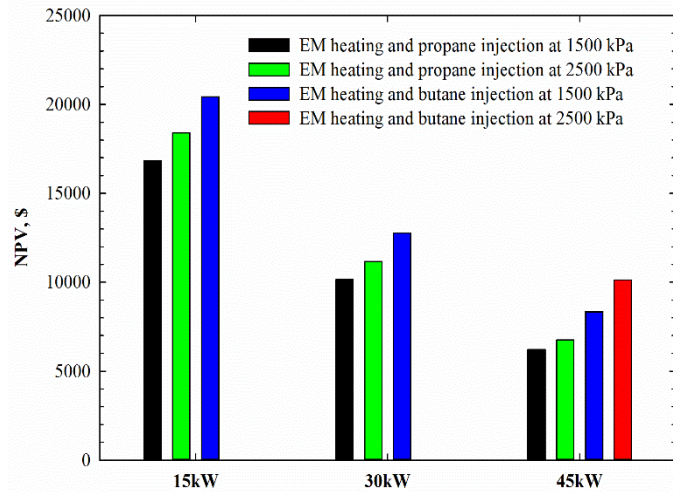


**Figure 5-13** Comparison of the NPVs provided by different production scenarios.

**Table 5-7** Solvent-oil ratios calculated for the different test cases.

Heating power, kW	Propane 1500 kPa	Propane 2500 kPa	n-Butane 1500 kPa	n-Butane 2500 kPa
15	0.033	0.064	0.051	*
30	0.032	0.060	0.048	*
45	0.031	0.058	0.046	0.096

\*Note: The solvent at these EM heating powers and solvent injection pressure is in the liquid phase, which is not applicable to the model.

We then calculate the energy oil ratio (EOR) of this hybrid process, and **Table 5-8** lists the calculated EORs at chamber spreading stage, chamber falling stage, and the total production duration for different cases. The energy consumption in the calculation is mainly electrical energy, while the energy of the injected solvent is neglected to simplify the calculation. It is found that the EOR of this hybrid method varies from 7 to 14 GJ/m<sup>3</sup>, which is equivalent to the EOR of SAGD process with a steam-oil ratio from 4 to 6 (Gates 2010). The large EORs of this

hybrid process are caused by the lower oil production and higher energy consumption at the chamber falling stage. The EORs at the chamber spreading stage are about 4-6 GJ/m<sup>3</sup>, which is lower than a typical EOR of SAGD operations of 7.5 GJ/m<sup>3</sup> corresponding to a steam oil ratio of 3 (Hassanzadeh and Harding 2016). For the given reservoir, EM heating configuration and oil price used in this case study, the combined EM heating and solvent-assisted gravity drainage can be considered as a promising alternative for traditional heavy oil recovery methods based on the above economic-feasibility and energy-efficiency analysis.

**Table 5-8** Energy oil ratios calculated for different test cases.

EOR, GJ/m <sup>3</sup>	Propane 1500 kPa			Propane 2500 kPa			<i>n</i> -Butane 1500 kPa			<i>n</i> -Butane 2500 kPa		
	SS <sup>a</sup>	FS <sup>b</sup>	TT <sup>c</sup>	SS	FS	TT	SS	FS	TT	SS	FS	TT
15	5.0	16.8	10.9	4.8	15.9	10.4	4.6	15.4	10.0			
30	5.8	20.1	13.0	5.7	19.4	12.5	5.5	18.8	12.2			
45	6.4	21.8	14.1	6.2	21.3	13.8	6.1	20.6	13.4	5.8	19.6	12.7
Note: <sup>a</sup> Chamber spreading stage <sup>b</sup> Chamber falling stage <sup>c</sup> Total production duration												

## 5.7 Conclusions

This paper presents a novel semi-analytical model for predicting the oil flow rate generated by the combined EM heating and solvent-assisted gravity drainage. The following conclusions can be drawn from the study:

- For given reservoir conditions, the proposed model can be used to predict the oil drainage behavior by this hybrid process in situations where the SAGD-like well configurations are adopted. By employing different attenuation coefficients within and beyond the vapor chamber, the model can properly calculate the absorbed power distribution. Based on the absorbed power and attenuation coefficient distributions, the model evaluates the temperatures within and beyond the vapor chamber. The average chamber edge temperature is used to evaluate the solvent distribution in the

drainage zone. On the basis of the calculated temperature and solvent distribution, the oil flow rates of this hybrid process can be obtained.

- The proposed semi-analytical model is validated against experimental tests we previously conducted. The calculated mass flow rate slightly shifts earlier in time compared with the measured rates because the model neglects the pre-heating stage. Apart from this, the calculated results from the model are in reasonably good agreement with the experimental results.
- In addition, the developed model can efficiently predict the oil flow rate within the EM excited zone and can be used to evaluate the effects of EM heating power, solvent type, solvent injection pressure, and initial reservoir temperature, on the process performances. The model also provides a quick screening tool for assessing the economic feasibilities of applying such hybrid process for a given reservoir.
- Lastly, based on calculation results from the proposed model, it is found that higher EM heating power, heavier solvent, and higher solvent injection pressure could provide a higher oil flow rate. But a higher heating power also increases the electricity fee and raises the cost and energy consumption of this hybrid process. The economic-feasibility and energy-efficiency analyses show that, as for the reservoir conditions considered in this study, EM heating at 15 kW and *n*-butane injection at 1500 kPa is the most profitable and energy-efficient scheme among the various production schemes examined.

## Nomenclature

$b$  = Constant in Eq. 22

$C$  = Solvent concentration ahead of the chamber edge, vol%

$C_a$  = Capital cost of purchasing and installing the antenna, \$/m

- $C_i$  = Solvent concentration at the chamber edge, vol%  
 $C_r$  = Initial solvent concentration in heavy oil ( $1 \times 10^{-5}$ ), vol%  
 $C_1, C_2, C_3, C_4$  = Coefficients in Eq.9  
 $C_{po}$  = Heat capacity of heavy oil, J/(kg $\times$ °C)  
 $C_{pt}$  = Volumetric heat capacity of reservoir, J/(kg $\times$ °C)  
 $d_1, d_2, d_{os}, d_{of}$  = Integrating ranges used in the oil flow rate calculation defined in Appendix C, m  
 $D$  = Distance between injector and producer, m  
 $D_s$  = Solvent diffusivity, m<sup>2</sup>/s  
 $EX$  = Expenditure, \$  
 $f$  = Volume fraction, dimensionless  
 $g$  = Gravitational acceleration (9.8 m/s<sup>2</sup>)  
 $h$  = Height of the payzone, m  
 $h_i$  = Chamber top location at the chamber falling stage, m  
 $H$  = Height of the drainage zone, m  
 $HP$  = EM heating power, kW  
 $i$  = Monthly interest, %  
 $I_o, I_1, I_2, I_3$  = Oil flow rate integrals used in the oil flow rate calculation  
 $I_{of}$  = Oil flow rate integral at the chamber falling stage  
 $I_{os}$  = Oil flow rate integral at the chamber spreading stage  
 $k$  = Effective thermal conductivity of reservoir, W/(m $\times$ °C)  
 $k_{v1}, k_{v2}, k_{v3}, k_{v4}, k_{v5}$  = Coefficients in Eq. 11  
 $K$  = Absolute permeability, Darcy  
 $K_{value}$  = Vapor/liquid equilibrium ratio, dimensionless  
 $l$  = Lateral well length ( $l = 1$  m)  
 $L$  = Coefficient in Eq. 14  
 $m$  = mass flow rate, kg/s  
 $M$  = Molecular weight, g/mol  
 $NCF$  = Net cash flow, \$  
 $NPV$  = Net present value, \$  
 $OPEX$  = Operational expenditure (monthly), \$/month

- $p_{inj}$  = Solvent injecting pressure  
 $P$  = Absorbed EM heating power distribution, W  
 $P_0$  = Incident power at the wellbore, W  
 $PX$  = Price, \$/m<sup>3</sup>  
 $q_o$  = Oil flow rate, m<sup>3</sup>/s  
 $q_{of}$  = Oil flow rate at the chamber spreading stage  
 $q_{os}$  = Oil flow rate at the chamber spreading stage  
 $Q_m$  = Monthly oil production, barrel  
 $r$  = Distance to antenna, m  
 $r_c$  = Distance from the chamber edge to the antenna, m  
 $r_0$  = Radius of wellbore (0.05 m)  
 $REV$  = Monthly revenue, \$/month  
 $S$  = Saturation, dimensionless  
 $\overline{S_{or}}$  = Average residual oil saturation  
 $\Delta S_o$  = Difference between the original and the residual oil saturation, dimensionless  
 $t$  = Time, s  
 $T$  = Temperature, °C  
 $T_{c-ave}$  = Average chamber temperature, °C  
 $T_{res}$  = Initial reservoir temperature, °C  
 $U$  = Chamber moving velocity, m/s  
 $U_m$  = Chamber moving velocity at the top ( $U \approx U_m$ ), m/s  
 $w_i$  = Chamber top location, m  
 $W$  = Width of the EM excited zone, m  
 $W_s$  = Width of the longitudinal section of the sandpack ( $W_s = 4$  cm)  
 $x$  = Mole fraction in liquid phase, dimensionless  
 $\alpha$  = Attenuation coefficient, 1/m  
 $\alpha_c$  = Attenuation coefficient of the vapor chamber, 1/m  
 $\alpha_r$  = Attenuation coefficient of the drainage zone, 1/m  
 $\delta_p$  = Penetration depth, m

- $\varepsilon^*$  = Complex permittivity, F/m  
 $\varepsilon_0$  = Permittivity of free space ( $8.85 \times 10^{-12}$  F/m)  
 $\varepsilon'$  = Real part of relative permittivity (Dielectric constant), dimensionless  
 $\varepsilon''$  = Imaginary part of the relative permittivity (Loss factor), dimensionless  
 $\varepsilon_r$  = Permittivity of reservoir outside the vapor chamber, dimensionless  
 $\varepsilon_c$  = Permittivity of reservoir within the vapor chamber, dimensionless  
 $\phi$  = Porosity, dimensionless  
 $\phi_s$  = Porosity of the sandpack, dimensionless  
 $\mu$  = Viscosity, cP  
 $\mu_0$  = Permeability (electromagnetism) of free space ( $1.26 \times 10^{-6}$  H/m)  
 $\nu$  = Kinematic viscosity,  $\text{m}^2/\text{s}$   
 $\theta$  = Angle between the chamber edge and the horizontal axis, degree  
 $\rho$  = Density,  $\text{kg}/\text{m}^3$   
 $\rho_t$  = Volumetric density of reservoir,  $\text{kg}/\text{m}^3$   
 $\rho_{vs}$  = Vapor solvent density,  $\text{kg}/\text{m}^3$   
 $\omega$  = Angular frequency, rad/s  
 $\zeta$  = Perpendicular distance to the chamber edge, m

## Subscripts

- $e$  = EM heating  
 $o$  = Heavy oil  
 $s$  = Solvent  
 $v$  = Vapor  
 $mix$  = Mixture  
 $ave$  = Average  
 $w$  = Water  
 $g$  = Formation rock  
 $or$  = Residual oil

## SI Metric Conversion Factors

- bbl  $\times 1.589\,873^*$  E-01 =  $\text{m}^3$   
 cp  $\times 1.0^*$  E-03 = Pa·s

ft	× 3.048 *	E-01	=	m
°F	(°F-32)/1.8		=	°C
°F	(°F+459.67)/1.8		=	°C
psi	× 6.894 757	E+00	=	kPa

## 5.8 References

- Abernethy, E.R. 1976. Production Increase of Heavy Oil by Electromagnetic Heating. *J. Can. Pet. Tech.* **15** (3): 91–97.
- Al-Harashsheh et al. 2009. Dielectric Properties of Jordanian Oil Shales. *Fuel Process. Technol.* **90**: 1259-1264.
- Allen, J.C. and Redford, D.A. 1978. Combination Solvent-Noncondensable Gas Injection Method for Recovering Petroleum from Viscous Petroleum-Containing Formations Including Tar Sand Deposits. US Patent No. 4,109,720.
- Bera, A. and Babadagli, T. 2017. Effect of Native and Injected Nano-Particles on the Efficiency of Heavy Oil Recovery by Radio Frequency Electromagnetic Heating. *J. Petr. Sci. and Eng.* **153**: 244-256.
- Bird, R.B., Steward, W.E., and Lightfoot, E.N. 2002. *Transport Phenomena*. New York City: John Wiley & Sons, Inc.
- Bogdanov et al. 2016. Heavy Oil Recovery via Combination of Radio-Frequency Heating With Solvent Injection. Paper SPE 180709 presented at the SPE Heavy Oil Conference-Canada, Calgary, 7–9 June.
- Butler, R.M. 1994. Steam-assisted Gravity Drainage: Concept, Development, Performance and Future. *J Can. Pet. Technol.* **33** (2): 44–50.
- Butler, R.M. 1997. Thermal Recovery of Oil and Bitumen. Calgary, Alberta: GravDrain Inc.
- Cardwell, W.T. and Parsons, R.L. 1949. Gravity Drainage Theory. *Trans. AIME.* **179** (1): 199–215.
- Carrizales, M.A., Lake, L.W., and Johns, R.T. 2010a. Multiphase Fluid Flow Simulation of Heavy Oil Recovery by Electromagnetic Heating. Paper SPE 129730 presented at the SPE Improved Oil Recovery Symposium held in Tulsa, Oklahoma, USA, 24–28 April.
- Carrizales, M.A. 2010b. Recovery of Stranded Heavy Oil by Electromagnetic Heating. Ph.D. dissertation, University of Texas at Austin, Austin, Texas, USA.

- CMG. 2013. *STARS User's Guide, Version 2013*. Calgary, Alberta: Computer Modelling Group (CMG).
- Das, S.K. and Butler, R.M. 1996. Diffusion Coefficients of Propane and Butane in Peace River Bitumen. *Can. J. Chem. Eng.* **74** (6): 985–992.
- Das, S.K. and Butler, R.M. 1998. Mechanism of the Vapor Extraction Process for Heavy Oil and Bitumen. *J. Pet. Sci. Eng.* **21** (1): 43–59.
- Davletbaev, A.Y., Kovaleva, L.A. and Nasyrov, N.M. 2008. Numerical Simulation of Injection of a Solvent into a Production Well Under Electromagnetic Action. *Fluid Dyn.* **43** (4): 583–589.
- Dong, L. 2012. Effect of Vapor-Liquid Phase Behavior of Steam-Light Hydrocarbon Systems on Steam Assisted Gravity Drainage Process for Bitumen Recovery. *Fuel* **95**: 159–168.
- Fanchi, J.R. 1993. Feasibility of Reservoir Heating by Electromagnetic Irradiation. *SPE Adv. Technol. Ser.* **1** (02): 161-169.
- Faradonbeh, M.R., Harding, T.G. and Abedi, J. 2017. Semianalytical Modeling of Steam/Solvent Gravity Drainage of Heavy Oil and Bitumen: Unsteady-State Model with Curved Interface. *SPE Res. Eval. & Eng.* **20** (1): 134 - 148.
- Gadani et al. 2012. Effect of Salinity on the Dielectric Properties of Water. *Indian J. Pure Appl. Phys.* **50**: 405–410.
- Gates, I.D. 2010. Solvent-Aided Steam-Assisted Gravity Drainage in Thin Oil Sand Reservoirs. *J. Petr. Sci. Eng.* **74**: 138-146.
- Ghannadi, S., Irani, M., and Chalaturnyk, R. 2016. Overview of Performance and Analytical Modeling Techniques for Electromagnetic Heating and Applications to Steam-Assisted-Gravity-Drainage Process Startup. *SPE J.* **21** (2): 311–333.
- Godard, A., and Rey-Bethbeder, F. 2011. Radio Frequency Heating, Oil Sand Recovery Improvement. Paper SPE 150561 presented at the SPE Heavy Oil Conference and Exhibition, Kuwait City, Kuwait, 12–14 December.
- Gupta, S.C. and Gittins, S.D. 2006. Christina Lake Solvent Aided Process Pilot. *J. Can. Pet. Tech.* **45** (9): 15–18.
- Gupta et al. 2010. Optimal Amount of Solvent in Solvent Aided Process. Paper SPE 137543 presented at the Canadian Unconventional Resources and International Petroleum Conference, Calgary, 19–21 October.

- Gupta, S.C. and Gittins, S.D. 2012. An Investigation into Optimal Solvent Use and Nature of Vapor/Liquid Interface in Solvent-Aided SAGD Process with a Semi-Analytical Approach. *SPE J.* **17** (4): 1255–1264.
- Haghighat, P. and Maini, B.B. 2013. Effect of Temperature on VAPEX Performance. *J. Can. Pet. Tech.* **52** (6): 408–416.
- Hassanzadeh, H. and Harding, T.G. 2016. Analysis of Conductive Heat Transfer During *in-situ* Electrical Heating of Oil Sands. *Fuel* **178**: 290–299.
- Hu, K. and Liu, C.R. 2000. Theoretical Study of the Dielectric Constant in Porous Sandstone Saturated with Hydrocarbon and Water. *IEEE Trans. Geosci. Remote Sens.* **38** (3): 1328–1336.
- Hu, L., Li, H.A., Babadagli, T., and Ahmadloo, M. 2016a. Experimental Investigation of Combined Electromagnetic Heating and Solvent Assisted Gravity Drainage for Heavy Oil Recovery. Paper SPE 180747 presented at the SPE Heavy Oil Conference-Canada, Calgary, 7–9 June.
- Hu, L., Li, H.A., Babadagli, T. et al. 2016b. A New Semi-Analytical Model for Simulating Combined Electromagnetic Heating and Solvent Assisted Gravity Drainage. WHOC16-165 presented at the World Heavy Oil Congress, Calgary, Alberta, Canada, 7–9 September.
- Hu, L., Li, H.A., Babadagli, T. et al. 2017. Experimental Investigation of Combined Electromagnetic Heating and Solvent Assisted Gravity Drainage for Heavy Oil Recovery. *J. Petr. Sci. Eng.* **154**: 589-601.
- Irani, M., and Cokar, M. 2016. Discussion on the Effects of Temperature on Thermal Properties in the Steam-Assisted-Gravity-Drainage (SAGD) Process. Part 1: Thermal Conductivity. *SPE J.* **21** (2): 334–352.
- Ivory et al. 2010. Investigation of Cyclic Solvent Injection Process for Heavy Oil Recovery. *J. Can. Pet. Tech.* **49** (9): 22–33.
- Jha, K.N., and Chakma, A. 1999. Heavy-Oil Recovery from Thin Pay Zones by EM Heating. *Energy Sources* **21** (1-2): 63–73.
- Keshavarz, M., Okuno, R., and Babadagli, T. 2014. A Semi-Analytical Solution to Optimize Single-Component Solvent Coinjection with Steam during SAGD. *Fuel* **144**: 400-414.
- Li, H., Zheng, S., and Yang, D., 2013. Enhanced Swelling Effect and Viscosity Reduction of Solvent(s)/CO<sub>2</sub>/Heavy-Oil Systems. *SPE J.* **18** (4): 695–707.

- Lin, B.Q., Li, H., Dai, H.M. et al. 2016. Three-Dimensional Simulation of Microwave Heating Coal Sample with Varying Parameters. *Appl. Therm. Eng.* **93**: 1145-1154.
- Liu et al. 2017. An Investigation into Temperature Distribution and Heat Loss Rate within the Steam Chamber in Expanding-Solvent SAGD Process. SPE-184963-MS presented at the SPE Canada Heavy Oil Technical Conference, Calgary, Alberta, Canada, 15–16 February.
- Lobe, V.M. 1973. *A Model for the Viscosity of Liquid-Liquid Mixtures*. MSc Thesis, University of Rochester, Rochester, New York.
- Lowe, D.F., Oubre, C.L., and Ward, C.H. 2000. *Soil Vapor Extraction Using Radio Frequency Heating: Resource Manual and Technology Demonstration*. Lewis Publishers, Boca Raton, FL.
- Metaxas, A.C. and Meredith, R.J. 1983. *Industrial Microwave Heating*. Peter Peregrinus.
- Nasr et al. 2003. Novel Expanding Solvent-SAGD Process ES-SAGD. *J. Can. Pet. Technol.* **42** (1): 13–16.
- Nenniger, J. and Nenniger, E. 2008. Method and Apparatus for Stimulating Heavy Oil Production. US Patent No. 7,363,973.
- Reid, R.C., Prausnitz, J.M., and Sherwood, T.K. 1977. *The Properties of Gases and Liquids*. New York City: McGraw-Hill.
- Reis, J.C. 1992. A Steam-Assisted Gravity Drainage Model for Tar Sands: Linear Geometry. *J. Can. Petrol. Technol.* **31** (10): 14–20.
- Rezaei, N., Mohammadzadeh, O., and Chatzis, I. 2010. Warm VAPEX: A Thermally Improved Vapor Extraction Process for Recovery of Heavy Oil and Bitumen. *Energy Fuels* **24** (11): 5934–5946.
- Rottenfusser, B., Ranger, M.A. Geological Comparison of Six Projects in the Athabasca Oil Sands. CSPG-Canadian Heavy Oil Association-CWLS Joint Conf. (ICE 2004), Calgary, Canada, May 31- June 4, 2004.
- Sahni, A., Kumar, M., and Knapp, R.B. 2000. EM Heating Methods for Heavy Oil Recovery. Paper SPE 62550 presented at the SPE/AAPG Western Regional Meeting, Long Beach, California, June 19–23.
- Trautman et al. 2013. Effective Solvent Extraction System Incorporating EM Heating. US Patent 8,616,273 B2.

- Wharton, R.P., Rau, R.N., and Best, D.L. 1980. Electromagnetic Propagation Logging: Advances in Technique and Interpretation. Paper SPE 9267 presented at the SPE Annual Technical Conference and Exhibition, Dallas, Texas, 21-24 September.
- Wise, S. and Patterson, C. 2016. Reducing Supply Cost with ESEIEH™ Pronounced Easy. Paper SPE 180729 presented at the SPE Heavy Oil Conference-Canada, Calgary, 7–9 June.
- Yaws, C.L. 2003. Yaws' Handbook of Thermodynamic and Physical Properties of Chemical Compounds. Knovel Corporation.
- Younglove, B.A., and Ely, J.F. 1987. Thermophysical Properties of Fluids. II. Methane, Ethane, Propane, Isobutane, and Normal Butane. *J. Phys. Chem. Ref. Data* **16** (4): 577-798.

## 5.9 Appendix

### Appendix 5A— Calculation of the Range of EM Excited Zone

In the EM heating process, the penetration depth varies with the chamber propagation due to the distinct attenuation coefficients within the vapor chamber and drainage zone. **Figure 5A1** shows a graphical illustration of the calculation of the EM excited zone width. Based on the assumption of an inverted triangle chamber and a rectangular reservoir, the radiation at the bottom right corner exhibits the lowest value because of its longest distance from the antenna as well as the largest attenuation effect. We define the distance, between producer and point  $E$  where the radiation of power decays to  $1/e$  ( $e = 2.718$ ) of its original level ( $\delta_p$ ), as the width ( $W$ ) of the EM excited zone. The height ( $H$ ) of the EM excited zone can be either determined as the penetration depth calculated with the attenuation coefficient of drainage zone and the antenna location, or determined by the thickness of the payzone. This definition assures that the reservoir lying in the EM excited zone stays inside the penetration depth of the EM radiation where EM radiation dominates the heating. This definition also gives the relationship:

$$\alpha_c r_1 + \alpha_r r_2 = 1 \quad (5A-1)$$

And the geometric relationships provide:

$$r_1 = \frac{D}{D+H} \sqrt{W^2 + D^2} \quad (5A-2a)$$

$$r_2 = \frac{H}{D+H} \sqrt{W^2 + D^2} \quad (5A-2b)$$

where  $H$  is the height of the reservoir,  $D$  is the distance between injector and producer,  $W$  is the width of EM excited zone. In this study, we choose  $H$  of 20 m and  $D$  of 10 m to exemplify the calculations; based on the calculated attenuation coefficients, the corresponding  $W$  is 22.06 m, which corresponds to the half size of the EM excited zone.

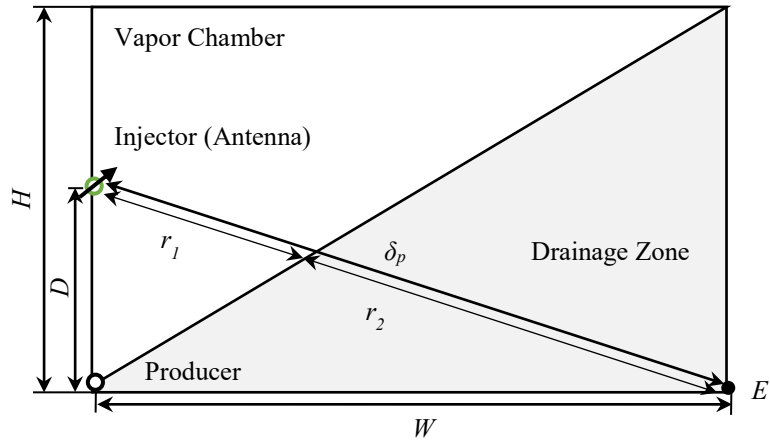


**Figure 5A-1** Schematic showing how to calculate the EM excited zone width.

## Appendix 5B—Approximation of the temperature distribution ahead of the chamber edge

The following procedures are used to approximate the temperature distribution ahead of the chamber edge:

- 1) We first discretize the EM excited zone with a width of  $W = 22$  m and height of  $H = 20$  m into  $400 \times 400$  grids.
- 2) For a given chamber edge location, we evaluate the distance of each grid to the antenna ( $r$ ) and its corresponding  $r_c$  (See **Figure 5B-1**, which illustrates how to transform the coordinate system from  $(w, h)$  to  $(\xi, \eta)$ ). For example, as the chamber edge moves to  $w_i$  at the chamber spreading stage (or  $h_i$  at the chamber falling stage), for a given grid at  $(w, h)$ , the distance from the chamber edge to the antenna ( $r_c$ ) is calculated by solving the intersection point of the following two lines: one line is the chamber edge with one end located at the injector  $(0, 0)$  and the other at  $(w_i, H)$ , and the other line connects the grid  $(w, h)$  to the antenna  $(0, D)$ .
- 3) Next, by substituting the calculated  $r$  and  $r_c$  into Eq. 5-5, we can obtain the absorbed power distribution.
- 4) Based on the obtained absorbed power and attenuation coefficient distributions, we use Eq. 5-7 to calculate the temperature distribution by EM heating over a 2D space.
- 5) We calculate the perpendicular distance of each grid to the chamber edge with the relationship of  $\xi = w - h \cot \theta$  during the chamber spreading stage and  $\xi = h - w \tan \theta$  during the chamber falling stage, respectively. The temperature changes along the  $\eta$  direction due to the varying distance to the antenna. To simplify the calculation, we use the average temperature ( $T_{ave}$ ) to approximate the temperature distribution along the  $\eta$  direction; we apply this approximation to estimate the average temperature along the chamber edge as

well. The average temperature is calculated on the basis of an average viscosity of heavy oil, which can provide the same oil flow rate as calculated with a varying viscosity:

$$\mu_{ave}(T_{ave}) = \frac{1}{\sum 1/\mu_i(T_{\eta})} \quad (5B-1)$$

where  $\mu_i$  is the heavy oil viscosity at different locations along the direction of  $\eta$  and  $\mu_{ave}$  is the average heavy oil viscosity. The average temperature ( $T_{ave}$ ) of the chamber edge, corresponding to the average viscosity ( $\mu_{ave}$ ), can thereby be obtained with the temperature-viscosity data of the heavy oil sample. By repetitively applying such averaging method in the  $\zeta$  direction, we can then obtain the average-temperature distribution of the drainage zone along the  $\zeta$  direction.

- 6) We perform curve fitting on the average-temperature data to obtain the coefficients appearing in Eq. 5-8. The obtained correlation can be then used in the following calculations to approximate the temperature distribution that is normal to the chamber edge ( $T(\xi)$ ). Considering that the EM heating power exponentially decays with distance, an exponential form is adopted by Eq. 5-9 to estimate the temperature profile ahead of the chamber edge. Note that the coefficients in Eq. 5-9 are updated at each time step.

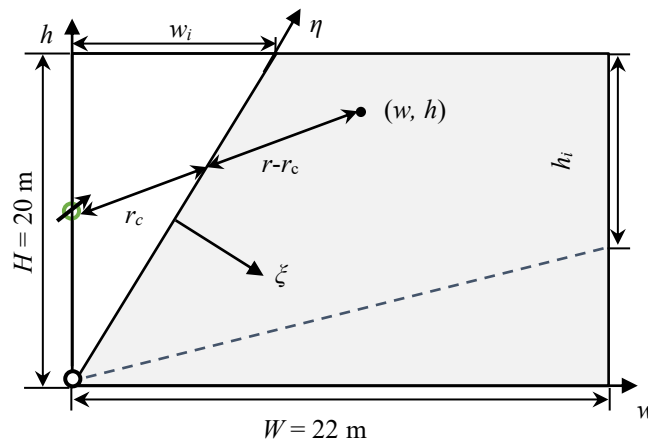


**Figure 5B-1** Schematic of how to transform the coordinate system from  $(w, h)$  to  $(\zeta, \eta)$ .

## Appendix 5C— Calculation of Oil Flow Rate Integrals and Derivation of Eq. 5-18

Based on the assumed chamber shape, geometry relationship and material balance, the oil flow rate of one-half of the reservoir per unit well length at the chamber spreading stage is (Reis 1992):

$$\begin{aligned} q_{os} &= \frac{d}{dt} \left( \frac{1}{2} \phi \Delta S_o H w_i \right) \\ &= \frac{1}{2} \phi \Delta S_o H \frac{U_m}{\sin \theta} \end{aligned} \quad (5C-1)$$

and Darcy's law gives:

$$q_{os} = Kg \sin \theta I_{os} \quad (5C-2a)$$

$$I_{os} = \int_0^{d_s} (1-C) \left( \frac{1}{v} - \frac{1}{v_r} \right) d\xi \quad (5C-2b)$$

where  $d_s$  is the integrating range corresponding to the chamber spreading stage, and  $I_{os}$  is the oil flow rate integral at the chamber spreading stage. Substituting  $\sin \theta$  from (5C-1) into (5C-2) results in:

$$q_{os} = \sqrt{\frac{1}{2} Kg \phi \Delta S_o U_m (H I_{os})} \quad (5C-3)$$

In this hybrid process, the oil flow rate is calculated by integrating over the entire drainage zone; the integrating range and the corresponding drainage height vary during the process. **Figure 5C-1** illustrates the drainage zone and its integrating ranges for the chamber spreading and falling stages, respectively. The integration range at the chamber spreading stage is determined by:

$$d_{os} = d_1 + d_2 = W \sin \theta \quad (5C-4a)$$

$$d_1 = (W - w_i) \sin \theta \quad (5C-4b)$$

$$d_2 = w_i \sin \theta \quad (5C-4c)$$

where  $d_{os}$  is the integration range corresponding to the chamber edge location of  $w_i$  at the chamber spreading phase,  $d_1$  is the integration range within which the height of the EM excited zone equals to  $H$ , and  $d_2$  is the integration range within which the height of the EM excited zone is less than  $H$ . Hence, the oil flow rate integral is divided into two intervals, and the product of  $H$  and  $I_o$  can be calculated by:

$$\begin{aligned}
 HI_{os} &= \int_0^{d_1} H(1-C)\left(\frac{1}{v} - \frac{1}{v_R}\right)d\xi + \int_{d_1}^{d_{os}} \left(H - \frac{\xi - d_1}{\cos\theta}\right)(1-C)\left(\frac{1}{v} - \frac{1}{v_R}\right)d\xi \\
 &= \int_0^{d_{os}} H(1-C)\left(\frac{1}{v} - \frac{1}{v_R}\right)d\xi - \int_{d_1}^{d_{os}} \frac{\xi - d_1}{\cos\theta}(1-C)\left(\frac{1}{v} - \frac{1}{v_R}\right)d\xi
 \end{aligned} \tag{5C-5}$$

Substituting Eq. 5C-4 and Eq. 5C-5 into Eq. 5C-3, we can obtain the oil flow rate at the chamber spreading stage as described in Eq. 5-18a. Likewise, the oil flow rate of one-half of the reservoir per unit well length at the chamber falling stage is:

$$\begin{aligned}
 q_{of} &= \frac{d}{dt} \left( \frac{1}{2} \phi \Delta S_o W h_i \right) \\
 &= \frac{1}{2} \phi \Delta S_o W \frac{U_m}{\cos\theta}
 \end{aligned} \tag{5C-6}$$

$$q_{of} = Kg \sin\theta I_{of} \tag{5C-7a}$$

$$I_{of} = \int_0^{d_f} (1-C)\left(\frac{1}{v} - \frac{1}{v_r}\right)d\xi \tag{5C-7b}$$

where  $d_f$  is the integrating range corresponding to the chamber falling stage, and  $I_{of}$  is the oil flow rate integral at the chamber spreading stage. Applying the same procedure and substituting  $\cos\theta$  from (5C-6) into (5C-7) results in:

$$q_{of} = \sqrt{\frac{(KgI_{of})^2 \pm \sqrt{(KgI_{of})^4 - (Kg\phi\Delta S_o U_m W I_{of})^2}}{2}} \tag{5C-8}$$

$$I_{of} = \int_0^{d_{of}} (1-C)\left(\frac{1}{v} - \frac{1}{v_R}\right)d\xi \tag{5C-9a}$$

$$WI_{of} = \int_0^{d_{of}} \left(W - \frac{\xi}{\sin \theta}\right) (1-C) \left(\frac{1}{v} - \frac{1}{v_R}\right) d\xi \quad (5C-9b)$$

$$d_{of} = W \sin \theta \quad (5C-9c)$$

where  $d_{of}$  is the integrating range corresponding to the chamber edge location of  $h_i$  at the chamber falling stage. Similarly, substituting Eq. 5C-9 into Eq. 5C-8, we can obtain the oil flow rate at the chamber falling stage as described in Eq. 5-18b.

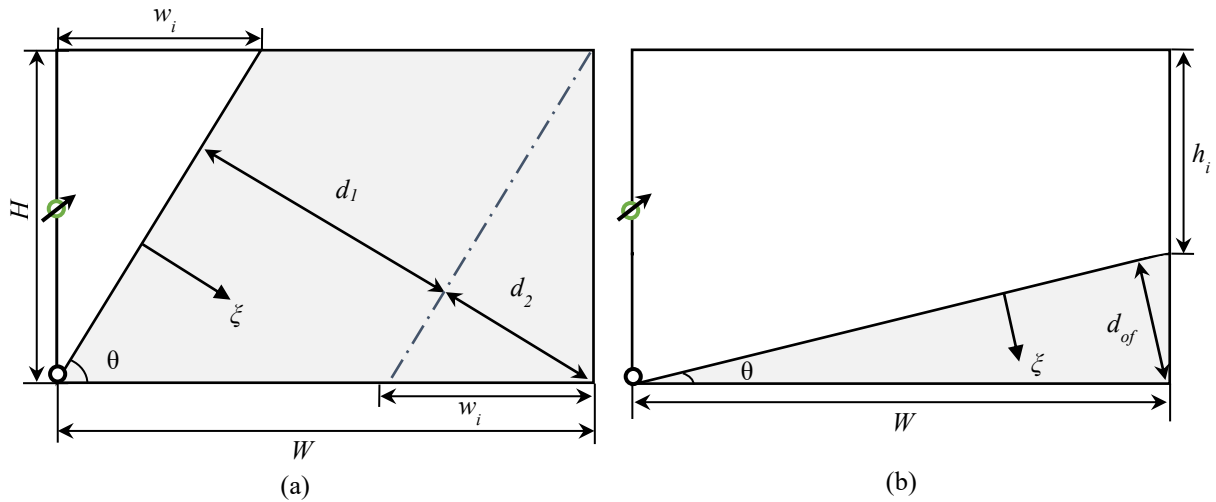


**Figure 5C-1** Illustration of the drainage zone and its integrating range used in the oil flow rate integral calculation: (a) chamber spreading stage calculated by Eq. 5-19a, and (b) chamber falling stage calculated by Eq. 5-19b. The darker areas represent the drainage zones which are calculated by Eq. 5-19.

## **CHAPTER 6 CONTRIBUTIONS AND RECOMMENDATIONS**

As this is a paper-based thesis, each chapter contains its own conclusions. In this chapter, only the contributions and recommendations made by this thesis are presented.

## **6.1 Scientific and Practical Contributions to the Literature and Industry**

The major scientific and practical contributions of this thesis to the literature and industry are:

1. The permittivity data of constituents of oil sands, oil sands, and solvent/oil sands mixtures over the range of 200MHz and 10GHz are obtained. The acquired permittivity data can assist us to quantify the effect of frequency, water content of oil sands, and solvent addition on the permittivity of oil sands mixtures. The obtained permittivity spectrum can also help to upscale the EM heating results obtained from a laboratory frequency to a field-application frequency. The commonly used mixing models are evaluated by their prediction accuracy for oil sands and solvent/oil sands mixtures. A modified permittivity mixing model, considering the interactions of constituents of oil sands after solvent addition, is proposed to enhance the prediction accuracy for solvent/oil sands mixtures.
2. A simple experimental workflow, including the experimental setup and procedures, for investigating this hybrid process has been proposed, which can be conveniently used to examine the performance of certain designs prior to a larger-scale application. The quantitative data obtained from the experiments can also be used to validate theoretical models developed to simulate this process.
3. How EM heating affects petrophysical properties of formation rocks is examined by both experiments and simulations. The mechanisms leading to the breakage of formation rock samples by EM heating are revealed, and petrophysical property variations of formation rocks by EM heating are quantified. A finite-element simulation is conducted to simulate the thermal stress of formation rocks induced by EM heating. It has been shown that EM

heating can be a promising green technique for stimulating the shale rock rich in clay and pyrite.

4. A semi-analytical model, capable of simulating the oil recovery of the combined EM heating and solvent injection in various scenarios, is developed. The developed model can be used to study the effects of key process parameters, operational strategies, and well configurations of this hybrid process. Based on the obtained simulation results, the proposed economic analysis and energy-consumption analysis approaches can be utilized to evaluate the economic feasibility of the hybrid process, to screen candidate reservoirs, and to assess the environmental footprint of the hybrid process.

## **6.2 Recommendations for Future Work**

A systematic study has been conducted to investigate the combined EM heating and solvent injection for heavy oil recovery. However, certain conditions have been neglected and assumptions have been made to simplify the problem at this stage, which can be improved in the future. The recommended future works are:

1. The effects of wettability of the formation rock and the water-oil emulsion on the permittivity of oil sands need to be investigated. Bitumen/heavy oil exhibit a relatively low permittivity which slightly reduces the efficiency of EM heating. Effective ways of enhancing the absorption of EM energy of heavy oil/bitumen can be explored in the future, such as the injection of nanoparticles, polymers, nanostructured carbon materials, and polarized solvent.
2. The experimental setup used in the research is simple, which uses a commercial microwave oven to supply the EM flux. 2-D or 3-D physical models, that are proportional to the field application cases and include wells, antenna, and reservoir materials, are

needed, which will enable the study of oil recovery of this process in a more realistic environment. The performance, efficiency, and durability of the antenna are the key factors in the EM heating process, which needs to be examined in the future.

3. How EM heating changes the petrophysical property of formation rocks at *in-situ* conditions remains to be investigated.
4. We developed a semi-analytical model in this research, while a more complex numerical simulator that incorporates electromagnetics, heat transfer, mass transfer, and mechanical modules is still much needed.
5. EM heating is a relatively new technology in the oil and gas industry, and its potential has not been fully exploited. In the future work, we can explore the smart EM heating schemes, such as adaptive heating (which can be achieved by varying frequencies at different stages of EM heating) and directional heat (which can achieve by blocking or intensifying the wave propagation in a certain direction) for further enhancing the process efficiency.

## BIBLIOGRAPHY

- Abdulagatov, I.M., Emirov, S.N., Tsomaeva, T.A., Gairbekov, K.A., Askerov, S.Y., and Magomedova, N.A. 2000. Thermal conductivity of fused quartz and quartz ceramic at high temperatures and high pressures. *J. Phys. Chem. Solids* **61** (5): 779-787.
- Abernethy, E.R. 1976. Production increase of heavy oil by electromagnetic heating. *J. Can. Pet. Tech.* **15** (3): 91-97.
- Alboudwarej, H., Felix, J.J., Taylor, S., Badry, R., Bremner, C., Brough, B., Skeates, C., Baker, A., Palmer, D., Pattison, K., Beshry, M., Krawchuk, P., Brown, G., Calvo, R., Triana, J.A.C., Hathcock, R., Koerner, K., Hughes, T., Kundu, D., de Cárdenas, J.L., and West, C. 2006. Highlighting heavy oil. *Oilfield Review*. **18** (2): 34-53.
- Al-Farsi, H., Pourafshary, P., and Al-Maamari, R.S. 2016. Application of nanoparticles to improve the performance of microwave assisted gravity drainage (MWAGD) as a thermal oil recovery method. Paper SPE-179764-MS presented at the SPE EOR Conference at Oil and Gas West Asia, Muscat, Oman, 21-23 March.
- Al-Harashsheh, M., Kingman, S., Saeid, A., Robinson, J., Dimitrakis, G., and Alnawafleh, H. 2009. Dielectric properties of Jordanian oil shales. *Fuel Process. Technol.* **90** (10): 1259-1264.
- Allen, J.C. and Redford, D.A. 1978. Combination solvent-noncondensable gas injection method for recovering petroleum from viscous petroleum-containing formations including tar sand deposits. US Patent No. 4,109,720. Washington, DC: U.S. Patent and Trademark Office.
- Alomair, O.A., Alarouj, M.A., Althenayyan, A.A., Al Saleh, A.H., Mohammad, H., Altaf, Y., Alhaidar, Y., Alansari, S., and Alshammari, Y. 2012. Improving heavy oil recovery by unconventional thermal methods. Paper SPE-163311-MS presented at the SPE Kuwait International Petroleum Conference and Exhibition, Kuwait City, Kuwait, 10-12 December.
- Bai, F., Sun, Y., Liu, Y., and Guo, M. 2017. Evaluation of the porous structure of Huadian oil shale during pyrolysis using multiple approaches. *Fuel* **187**: 1-8.
- Barrett, E.P., Joyner, L.G., and Halenda, P.P. 1951. The determination of pore volume and area distributions in porous substances. I. Computations from nitrogen isotherms. *J. Am. Chem. Soc.* **60** (2): 309-319.
- Baumann, T. and Zunft, S. 2015. Properties of granular materials as heat transfer and storage medium in CSP application. *Sol. Energy Mater. Sol. Cells*. **143**: 38-47.

- Bera A. and Babadagli, T. 2015. Efficiency of heavy-oil recovery by radio frequency EM heating: An experimental approach. Paper SPE-176113-MS presented at the SPE Asia Pacific Oil & Gas Conference and Exhibition, Bali, Indonesia, 20–22 October.
- Bera, A. and Babadagli, T. 2015. Status of EM heating for enhanced heavy oil/bitumen recovery and future prospects: A review. *Appl. Energy* **151**: 206-226.
- Bera, A. and Babadagli, T. 2017. Effect of native and injected nano-particles on the efficiency of heavy oil recovery by radio frequency electromagnetic heating. *J. Petr. Sci. and Eng.* **153**: 244-256.
- Bientinesi, M., Petarca, L., Cerutti, A., Bandinelli, M., De Simoni, M., Manotti, M., and Maddinelli, G. 2013. A radiofrequency/microwave heating for thermal heavy oil recovery based on a novel tight-shell conceptual design. *J. Pet. Sci. Eng.* **107**: 18–30.
- Bird, R.B., Stewart, W.E., and Lightfoot, E.N. 2002. *Transport Phenomena*. New York City: John Wiley & Sons, Inc.
- Bogdanov, I., Cambon, S., Mujica, M., and Brisset, A. 2016. Heavy oil recovery via combination of radio-frequency heating with solvent injection. Paper SPE-180709-MS presented at the SPE Heavy Oil Conference-Canada, Calgary, 7–9 June.
- Buffler, C.R. 1995. A new, low power 915 MHz microwave system for efficient industrial scale-up prototyping. Chicago: Microwave Industrial Food Processing Inc.
- Butler, R.M., and Mokrys, I.J. 1993. Recovery of heavy oils using vaporized hydrocarbon solvents: Further development of the VAPEX process. *J. Can. Pet. Technol.* **32**: 77–86.
- Butler, R.M. 1994. Steam-assisted gravity drainage: concept, development, performance and future. *J Can. Pet. Technol.* **33** (2): 44–50.
- Butler, R.M. 1997. Thermal recovery of oil and bitumen. Calgary, Alberta: GravDrain Inc.
- Cardwell, W.T. and Parsons, R.L. 1949. Gravity drainage theory. *Trans. AIME.* **179** (1): 199–215.
- Carrizales, M.A., Lake, L.W., and Johns, R.T. 2010a. Multiphase fluid flow simulation of heavy oil recovery by electromagnetic heating. Paper SPE-129730-MS presented at the SPE Improved Oil Recovery Symposium held in Tulsa, Oklahoma, USA, 24–28 April.
- Carrizales, M.A. 2010b. Recovery of stranded heavy oil by electromagnetic heating. Ph.D. dissertation, University of Texas at Austin, Austin, Texas, USA.

- Chen, J.H., Georgi, D., Liu, H.H., and Lai, B. 2015. Fracturing tight rocks by elevated pore-water pressure using microwaving and its applications. Paper SPWLA-2015-RRR presented at the 56th Annual Logging Symposium, Long Beach, California, USA, 18-22 July.
- Cheng, Y.M., Guo, C.Z., and Gong, L. 1995. A mathematic model of electrical heating in hollow pump rod and its application. Paper SPE-30317-MS presented at the SPE International Heavy Oil Symposium, Calgary, Alberta, Canada, 19-21 June.
- Churcher, P.L., French, P.R., Shaw, J.C., and Schramm, L.L. 1991. Rock properties of Berea sandstone, Baker dolomite, and Indiana limestone. Paper SPE-21044-MS presented at the SPE International Symposium on Oilfield Chemistry, Anaheim, California, USA, 20-22 February.
- Chute, F.S., Vermeulen, F.E., Cervenak, M.R., and McVea, F.J. 1979. Electrical properties of Athabasca oil sands. *Can. J. Earth Sci.* **16** (10): 2009-2021.
- CMG. 2013. *STARS User's Guide, Version 2013*. Calgary, Alberta: Computer Modelling Group (CMG).
- COMSOL Multiphysics Reference Manual, version 5.3, COMSOL Inc. ([www.comsol.com](http://www.comsol.com)).
- Czarnecki, J., Radoev, B., Schramm, L.L., and Slavchev, R. 2005. On the nature of Athabasca oil sands. *Adv. Colloid Interf. Sci.* **114**: 53-60.
- Das, M., Thapar, R., Rajeshwar K., and DuBow, J. 1981. Thermophysical characterization of oil sands: 3. Electrical properties. *Can. J. Earth Sci.* **18** (4): 742-750.
- Das, S.K. and Butler, R.M. 1996. Diffusion coefficients of propane and butane in Peace River bitumen. *Can. J. Chem. Eng.* **74** (6): 985-992.
- Das, S.K. and Butler, R.M. 1998. Mechanism of the vapor extraction process for heavy oil and bitumen. *J. Pet. Sci. Eng.* **21** (1): 43-59.
- Datta, A.K. and Rakesh, V. 2013. Principles of microwave combination heating. *Compr. Rev. Food Sci. Food Saf.* **12** (1): 24-39.
- Davletbaev, A.Y., Kovaleva, L.A., and Nasyrov, N.M. 2008. Numerical simulation of injection of a solvent into a production well under electromagnetic action. *Fluid Dyn.* **43** (4): 583-589.
- Donadille, J.M. and Faivre, O. 2015. Water complex permittivity model for dielectric logging. Paper SPE-172566-MS presented at the SPE Middle East Oil & Gas Show and Conference, Manama, Bahrain, 8-11 March.

- Dondi, M., Mazzanti, F., Principi, P., Raimondo, M., and Zanarini, G. 2004. Thermal conductivity of clay bricks. *J. Mater. Civ. Eng.* **16** (1): 8-14.
- Dong, L. 2012. Effect of vapor-liquid phase behavior of steam-light hydrocarbon systems on steam assisted gravity drainage process for bitumen recovery. *Fuel* **95**: 159–168.
- Egboga, N.U., Mohanty, K.K., and Balhoff, M.T. 2017. A feasibility study of thermal stimulation in unconventional shale reservoirs. *J. Petr. Sci. Eng.* **154**: 576-588.
- Eppelbaum, L., Kutasov, I., and Pilchin, A. 2014. *Applied Geothermics*. Springer: Heidelberg.
- Erdogan, L., Akyel, C., and Ghannouchi, F.M. 2011. Dielectric properties of oil sands at 2.45 GHz with TE<sub>1,0,11</sub> mode determined by a rectangular cavity resonator. *J. Microwave Power Electromagn. Energy* **45**: 15-23.
- Fanchi, J.R. 1993. Feasibility of reservoir heating by electromagnetic irradiation. *SPE Adv. Technol. Ser.* **1** (02): 161-169.
- Faradonbeh, M.R., Harding, T.G., and Abedi, J. 2017. Semianalytical modeling of steam/solvent gravity drainage of heavy oil and bitumen: unsteady-state model with curved interface. *SPE Res. Eval. & Eng.* **20** (1): 134-148.
- Gadani, D.H., Rana, V.A., Bhatnagar, S.P., Prajapati, A.N., and Vyas, A.D. 2012. Effect of salinity on the dielectric properties of water. *Indian J. Pure Appl. Phys.* **50**: 405-410.
- Gaikwad, R. 2014. Electrical properties estimation of oil sands, Master Dissertation, University of Alberta, Edmonton, Alberta, Canada.
- Gao, Q., Tao, J., Hu, J., and Yu, X.B. 2015. Laboratory study on the mechanical behaviors of an anisotropic shale rock. *J. Rock Mech. Geotech. Eng.* **7** (2): 213-219.
- Gates, I.D. 2010. Solvent-aided steam-assisted gravity drainage in thin oil sand reservoirs. *J. Petr. Sci. Eng.* **74**: 138-146.
- Ghannadi, S., Irani, M., and Chalaturnyk, R. 2016. Overview of performance and analytical modeling techniques for electromagnetic heating and applications to steam-assisted-gravity-drainage process startup. *SPE J.* **21** (2): 311-333.
- Gill, H. 1983. The electrothermic system for enhancing oil recovery. *J. Micro. Power* **18** (1983): 107-110.
- Godard, A. and Rey-Bethbeder, F. 2011. Radio frequency heating, oil sand recovery improvement. Paper SPE-150561-MS presented at the SPE Heavy Oil Conference and Exhibition, Kuwait City, Kuwait, 12-14 December.

- Goual, L. and Firoozabadi, A. 2002. Measuring asphaltenes and resins, and dipole moment in petroleum fluids. *AIChE J.* **48** (11): 2646-2663.
- Greff, J. and Babadagli, T. 2013. Use of nano-metal particles as catalyst under electromagnetic heating for in-situ heavy oil recovery. *J. Pet. Sci. Eng.* **112**: 258-265.
- Gupta, S.C., Gittins, S., Sood, A., and Zeidani, K. 2010. Optimal amount of solvent in Solvent Aided Process. Paper SPE-137543-MS presented at the Canadian Unconventional Resources and International Petroleum Conference, Calgary, 19-21 October.
- Gupta, S.C. and Gittins, S.D. 2006. Christina lake solvent aided process pilot. *J. Can. Pet. Tech.* **45** (9): 15-18.
- Gupta, S.C. and Gittins, S.D. 2012. An investigation into optimal solvent use and the nature of vapor/liquid interface in solvent-aided SAGD process with a semianalytical approach. *SPE J.* **17** (4): 1255-1264.
- Haghighat, P. and Maini, B.B. 2013. Effect of temperature on VAPEX performance. *J. Can. Pet. Tech.* **52** (6): 408-416.
- Harvey, A., Arnold, M.D., and El-Feky, S.A. 1979. Selective electric reservoir heating. *J. Can. Pet. Technol.* **18** (3): 47-57.
- Harvey, R.D. 1967. Thermal expansion of certain Illinois limestones and dolomites. Illinois State Geological Survey. *Circular no. 415*.
- Hascakir, B., Acar, C., and Akin, S. 2009. Microwave-assisted heavy oil production: an experimental approach. *Energy & Fuels* **23** (12): 6033-6039.
- Hasmaliza, M., Zainal, A.A., and Norfadhulah, I. 2015. Dolomite addition in non-stoichiometric cordierite glass-ceramic: effects on dielectric constant. *J. Solid State Sci. Technol.* **23** (1-2): 20-25.
- Hassani, F., Nekoovaght, P.M., and Gharib, N. 2016. The influence of microwave irradiation on rocks for microwave-assisted underground excavation. *J. Rock Mech. Geotech. Eng.* **8** (1): 1-15.
- Hassanzadeh, H. and Harding, T.G. 2016. Analysis of conductive heat transfer during *in-situ* electrical heating of oil sands. *Fuel* **178**: 290-299.
- Hemingway, B.S., Krupka, K.M., and Robie, R.A. 1981. Heat capacities of the alkali feldspars between 350 and 1000 K from differential scanning calorimetry, the thermodynamic

functions of the alkali feldspars from 298. 15 to 1400 K, and the reaction quartz + jadeite= analbite. *Am. Mineral* **66**: 1202-1215.

- Hoekstra, P. and Delaney, A. 1974. Dielectric properties of soils at UHF and microwave frequencies. *J. Geophys. Res.* **79**: 1699-1708.
- Horikoshi, S., Matsuzaki, S., Mitani, T., and Serpone, N. 2012. Microwave frequency effects on dielectric properties of some common solvents and on microwave-assisted syntheses: 2-Allylphenol and the C12-C2-C12 Gemini surfactant. *Rad. Physics Chem.* **81** (12): 1885-1895.
- Hu, H., Dai, L., Li, H., Jiang, J., and Hui, K. 2014. Electrical conductivity of K-feldspar at high temperature and high pressure. *Miner. Petro.* **108** (5): 609-618.
- Hu, K. and Liu, C.R. 2000. Theoretical study of the dielectric constant in porous sandstone saturated with hydrocarbon and water. *IEEE Trans. Geosci. Remote Sens.* **38** (3): 1328-1336.
- Hu, L., Li, H.A., and Ahmadloo, M. 2018b. Determination of the permittivity of n-hexane/oil sands mixtures over the frequency range of 200 MHz to 10 GHz. *Can. J. Chem. Eng.*, Preprint.
- Hu, L., Li, H.A., Babadagli, T., and Ahmadloo, M. 2017. Experimental investigation of combined electromagnetic heating and solvent assisted gravity drainage for heavy oil recovery. *J. Petr. Sci. Eng.* **154**: 589-601.
- Hu, L., Li, H.A., Babadagli, T., and Ahmadloo, M. 2018a. A semi-analytical model for simulating the combined electromagnetic heating and solvent-assisted gravity drainage. *SPE J.* **23** (4): 1248-1270.
- Hu, L., Li, H.A., Babadagli, T., and Ahmadloo, M. 2016b. A new semi-analytical model for simulating combined electromagnetic heating and solvent assisted gravity drainage. Paper WHOC16-165 presented at the World Heavy Oil Congress, Calgary, Alberta, Canada, 7-9 September.
- Hu, L., Li, H.A., Babadagli, T., and Ahmadloo, M. 2017. Experimental investigation of combined electromagnetic heating and solvent assisted gravity drainage for heavy oil recovery. *J. Petr. Sci. Eng.* **154**: 589-601.
- Hu, L., Li, H.A., Babadagli, T., and Ahmadloo, M. 2016a. Experimental investigation of combined electromagnetic heating and solvent assisted gravity drainage for heavy oil

- recovery. Paper SPE-180747-MS presented at the SPE Heavy Oil Conference-Canada, Calgary, 7–9 June.
- Huotari, T. and Kukkonen, I. 2004. Thermal expansion properties of rocks: Literature survey and estimation of thermal expansion coefficient for Olkiluoto mica gneiss. Posiva Oy, Olkiluoto, Working Report 4.
- Hussain, M. and Ansari, M. 2017. X-Ray determination of thermal expansion of Iron Sulphide. *IOSR J. Appl. Phys.* **9** (5): 61-63.
- Ilozobhie, A.J., Obi, D. A., and George, A.M. 2016. Determination of thermal conductivity of some shale samples in Awi formation and its geophysical implications, Cross River State, Nigeria. *J. Environ. Earth Sci.* **6** (8): 102-111.
- Irani, M. and Cokar, M. 2016. Discussion on the effects of temperature on thermal properties in the steam-assisted-gravity-drainage (SAGD) process. Part 1: Thermal conductivity. *SPE J.* **21** (2): 334–352.
- Ivory, J., Chang, J., Coates, R., and Forshner, K. 2010. Investigation of cyclic solvent injection process for heavy oil recovery. *J. Can. Pet. Tech.* **49** (9): 22–33.
- Jamaluddin, A.K.M., Vandamme, M., and Mann, B.K. 1995. Formation heat treatment (FHT): A state-of-the-art technology for near-wellbore formation damage treatment. Paper PETSOC-95-67 presented at the 46th Annual Technical Meeting, Calgary, Alberta, Canada, 7-9 June.
- James, L.A., Rezaei, N., and Chatzis, I., 2008. VAPEX, warm VAPEX and hybrid VAPEX - the state of enhanced oil recovery for in Situ heavy oils in Canada. *J. Can. Pet. Technol.* **47** (04): 1-7.
- Jha, K.N. and Chakma, A. 1999. Heavy-oil recovery from thin pay zones by EM heating. *Energy Sources* **21** (1-2): 63–73.
- Johnson, R.B. and DeGraff, J.V. 1988. *Principles of engineering geology.* **497**. New York, Wiley.
- Josh, M. and Clennell, B. 2015. Broadband electrical properties of clays and shales: Comparative investigations of remolded and preserved samples. *Geophysics.* **80** (2): 129–143.
- Junior, I.P., Pereira, M.S., dos Santos, J.M., Duarte, C.R., Ataíde, C.H., and Panisset, C.M.D.Á. 2015. Microwave remediation of oil well drill cuttings. *J. Petr. Sci. Eng.* **134**: 23-29.
- Jury, W.A. and Horton, R. 2004. *Soil Physics*, 6th Edition, Wiley.

- Kang, Y., Chen, M., Chen, Z., You, L., and Hao, Z. 2016. Investigation of formation heat treatment to enhance the multiscale gas transportability of shale. *J. Nat. Gas Sci. Eng.* **35**: 265-275.
- Kar, T. and Hascakir, B. 2015. The role of resins, asphaltenes, and water in water–oil emulsion breaking with microwave heating. *Energy Fuels* **29** (6): 3684-3690.
- Kaur, R., Newborough, M., and Probert, S.D. 1993. Multi-purpose mathematical model for electromagnetic-heating processes. *Appl. Energy* **44** (4): 337-386.
- Kasevich, R.S., Price, S.L., Faust, D.L., and Fontaine, M.F. 1994. Pilot testing of a radio frequency heating system for enhanced oil recovery from diatomaceous earth. Paper SPE-28619-MS presented at the SPE Annual Technical Conference and Exhibition, New Orleans, Louisiana, U.S.A., 25-28 September.
- Keshavarz, M., Okuno, R., and Babadagli, T. 2014. A semi-analytical solution to optimize single-component solvent coinjection with steam during SAGD. *Fuel* **144**: 400-414.
- Keysight Technology, Keysight (Agilent) 85070E dielectric probe kit 200MHz to 50GHz, USA, June 14, 2012.
- Keysight Technology, Basics of measuring the dielectric properties of materials, Application Note, USA, November 19, 2014.
- Koch, A., Sotskiy, S., Mustafina D., and Danov, V. 2013. Mechanism of heavy oil recovery driven by electromagnetic inductive heating. Paper SPE-165507-MS presented at the SPE Heavy Oil Conference-Canada, Calgary, Alberta, Canada, 11–13 June.
- Komarov, V.V. 2012. Handbook of dielectric and thermal properties of materials at microwave frequencies. Artech House, Boston, London.
- Koolman, M., Huber, N., Diehl, D., and Wacker, B. 2008. EM heating method to improve steam assisted gravity drainage. Paper SPE-117481-MS presented at the SPE International Thermal Operations and Heavy Oil Symposium, Calgary, Alberta, Canada, 20–23 October.
- Kovaleva, L., Davletbaev, A., Babadagli, T., and Stepanova, Z. 2010. Effects of electrical and radio-frequency electromagnetic heating on the mass-transfer process during miscible injection for heavy-oil recovery. *Energy Fuels* **25** (2): 482–486.
- Kulkarni, M.M. and Rao, D.N. 2006. Characterization of operative mechanisms in gravity drainage field projects through dimensional analysis. Paper SPE-103230-MS presented at the

SPE Annual Technical Conference and Exhibition, San Antonio, Texas, USA, 24-27 September.

- Lashgari, H.R., Delshad, M., Sepehrnoori, K., and de Rouffignac, E. 2016. Development and application of electrical-joule-heating simulator for heavy-oil reservoirs. *SPE J.* **21** (1): 87-100.
- Lasne, Y., Paillou, P., Freeman, A., Farr, T., McDonald, K.C., Ruffie, G., Malezieux, J.M., Chapman, B., and Demontoux, F. 2008. Effect of salinity on the dielectric properties of geological materials: Implication for soil moisture detection by means of radar remote sensing. *IEEE Trans. Geosci. Remote Sens.* **46**: 1674-1688.
- Leão, T.P., Perfect, E., and Tyner, J.S. 2015. Evaluation of Lichtenecker's mixing model for predicting effective permittivity of soils at 50 MHz. *Trans. ASABE.* **58** (1): 83-91.
- Lee, B.I. and Kesler, M.G. 1975. A generalized thermodynamic correlation based on three parameter corresponding states. *AIChE J.* **21** (3): 510-527.
- Lesaint, C., Simon, S., Lesaint, C., Glomm, W.R., Berg, G., Lundgaard, L.E., and Sjöblom, J. 2012. Dielectric properties of asphaltene solutions: Solvency effect on conductivity. *Energy Fuels* **27** (1): 75-81.
- Lesaint, C., Spets, Ø., Glomm, W. R., Simon, S., and Sjöblom, J. 2010. Dielectric response as a function of viscosity for two crude oils with different conductivities. *Colloids Surf. A: Physicochem. Eng. Aspects* **369** (1-3): 20-26.
- Leyva-Gomez, H. and Babadagli, T. 2014. Optimal application conditions of steam-solvent injection for heavy oil/bitumen recovery from fractured reservoirs: An experimental approach. Paper SPE-172901-MS presented at the SPE International Heavy Oil Conference and Exhibition, Mangaf, Kuwait, 8-10 December.
- Li, G., Meng, Y., and Tang, H. 2006. Clean up water blocking in gas reservoirs by microwave heating: laboratory studies. Paper SPE-101072-MS presented at the SPE International Oil & Gas Conference and Exhibition, Beijing, China, 5-7 December.
- Li, H., Zheng, S., and Yang, D.T. 2013. Enhanced swelling effect and viscosity reduction of solvent(s)/CO<sub>2</sub>/Heavy-oil systems. *SPE J.* **18** (4): 695-707.
- Lin, B.Q., Li, H., Dai, H.M., Zhu, C.J., and Yao, H. 2016. Three-dimensional simulation of microwave heating coal sample with varying parameters. *Appl. Therm. Eng.* **93**: 1145-1154.

- Liu, H., Cheng, L., Li, C., Xiong, H., and Xiao, P. 2017. An investigation into temperature distribution and heat loss rate within the steam chamber in expanding-solvent SAGD process. Paper SPE-184963-MS presented at the SPE Canada Heavy Oil Technical Conference, Calgary, Alberta, Canada, 15–16 February.
- Lobe, V.M. 1973. *A Model for the Viscosity of Liquid-Liquid Mixtures*. MSc Thesis, University of Rochester, Rochester, New York.
- Lowe, D.F., Oubre, C.L., and Ward, C.H., 2000. Soil vapor extraction using radio frequency heating: Resource manual and technology demonstration. Boca Raton, FL, Lewis Publishers.
- Luque, A., Leiss, B., Alvarez-Lloret, P., Cultrone, G., Siegesmund, S., Sebastian, E., and Cardell, C. 2011. Potential thermal expansion of calcitic and dolomitic marbles from Andalusia (Spain). *J. Appl. Crystallogr.* **44** (6): 1227-1237.
- Majdzadeh-Ardakani, K. and Holl, M.M.B. 2017. Nanostructured materials for microwave receptors. *Prog. Mater Sci.* **87**: 221-245.
- McGee, B.C. 2008. Electro-thermal pilot in the Athabasca oil sands: Theory versus performance. Paper PETSOC-2008-209 presented at the Canadian International Petroleum Conference, Calgary, Canada, 17-19 June.
- Metaxas, A.C. and Meredith, R.J. 1983. Industrial microwave heating. London : Peter Peregrinus Ltd. on behalf of the Institution of Electrical Engineers, 1983.
- Molaro, J.L., Byrne, S., and Le, J.L. 2017. Thermally induced stresses in boulders on airless body surfaces, and implications for rock breakdown. *Icarus* **294**: 247-261.
- Moreno, L. and Babadagli, T. 2014. Asphaltene precipitation, flocculation and deposition during solvent injection at elevated temperatures for heavy oil recovery. *Fuel* **124**: 202-211.
- Nasr, T.N., Beaulieu, G., Golbeck, H., and Heck, G. 2003. Novel expanding solvent-SAGD process “ES-SAGD”. *J. Can. Pet. Technol.* **42** (1): 13–16.
- Nenniger, J. and Nenniger, E. 2008. Method and apparatus for stimulating heavy oil production. US Patent No. 7,363,973.
- Okassa, F.D., Godi, A., De Simoni, M., Manotti, M., and Maddinelli, G. 2010. A nonconventional EOR technology using RF/MW heating coupled with a new patented well/reservoir interface. Paper SPE-134324-MS presented at the SPE Annual Technical Conference and Exhibition, Florence, Italy, 22-23 September.

- Ono, S. and Kenji M. 2015. Influence of pressure and temperature on the electrical conductivity of dolomite. *Phys. Chem. Miner.* **42** (9): 773-779.
- Pasalic, D., Vaca, P., Okoniewski, M., and Diaz-Goano, C. 2015. EM heating: A SAGD alternative strategy to exploit heavy oil reservoirs. Paper WHOC15-150 presented at the World Heavy Congress, Edmonton, Alberta, Canada, 24–26 March.
- Peng, D.Y. and Robinson, D.B. 1978. The characterization of the heptanes and heavier fractions for the GPA Peng-Robinson Programs. GPA Research Report RR-28.
- Peng, Z., Hwang, J.Y., Kim, B.G., Kim, J.Y., and Wang, X. Microwave permittivity, permeability, and penetration depth of pyrite. *Characterization of Minerals, Metals, and Materials 2014*, John Wiley & Sons, Inc.
- PetroWiki. 2015. Isotropic elastic properties of minerals. [http://petrowiki.org/index.php?title=Isotropic\\_elastic\\_properties\\_of\\_minerals&oldid=48038](http://petrowiki.org/index.php?title=Isotropic_elastic_properties_of_minerals&oldid=48038)
- Pizarro, J.O.S. and Trevisan, O.V. 1990. Electrical heating of oil reservoirs: Numerical simulation and field test results. *J. Pet. Technol.* **42** (10): 1320–1326.
- Popescu, M.A., Isopescu, R., Matei, C., Fagarasan, G., and Plesu, V. 2014. Thermal decomposition of calcium carbonate polymorphs precipitated in the presence of ammonia and alkylamines. *Adv. Powder Technol.* **25**: 500–507.
- Prokopenko, A. 2011. Microwave heating for emolliating and fracture of rocks. *Advances in Induction and Microwave Heating of Mineral and Organic Materials*, InTech.
- Punase, A. and Hascakir, B. 2016. Stability determination of asphaltenes through dielectric constant measurements of polar oil fractions. *Energy Fuels* **31** (1): 65-72.
- Reid, R.C., Prausnitz, J.M., and Sherwood, T.K. 1977. *The Properties of Gases and Liquids*. New York City: McGraw-Hill.
- Reis, J.C. 1992. A steam-assisted gravity drainage model for Tar Sands: Linear Geometry. *J. Can. Petrol. Technol.* **31** (10): 14-20.
- Rezaei, N., Mohammadzadeh, O., and Chatzis, I. 2010. Warm VAPEX: A thermally improved vapor extraction process for recovery of heavy oil and bitumen. *Energy Fuels* **24** (11): 5934-5946.
- Robinson, J.P., Kingman, S.W., and Onobrakpeya, O. 2008. Microwave-assisted stripping of oil contaminated drill cuttings. *J. Environ. Manage.* **88**: 211-218.

- Rottenfusser, B. and Ranger, M.A. 2004. Geological comparison of six projects in the Athabasca oil sands. CSPG-Canadian Heavy Oil Association-CWLS Joint Conf. (ICE 2004), Calgary, Canada, May 31- June 4.
- Sadeghi, A., Hassanzadeh, H., and Harding, T.G. 2017. Modeling of desiccated zone development during electromagnetic heating of oil sands. *J. Petr. Sci. and Eng.* **154**: 163-171.
- Sadeghi, A., Hassanzadeh, H., and Harding, T.G. 2017. Thermal analysis of high frequency electromagnetic heating of lossy porous media. *Chem. Eng. Sci.* **172**: 13-22.
- Sadeghi, A., Hassanzadeh, H., and Harding, T.G. 2017. A comparative study of oil sands preheating using electromagnetic waves, electrical heaters and steam circulation. *Int. J. Heat Mass Transfer* **111**: 908-916.
- Sahni, A., Kumar, M., and Knapp, R.B. 2000. EM heating methods for heavy oil recovery. Paper SPE-62550-MS presented at the SPE/AAPG Western Regional Meeting, Long Beach, California, 19-23 June.
- Saidian, M., Godinez, L.J., and Prasad, M. 2016. Effect of clay and organic matter on nitrogen adsorption specific surface area and cation exchange capacity in shales (mudrocks). *J. Nat. Gas Sci. Eng.* **33**: 1095–1106.
- Sass, J.H. 1965. The thermal conductivity of fifteen feldspar specimens. *J. Geophys. Res.* **70** (16): 4064-4065.
- Schieck, R., Hartmann, A., Fiechter, S., Könenkamp, R., and Wetzels, H. 1990. Electrical properties of natural and synthetic pyrite (FeS<sub>2</sub>) crystals. *J. Mater. Res.* **5** (7): 1567-1572.
- Shabro, V., Kelly, S., Torres-Verdín, C., Sepehrnoori, K., and Revil, A. 2014. Pore-scale modeling of electrical resistivity and permeability in FIB-SEM images of organic mudrock. *Geophys.* **79** (5): 289-299.
- Sheu, E.Y. and Acevedo, S. 2006. A dielectric relaxation study of precipitation and curing of Furril crude oil. *Fuel* **85** (14-15): 1953-1959.
- Sheu, E.Y., Storm, D.A., and Shields, M.B. 1994. Dielectric response of asphaltenes in solvent. *Energy Fuels* **8** (3): 552-556.
- Skauge, A., Fuller, N., and Hepler, L.G. 1983. Specific heats of clay minerals: sodium and calcium kaolinites, sodium and calcium montmorillonites, illite, and attapulgite. *Thermochim. Acta.* **61** (1-2): 139-145.

- Sresty, G.C., Dev, H., and Snow, R.H. 1986. Recovery of bitumen from Tar sand deposits with the radio frequency process. *SPE Res. Eng.* **1** (1): 85–94.
- Tang, J., Feng, H., and Lau, M. 2001. *Microwave heating in food processing. Advances in Agricultural Engineering*, World Scientific Publisher, New York, Chap. 1.
- Tiwari, P., Deo, M., Lin, C.L., and Miller, J.D. 2013. Characterization of oil shale pore structure before and after pyrolysis by using X-ray micro CT. *Fuel* **107**: 547–554.
- Toifl, M., Meisels, R., Hartlieb, P., Kuchar, F., and Antretter, T. 2016. 3D numerical study on microwave induced stresses in inhomogeneous hard rocks. *Miner. Eng.* **90**: 29-42.
- Trautman, M., Ehresman, D., Edmunds, N., Taylor, G., and Cimolai, M. 2013. Effective solvent extraction system incorporating EM heating. U.S. Patent No. 8,616,273. Washington, DC.
- Twu, C.H. 1984. An internally consistent correlation for predicting the critical properties and molecular weights for petroleum and coal-tar liquids. *Fluid Phase Equilibria* **16** (2): 137–150.
- Ungerer, P., Collell, J., and Yiannourakou, M. 2014. Molecular modeling of the volumetric and thermodynamic properties of kerogen: Influence of organic type and maturity. *Energy Fuels* **29** (1): 91-105.
- Wacker, B., Karmeileopardus, D., Trautmann, B., Helget, A., and Torlak, M. 2011. Electromagnetic heating for in-situ production of heavy oil and bitumen Reservoirs. Paper SPE-148932-MS presented at the Canadian Unconventional Resources Conference, Alberta, Canada, 15-17 November.
- Wagner, N., Bore, T., Robinet, J.C., Coelho, D., Taillade, F., and Delepine-Lesoille, S. 2013. Dielectric relaxation behavior of Callovo-Oxfordian clay rock: A hydraulic-mechanical-electromagnetic coupling approach. *J. Geophys. Res: Solid Earth* **118** (9): 4729-4744.
- Wang, H., Rezaee, R., and Saeedi, A. 2016. Preliminary study of improving reservoir quality of tight gas sands in the near wellbore region by microwave heating. *J. Nat. Gas Sci. Eng.* **32**: 395–406.
- Wang, J.R. and Schmugge, T.J. 1980. An empirical model for the complex dielectric permittivity of soils as a function of water content. *Geosci. Remote Sens.* **4**: 288-295.
- Wang, Y. and Djordjevic, N. 2014. Thermal stress FEM analysis of rock with microwave energy. *Int. J. Miner. Process.* **130**: 74–81.

- Wharton, R.P., Rau, R.N., and Best, D.L. 1980. Electromagnetic propagation logging: Advances in technique and interpretation. Paper SPE-9267-MS presented at the SPE Annual Technical Conference and Exhibition, Dallas, Texas, 21-24 September.
- Wise, S. and Patterson, C. 2016. Reducing supply cost with ESEIEH<sup>TM</sup> pronounced easy. Paper SPE-180729-MS presented at the SPE Heavy Oil Conference-Canada, Calgary, 7–9 June.
- Yang, L., Marshall, A.M., Wanatowski, D., Stace, R., and Ekneligoda, T. 2017. Effect of high temperatures on sandstone - A computed tomography scan study. *Int. J. Phys. Modell. Geotech.* **17** (2): 75–90.
- Yaws, C.L. 2003. *Yaws' handbook of thermodynamic and physical properties of chemical compounds*. Knovel Corporation.
- Younglove, B.A. and Ely, J.F. 1987. Thermophysical properties of fluids. II. Methane, Ethane, Propane, Isobutane, and Normal Butane. *J. Phys. Chem. Ref. Data* **16** (4): 577-798.
- Zhang, Y., Chen, P., Liu, S., Peng, P., Min, M., Cheng, Y., Anderson, E., Zhou, N., Fan, L., Liu, C., and Chen, G. 2017. Effects of feedstock characteristics on microwave-assisted pyrolysis - A review. *Bioresour. Technol.* **230**: 143-151.
- Zhou, W., Chen, S., and Dong, M. 2016. Novel insights on initial water mobility: Its effects on steam-assisted gravity drainage performance. *Fuel* **174**: 274-286.